

Faculty of Mathematics, Informatics and Natural Science  
Department of Chemistry at the University of Hamburg

Dissertation

---

*Water-based Cryogenic Mass Spectrometry  
with Ultra-short Laser Pulses*

---

Submitted by Andrey Krutilin

In partial fulfillment of the requirements for the degree of  
Doctor of Natural Sciences (Dr. rer. nat.)

Hamburg 2022

---

**Submission**

20 May 2022

**Print Permission**

05 December 2022

**Supervisors of the Thesis**

Prof. Dr. Dwayne R. J. Miller

Prof. Dr. Hartmut Schlüter

**Date of Disputation**

08 July 2022

**In the Presence of the Committee Members**

Prof. Dr. Hartmut Schlüter

Prof. Dr. Arwen Pearson

Dr. Maria Riedner

Prof. Dr. Sadia Bari

Dr. Sascha W. Epp

---

---

---

The research was conducted from 09.2017 until 09.2021 in the Max Planck Institute for Structure and Dynamics of the Matter in the group of Prof. Dr. R. J. Dwayne Miller.



---

*For my Family*

---

## Publications

Kwiatkowski, M., Wurlitzer, M., Krutilin, A., Kiani, P., Nimer, R., Omid, M., Schlüter, H. (2016). Homogenization of tissues via picosecond-infrared laser (PIRL) ablation: Giving a closer view on the in-vivo composition of protein species as compared to mechanical homogenization. *Journal of Proteomics*, no. 134, pp. 193–202. <https://doi.org/10.1016/j.jprot.2015.12.029>

Krutilin, A., Maier, S., Schuster, R., Kruber, S., Kwiatkowski, M., Robertson, W. D., Schlüter, H. (2019). Sampling of Tissues with Laser Ablation for Proteomics: Comparison of Picosecond Infrared Laser (PIRL) and Microsecond Infrared Laser (MIRL). *Journal of Proteome Research*, no. 18, pp. 1451–1457. <https://doi.org/10.1021/acs.jproteome.9b00009>

Krutilin, A., Epp, S. W., Alejo, G. M. L., Busse, F., Gitaric, D., Schikora, H., Schwoerer H., Tellkamp F. Peptide Mass Spectra from Micrometer Thick Ice Films Produced with Femtosecond Pulses. *Analytical Chemistry*, vol. 94, no. 39, pp. 13359 - 13367 2022. [10.1021/acs.analchem.2c01810](https://doi.org/10.1021/acs.analchem.2c01810)

Krutilin, A., Epp, W. S., Busse, F., Alejo, G. M. L., Miller, D. R. J., Cryogenic Mass Spectrometry of Peptides and Proteins from Ice Films with Different Thickness in Transmission and Reflection Geometry. *Manuscript*

---

# Contents

Publications .....	VI
Contents .....	VII
Abbreviations .....	X
Kurzzusammenfassung.....	XII
Abstract .....	XIV
<b>1 Introduction.....</b>	<b>1</b>
1.1 Aim of the Thesis.....	7
1.2 Thesis Outline.....	8
<b>2 Laser-based Mass Spectrometry.....</b>	<b>9</b>
2.1 Instrumentation in the Present Work.....	9
2.2 Laser-based Ion Sources .....	10
2.2.1 General Ion Sources .....	10
2.2.2 Matrix-assisted Laser Desorption and Ionization (MALDI) .....	11
2.2.3 IR-MALDI with Water and other Organic Solvents .....	14
2.2.4 Desorption by Impulsive Excitation (DIVE) .....	14
2.2.5 Laser Desorption and Ionization without a Matrix .....	16
2.2.6 Desorption and Ionization with Ultra-short Pulses .....	17
2.3 Time-of-flight Mass Spectrometry .....	18
<b>3 Materials and Methods for Cryogenic-based Mass Spectrometry ..</b>	<b>21</b>
3.1 Materials .....	22
3.2 Methods .....	23
3.2.1 Laser Systems.....	23
3.2.2 Microscopy .....	24
3.2.3 Sample Preparation.....	25
3.2.4 Time-of-flight Mass Spectrometer .....	28
3.2.5 Data Acquisition and Processing.....	33
3.3 Summary .....	39
<b>4 DIVE Mass Spectrometry with Cryogenic Thin Films .....</b>	<b>41</b>
4.1 Introduction .....	41
4.2 Pure Water as Matrix for Infrared Laser Desorption and Ionization.....	43

---

4.2.1	Bulk Frozen Water Droplets.....	43
4.2.2	Semi-thick Aqueous Films .....	45
4.2.3	Thin Ice Films.....	48
4.2.4	Ultra-thin Ice Films .....	51
4.3	Additives for Infrared Laser Desorption and Ionization .....	56
4.3.1	Sucrose and Glycerol.....	56
4.3.2	Semi-Thick Films with Water and Glycerol .....	57
4.3.3	Ultra-thin Films with Water and Glycerol .....	60
4.4	Analytical Performance of DIVE Mass Spectrometry .....	67
4.4.1	Limit of Detection – Water .....	67
4.4.2	Limit of Detection – Glycerol .....	68
4.4.3	Mass Limit – Water .....	70
4.4.4	Mass Limit – Glycerol .....	71
4.4.5	Multimer Formation for Mass Calibration .....	73
4.5	Ion Collection Yield .....	73
4.6	Substrate Contribution to Desorption and Ionization .....	74
4.7	Summary .....	77

## **5 Non-resonant Femtosecond Pulses for Matrix-free Detection of**

### **Peptides and other Organic Molecules..... 81**

5.1	Introduction .....	82
5.2	Substrate Effect and Signal Onset in Femtosecond Laser Mass Spectrometry.....	83
5.2.1	Ablation Crater Produced with Femtosecond Pulses .....	85
5.2.2	Femtosecond Pulse Interaction with Substrates at Different Temperature and the Impact on Film Thickness .....	87
5.3	Femtosecond Laser Mass Spectrometry at Different Temperatures .....	89
5.4	Fragmentation .....	94
5.5	Analytical Performance of Femtosecond Laser Mass Spectrometry.....	96
5.5.1	Shot-to-shot Repeatability .....	96
5.5.2	Limit of Detection .....	97
5.5.3	Mass Limit .....	97
5.5.4	Mass Calibration .....	99
5.6	C60 Fullerene – A Hydrophobic Molecule in a Non-polar Solvent .....	100
5.7	Ion Collection Yield .....	103
5.8	Summary .....	104

## **6 Discussion.....107**

---

---

<b>7</b>	<b>Outlook .....</b>	<b>123</b>
<b>8</b>	<b>Bibliography .....</b>	<b>125</b>
<b>9</b>	<b>Appendix .....</b>	<b>137</b>
9.1	Figures.....	137
9.2	Tables .....	145
<b>10</b>	<b>Acknowledgment.....</b>	<b>147</b>
<b>11</b>	<b>CMR-Chemicals.....</b>	<b>149</b>
<b>12</b>	<b>Affidavit (eidesstatliche Erklärung) .....</b>	<b>150</b>

---

## Abbreviations

°C	Grad Celsius
µg	Microgram
µl	Microliter
µm	Micrometer
a.u.	Arbitrary units
abs	Absolute
AFM	Atomic force microscopy
amol	attomole
AP IR-MALDI	Atmospheric pressure infrared matrix-assisted laser desorption ionization
cm	Centimetre
CPCD	Chemical dynamics model
DIOS	Desorption and ionization on silicon
DIVE	Desorption ionization by vibrational excitation
DNA	Deoxyribonucleic acid
ESI	Electrospray ionization
fmol	femtomole
fs	Femtosecond
FWHM	Full width half maximum
g	Gram
IMS	Imaging mass spectrometry
IR	Infrared
J	Joule
kDa	Kilodaltons
LA	Laser ablation
LA ESI	Laser ablation and electron spray ionization
LDI	Laser Desorption and ionization
M	Mol·l <sup>-1</sup>
m/z	Mass-to-charge ratio
MALDI	Matrix-assisted laser desorption ionization
MCP	Microchannel plate
mg	Milligram
ml	Millilitre
mmol	Millimole
MS	Mass spectrometry
MS/MS	Tandem mass spectrometry
nl	Nanoliter

---

Non-resonant fs IR-LDI	Non-resonant femtosecond Infrared laser desorption ionization
Non-resonant IR-(MA)LDI	Infrared matrix-assisted laser desorption ionization with water
ns	nanosecond
PFM	Polar fluid model
PIRL	Picosecond infrared laser
pmol	Picomol
ps	Picosecond
REMPI	Resonance enhanced multiphoton ionization
resonant IR-MALDESI	Resonant infrared matrix assisted laser desorption and electrospray ionization
Resonant IR-MALDI	Infrared matrix-assisted laser desorption ionization
RG	Reflection geometry
RGA	Residual Gas analyser
RIMS	Resonance ionization mass spectrometry
RNA	Ribonucleic acid
rpm	Revolutions per minute
SALDI	Surface-assisted laser desorption and ionization
SSD	Sample standard deviation
SSpS	Single shot per spot
TFA	Trifluoroacetic acid
TG	Transmission geometry
TOF-MS	Time-of-flight mass spectrometry
UV	Ultraviolet
UV-MALDI	Ultraviolet matrix-assisted laser desorption ionization
$\lambda$	Wavelength

---

---

## Kurzzusammenfassung

Das Aufkommen sogenannter weicher Ionisationstechniken wie der matrix-unterstützten Laser Desorption und Ionisierung und der Elektrosprayionisierung ermöglicht die Untersuchung nichtflüchtiger und fragiler Moleküle bei geringfügiger Fragmentierung. Seither ist die Massenspektrometrie (MS) zu einer unverzichtbaren analytischen Methodik in der biochemischen und medizinischen Forschung avanciert und hat neue Forschungsbereiche wie die Proteomik erschlossen. Eine zentrale, noch Frage in der Biochemie, ist die Identifizierung und Untersuchung aller Arten von Proteinen in einer einzelnen Zelle. Da mit den aktuellen Technologien im wesentlichen Zellcluster untersucht werden, bleibt die Frage, wie eine Veränderung auf der molekularen Ebene in einer einzelnen Zelle zu einer Krankheit wie Krebs führen kann, unbeantwortet. Ein tiefgreifendes Verständnis der Ursache einer Erkrankung kann jedoch lediglich erreicht werden, wenn alle Proteinfunktionen und die Entwicklung von Fehlfunktionen in einer einzelnen Zelle verstanden sind. Bei mehr als einer Milliarde Proteinspezies ist dies eine anspruchsvolle Aufgabe mit hohen Anforderungen an die wissenschaftlichen Apparaturen. Obwohl MALDI und ESI aufgrund ihrer Robustheit und Wartungsfreundlichkeit die am häufigsten eingesetzten analytische Methoden sind, stellt die Probenvorbereitung, die für diese Methoden notwendig ist, ein wesentliches Problem dar. Auch arbeiten diese Methoden nicht unter *in vivo*-Bedingungen und erfüllen somit nicht die Voraussetzungen, Proteine in ihrer natürlichen Umgebung in einer einzelnen Zelle zu untersuchen.

In diesem Projekt wurden Peptide und Proteine im Wasser und ohne weitere Additive massenspektrometrisch untersucht. Die Analyse von Biomolekülen aus ihrem nativen Milieu vereinfacht erheblich die Probenvorbereitung und ermöglicht am ehesten den Analyten *in vivo* abzubilden – ein grundlegender Schritt für die Proteomik einer einzelnen Zelle. Zu Beginn wurde ein neues Protokoll für biologische Proben, die in dünnen wässrigen Schichten eingebettet sind, vorgestellt. Anschliessend wurden Infrarot Pulse (resonante IR-(MA)LDI) verwendet, die mit Wasser resonant wechselwirken, um die Desorption und Ionisation hervorzurufen. Im zweiten Abschnitt werden nicht-resonante Femtosekunden Infrarot Pulse (nicht-resonante IR-LDI) verwendet, um primär eine Wechselwirkung mit dem Substrat auszunutzen und dadurch eine oberflächenunterstützte Desorption und Ionisation des Analyten zu erreichen. In beiden Abschnitten wurden Biomoleküle in einem Flugzeitmassenspektrometer untersucht.

Die resonante IR-(MA)LDI ist besonders praktisch, weil bei dieser Technik Wasser als Matrix verwendet wird, um Biomoleküle aus dem Probengemisch zu extrahieren.

---



---

Da Wasser in allen lebenden Organismen vorkommt, sind aufwendige Probenvorbereitungen und andere Voruntersuchungen minimal. Es wurde ein Pikosekunden-Infrarotlaser (PIRL) verwendet, der auf eine Wellenlänge von 3  $\mu\text{m}$  abgestimmt ist, wo Wasser einen hohen Absorptionskoeffizienten hat. Unsere Ergebnisse zeigen, dass infrarot basierte Massenspektrometrie erfolgreich Massenspektren von Peptiden und Proteinen erzeugt. Wir haben mehrere Probenvorbereitungen entwickelt, die die etablierten Probenvorbereitungsprotokolle unter kryogenen Bedingungen erheblich vereinfachen. Ein entscheidendes Merkmal unseres Probenvorbereitungsprotokolls ist die Reproduzierbarkeit und die Einfachheit der Durchführung, die nur wenige Minuten dauert. Mit diesen Errungenschaften ist die (Infrarot) Laser basierte Massenspektrometrie einer breiteren Gemeinschaft zugänglich. Neben reproduzierbaren Probenvorbereitung wurden unterschiedliche Ablationstechniken getestet und eine hohe Empfindlichkeit erreicht. Wir haben festgestellt, dass das *Oversampling*, d. h. die Rasterung des Probenbereichs in Abständen, die kleiner sind als der Laserdurchmesser, die Qualität der Ergebnisse erheblich verbessert, insbesondere wenn die Schrittweite auf wenige Mikrometer begrenzt ist. Schließlich erreichen wir eine Empfindlichkeit von 200 fmol pro Laserschuss, die für eine biologische oder biochemische Fragestellung ausreichend ist. In darauf folgenden Experimenten wurde Glycerol als Additive zur Steigerung der Empfindlichkeit verwendet was zu 1 fmol pro Laserschuss führte.

Im zweiten Abschnitt wurde nicht-resonante IR-LDI, die primär mit den Substraten wechselwirken, erforscht. Hierbei wurden Peptide in Wasser und ohne weitere Zusätze auf verschiedenen Substraten erfolgreich nachgewiesen. Eine zentrale Erkenntnis ist, dass keine Oberflächenmodifikation des Substrates erforderlich ist, um qualitativ hochwertige Analytsignale zu erhalten. Eine systematische Studie mit temperaturabhängigen Messungen zeigt, dass ein niedriges Analyt-Wasser-Verhältnis einen Vorteil für Analytsignale mit hoher Intensität darstellt. Weiterhin wurde eine außergewöhnlich hohe Empfindlichkeit von 25 amol und eine Massengrenze von 2.5 kDa erreicht. Schließlich beobachteten wir eine Vielzahl an Fragmenten, die jedoch eine geringere Signalintensität als der Molekülionenpeak aufwies. Die Methode kann daher auch für die Aufklärung von Strukturen genutzt werden. Die Ergebnisse zeigen, dass die Analyse wässriger Proben ohne aufwändige Probenvorbereitung oder Oberflächenmodifikation bei verschiedenen Substraten und mit unterschiedlichen (Laser) Wellenlängen funktioniert.

---

## Abstract

The advent of soft ionization techniques such as MALDI and ESI has facilitated the study of non-volatile and fragile molecules with high masses in the absence of fragmentation. Since then, mass spectrometry (MS) has become a vital tool in biochemical and medical research, and these methods have paved the way for new research fields such as proteomics. A central yet unanswered scientific question is identifying and investigating every type of protein and its location within a single cell. Recent technologies have targeted clusters of cells to analyze and investigate diseases such as cancer. However, an in-depth understanding of cancer can only be reached when all protein functions and the evolution of malfunctions in a single cell are investigated and understood. With more than a billion different protein species, this is a challenging task and the requirements for scientific instrumentation are demanding.

Although MALDI and ESI are the most frequently employed analytical methods due to their robustness and maintainability, they also pose severe challenges, especially during sample preparation. The present work investigates new soft ionization techniques, which operate close to *in vivo* conditions while requiring minimal sample preparation - a foundational step in single-cell proteomics. First, a novel water-based sample preparation protocol is developed. Subsequently, two laser systems are employed to desorb and ionize the biomolecules in a resonant or non-resonant regime, which defines how laser pulses interact with water. The first method is coined resonant infrared laser-based matrix-assisted laser desorption and ionization (resonant IR-MALDI), and the second non-resonant femtosecond laser desorption and ionization (non-resonant fs IR-LDI).

Resonant IR-MALDI is especially useful as this technique targets water as an intermediate energy carrier to extract biomolecules from their native environment. Rigorous samples preparation and other pre-experimental steps are obsolete as water can be found in all living organisms. The present results show that such an approach can successfully produce mass spectra of peptides and proteins embedded in frozen aqueous solutions. Several sample preparation techniques were developed, which greatly simplify the established preparation protocols for specimens investigated under cryogenic conditions. Most importantly, a sample preparation protocol is reproducible and can be conducted within a few minutes. With these achievements, the IR laser-based MS is more streamlined and accessible to a broader scientific community. In addition to highly reproducible sample preparation, superior sensitivity have been achieved using various ablation techniques. We have discovered that oversampling, rastering the specimen area with distances smaller than the laser

---

---

diameter, greatly enhances the quality of the results, particularly when the step size is limited to a few micrometers. Ultimately, we can obtain a sensitivity of 200 fmol per laser shot, which is suitable for most biological and biochemical specimens, but with greatly reduced effort in sample preparation and access to *in vivo* conditions. In follow-up experiments glycerol was used as an additive to push the limit of detection leading ultimately to a sensitivity of 1 fmol per laser shot.

In the second project, non-resonant fs IR-LDI is used in the second project to detect peptides around 1 kDa by irradiating specimens deposited on different substrates. An important finding is that no surface modification is necessary to obtain high-quality analyte signals. A systematic study with temperature-dependent measurements reveals that a low water-analyte ratio is beneficial for the signal onset. Furthermore, an exceptional sensitivity of 25 amol and a mass limit of 2.5 kDa have been achieved. Finally, a vibrant fragmentation pattern for the investigated analytes have been observed, but those fragments show only a fraction of the intensity of the intact species. In this work, the developed method have shown that water targets can be detected without rigorous sample preparation or surface modification and that 2D imaging is possible for different specimens.



# 1 Introduction

Human physiology and pathology arise from coordinated interactions of various single cells. Within these cells, macromolecules such as RNA, DNA, and proteins are the protagonists in metabolic pathways [1]. For a better understanding of such interactions, advanced analytical instruments have been developed, but the low sensitivity and lack of throughput of the analytical methods hampered single-cell analysis [2]. In recent years, in the research area of genomics, a method known as next-generation sequencing [3] has facilitated the analysis of genes in a cell, but single-cell protein analysis, which is a niche of the research field of proteomics, remains limited due to the dynamics and the sheer amount of unique species compared to the static nature of the genes. At the current stage, researchers rely on methods that investigate cell clusters [4], effectively averaging the changes associated with a pathological pattern, and changes on the single-cell and molecular level remain elusive. The investigation of molecular species is a greater promise to obtain a holistic understanding of physiological changes.

Today, most proteomics laboratories are equipped with a mass spectrometer, which has the main function of determining the molecular weight of a given molecule, also known as an analyte. The molecule's weight is measured but, unlike in a balance, the mass-to-charge ratio is measured instead. A mass spectrometer consists of three main components: The ionization source, the mass analyzer, and the detector (**Figure 1.1A**). The latter two are operated in low-pressure conditions to assure high ion transmission and high voltage application, respectively, while the ionization source can be operated under ambient conditions and in a vacuum. Mass spectrometers only successfully detect charged species, and the task of the ionization source is to transform neutral species into charged particles. These charged particles are subjected to electric or magnetic fields, and each particle has unique interactions allow separation to be performed. Finally, the detector measures the arriving particles. J. J. Thomson introduced the initial design and concept of a mass spectrometer at the end of the nineteenth century [5], but it did not become a commonly used method until 50 years later.

A simple mass analyzer, also used in the present work, is time-of-flight, in which the flight time measurement determines the ions' mass-to-charge ratio [6]. The TOF-MS

ion source comprises two plates attached to a high voltage device and an ionization source (Figure 1.1B). One of the plates has a hole connected to the drift-free region, which has no potential. Finally, the detector records the arriving particles. The experiment begins by forming ions using a suitable ionization source, and once produced, the ions experience a repulsive field from the target plate and move towards the drift-free region. The separation principle of the TOF-MS correlates with lighter ions possessing higher kinetic energies and arriving at the detector earlier than heavier ions. The time spent in the source and the drift-free region before hitting the detector is measured. If all experimental parameters are known, a specific ion can be identified.

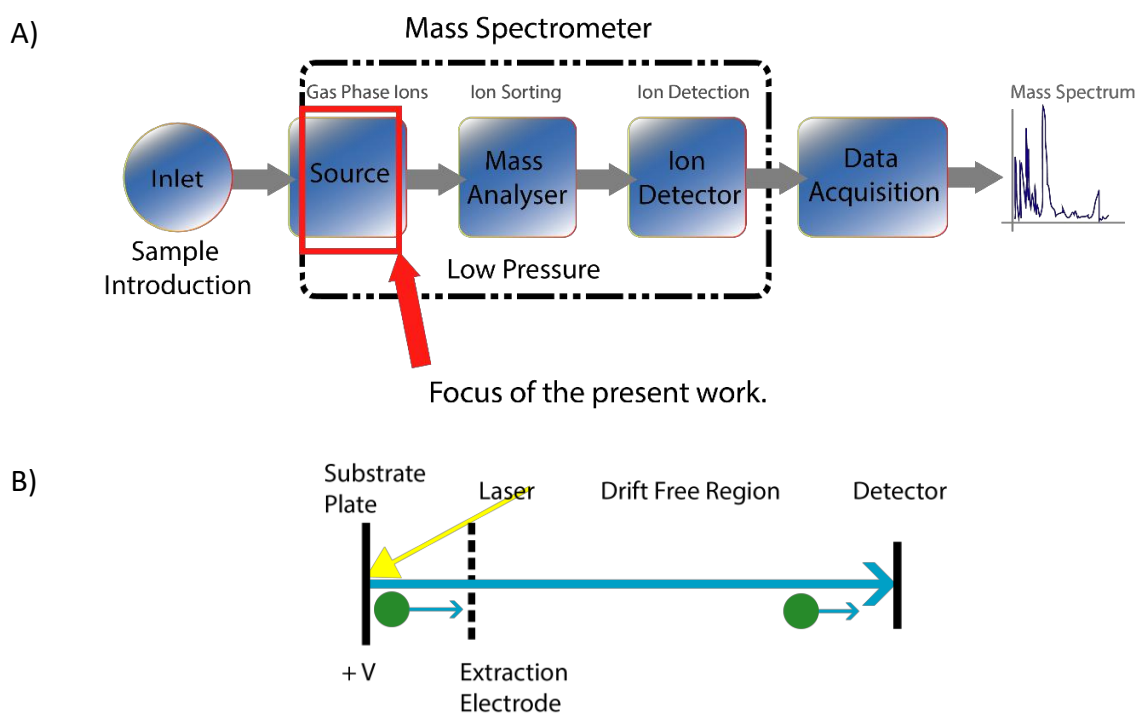


**Figure 1.1** A general mass spectrometer setup. A) Components of a mass spectrometer. Ion sources transform neutral species into ions. This transformation can occur in low-pressure or under ambient conditions. A mass analyzer sorts the ions according to their mass-to-charge ratio in the following step. A detector system provides an electrical signal after the particles' impact. The red square shows the focus of the present work. B) A simple TOF-MS, in which the yellow arrow indicates the ionization location.

The late adoption of the mass spectrometer in the research environment is linked to the lack of ionization sources for the larger biomolecules, which are highly relevant in biochemical processes. An important milestone was the advent of the laser in the 1960s [7], which has facilitated the ionization of larger biomolecules and laid the

foundation for the modern MS field [8]. The major difference between white light and laser light is that the latter is monochromatic, directional, and coherent. “Monochromatic” refers to the fact that a single central wavelength is emitted, while “directional” describes the low divergence angle of laser light compared to conventional light sources; lastly, “coherent” means that all light waves are in phase with each other. These features allow scientists to manipulate the laser light to their specific needs and, for instance, focus the laser beam to smaller spot sizes compared to a white light source. With this property, spot sizes of between 1 - 3  $\mu\text{m}$ , smaller than the size of a typical eukaryotic cell of 10 - 100  $\mu\text{m}$ , can be routinely achieved [9].

Lasers can be operated in two different modes. A continuous-wave laser (CW) operates with stable output power, while pulsed lasers’ output is characterized by a pulse train occurring at a repetition frequency. However, almost all mass spectrometric experiments are performed with a pulsed laser. As the name suggests, pulsed lasers emit pulses of light with a specific repetition rate and high energies are delivered within a particular time window. The time window is usually described as pulse duration and is an important parameter in laser-matter interaction. In general, the shorter the pulse duration, the higher the peak power and, therefore, the associated ionization rate. Hence, femto-, pico-, and nanosecond pulses show descending peak powers. Pulsed lasers were developed in the 1960s, and in conjunction with a mass spectrometer [10], particularly the TOF-MS, they provided a versatile ionization source to obtain structural information for glycopeptides and polysaccharides. However, non-volatile proteins and heavier biomolecules were still not accessible with direct laser irradiation leading to fragmentation.

Proteomics popularity grew when “soft” - ionization techniques such as MALDI [11], [12], and ESI [13], which have facilitated the investigation of large non-volatile biomolecules, were introduced in the 1980’. The term “soft” is associated with the analytes detection as an intact species without fragmentation of the peptide backbone.

UV-MALDI utilizes an artificial organic matrix, which is mixed with the analyte prior to the experiment. The principal purpose of the matrix is to absorb the incident laser light and hence the energy. Subsequently, the excited volume expands, and the ejected particles form a plume above the irradiated surface. However, the matrix’s properties of light absorption and matrix crystallization impact the analyte signal. Subsequently, in a little understood pathway [14], non-volatile and labile biomolecules are desorbed and ionized intact by protonation. In general, UV-MALDI is performed in acid conditions. Peptide and protein mixtures are simple to investigate with UV-MALDI, and scientists have progressed to more complex systems such as tissue sections [15], [16]. Applying a geometrical lattice of laser shots to the specimen in a documented location is termed IMS, and MALDI plays a central role [17]. Recently, a group

---

---

concerned with UV-MALDI IMS published a tissue image with a resolution of close to 1  $\mu\text{m}$  smaller than the dimensions of a single cell [18]. However, despite the triumphant advances in academia and industry, the method still encounters several obstacles. For instance, critical matrix size depends greatly upon a sample preparation protocol, which ultimately impacts the ablation area, reducing spatial resolution [19]. New spray devices have been developed to minimize matrix crystal size, but these efforts do not fully remedy the problem [20]. From a quantitative point of view, sample losses associated with sample preparation have also been reported [21]. On a qualitative level, the matrix effect can lead to analyte ion suppression and drastically alter the statement of an MS spectrum [19]. Consequently, an suitable choice of the matrix before the experiment [22] or even the application of multiple matrices increases the analytical performance [23]. However, introducing an additional sample preparation step can also reduce the overall MS performance. Hence, a reduction of sample preparation steps before the analysis is desirable.

Shortly after the introduction of UV-MALDI, scientists began to investigate other suitable matrices. Water became the focus, as it is found all living organisms and is the most abundant component. In principle, this feature allows the investigation of the specimen in *in vivo* conditions without any sample preparation steps as in UV-MALDI. Working with matrices sensitive to IR irradiation changes the acronym to IR-MALDI. However, if water is exclusively used as a matrix, the acronym is IR-(MA)LDI, while IR-MALDI employs other IR-sensitive matrices. IR-MALDI can work in principle under non-denaturing and acid-free conditions providing access to proteins, which otherwise precipitate [24] and are not accessible with UV-MALDI. To perform MALDI experiments with water, other laser systems must be used. As water has a high absorption coefficient at 2.94  $\mu\text{m}$  (**Figure 1.2**) laser systems were initially tuned to this wavelength, and the ablation was performed in a resonant regime. Water has a high absorption coefficient at 170 nm and below, but working with such a wavelength or even shorter is not practical as air is absorbed in this region, and the guidance of the laser beam should ideally take place in vacuum.



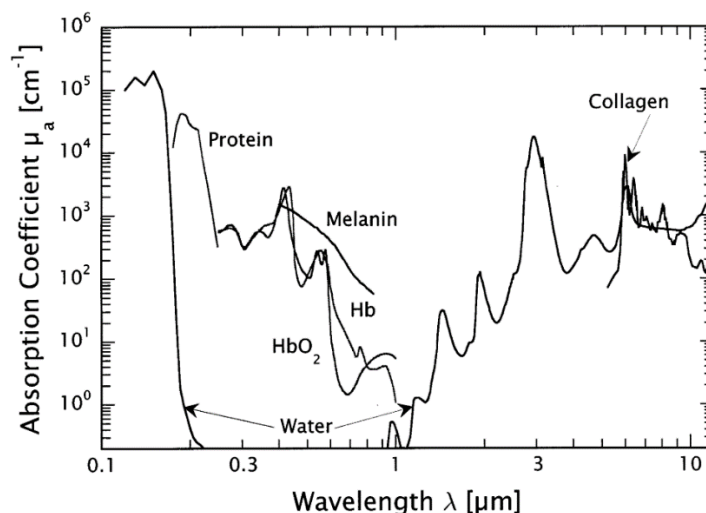


**Figure 1.2** Optical absorption coefficient of water and other tissue chromophores [25]. Reprinted with permission from *Mechanisms of Pulsed Laser Ablation of Biological Tissues*, copyright 2003, American Chemical Society.

Although water seems to be the ideal candidate to carry biomolecules, its high vapor pressure prevents it from remaining liquid in low-pressure conditions, as is the case in a mass spectrometer. One solution is to work with the water under ambient conditions or AP IR-MALDI, which is popular and is reflected in the high number of publications concerned with this topic [26]–[30]. In the published works, the irradiation of the specimen and the expanding plume is directly coupled to a mass spectrometer, but this setup leads to low ion yields, where the ion yield is defined as the number of ionized particles divided by the amount of total ejected particles. To overcome this limitation, additional post-ionization methods have been implemented. Most popular is resonant IR-MALDESI, where the laser-induced plume is cross-sectioned with an ESI and subsequently improves ion yield by several factors [31]–[34].

Increasing the ion yield further requires working under low-pressure conditions. As already mentioned, water is not suitable as a liquid matrix unless the specimen is actively cooled and remains frozen. In fact, this approach was the first cryogenic MS [35] publication after the initial UV-MALDI experiment.

Despite the exciting features of IR-(MA)LDESI referred above, several issues have impeded the wider use of low-pressure resonant IR-(MA)LDI. Due to the lack of IR-(MA)LDI studies, a general sample preparation protocol is lacking, and, as stated previously, sample preparation in UV-MALDI is crucial. Furthermore, resonant IR-(MA)LDI produces low ion yields because of the low photon energy delivered by the IR wavelength. Most intriguing is that the existing studies spent little time optimizing various laser parameters, sample preparation conditions, and sampling strategies

---

[35], [36]. In Dwayne R. J. Miller's working group, a laser system was designed to produce 2.94  $\mu\text{m}$  wavelength pulses with a duration of 400 picoseconds and has the acronym PIRL. This pulse duration stands in great contrast to previous IR-(MA)LDI studies, where pulse duration was on a nanosecond timescale. A study concerned with the PIRL mechanism [37] suggested that energy is efficiently coupled to the O-H vibration mode of water. Subsequently, due to the strong hydrogen-bond network of water molecules, the deposited energy is rapidly redistributed and converted into heat. Such a regime is coined as DIVE. DIVE has been postulated to produce a high ion yield providing a promising tool for mass spectrometry [38]. Such a feature is intriguing as it can open the door for high sensitivity mass spectrometry with few sample preparation steps and, therefore, making single-cell investigation in principle possible.

Parallel to the developments of resonant IR-(MA)LDI, a non-resonant approach was also investigated in ambient and low-pressure conditions. Lasers operating in a non-resonant regime target the sample carrier, also known as the substrate. If water is a sample carrier, then non-resonant conditions are achieved when wavelengths between 200 and 1000 nm are employed. The exploitation of the substrate for desorption and ionization is not limited to water-rich samples. Ultimately, no matrix is needed to trigger a desorption and ionization process. This method is usually referred as SALDI [39], and hence non-resonant IR-LDI is more appropriate. SALDI's avoidance of matrix is a welcomed simplification, but the sample carrier must be chemically or mechanically modified [40]–[49]. Similar to the correct choice of the MALDI matrix, this is a time-consuming step. However, the need for substrate modification is not fully clarified because most SALDI studies lack laser parameter variation. Most SALDI measurements are performed in a commercial instrument designed for UV-MALDI experiments and use the provided laser with nanosecond pulses and wavelength in a UV region. However, femtosecond lasers as an ionization source have been moving into focus recently because of their high ionization rates connected to the high peak powers. Femtosecond MS is mostly used for elemental or small molecule analysis, which also works on a single cell level [50]. Complex samples such as tissue sections [51] are challenging to measure, and some reports showed severe fragmentation and provided ambiguous results [52]. However, a promising study conducted by Berry *et al.* [53] showed that intact proteins of up to 6 kDa were extracted from the aqueous thin film in low-pressure conditions. Unfortunately, further studies concerning the topic were not followed up. Therefore, a better understanding of fs interaction is desirable, especially if single cell analysis should become a routine procedure. Additionally, the small number of fs studies combined with cryogenic MS it is important to investigate laser-substrate interactions.

## 1.1 Aim of the Thesis

Laser Parameter in Combination with Cryogenic Mass Spectrometry

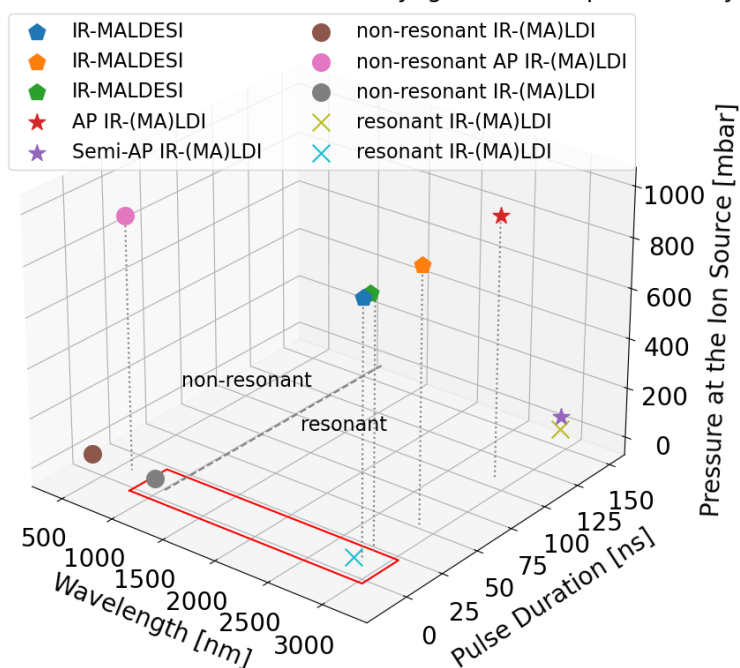


**Figure 1.3** This three-dimensional plot summarizes the laser and ion source parameters used from selected publications [29], [31], [35], [36], [53]–[56] combined with cryogenic MS. The axis wavelength and pulse duration represent the emitted laser beam, while pressure at the ion source axis indicates the pressure at the position of the ionization process. The red square highlights the laser parameters used in the present work. The dashed line divides the region where the emitted laser wavelength is mainly interacting with water as a sample carrier either in resonant or non-resonant regimes. The vertical dotted lines connected to top data points to increase readability.

This work exploits the domain of ultra-short pulses in conjunction with cryogenic MS under low-pressure conditions in resonant and non-resonant regimes (**Figure 1.3**). As mentioned before, multiple studies have already investigated the direct extraction of biomolecules using IR lasers with various pulse durations, but most of these were performed under ambient conditions. Forming molecules of interest under the latter condition leads to lower sensitivity due to the ongoing collisions with the air molecules. A possible solution would be to investigate water-rich targets in low-pressure conditions to minimize molecular collisions. This is especially important when investigating complex specimens in which high sensitivity for low

---

abundance molecules is important. However, only a few publications report work with IR lasers and cryogenic samples in the resonant and non-resonant regimes. Besides the establishment of new sample preparation protocols, the present work aims to provide a better understanding of the desorption and ionization process of water-based samples.

## 1.2 Thesis Outline

Chapter 2 gives a brief historical perspective on analytical instruments, followed by a short introduction to the existing laser-based MS methods. The chapter ends with an overview of the current understanding of the mechanism driving the desorption and ionization processes.

In chapter 3, methods and techniques used in the laboratory context are elaborated and explained. In addition, a home-built software pipeline is introduced for the analysis of the obtained data.

In chapter 4 a description of the novel picosecond infrared laser (PIRL) source used to desorb and ionize specimens embedded in ice is given. The mechanism produced with PIRL is called desorption by impulsive excitation (DIVE). PIRL was tuned to 3  $\mu\text{m}$  wavelength, where the O-H stretching vibration can be efficiently excited. The energy absorbed is quickly redistributed from the initial vibrational modes dissipating on the picosecond scale and converted rapidly into heat. Such a regime was investigated, and a study postulated an increase in ionization yield [57]. The PIRL was coupled to a linear time-of-flight mass spectrometer equipped with a cryogenic stage. An in-house developed sample preparation protocol assured different sample thicknesses ranging from 2  $\mu\text{m}$  to 30  $\mu\text{m}$ . Those samples containing peptides and proteins were investigated under front-side and back-side illumination. Finally, further studies were performed to elucidate the PIRL-DIVE mechanism.

In chapter 5, a fs-laser was coupled to the linear time-of-flight mass spectrometer. Several target plates containing peptides were investigated under cryogenic and non-cryogenic conditions. Angiotensin I and bradykinin were chosen as model systems to reveal a rich fragmentation pattern produced by fs-laser irradiation. Finally, in a systematic study, the impact of the temperature was examined, which provides additional insights into the desorption and ionization mechanism of fs IR-LDI.

In chapter 6 the work of chapter 4 and 5 is discussed in greater detail, and chapter 7 provides an outlook.

## 2 Laser-based Mass Spectrometry

- **Preamble**

In this chapter, the reader is familiarized with the foundational background for the work at hand. The first part discusses the development of soft ionization methods to liberate non-volatile and labile biological components without fragmentation. MALDI is the gold standard for detecting and analyzing biological macromolecules. Based on its popularity, many studies investigated the desorption and ionization mechanism and nurtured an understanding of a general laser-matter interaction involving biomolecules. Knowing the basic principles of MALDI will help the reader understand the laser desorption interaction processes with pure water samples or even without any matrix. Furthermore, MS-related historical developments will be presented.

### 2.1 Instrumentation in the Present Work

The setup illustrated in **Figure 2.1** was built in-house and maintained throughout the present work. Two different laser sources were employed in this work, which are described in detail in the method chapter, but the upcoming subsection describes a general laser-matter interaction with a focus on ion creation followed by the working principles of a TOF-MS and how the detection of biological species is realized.

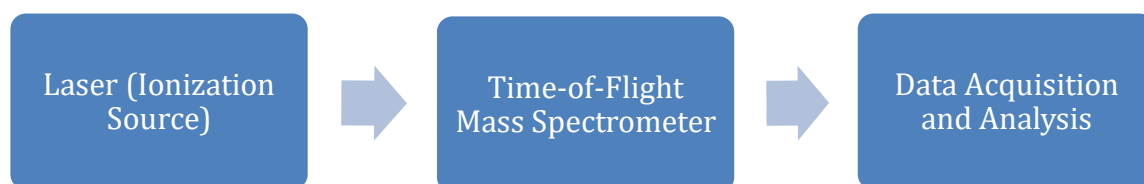


**Figure 2.1** The stages of the analyte in a time-of-flight mass spectrometer.

---

## 2.2 Laser-based Ion Sources

The following paragraph explores the current understanding of the laser-based desorption and ionization of analyte molecules in UV-MALDI and LDI processes.

### 2.2.1 General Ion Sources

MS is a separation technique that relies on charged particle detection. An ion source is an element in the mass spectrometer that creates ions. Ionization can be achieved through multiple methods, but the main distinction is whether this process is performed under ambient or low-pressure conditions. ESI is the first choice under ambient conditions and is broadly used as the interface between liquid chromatography and a mass spectrometer. ESI's working principle is not discussed here, since the work presented deals solely with ionization under low-pressure, vacuum conditions. For the interested reader, the following works provide an excellent overview of instrumentation [58], the fundamental mechanism [59], and applications [60], [61].

Depending on the investigated class of molecules, a diversity of ionization methods under low-pressure conditions exists [62]. Electron impact ionization (EI) uses high-energy electrons to produce an electron deficit in the molecule of interest, hence a positive ionic species which can be detected [63]. This method is useful for monitoring small masses, but higher masses show severe fragmentation, hindering direct interpretation. Chemical ionization (CI) relies on gas-phase collision between the analyte and a charged carrier. A reaction causes a charge transfer from the carrier gas onto the analyte. Such an ionization principle imparts much less internal energy, hence higher masses can be detected without fragmentation.

With the advent of the laser in 1960, a new ionization source was available in conjunction with MS. LDI was capable of generating molecular ions of non-volatile compounds [8]. No matrix or extensive sample preparation is needed for this technique, and the main interactions can be reduced to the substrate, incident light, and the analyte. However, multiple parameters have to be considered for a successful experiment. The ablated amount of material depends on the wavelengths, pulse duration, pulse energy, the specimen, and substrate optical properties. Although successful studies were conducted and simple sample preparation is attractive, the mass limit for detecting intact biological species did not surpass 3 kDa [64].

Along with ESI, MALDI was simultaneously introduced and allowed the investigation of non-volatile compounds of masses up to 300 kDa [11], [65]. However, MALDI is nowadays an indispensable tool in scientific laboratories [66], [67], but it also has some shortcomings, including the fact that a sample is investigated under

---

non-native conditions and the requirement for each specimen to frequently test the sample preparation protocol, which makes the real-time analysis not feasible.

### 2.2.2 Matrix-assisted Laser Desorption and Ionization (MALDI)

Most studies deal with MALDI-related desorption and ionization mechanism [68]–[74] (**Figure 2.2**), and only a few are dedicated to laser desorption and ionization under cryogenic conditions [72]. The trend is explained by the large and far progressed community, which enjoys the benefits of the simple MALDI workflow and high throughput. However, the insights gained from MALDI experiments also provide a better understanding of the laser-induced desorption and ionization processes in laser desorption and ionization. Therefore, some aspects of the MALDI process will be governed before other laser-based techniques.

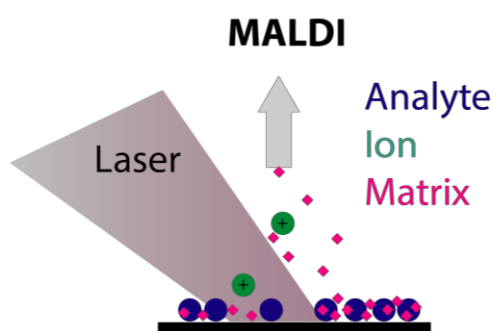


**Figure 2.2** Basic principle of MALDI. The analyte is embedded into a small organic chromophore termed as a matrix. The matrix has two functions. It shields the incoming laser light from the analyte by absorbing the energy. Afterward, a proton exchange from the matrix to the analyte ionizes the latter.

MALDI involves the incorporation of the specimen into a matrix. The latter is a small organic molecule consisting of an organic  $\pi$ -system tailored to absorb the incident laser light. Two major tasks are associated with the matrix: The facilitation of ablation and ionization by donating a proton to the analyte. However, since the major fraction of the pulse energy is absorbed by the matrix, the analyte fragmentation is almost absent. Besides pulse energies [68], other parameters, such as pulse duration [75], repetition rate [76], and intensity profile (Gaussian or flat-top profile) [77], have a considerable effect on mass spectra quality and remain under investigation. Although UV-MALDI is a highly advanced, widely employed technique, improvements are still ongoing [76].

---

In general, studies distinguish between desorption and ionization processes. Desorption caused by laser irradiation can produce material removal, but not necessarily ionization. Ablation removes material induced by rapid overheating of the excited volume [78]. When the laser-induced temperature rise reaches a certain threshold, a desorption process occurs, characterized by the complete phase transition of the superficial layer from solid to a mixed phase.

The ionization process, on the one hand, is based on a highly complex cascade of events, and multiple stages exist where ion creation can occur. Some studies show that ions can already be pre-formed in the matrix [79]. However, the transformation of neutral species into ions after laser impact is considered the driving event for ion formation. Finally, gas-phase reactions are also considered essential when neutral species collide and form ions [69].

Ablation/desorption can be achieved with various wavelengths and pulse durations, although the most crucial factor is the matrix's ability to absorb incident laser light and correlates with overall sample removal. Longer laser pulses ( $> 1\text{ ns}$ ) lead to phase explosion of the overheated material and are usually accompanied by aggregates and cluster formation. The latter process is described as a thermal confinement regime. For shorter pulses ( $< 1\text{ ns}$ ), a stress confinement regime is postulated, which results in a lower fluence threshold for desorption onset [80]. Several quantitative models were developed to describe the aforementioned phenomena. If desorption is the dominant process, the surface model [81], [82] can be applied for a better understanding, whereas the ablation process is better described by volume models [83], [84]. For the former such condition would be fulfilled if layer-by-layer evaporation occurs, while the latter describes the ejection of clusters and aggregates and a subsequent ion formation.

In the traditional MALDI sample preparation (dry-droplet), data acquisition can be achieved by shooting multiple times on the same spot with the laser. However, the first shot is analytically less informative, and consecutive shots on the same spot provide more information [85]. A possible explanation might be the sample change initiated by the first laser shot. Due to the material ejection, the analyte-to-matrix ratio is changed, which is also accompanied by sample thinning through additional shots on the same spot exposing the underlying target to play a more significant role in signal onset.

Ionization is the process where a neutral species acquires a net charge, either by proton attachment, detachment, a loss or gain of an electron or, in general, of any charged adduct. Due to the complexity of the process in MALDI, several models have been suggested, which can be split in two phases. The primary ionization [86] considers the initial charge separation on a nanosecond timescale. Secondary ionization [87] occurs during plume expansion on a nanosecond/microsecond

---



timescale. However, the reaction rate in the plume decreases with the propagated time, and effectively, only reactions at the beginning of the expansion are relevant. The most abundant plume-associated interaction is the ion-matrix, as the matrix is usually the most abundant species in the sample, while analyte reaction with matrix ions is considered a less frequent event [88], because of the low number of the former.

In the photophysics and chemical dynamics model (CPCD) [89], [90], the matrix's electronically excited states are fundamental to primary ionization. The model treats the matrix as a solid-state material prior to ablation, where charges are mobile and approximated as excitons. This assumption is driven by the fact that the photo energy provided by a single UV photon is not enough to overcome the ionization potential of the matrix. Therefore exciton hopping and pooling are crucial in reducing the ionization potential of the matrix. Charge transfer to the analyte is assumed to dominate during the plume expansion; therefore, the model is sometimes called gas-phase proton-transfer. The mechanism works well to predict the fluence threshold to liberate the matrix and the analyte, ion collection yield, plume temperature, and plume expansion velocities.

Another extensively discussed model is cluster ionization, also known as the “lucky survivor” [69], [91]. The premise here is that all ions are pre-formed and liberated after ablation. Most ions statistically recombine with the counterions during ablation, resulting in neutral species and therefore are not accessible for detection. Those ions which evade the geminate recombination are detected. Some experiments indicate that the CPCD mechanism is favored at higher laser fluence, while the lucky survivor approach becomes increasingly dominant when high mass species are investigated [69].

Finally, thermal models are not new and were already applied to MALDI, but recent studies have emphasized the influence of thermal processes on ion formation [92], [93]; especially relevant is the polar fluid model (PFM) [94]. PFM approximates a dense but not fluid plume shortly after the impact of the laser. This state facilitates ion-pair separation under similar conditions, which are known in aqueous solutions. Since charge separation is a very energetic process and involves the autoprotolysis of the matrix, the ion yield was predicted to be low ( $10^{-7}$ ), however, this was not the observation in regular UV-MALDI experiments, which resulted in ion yields between  $10^{-4}$  and  $10^{-5}$  [76], [95], [96]. To account for this discrepancy in PFM, the rate of autoprotolysis must increase. The assumption is that the barrier for autoprotolysis is lower when a polar solvent is screening the charge.

The three models for desorption and ionization introduced above are the most accepted in the MALDI community. Nevertheless, other models exist, but they are usually less accurate in experiment prediction [72].

---

### 2.2.3 IR-MALDI with Water and other Organic Solvents

A scenario where MS could be performed *in situ* with minor sample pretreatment under protein-friendly non-denaturing conditions is preferable from a practical and scientific point of view. As water is found in all living organisms, it is the ideal candidate. Shortly after the introduction of UV-MALDI, an infrared laser-based approach with a pure water sample was proposed and termed IR-MALDI [65]. Throughout this work, the term IR-(MA)LDI refers to the irradiation of water-based samples, while IR-MALDI refers to the irradiation of organic substances such as glycerol or 2, 5-Dihydroxybenzoic acid. The infrared laser wavelength is tuned to the local maximum absorption coefficient (2.94  $\mu\text{m}$ ) of water in the infrared window between 1  $\mu\text{m}$  and 10  $\mu\text{m}$  (**Figure 1.2**). Water excitation leads to temperature rise followed by evaporation, which drives the desorption [97]. The desorption process is considered soft because biological components are not excited by the wavelength [84]. However, due to the lack of systematic studies on the IR-MALDI with water, some differences and similarities between UV-MALDI and IR-MALDI are highlighted, as the principles of the desorption mechanism from the former also apply to the latter.

The traditional UV-MALDI matrices absorb infrared radiation, as most of them possess a hydroxyl group that is strongly coupled to the radiation at 2.94  $\mu\text{m}$ . However, the absorption coefficient for the MALDI matrix in infrared is lower than in the ultraviolet region. Hence, the penetration depth is higher for the former, resulting in a 100 times higher material consumption and ultimately leading to sensitivity loss. Increased sample consumption in combination with sample inhomogeneity also amplifies the shot-to-shot fluctuations. Acquisition of high-quality data becomes challenging under such conditions since the mass resolution suffers. Tackling the aforementioned issues with thin-film preparation was so far only reported once [98]. Considering all the drawbacks appearing in IR-MALDI, the same must also apply in IR-(MA)LDI and explain why IR-LDI with ice has been of little interest in the mass spectrometric community.

Systematic studies dealing with the ionization process in IR-LDI are absent in the literature. However, studies on IR-(MA)LDI reported mass spectra similar to UV-MALDI [99]–[102]. In general, IR-(MA)LDI is less sensitive than UV-MALDI, which leads to lower ion yield [101]. Consequently, polar fluid models (PMF) may be applied to IR-(MA)LDI to describe the ionization process, predicting a low ion yields.

### 2.2.4 Desorption by Impulsive Excitation (DIVE)

A picosecond infrared laser system (PIRL) was used to produce charged particles, and for a better understanding of the generated mass spectra, the fundamental

---

interaction between the laser pulse, the specimen, and the substrate are highlighted in this subsection.

If the excitation of vibrational modes of water is conducted under stress confinement conditions, pulse durations are limited to be sub-nanosecond. Under stress confinement regime, shock or sound waves are not transcending out of the excited volume. This regime assures that all incoming energy is contributing to the ablation process. The laser energy is deposited through the O-H stretch and redistributed through the strongly coupled hydrogen network, resulting in complete thermalization within a few picoseconds. Franjic *et al.* [57] introduced laser parameters for such conditions and termed it desorption by impulsive vibrational excitation (DIVE). Laser pulses on a picosecond timescale and tuned to 2.94  $\mu\text{m}$  (local absorption maximum of water, **Figure 1.2**) trigger the abovementioned conditions. The laser for such an operation is called a picosecond infrared laser (PIRL).

A threshold energy must be reached in order to drive the ablation. Numerical hydrodynamic modelling [103] for pure water showed that 0.7  $\text{J}\cdot\text{cm}^{-2}$  pulse energy excites a  $\sim 2$   $\mu\text{m}$  thick layer to a supercritical state with  $T > 647.1$  K and  $p > 22.1$  MPa. Such small pulse energy minimizes the effect of nonlinear optical excitation of higher-lying molecular states and results in a gentle desorption and ionization.

DIVE conditions can be applied in ambient and vacuum environments. A study working with *S. cerevisiae* cells observed enzymatic activity after the DIVE-driven ablation [104]. DIVE can also be used for tissue sampling, and subsequent MALDI analysis revealed a preserved enzyme activity [105], [106]. Extraction of intact species is associated with shorter pulse durations was reported in a study that compared picosecond to microsecond pulses [107]. Finally, in a healing study, a DIVE-driven incision produced substantially less scar formation on a mouse's skin when compared to a traditional scalpel or gain-switched microsecond Er:YAG laser [108]. Under ambient conditions, PIRL was used to irradiate the specimen while the expanding plume was post-ionized with an ESI source [54]. Such configuration is known as laser (assisted) ablation electrospray ionization (LA-ESI) [109]. However, the authors of this study improved the limit-of-detection (LOD) limit fivefold compared to the regular nanosecond laser source.

Finally, a molecular dynamics simulation showed that the separation of charged proteins and counter ions (e.g., lysozyme with sodium) is conceivable with DIVE-ablation [110]. The study also suggested that small ablated volumes are favorable in order to observe a high ion collection yield. Small volumes can either be achieved by reducing the focal spot size or using thin-films.

---

## 2.2.5 Laser Desorption and Ionization without a Matrix

A second approach avoids the use of any matrix, and instead, the substrate surface serves as an additional interaction partner to promote analyte desorption and ionization. In the process of laser desorption and ionization (LDI) without any matrix, the number of interaction partners is decreased, nevertheless, a robust understanding is still missing [39] (**Figure 2.3**).

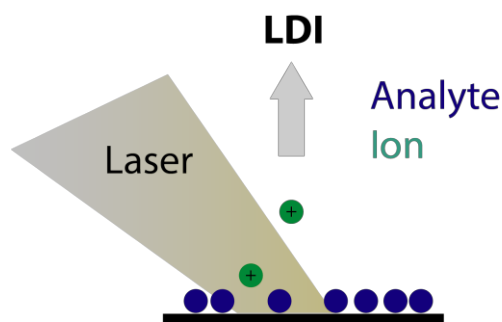


**Figure 2.3** Basic principle of LDI. The analyte is deposited on a substrate without any matrix. Two scenarios for desorption and ionization are possible and can be roughly sorted into laser-substrate or laser-analyte-driven events. However, both scenarios usually occur simultaneously.

The most popular technique is surface-assisted laser desorption and ionization (SALDI) which modifies and manipulates substrate surfaces to promote molecular ion signals after laser irradiation. The most prominent surface modification is achieved through nanoparticle attachment. However, understanding the underlying SALDI process remains incomplete [39], [111]. The debate about the thermal and non-thermal mechanism is still ongoing, but the former is considered to be the dominant mechanism in SALDI for desorption [111], [97], [39]. The latter is highly dependent on the optical properties as well as the thermal conductivity of the irradiated medium [112].

A particular version of SALDI is desorption ionization on silicon (DIOS) [113]. This technique is built around silicon as a substrate and explores the impact of modified silicon surface on the mass spectra. Different pore sizes, depth, surface porosity, and roughness impact the DIOS efficacy [114]. Most studies employ a nitrogen laser with a wavelength of 337 nm and 3 ns pulse duration [112], [115]–[118]. The ultimate mass limit is inferior to MALDI and is limited to proteins below 25 kDa [39]. However, studies also showed that fs pulses (200 fs) and 800 nm wavelength produce mass spectra of C<sub>60</sub> fullerene [119], [120], without any silicon pre-treatment.

The ionization process in SALDI remains up to now largely unclear. Various pathways are considered, such as the emission of electrons from the surface, the presence of preformed ions, proton transfer between surface and analyte, photoionization reactions, and finally, surface melting and destruction can lead to ion formation [39]. SALDI is described as a non-thermal process for desorption and ionization [51], [50].

### 2.2.6 Desorption and Ionization with Ultra-short Pulses

The fundamental interactions between the ultra-short laser pulses, the specimen, and the substrate are highlighted in this paragraph. The ability of fs lasers to deposit large energies within a small time-domain makes it possible to perform selective target modification, and at the same time, provides the possibility to investigate materials under extreme conditions of strong electronic excitation [121]. Resonance enhanced multiphoton ionization (REMPI), and resonance ionization mass spectrometry (RIMS) and their non-resonant equivalents are laser-based ionization sources utilized in a mass spectrometer for the first time [122], [123] in the late '70s and '80s. The laser pulse width was initially on a nanosecond timescale, but with the advent of fs lasers in 1990 [124], the latter superseded the former and became increasingly popular. Femtosecond table-top lasers are capable of generating peak powers between  $10^{12} - 10^{15} \text{ W}\cdot\text{cm}^{-2}$ , and consequently, molecular species and especially biomolecules can be easily ionized. On the one hand, high ionization efficacies lead to high sensitivity, which is desired in the mass spectrometric context, but on the other hand, ionization and dissociation are processes that compete for reaction pathways. An undesired pathway is where dissociation energy is below the ionization limit, leading to low-intensity or no parent ion and ultimately leads to an ambiguous analysis, where the fragment ions dominate the mass spectrum. In the following common reaction, pathways are briefly discussed.

Two distinct mechanisms explain how fs pulses lead to fragmentation [125]. First, a molecular species can absorb several photons resonantly or non-resonantly and reach the transition state but fail to ionize. If the state's lifetime is shorter than the pulse length, the molecular species dissociates to form neutral moieties. In the case of higher laser intensity, the neutral fragment can absorb additional photons to ionize or further fragment. This process is called ladder switching and can theoretically repeat multiple times until the molecular species is atomized. Conversely, when multiple photons are absorbed and the transition state's lifetime is longer than the pulse length then enough photons can be absorbed to reach the ionization level. In addition to the transition state's lifetime, a high photon density is essential as this enhances the probability of the absorption of an additional photon during the lifetime

---

of the excited state. This process is referred to as ionization, followed by dissociation or ladder climbing.

Usually, REMPI or the non-resonant equivalent is described as (1 + 1) process. The first photon excited the molecular species to the transition state or an intermediate electronic state while capturing the second photon results in ionization. If two or three photons are needed to elevate the molecular species to the transition state, the process will be described as (2 + 1) or (3 + 1) REMPI, respectively. In the latter case, high photon fluxes are needed to ensure high photon absorption, resulting in higher fragmentation than the (1 + 1) REMPI [126].

Several studies successfully coupled fs laser to the mass spectrometer under ambient conditions [56], [127]–[131]. Here, a fs laser is used to vaporize the specimen, and expanding plume is post-ionized by the aid of electrospray. Despite the fact that fs pulses are likely to introduce fragmentation to biological components, Brady *et al.* [56] were able to show that species with masses up to 45 kDa are arriving intact at the detector. Such a technique is especially attractive since sample preparation is simple and analysis can be performed in real-time, making this analytical method especially attractive in the clinical environment.

## 2.3 Time-of-flight Mass Spectrometry

TOF-MS is one of many mass analysers used throw-out the scientific landscape. The main task of a mass analyzer is separating the charged particles according to their mass-to-charge ratio. Several mass analyzers exist, and they can be used alone or combined to take advantage of their individual strengths.

The first concept of a TOF-MS was introduced 50 years ago by Wiley and McLaren [6], although Joseph J. Thomson discovered the first working principle during his study of *Kannalstrahlen* 50 years earlier [5], [132]. A simple TOF-MS is illustrated in the **Figure 1.1**, and the fundamental working principles are described in chapter 1. As sad, TOF-MS primarily measures the ion's flight time, but scientists are less interested in that value and want to know the mass-to-charge ratio.

The amount of energy experienced by the ion in the extraction region depends on its charge and the applied voltage.

$$E = qE = e_0zU \tag{E. 1.1}$$

As ions are accelerated in the extraction region, their energy is converted into kinetic energy.

$$E_k = e_0 z U = \frac{1}{2} m v^2 \quad \text{E. 1.2}$$

Therefore, the velocity of an ion with the mass  $m$  and a charge  $z$  is given by:

$$v = \sqrt{\frac{2e_0 z U}{m}} \quad \text{E. 1.3}$$

The travel distance between the extraction plate and detector is expressed by:

$$t = \frac{s}{\sqrt{2e_0 U}} \sqrt{\frac{m}{z}} \quad \text{E. 1.4}$$

And equation 1.4 can be rewritten to give the mass-to-charge ratio.

$$\frac{m}{z} = \frac{2t^2 e_0 U}{s^2} \quad \text{E. 1.5}$$

However, although simple in design and easy to maintain, initially, TOF-MS were only used for exotic studies of ion properties. Several factors hampered the wider use of TOF-MS, but the main reason was the lack of ionization sources creating ions within a short time interval. This requirement is crucial for TOF-MS as the flight time is determined between the ion creation and the impact on the detector. A larger time period for ion creation causes a long arrival time window at the detector and reduces the mass resolution, limiting the analytical performance, ultimately leading to a decreased method applicability. Therefore, ion creation would happen for all molecules instantly in an ideal case. The renaissance of the TOF-MS was invoked when pulsed ionization source where introduce such as  $^{252}\text{CF}$  plasma desorption [133], secondary ion mass spectrometry [134], and most importantly MALDI [11]. Those methods provided high mass resolution not seen before, but demands were rising and researchers were searching for improvements. The delayed extraction or time lag focusing design was the next iteration of the instrument, which improved the mass resolution significantly. Before that TOF-MS operated in a continuous extraction mode, and it is important to understand the workflow. In a continuous mode extraction, the ionization region has a permanent potential field. Once a laser is impinging on a sample, that creates an expanding plume containing neutrals and ions. Those species inherently contain different kinetic energies and the time point of ion creations varies. While both features decrease mass resolution, they are not addressed in continuous extraction mode. The delay extraction workflow is conveys

---

the aforementioned problems in the following manner: Before sample ionization the extraction region has no potential. Once exited, the plume can expand in a field-free region. At the end of the ionization period ions are randomly distributed in the plume. Now the extraction electrode is pulsed creating a potential field. Those ions, which are close to the extraction electrode, receive less kinetic energy from the potential field than those closer to the substrate plate. As a consequence, both ion groups arrive at the same time at the detector (**Figure 1.1**). Unfortunately, the mass spectrometer used in the present work was not equipped with such feature. As seen later the strategy was to counter the low mass resolution under the continuous extraction mode with less ejected material.

The biggest advantage of the TOF-MS is the short duty cycle, which describes the time interval needed for a single measurement and the fact that masses from a few Da to several hundred kDa are simultaneously measurable in a single run. For high throughput analysis, especially in the clinical context, such a device would short the waiting time, which is important when the waiting window for the analysis is limited, such as during a surgery. Unfortunately, from all mass analyzers, the TOF-MS mass resolution is the lowest, but recent developments showed that coupling a TOF-MS to ion mobility provides a better mass resolution, accuracy, and ion transmission, while the benefits of the high duty cycle are still present [135].

Finally, MS is an indispensable tool used throughout all scientific disciplines. Advances are made on the instrumental [136], sample preparation [137], and the computational site [138]. The ability of MS to identify, and increasingly in recent years, accurately quantify proteins and other biomolecules out of a complex specimen will impact biology and medicine broadly [139].



### 3 Materials and Methods for Cryogenic-based Mass Spectrometry

*Several people contributed to the success of this chapter. The idea to use two coverslips and a thin Prolene film for ice layers came from Sascha W. Epp. Jan Leimkohl conducted the design of the copper sample carrier. In close collaboration with Hendrik Schikora, the temperature profile and a series of brightfield images of a thin film were conducted. Djordje Gitaric and Josef Gonshior conceived the design and assembly of the time-of-flight mass spectrometer. The communication between several devices was established through the LabView software framework supplied by Friedjof Tellkamp. Glaynel Alejo wrote the scripts for data analysis in PYTHON. In addition, she also worked on the ion count analysis problem for Gaussian-shaped signals [140]. This script was used as a basis for the ion count analysis for signals with a non-Gaussian shape.*

















- **Preamble**

This paragraph provides the reader with all instruments and methods used in chapter 4 and 5. In the first part, all materials are listed. Then the two laser systems are described in detail and how they were coupled into the mass spectrometer. Next, the features of the home-built mass spectrometer are presented. In this project, the mass spectrometer was equipped with a cryogenic stage, and the analysis of volatile solvents such as water was possible under low-pressure conditions. Then the reader is introduced to the possibility of changing the temperature at the sample stage, which provided an additional dimension to investigate frozen samples. Next, the in-house developed protocol for thin films with the capability of producing various thicknesses is described in great detail. Finally, basic data processing workflows conducted in PYTHON are highlighted.

### 3.1 Materials

The following table summarizes the chemicals, which were used throughout this work.

**Table 3-1** below shows the used chemical and their hazard and prepare statements.

Substance	Pictograms	H-sentences	P-sentences
Acetic acid	 	226, 314	280, 305+351+338, 310
Acetonitrile	 	210- 305+351+338- 403+235	225-332-302- 312-319
Angiotensin I	-	-	-
Bradykinin	-	-	-
Deuteriumoxide	-	-	-
Dithiothreitol		302+352- 305+351+338	302-315-319
Endothelin I	-	-	-
Ethanol		225	210
Formic acid		260-280- 301+330+331- 305+351+338- 308+310	226-314
Fullerene C60		319-335	305+351+338
Lysozyme	 	261-280- 301+310- 342+311	301-317-334- 413
Nitrogen		282-336+315- 403	281
Toluene	 	225-304-315-336 - 361d-373-412	202-210-273- 301+310- 303+361+353-331
Trifluoroacetic acid	  	314- 332-412	261-273-280-303 +361+353-304+ 340+310-305+ 351+338
Water, Cromosolv gradient grade for HPLC	-	-	-

## 3.2 Methods

### 3.2.1 Laser Systems

Two different laser systems were used throughout this work and are introduced in the upcoming subsections.

#### 3.2.1.1 Picosecond Mid-infrared Laser

An infrared laser system (PIRL III ND, Light Matter Interaction Inc., Toronto, Canada) generated gaseous molecules ions under resonant water excitation. The latter refers to the laser's output wavelength, which was tuned to a spectral range where water exhibits a high absorption coefficient. The laser system's fundamental is at 2920 nm with a spectral bandwidth of 30 nm and pulse widths of 400 ps. The relative standard deviation of the pulse energy was below 5 %. For the RG, the laser beam was focused with an incident angle of  $35^\circ$  onto the sample plane with  $f = 75$  mm lens (LA0270-E, ThorLabs, Newton, USA). For the TG setup, the  $f = 75$  mm (110-5509E, Eksma Optics UAB, Vilnius, Lithuania) lens was placed behind the sample stage (Figure 3.1A).

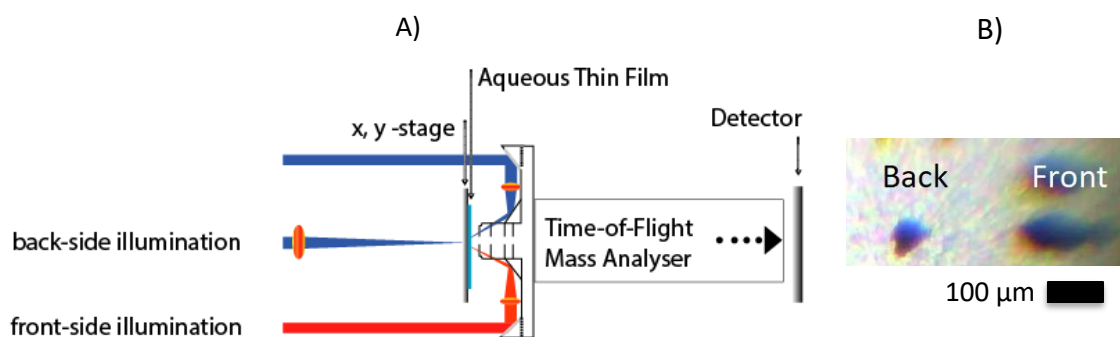


**Figure 3.1** Schematic drawing of the custom built linear time-of-flight mass spectrometer. Throughout the work, the term reflection geometry (RG) refers to the specimen being irradiated from the front, and transmission geometry (TG) implies irradiation from the back. A) The blue rays indicate the picosecond infrared laser beam path, while the orange-ray represents the fs laser beam path. B) A brightfield image of a thin ice film in the mass spectrometer during an experiment. The left and the right crater were produced by the back and front illumination, respectively. As crater sizes with the fs laser were not visible in the present setup, hence the sample carrier was studied under a microscope with a higher resolution (Subsection 5.2.1).

---

The infrared laser beam was guided into the center of the extraction region with the aid of a HeNe laser (Green HeNe, ThorLabs, Newton, USA). Optimal focusing for the laser beam on the target for RG and TG was established by manually varying the distance between the lens and the substrate. The lens distance was fixed once plasma on the substrate was observed. Fine-tuning of the ablation spot was achieved in preliminary experiments with cryogenic samples shortly before initial experiments. The setup was stable for several weeks before additional realignment was necessary. **Figure 3.1B** shows an ablation spot on a thin ice film for the back and front illumination. The focusing area in back illumination was smaller, as the beam cross-section was more circular than for front illumination. The difference comes mainly from the incident angle of the incoming laser beam. Laser power was monitored with a commercial power meter (S314C and PM100D ThorLabs, Newton, USA) at each experiment's beginning.

### 3.2.1.2 Femtosecond Near-infrared Laser

Non-resonant infrared laser desorption ionization studies were conducted with a commercial Pharos laser system (Light Conversion UAB, Vilnius, Lithuania) in RG only (**Figure 3.1A**). The laser emits at 1026 nm wavelength with a spectral bandwidth of 5 nm and a temporal full-width-at-half-maximum of 190 fs. Laser power was monitored with a commercial power meter (S120VC and LabMax-TOP, Coherent, Santa Clara, USA) at the experiment's beginning and end. The relative standard deviation of pulse to pulse energies was, on average, below 0.5 %. The fundamental (1026 nm) and the second harmonic (513 nm) of the laser are used in the experiments. The latter was generated with a half-wave plate (WPH225H, Dayoptics, Fujian, China) and a non-linear crystal (BBO-654H, Eksma Optics, Vilnius, Lithuania). Both wavelengths were coupled into the mass spectrometer at an incidence angle of 35° towards the normal of the sample surface. Focusing was achieved with a single lens (LA1509,  $f = 100$  mm, ThorLabs, Newton, USA) for both wavelengths. The dispersion introduced through optical elements to the second harmonic laser beam was not compensated. Neutral density filters were applied to attenuate the laser power. The final pulse energies are mentioned in the figures presented in this study. The crater sizes produced on the substrates with one and two laser shots vary with laser energies and are discussed in more depth in subsection 5.2.1.

### 3.2.2 Microscopy

In this work, silicon wafers were investigated with a bright field microscope (Axioscope 7, Zeiss Jena, Germany), and images were evaluated using the proprietary software provided by the instrument developer (ZenCore, Version 3.1).

---

In addition to bright field images, the silicon wafers were investigated using an atomic force microscope (Dimension Icon, Bruker Daltonics, Bremen, Germany), sitting on an isolated vibration table and covered in an acoustic enclosure. The selected atomic force microscope (AFM) probe tip throughout all measurements was MESP (Bruker Daltonics, Bremen, Germany). The high lateral picture images were edited using the NanoScope Analysis (Version 1.9) software provided by the instruments developer.

### 3.2.3 Sample Preparation

Analytes were used without further purification and dissolved either in ultrapure water or a glycerol-water mixture to the desired concentrations and stored at 4 °C before usage. Silicon wafers two side polished n-type doped with phosphor ( $0.1\text{-}1.0\ \text{Ohm} \cdot \text{cm}^{-1}$ ) and a thickness  $300 \pm 25\ \mu\text{m}$  were obtained from MicroChemicals GmbH (Ulm, Germany). Two additional coverslips were purchased and used for the studies with the fs near-infrared laser: Indium tin oxide coated coverslips (70-100  $\Omega$ , thickness 160  $\mu\text{m}$ , Lot# 1221213) were purchased from SPI Supplies (West Chester, USA), borosilicate glass was bought from VWR (Hannover, Germany) and chalcogenide glass was procured from Vitron (Jena-Maua, Germany).

Thin-film specimens containing only water or water-glycerol mixture were prepared in the same manner. First, different concentrations of peptides and proteins were mixed in an appropriate solvent. Then 0.20 - 2  $\mu\text{l}$  of the peptide solution was deposited on a coverslip mounted into a copper sample stage. Further, a second coverslip was placed on top, causing the sample droplet to spread between the coverslips. This scaffold was then placed 1 cm above a liquid nitrogen surface. After 30 seconds, the upper coverslip was tempered up to 35 °C with a custom-made heating block (**Figure 3.2**). The following step is time-critical since the heating block and the coverslip have to be simultaneously removed. The pipetting of 200 nl sample solution led to an average sample thickness of 2  $\mu\text{m}$ , while 750 nl led to an average sample thickness of 12  $\mu\text{m}$ .

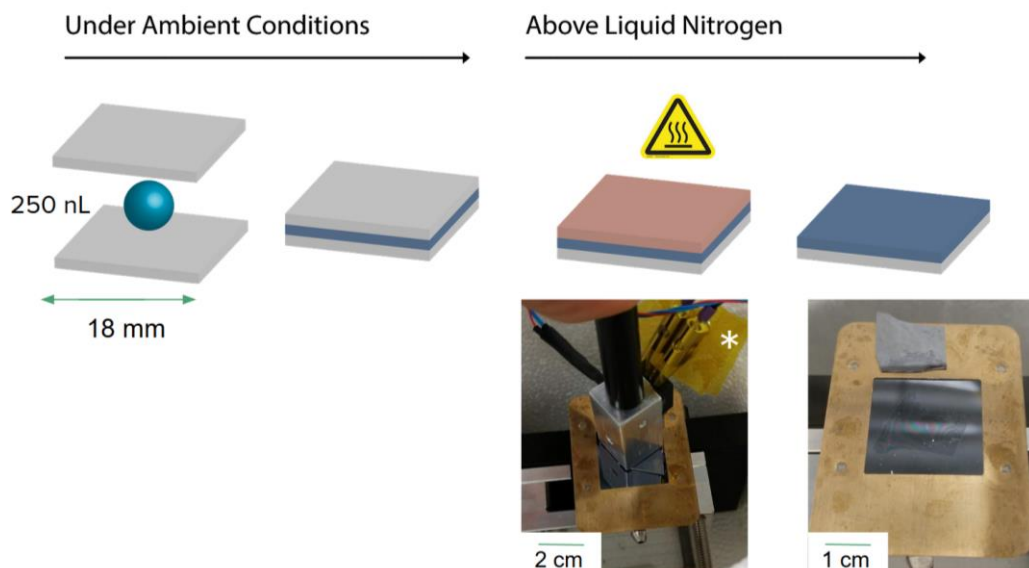


**Figure 3.2** Sample preparation protocol to create thin and ultra-thin ice films with a sample thickness of 2 and 12  $\mu\text{m}$ , respectively. A heating block was tempered up to 35  $^{\circ}\text{C}$  and positioned on top of the coverslip for several seconds.

In general, the silicon substrate could be reused, while ITO and CG could be used only once. First, the contaminated substrate was sonicated in acetone for 15 minutes, followed by another sonification step in pure water. The steps were repeated one more time before the solvent was purged with a gaseous nitrogen stream to prevent streak formation. If contamination persisted, optical cleaning tissue (MC-5, ThorLabs, USA) was used to remove residual contamination mechanically, and the sonication steps were repeated.

To achieve sample thickness above 12  $\mu\text{m}$ , a different strategy was followed (**Figure 3.3**). The limitation with the two coverslips approach is that once the pipetted volume is too large, the applied liquid was squeezed out of the coverslip scaffold, technically reducing the thickness. By exchanging the top coverslip with a *Prolene* foil (PR, Chemplex Industries, Inc, Florida, USA) the leakage of the sample liquid was prevented. After pipetting 2  $\mu\text{l}$  between the coverslip and the PR, the scaffold was plunged into liquid nitrogen. Then 20 seconds later, the PR was removed. This protocol led to an average sample thickness of 30  $\mu\text{m}$ .

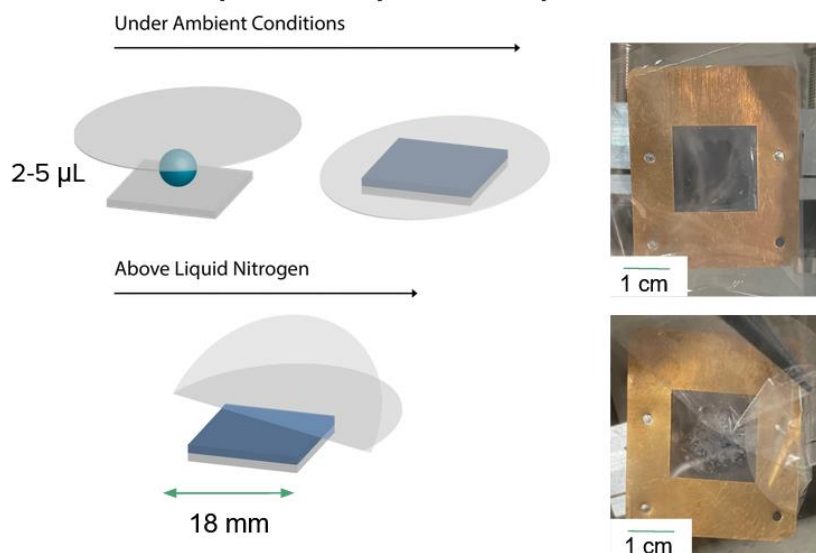


**Figure 3.3** Sample preparation protocol to create semi-thick films with an average sample thickness of 30 µm.

**Figure 3.4** illustrates the loading process. In panel A), the valves for gaseous nitrogen and the inlet for the sample stage were opened. In such a configuration, nitrogen is flooding the arm and displacing the ambient air. Then the loading arm was placed above the liquid nitrogen, and the sample stage was pulled out of the storage cage, which was in liquid nitrogen. After the sample stage was loaded, the inlet valve was closed first, followed by the valve for gaseous nitrogen. Finally, the valve connected to the scroll pump was opened, and the loading arm depressurized. The loading procedure takes less than 3 minutes while low-pressure conditions prevent additional condensation ( $10^{-1}$  mbar). The nitrogen used in the experiments had a purity of 5.0.

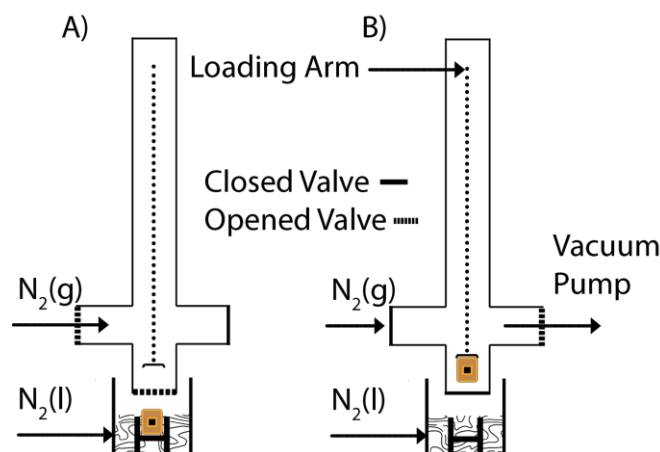


**Figure 3.4** Sample transfer system to minimize ambient air condensation. A) The loading arm is flooded with nitrogen 5.0 before the loading protocol for the sample stage begins. B) After loading the sample stage, the valves connected to the nitrogen line and the sample inlet are closed. Then, the scroll pump valve was opened, and the depressurization began. Finally, the loading arm was attached to the mass spectrometer, and the sample carrier was mounted.

### 3.2.4 Time-of-flight Mass Spectrometer

Design and assembly of the linear time-of-flight mass spectrometer (TOF-MS) was carried out in-house. Sample loading into the mass spectrometer was achieved with a patented lock mechanism and cannot be shown in detail. The ion region was based on the ion optics used in commercial Bruker instruments. All mass spectra were recorded in a linear TOF-MS, continuous extraction, and positive ion mode. The length of the linear flight tube varied between 1.06 and 1.14 m. A commercial power supply provided voltages (Ultravolt, USA) for the backing plate, extraction plate, and Einzel lens, 16 kV, 14.5 kV, and 8.5 kV, respectively.

All mass spectra presented here were acquired with a flange-mounted dual-stage microchannel plate (MCP) detector assembly (F9890-31 with F1552-011G, Hamamatsu City, Hamamatsu, Japan), which has an effective diameter of 27 mm, 12  $\mu\text{m}$  channel diameter, and a gain of  $10^6$ . The voltages (EHS 80 40, ISEG, Germany) for the front plate, back plate, and anode were -2 V, 1450 V, and 1700 V, respectively. Some experiments were conducted with a phosphor MCP (PHOS-F2225P431, Hamamatsu City, Japan). The MCP used in this experiment has an effective diameter of 40 mm, 12  $\mu\text{m}$  channel diameter, and a gain of  $10^6$ . The voltages for the front plate, back plate, and anode were -1650 V, 0 V, and 50 V, respectively. For both MCPs, a 20 dB preamplifier TA1800B with 1.8 GHz bandwidth (fastcomtech, Munich,



Germany) was used to extract the signal. Mass spectra were recorded at 1 GS/s with an 8-bit digitizer (Acqiris DC211, Agilent, USA).

Both the sample carrier and sample stage were custom-made. The sample carrier was mounted onto a nanometer precision piezo translation stage (SLC Series, SmarAct, Oldenburg, Germany) with a PEEK insulator's aid. Liquid nitrogen was used to cool the sample stage. For this purpose, the cooling block and the sample stage were connected through ultra-flexible copper braids. The possibility of interrupting liquid nitrogen supply provided temperature-dependent measurements.

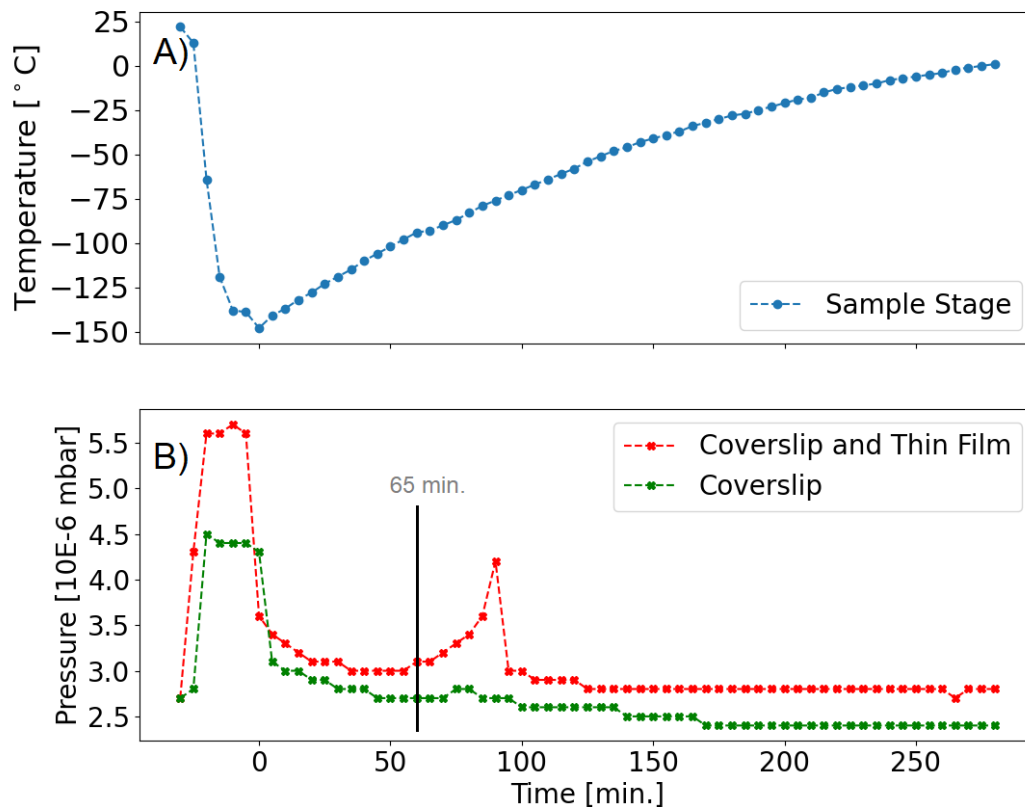


**Figure 3.5** Temperature and pressure time series in the mass spectrometer. A) For the first 30 minutes before  $t = 0$  min., the sample stage was cooled, and the temperature dropped. After  $t = 0$  the temperature gradually rose. B) The green and red traces show the pressure profile with a coverslip and sample and an empty sample carrier, respectively. In the beginning, the pressure increased due to a small leak in the liquid nitrogen pipeline.

While the attachment of a Pt1000 sensor to the sample stage made it possible to record a temperature profile in time, experiments typically requiring high voltage were not simultaneously feasible. However, since the evolution of the measured temperature was highly reproducible, we used the elapsed time to estimate the

---

temperature for a given time point. **Figure 3.5** panel A shows the temperature gradient of the sample stage after the liquid nitrogen supply was stopped. A gradual temperature rise was observed as expected. The sample stage's lowest temperature can reach  $-140\text{ }^{\circ}\text{C}$ , while the cooling block is at  $-190\text{ }^{\circ}\text{C}$  (data not shown).

In addition to temperature profile measurements, we also recorded the pressure profile in the mass spectrometer. For this, a regular thin film preparation protocol was applied, and the sample was introduced into the mass spectrometer. After the liquid nitrogen supply had been cut, the pressure measurement revealed an elevated pressure level after 70 minutes (**Figure 3.5**, red trace). Identical measurement with the coverslip but without the thin ice film showed no peak at this point (**Figure 3.5**, green trace). We suspected the ice sublimation was the prime reason for pressure change and therefore conducted an additional experiment to support our reasoning.

First, a residual gas analyzer was mounted on the time-of-flight mass spectrometer. **Figure 3.6**, panel G reflects a general pressure profile with a coverslip observed after cutting the liquid nitrogen supply. The colored squares indicate the different time points at which electronic ionization (EI) mass spectra were recorded. The color of the square matches the color of the corresponding EI mass spectrum (**Figure 3.6**, panels A-F). After the liquid nitrogen cooling was turned off, the first EI mass spectrum (**Figure 3.6**, panel A) shows nitrogen as the most abundant species in the time-of-flight mass spectrometer. Nitrogen persisted as the most abundant species in the residual gas throughout the experiment. Shortly before pressure increased, a water signal was visible for the first time (**Figure 3.6**, panel B). During the elevated pressure in the mass spectrometer, the water signal intensity surged in EI mass spectra (**Figure 3.6**, panels C-D). Towards the end, when pressure stabilized, the water signal decreased (**Figure 3.6**, panel E) and vanished almost after two hours (**Figure 3.6**, panel F).

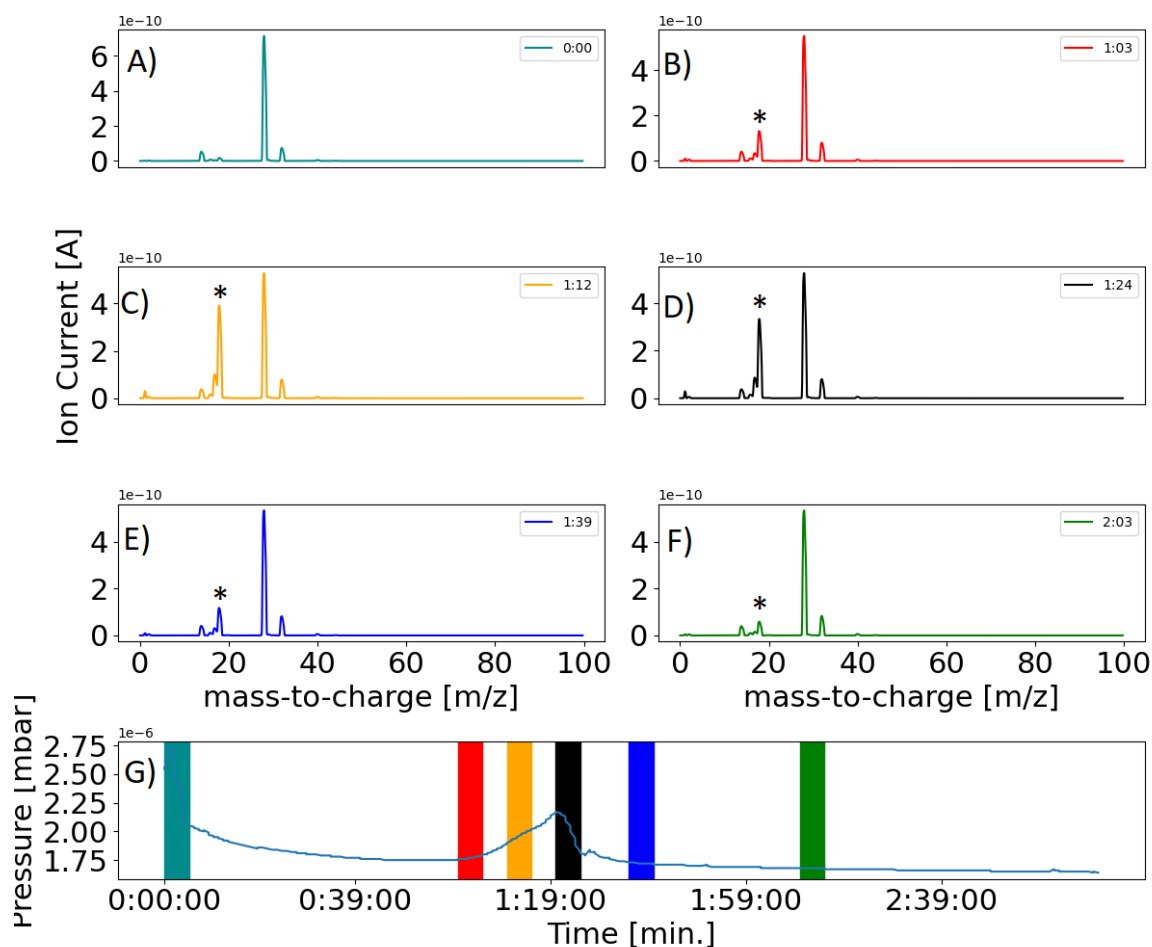


**Figure 3.6** Residual gas analyzer mass spectra at different points after turning off the liquid nitrogen supply. The experiment started with a sample stage at  $-140\text{ }^{\circ}\text{C}$ . A-F) Electronic ionization mass spectra with a mass range from 0 to 100 m/z. The asterisks marks the radical water ion position in the mass spectrum. G) Pressure profile in the mass spectrometer during the experiment. The color bars in the graph indicate when a mass spectrum was recorded and match the colors in A-F). At the beginning of the experiment, the first mass spectrum lacked a water ion signal. When the pressure increased, the water ion signal also surged in the mass spectrum. During elevated pressure inside the mass spectrometer, the water ion signal was also high. The water signal intensity is significantly reduced when the pressure inside the mass spectrometer was stabilized. The unit for the y-axis of the EI mass spectra is  $10^{-10}$  Ampere, and for the pressure profile graph,  $10^{-6}$  mbar.

Finally, the impact of temperature rise on the microscopic scale of the thin-film was investigated in a cryogenic suitcase where the sample stage was accessible with a bright field camera. The sample carrier in the mass spectrometer and the carrier inside the cryogenic case have an identical design, making comparison easier as both sample carriers experienced the same temperature rise. **Figure 3.7** shows screenshots of a video of an ultra-thin ice film under low-pressure conditions. The

experiment started at  $-108^{\circ}\text{C}$  and  $32^{\circ}\text{C}$  higher than the original experiment in the mass spectrometer. Thus, we expected the ice sublimation earlier but still around  $-72^{\circ}\text{C}$  (**Figure 3.7**).

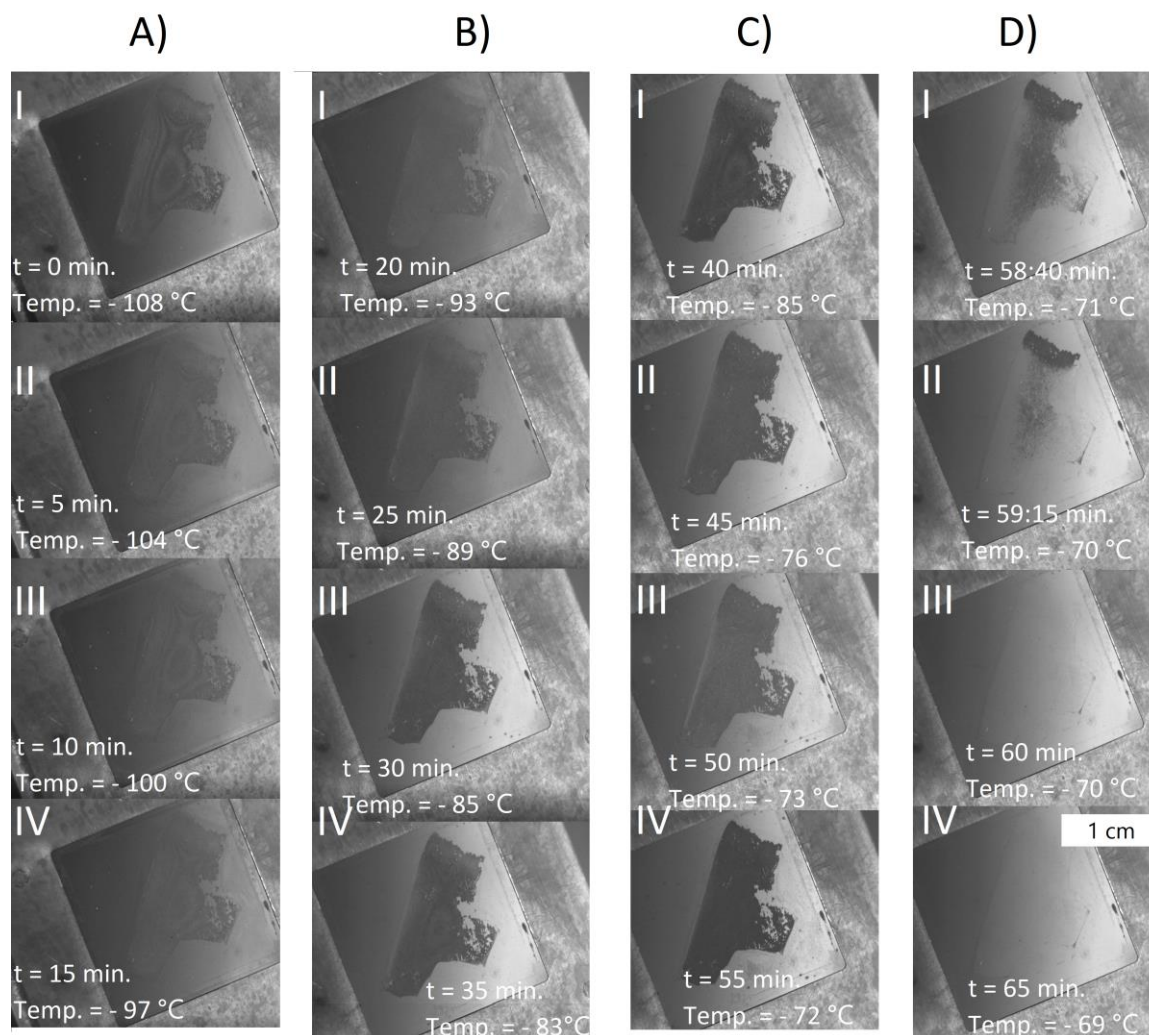


**Figure 3.7** Thin ice thin film at different temperatures. For thin-film preparation, 200 nl of a  $100\ \mu\text{M}$  bradykinin solution were consumed. The vacuum conditions were similar to those in the mass spectrometer and reached  $5\cdot 10^{-7}$  mbar. Panel A) – C) show 12 screenshots of a video film recorded during the ongoing temperature increase. The temperature during the record pivoted between  $-108^{\circ}\text{C}$  and  $-72^{\circ}\text{C}$ . In panel D) the sublimation onset is recorded 58 minutes after the experiment started. Most of the thin film sublimated within 1 minute.

**Figure 3.7** panel A) subplot I show the ice film with well pronounced white light interferences at the beginning of the experiment. The latter was stable in subplot II and III and started to vanish in subplot IV. The thin ice film without white light

interferences was recorded in **Figure 3.7** panel B) subplots I-III, yet subplot IV revealed interferences again. **Figure 3.7** panel C) subplot I still showed interferences, which finally disappeared in subplots II-IV. **Figure 3.7** panel D) catches the sublimation of the ultra-thin film in the subplots I-II, which lasted less than a minute. The sublimation procedure took less than a minute. Subplots III and IV show the sample stage without any ice.

Since sublimation was observed at the same temperature inside the mass spectrometer as well as in the cryogenic case, we are confident that water is the prime reason for the pressure surge during the experiment. However, changes in sample thickness, which were reflected by changing white light interferences, were observed before ice sublimation. The fluctuation in thickness was expected to be in the range of hundreds of nanometers.

### 3.2.5 Data Acquisition and Processing

Cameca Instruments Inc. (Madison, USA) provided the recording software, which generated the raw data in the binary code. These were subsequently processed by MATLAB (Version R2019a) or PYTHON-scripts (Version 3.7). MATLAB was exclusively used for two-dimensional images, while PYTHON was used to visualize the data and quantify the ions producing a signal.

Since the raw data comprised the flight times of the ions, a translation into the  $m/z$  range was desired. This task was tackled by implementing the equations elaborated by Wiley *et al.* [141]. The reference concludes that the overall flight time is described by equation E 3.1.

$$t_{flight\ time} = t_s + t_D = 2s \left( \frac{m}{2e\Delta U} \right)^{1/2} + D \left( \frac{m}{2e\Delta U} \right)^{1/2} \quad \text{E 3.1}$$

Whereby  $t_s$  represents the ion time spent in the extraction region, while  $t_D$  is the time spent in the drift-free region. Both terms include the mass  $m$ , charge  $e$ , and the voltage difference  $\Delta U$  over the distance. Arrival time fluctuations were observed because the same kind of ions can be created in unequal positions  $s$ .

For plotting, the script was initially searching for the proton signal. The latter was the first signal in the time trace with an arrival time between 400 – 600 ns and dependent on the laser system used for the ablation. Once found, the flight time was accordingly converted to the mass-to-charge, leading to a mass accuracy in the range of 15000 ppm for peptides around 1 kDa. In this work, we rely on the terminology and treatment of data provided by Brenton *et al.* [142]. Therefore the accurate mass is the experimentally determined mass of an ion measured to an appropriate degree of accuracy and precision. Ultimately, high mass accuracy reduces the elemental formula

of potential candidates [143]. However, the results were not satisfying, and another strategy was introduced. A more accurate mass calibration relies on the known flight times of two or more known exact masses [144], [145]. For this purpose, a set of signals was chosen, fulfilling the following criteria. First, they regularly appear in the MS, and secondly, the signal-to-noise ratio is above 3:1. Third and foremost, the species creating the signal was distinctly identified. For the obtained mass spectra, it was the proton and analyte signal. This led to a series of experiments with different analytes to assure our reasoning. **Table 3-2** summarizes a typical data set for mass calibration. The data points were fed into the OriginPro (Version 2018G) software to determine the constants a and b for  $t = am^{1/2} + b$ . This strategy improved the mass accuracy tenfold from the previous approach and ultimately led to 1500 ppm.

**Table 3-2** Frequently observed signals in the mass spectrometer used in the experiments. The data points were fed into the OriginPro software, and an exponential fit was applied. With this fit, the time trace of the mass spectrum was converted to the mass-to-charge.

Species	Flight Time [ $\mu$ s]	Theoretical Mass [Da]
H <sup>+</sup>	0.680	1.008
H <sub>2</sub> <sup>+</sup>	0.968	2.016
C <sup>+</sup>	2.379	12.011
O <sup>+</sup>	2.747	15.999
H <sub>2</sub> O <sup>+</sup>	2.934	18.015
H <sub>3</sub> O <sup>+</sup>	3.012	19.023
Na <sup>+</sup>	3.312	22.989
K <sup>+</sup>	4.318	39.098
Bradykinin + H <sup>+</sup>	19.87	1061.23
Angiotensin + H <sup>+</sup>	21.98	1296.48

The workflow mentioned above was performed for mass spectra generated in the reflection geometry and is valid for experiments with picosecond mid-IR laser as well as fs near-IR laser. In paragraph 4, mass spectra in TG, which were only generated with the picosecond mid-IR laser, experienced the same calibration procedure as in RG. However, for TG, the mean arrival time of bradykinin is 120 nanoseconds later than in reflection geometry. The previous numbers were drawn from the bradykinin peak. This corresponds to a flight time deviation of 0.5 %. A study concerned with UV-MALDI in transmission and reflection geometry did not report such differences in continuous extraction mode [146]. Individual travel paths for each ablation geometry on the optical table can be neglected since the difference in light travel distances was less than a meter. However, as this phenomenon did not negatively affect the conducted measurements.

A common technique is averaging multiple mass spectra to improve the signal-to-noise ratio. However, mass accuracy can worsen if single-shot mass spectra from different sample areas were averaged. The reasons are, in general, a change in the flight path length. A reason for a change in the flight time for the same species can be a tilt of the sample plate, changing the extraction region size. In addition, consecutive laser shots on the same spot change the sample's surface. Especially the second point is for a picosecond mid-IR laser is a concern since the total ablated volume for frozen water sample is immense compared to UV-MALDI. Finally, the sample thickness inhomogeneity is also a source for flight time deviation since it also changes the length of the extraction region. To minimize the aforementioned constraints, sampling was conducted on a small area (5 x 3 mm). With the interlaced shot protocol, it was assured that first, a small area was irradiated, which reduced the impact of extraction plate tilt, and second, since spots were irradiated only once, sample changes initiated by the laser and leading to a changed length of the extraction region was minimized. This approach was called a single-shot-per-spot (SSpS) mode. However, if the sample were sufficiently thin oversampling mode provided results of similar quality.

#### 3.2.5.1 Statistics for Ion Collection Yield

Sensitivity is an important parameter in MS since it tells the user an analytical system response to an analyte under well-defined conditions. Sensitivity is characterized as the slope of a curve when an analyte amount is plotted against signal intensity [58]. High sensitivity is usually associated with an ionization source with a high ionization efficacy. Ionization efficacy is the ratio between the ionized and neutral particles in the excited volume. However, other factors such as the ion transmission of the mass analyzer, as well as the ion extraction optics from the ion source and the detectors (microchannel plate, MCP) response to the incoming ions, reduce the overall number of initially produced ions.

To calculate the initial ionization efficacy, the aforementioned factors have to be known or approximated. For instance, a MCP's response efficacy for ions around 1 kDa was experimentally determined to be close to 100 % [147]. This assumption was also implemented in our upcoming consideration. Further, the time-of-flight mass analyzer has a high ion transmission of close to 100 %, and for simplification purposes, we round up [147]. Conclusively, the ion extraction region is the part of the mass spectrometer which impacts the amount of transported ions. A general term called ion collection yield may be chosen when all components are considered. The latter is the ratio between the ionized particles arriving at the detector divided by the number of particles interacting with the laser beam.

In our case, laser focal spot size and the sample thickness are determined accurately to calculate the total ablated volume. Additional knowledge about the sample

---

concentration gives the total number of particles in the excited volume. Finally, under ideal conditions, same particles produced the same signal intensity when colliding with the MCP. Some commercial instruments have a build-in feature, determining the number of ions producing a signal [76]. However, since we used a home-build instrument, another strategy was applied.

Another approach is to look at the count statistics in the TOF instrument. The count statistic in TOF is dominated by Gaussian noise for the background and by Poisson noise for the analyte signal [148]. Both statistics overlap in a regular mass spectrum, but once the peaks are cleaned from the Gaussian noise, the Poisson statistic can be used to estimate the number of ions, which produce a signal.

The approach here follows the hypothesis that a low number of ions is causing high voltage fluctuation and *vice versa*. These fluctuations can be expressed in sample standard deviations, ultimately revealing the current intensity triggered by a single ion.

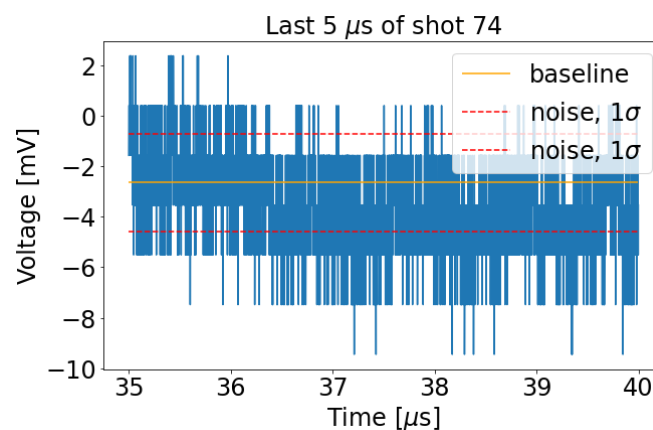


**Figure 3.8** Gaussian noise determination for the time-of-flight mass spectrometer. The last 5 μs of each single-shot mass spectrum was taken into the calculation process. The yellow baseline represents the average voltage obtained from all data sets. The dotted red lines indicate the first sample standard deviation of the mean. The blue trace is the raw data, and serves referential reasons only.

We first determined the Gaussian noise by looking at the position where ions were not expected to arrive (**Figure 3.8**). In our case, the recorded time was 40 μs for a single mass spectrum, and in the last 5 μs, the arrival of ions was never observed. This time-domain was utilized to determine the sample standard deviation (SSD,  $s_{system\ noise}^2$ ). System noise consists of several factors, including electrical and thermal effects, misalignment of equivalent bins as well as charging and discharging effects



causing non-zero baseline [149]. For simplification reasons, we accounted only for electrical effects in our calculation.

Next, we choose up to 40 single-shot mass spectra with an analyte signal and comparable arrival time but not necessarily the same intensity. Jittering of the bradykinin signal in time produces a higher variation, therefore, we investigated analytes arrival times within a 2 ns in the case of the femtosecond laser and for the picosecond infrared laser, we chose a 10 ns window (**Figure 3.9A**). The PYTHON package SciPy.find\_peaks (Version 1.7.1) was used to find the analyte peak, which represents the arrival time (**Figure 3.9B**).

Once the mass spectra with the analyte signal were identified, further processing was applied. In the case of the picosecond infrared laser, the intensity for the analyte signal fluctuated significantly, reducing the analytical performance of our method. Therefore, an additional step was introduced to detect and remove the outliers. For most datasets, a threshold voltage of 20 mV for the analyte signal was sufficient.

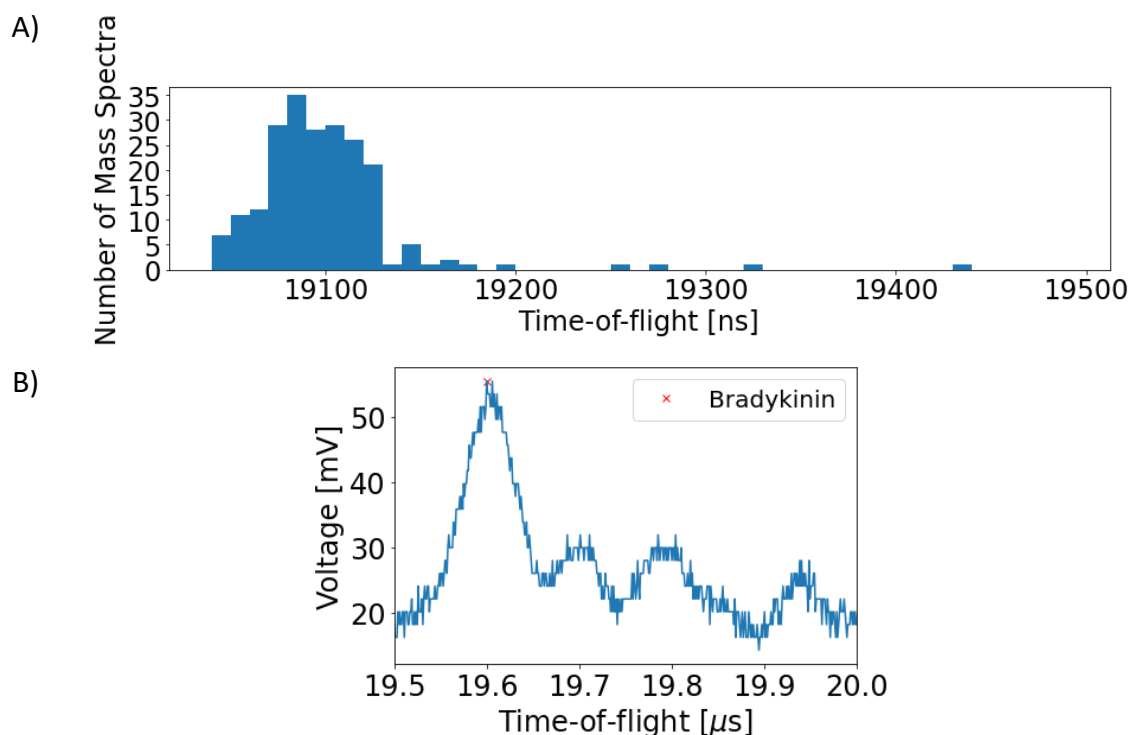


**Figure 3.9** Data cleaning process to sort the arrival time into bins. A) A histogram summarizes different bradykinin arrival times in 10 ns bins. B) The PYTHON module find\_peaks identifies the bradykinin peak and readouts the arrival time. A hit was considered when the analyte voltage was at least 30 mV.

The upcoming workflow applies to the mass spectra generated with the fs as well as the picosecond laser. First, a baseline correction for each mass spectrum was

performed by subtracting or adding a constant, and a data set mean mass spectrum was calculated. As the digitizer recorded each nanosecond as a data point, binning was performed to reduce the noise. The size of a bin was 8 ns, hence 8 data points were averaged. As a next step, an integral for a single and the mean mass spectrum was calculated using SciPy (Version 1.7.1). The integral of the mean mass spectrum served to weigh the single-shot bradykinin signals. This approach considered different signal intensities and their impact on the upcoming  $\chi^2$  statistics, ultimately allowing the investigation of low and high-intensity signals in one data set (**Figure 3.10**).

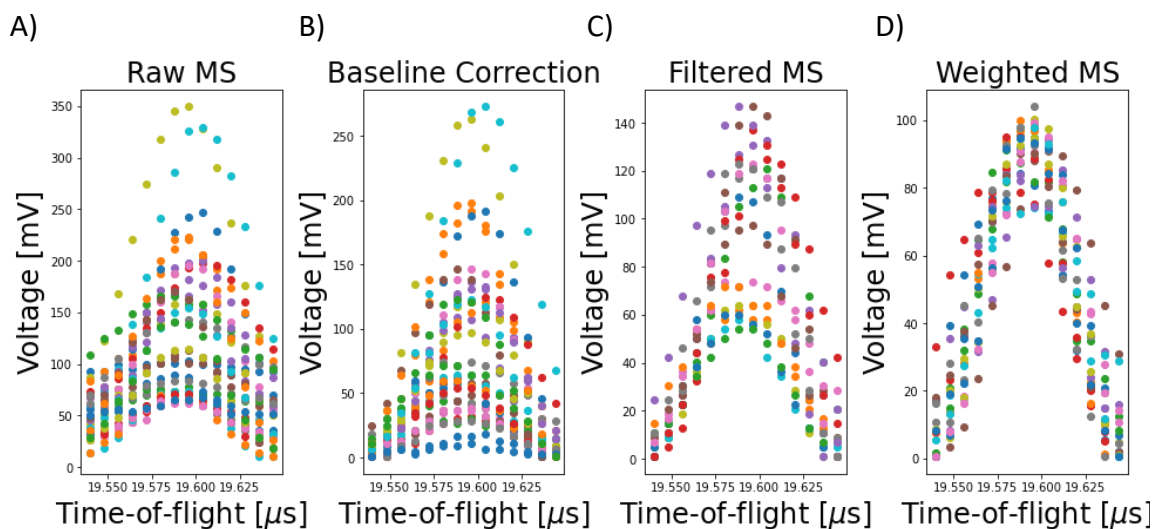


**Figure 3.10** Data processing of bradykinin signal. A) A data set of several unprocessed mass spectra. Dots of the same color indicate the same mass spectrum. Dots of different colors were arranged in vertical stacks, indicating a bin unit. B) Baseline correction was performed. C) Additional filtering was applied to filter outliers. D) Each mass spectrum's integral was divided by the mean mass spectrum integral. The ratio was then used to weigh the bradykinin signal for greater comparability.

As we deal with categorical data, PYTHON module lmfit (Version 1.0.2) was used to determine the reduced  $\chi^2$ . Additionally, reduced  $\chi^2$  served as a correction estimate *a posteriori* to obtain the SSD ( $S_{bradykinin\ signal\ noise}^2$ ).

$$S_{bradykinin\ signal\ noise}^2 = S_{bradykinin\ ions}^2 + S_{system\ noise}^2 \quad E\ 3.2$$

Now the system SSD was subtracted from the bradykinin signal noise SSD, leaving bradykinin ions SSD ( $S_{bradykinin\ ions}^2$ ). Finally, integral weights were removed, and

further processing was performed for each laser system individually. The final steps for ion collection yield determination for the picosecond and fs-laser systems are found in subsections 4.5 and 5.7, respectively.

The programming scripts can be found in the GitHub repository under the following address [150].

### 3.3 Summary

This chapter established a protocol for thin films essential to perform the experiments utilized in the following paragraphs. Until now, no simple yet effective method for thin water film production has been reported in the literature. However, depending on the pipetted volume and sample preparation protocol, film thickness between 2  $\mu\text{m}$  and 30  $\mu\text{m}$  are now achievable.

The mass spectrometer is equipped with a cryogenic stage, which allows experiments at cryogenic temperatures and measurements at different temperatures. However, as the temperature cannot be measured simultaneously during the initial experiments, a systematic study to plot a temperature profile depending on the elapsed time was performed. This study served as a reference for the following chapter.

Finally, in a bright field setup, the thin film behaviour was captured during the temperature rise. The vacuum chamber was equipped with the same sample carrier, found in the time-of-flight mass spectrometer. A constant movement of interferences during temperature rise was observed, indicating that the thin film thickness was highly dynamic before ice sublimation. Residual gas analyzer experiments verified that sample stage temperature above  $-100\text{ }^{\circ}\text{C}$  triggers ice sublimating.



## 4 DIVE Mass Spectrometry with Cryogenic Thin Films

*Preliminary results of frozen bulk water droplets were elaborated in close collaboration with Frederik Busse. The extraction region was adopted from a Bruker time-of-flight mass spectrometer and was implemented by Djordje Gitaric. The sample carrier loading mechanism was conceived by the scientific supporting unit Friedjof Tellkamp, Hendrik Schikora, Jan Leimkohl, and Martin Kollwe.*

### ● Preamble

In this paragraph, the reader will be introduced to the concept of DIVE, which can be implemented in the mass spectrometric environment. DIVE was already explained in paragraph 2 and can be put into a broader context of infrared laser (water) matrix-assisted desorption and ionization (IR-(MA)LDI). In the beginning, the direct analysis of biological samples from frozen aqueous solutions was investigated. Afterward, different sample preparation techniques and their impact on spectral quality will be discussed. Then the limit of detection and mass limits for pure water IR-(MA)LDI is determined. Through different strategies, the improvement of IR-(MA)LDI sensitivity is addressed, including the use of glycerol as an additive. Then, temperature-dependent measurements give some insights into the solvent role and substrate contribution to the analyte signal onset. In the final part, the ion collection yield was calculated.

### 4.1 Introduction

The gold standard to investigate considerable large biological molecules in a vacuum is the MALDI [11]. Utilizing small ultraviolet light absorptive synthetic molecules as a mediator between the incident laser light and the analyte allows for detecting labile molecules with a negligible amount of fragmentation. The possibility of focusing the laser beam on a small area opened the door for MALDI to perform IMS, which is applied to explore different living organisms and their tissues on a molecular

---

level and in an unprecedented amount of detail [18]. However, the mediator is commonly referred to as the (MALDI) matrix and is unfortunately not a universal agent, and dozens of different matrices exist that are tailored to a specific class of a biological component. Choosing the suitable matrix requires frequent testing, and usually, the application of two matrices on the same specimen reveals a higher number of biomolecules in contrast to a single matrix [151]. Although MALDI is a highly advanced technique, the question remains how close it is to the true native condition. The sample preparation protocol in MALDI involves multiple steps, but every additional step in sample preparation potentially changes the specimen's original composition, making data evaluation ambiguous. Therefore, a reduction of sample preparation steps is an essential factor. A possible solution is to use water as it can be found in all living organisms, and in combination with a laser system, which is tuned to excite the vibrational modes of water, the usage of an artificial matrix can be avoided. Since water possesses a high absorption coefficient of around 3  $\mu\text{m}$  and most biomolecules are not excited by that spectral width, making the wavelength ideal for a gentle desorption and ionization process.

Water as a matrix was successfully employed under ambient conditions for a complex specimen like tissue sections and cells [152]. However, high sensitivity was achieved with the aid of other ionization sources like ESI [153], [54]. Only a few studies exist under low-pressure conditions, where ion transmission is considered to be higher. A unique approach is the implementation of a low-pressure (2 mbar) pre-chamber by the Dreisewerd group showing IR-(MA)LDI mass spectra of peptides and proteins with a comparable UV-MALDI quality [36], [102]. Studies performed at even low-pressure conditions reported problems obtaining peptides and proteins directly from ice. Berkenkamp *et al.* [35] showed exciting results with the frozen droplets under mid-IR irradiation, and they were able to identify masses up to 17 kDa. Unfortunately, the authors used trifluoroacetic acid (TFA), a typical proton donor in MS, adding a sample preparation step and moving away from native conditions. Also, for the detection of higher masses, TFA was not sufficient, and Tris·HCl was used. Other studies focused on using additives in the water to obtain a more robust and reproducible result [100], [154]. Other strategies targeted sodium, as water it can be found in all living organisms [155]–[158], but often suffered from high deviations of signal intensity. Despite the encouraging results, IR-(MA)LDI has been hampered by some factors, most importantly the lack of focus on sample preparation and sampling, which stays in great contrast to the well-established sample preparation protocols for UV-MALDI.

However, all these studies reported a lack of sensitivity compared to UV-MALDI. Some even stated that water as a matrix is unsuitable for MS. In general, these reports put little effort into investigating different sampling methods and provided minimal details about sample preparation.

---

## 4.2 Pure Water as Matrix for Infrared Laser Desorption and Ionization

Since water is the most abundant chemical in all living organisms, it conveys the opportunity to investigate specimens without rigorous pre-treatment and under native conditions. In the upcoming subchapter, the feasibility of the water as IR-(MA)LDI matrix is explored.

### 4.2.1 Bulk Frozen Water Droplets

In our first attempt, we tried to reproduce the results already published by Berkenkamp *et al.* [35]. Here, the specimen was first applied to the coverslip and dried under ambient conditions. Then the sample carrier was plunged into liquid nitrogen, transferred into the mass spectrometer, and analyzed. However, the sample preparation protocol suggested in the publication did not give satisfactory results.

In search to obtain high-quality mass spectra, we developed a novel sample preparation protocol. After pipetting 1  $\mu\text{l}$  of the analyte onto the substrate, the specimen was slowly dipped into liquid nitrogen and subjected to mass spectrometric analysis. To our surprise, we can obtain mass spectra from the very rim of a droplet but only after several shots on the same spot. These findings stand in great contrast to the literature [35], where water as a matrix has shown unsatisfactory results. However, superior mass spectra were recorded when oversampling with less than 20  $\mu\text{m}$  step size was applied. Any deviation from such sampling mode caused a dramatic decrease in analyte signal quality. However, when the laser spot was moved from the edge of the droplet towards the center, the signal abruptly vanished. A typical specimen is shown in **Figure 4.1**, panel A, while the dark area was produced by the incoming laser beam. Once the laser beam intersects with the edge of the droplet mass spectra as in **Figure 4.1**, panel B were obtained. A signal with a low shot-to-shot fluctuation can be generated up to 200 times from the same spot. We like to stress the fact by saying that proton agents known to improve signal quality, like trifluoroacetic, were not used in this work. However, the signal has a signal-to-noise ratio of 60:1 and a mass resolution of 50 (full width half maximum, FWHM). Two reasons for the low mass resolution might be mentioned here. First, IR-MALDI is known to have a lower mass resolution than UV-MALDI. The low mean initial ion velocity can explain the low mass resolution for peptides around 1 kDa [159]. Second, the major factor for the drop in mass resolution is the static extraction field used in our setup, compared to delayed extraction [160]. Aside from the low mass resolution, the intact analyte, a doubly charged species, angiotensin dimer along with an angiotensin II signal, reflecting a cleavage between the 8 and 9 residues [161], were

---

observed. Angiotensin II might be a fragment from the desorption and ionization process, but contamination in a commercial vial was also possible, as we did not purify the chemicals before usage. As the dimer, as well as angiotensin II signal, were considerably lower in intensity than the intact species, we did not investigate the source. An interesting feature of the mass spectrum is the intensity of doubly charged angiotensin. In a traditional MALDI experiment, the doubly protonated species is barely visible or absent [91], [107], [161]. A more pronounced doubly charged species can be found in mass spectra generated with ESI [162], [163], or by atmospheric pressure UV-MALDI [164].

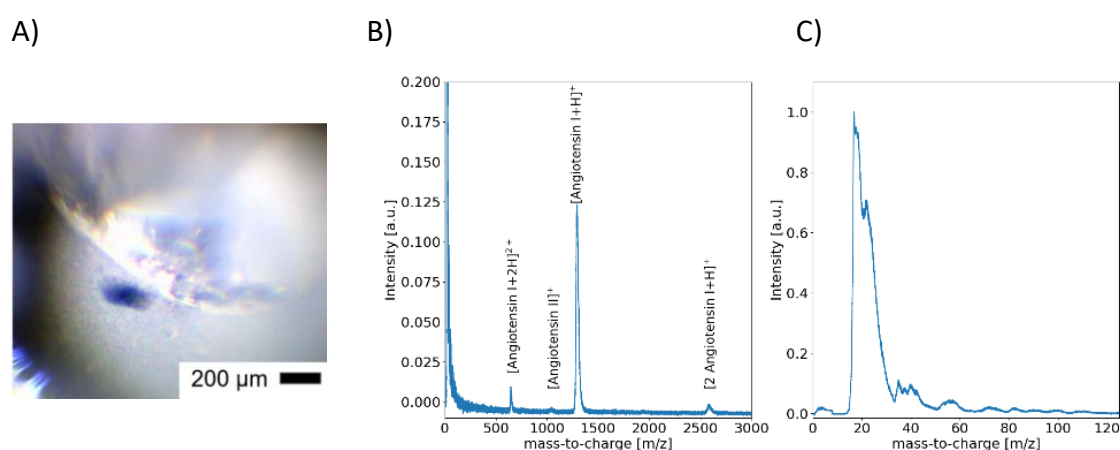


**Figure 4.1** Angiotensin mass spectrum from bulk frozen water. A) A brightfield image of the original sample inside the mass spectrometer. The incident laser beam has removed some ice from the surface (dark area). B) 100  $\mu\text{M}$  angiotensin solution was used for the presented mass spectrum, and data acquisition was performed in oversampling mode. C) Zoom into the small mass region, most likely consisting mainly of a single signal produced by water and sodium ions. The stage was moved 20  $\mu\text{m}$  to the left for data acquisition, and the laser was operated at 1 Hz. The temperature during the recording was -140  $^{\circ}\text{C}$ , and the pulse energy at the sample stage was 56  $\mu\text{J}$ . In total, 122 single shots were averaged for the mass spectrum.

Panel C in **Figure 4.1** is focused on the small mass region of the angiotensin mass spectrum. This window reveals a strong signal covering the mass range between 18 and 35  $\text{m/z}$ . Unfortunately, the mass resolution is not sufficient to distinguish separate elements. Still, considering the limited options of elements that can possess such mass, it is most likely to be water and sodium ions. However, sodium and water ions prevented higher pulse energies because those species oversaturated the detector and decreased analytical performance. The mass spectrometer was not



equipped with a deflection plate, and therefore, the ion suppression for abundant species was impossible.

The results so far discussed here were elaborated in our laboratory and published in a previous work [165]. The next step is to investigate different sample preparation techniques, which have not been examined yet.

#### 4.2.2 Semi-thick Aqueous Films

Our previous observation showed that the droplets rim gave a good signal, while the center lacked any signal. As the specimen is thinner at the rim in comparison with the center of the droplet, we were motivated to change the sample preparation protocol, which yields moderate sample thickness throughout a larger area.

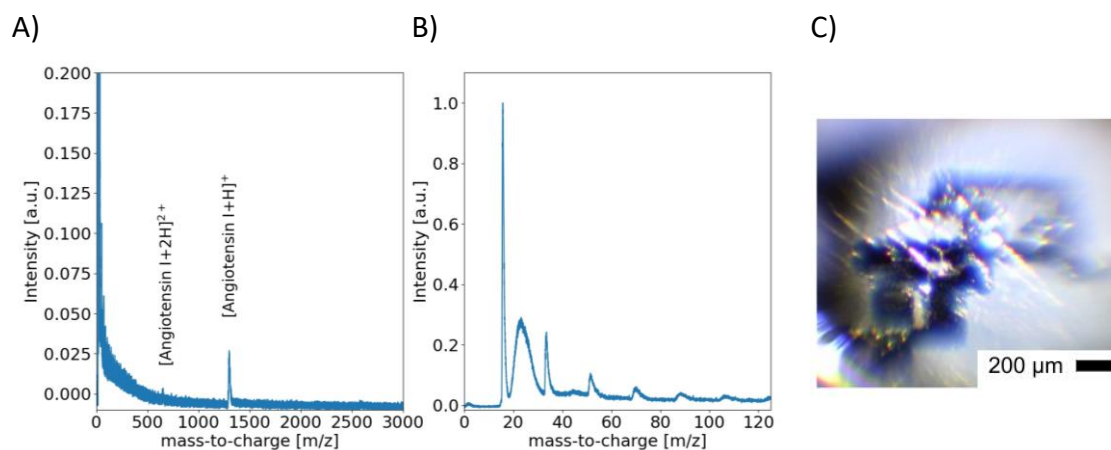


**Figure 4.2** Angiotensin mass spectrum obtained from a semi-thick sample (30 μm). Semi-thick films were prepared using a *Prolene* polymer film. A) The presented mass spectrum was obtained from a 100 μM angiotensin solution in an oversampling mode. B) Zoom into the small mass region, showing water clusters up to 110 m/z. C) A bright-field image of the original sample. The incident laser beam has removed some ice from the surface (dark area). For data acquisition, oversampling with 20 μm step size at 1 Hz was applied. The temperature during the recording was - 140 °C, and the pulse energy at the sample stage was 60 μJ. In total, 108 single shots were averaged for the represented mass spectrum.

The detailed workflow of the preparation of a semi-thick specimen is described in subsection 3.2.3 Briefly, 2 μl of the analyte's solution is pipetted on the substrate. On top, a commercially available *Prolene* polymer film encloses the drop with the substrate. Without any additional pressure, the target was dropped into liquid nitrogen. A feature of this method is that the polymer film can be removed above the

---

liquid nitrogen surface as well as in liquid nitrogen if contact between the specimen and ambient air is not desired. The resulting film thickness is on average 30  $\mu\text{m}$ .

**Figure 4.2**, panel A, features the angiotensin's mass spectrum obtained from semi-thick frozen water film, which shows high similarity with the mass spectrum obtained from frozen bulk water (**Figure 4.1**, panel B). In addition, the singly and doubly charged species can be identified with pulse energies comparable to those used in IR-(MA)LDI experiments with artificial matrices [139].

**Figure 4.2**, panel B shows the low mass region of angiotensin's mass spectrum. Several distinct peaks can be identified, associated with protonated water clusters starting with  $\text{H}_3\text{O}^+$  (19,0 m/z) and reaching masses up to 160 m/z. These findings differ from the previous report [35], which recorded water clusters only with sodium as an adduct. Between water monomer and dimer, an additional broad signal covers the range between 21 and 30 m/z. This peak can be expected to consist of several species, but due to the lack of mass resolving power, those signals are overlapping.

However, the sample preparation protocol impacts the mass resolution. For the semi-thick film, the mass resolution was at  $R = 92$  (FWHM), while for bulk frozen droplets, the number is almost twice as low ( $R = 52$ , FWHM). This advance may be attributed to a more even thin film morphology [166] than the bulk frozen droplet. The droplet's rim has a slope, and the constant moving of the laser spot towards the center of the droplet effectively reduces the distance in the extraction region and, hence, changes the analyte's flight time, which ultimately leads to reduced mass resolution when several single-shot mass spectra were averaged. Such a scenario can be accounted for by adjusting the arrival time of the same species through different runs with a software, but such a feature was not built in our data analysis pipeline. Conversely, in terms of the signal-to-noise ratio of the analyte signal, the bulk frozen droplets performed better (11:1 vs. 60:1). A possible explanation for this finding is that in the case of frozen bulk water, up to 200 high-quality mass spectra could be recorded from a single spot once a suitable position was found. The data acquisition for semi-thick samples was different. The laser and the stage were operated at 1 Hz, while the latter was moved each time 20  $\mu\text{m}$  in different directions **Figure 4.2** panel C). Although variation in sample thickness can cause signal fluctuation, it did not affect the mass resolution as the extraction of bradykinin from frozen bulk water droplets.

The most important finding here is that, in contrast to data collection in single-shot-per-spot mode, oversampling delivered the most robust and reproducible results. As only a fraction of the focal spot was used to desorb the frozen aqueous film, the volume of laser analyte interaction must be smaller than the beam waist diameter. However, if the ablation volume is cylindrical with a 150  $\mu\text{m}$  for the diameter and 30  $\mu\text{m}$  for the height, the single-shot sensitivity is at 200 fmol, but probably due to the aforementioned reasons, even less. This result surpasses the sensitivity values previously published for IR-(MA)LDI by several orders of magnitude [35].

---

After presenting the setup's capability to produce mass spectra with resonant infrared laser light in RG, and the possibility of creating analyte signals in TG was investigated. Several studies concerning MALDI successfully analyzed peptides in such configuration [167], [168], [169]. Furthermore, as already mentioned in the introduction, back illumination allows high numerical aperture lenses, hence facilitating a smaller laser spot. This feature is desirable as a tighter focus also provides a more detailed picture in mass spectrometric imaging [170].

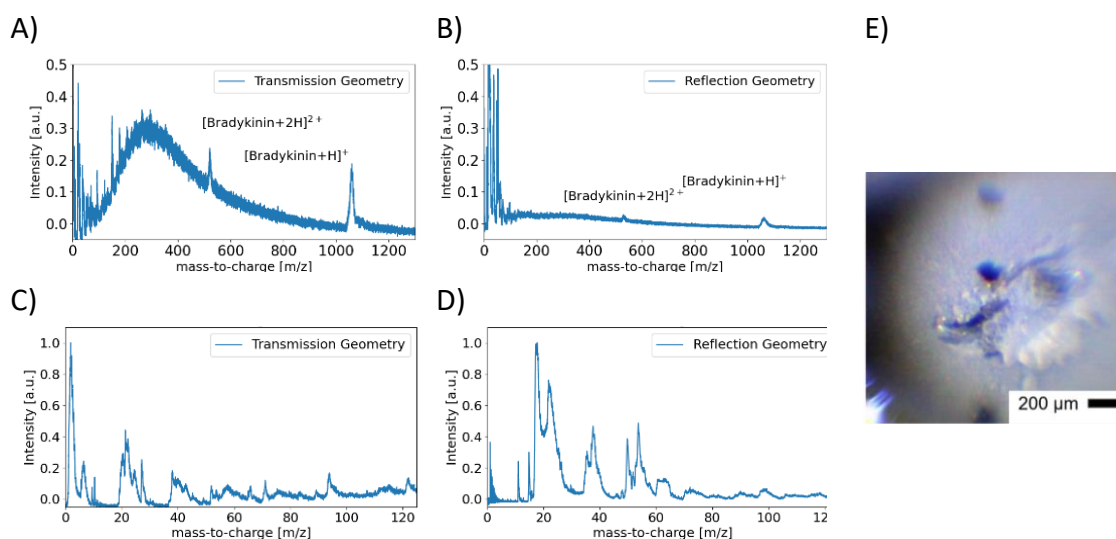


**Figure 4.3** Bradykinin mass spectrum from semi-thick sample produced with a *Prolene* polymer film. A) Bradykinin solution was prepared and irradiated from the back for the present mass spectrum. B) Mass spectrum produced by irradiation from the front near the back ablation. The generated mass spectrum was obtained in oversampling mode. The y-axes in A and B are cut for a better visibility C) Zoom into the small mass region, showing water clusters up to 56 m/z. D) Zoom into the small mass region, showing water clusters up to 56 m/z. E) A brightfield image of the original sample. Data acquisition was mainly on the rim of the semi-thick layer. The temperature during the recording was  $-140^{\circ}\text{C}$ , and bradykinin concentration was  $200\ \mu\text{M}$ , while  $1\ \mu\text{l}$  was pipetted during sample preparation. The pulse energy at the sample stage was  $55\ \mu\text{J}$ . In total, around 300 single shots were averaged for the given mass spectra.

Unfortunately, all attempts to produce mass spectra quality comparable with those in reflection geometry by varying voltages, the magnitude of irradiance (up to  $180\ \mu\text{J}$  per laser pulse), and realignment of the ablation laser ended in unsatisfactory results. One particular highlight is depicted in **Figure 4.3**, panel A). Here bradykinin signal could be obtained in TG in an acceptable quality; however, only from the rim of the semi-thick film (**Figure 4.3**, panel E). The doubly charged bradykinin is also visible in

---

the mass spectrum in addition to the quasimolecular ion species. The mass spectrum is accompanied by an elevated baseline reaching its peak around 300 m/z. Attempts to reduce this undefined signal by varying the extraction voltage led to the following observation. Increasing the extraction electrode voltage above the sample stage voltage suppressed the bradykinin signal immediately while the non-zero signal persisted. Under this condition, only those ions reach the detector formed after the extraction electrode, suggesting that the source of these ions was initially neutrals between the sample stage and the extraction electrode. An explanation concerning the signal broadness is that neutral ice aggregates and/or clusters [171], [172] are ejected after the laser pulse and conveyed along the ion path with the kinetic energies they experienced after the laser impact. As these energies are widely distributed, so are the arrival times at the detector. These events are also known for UV-MALDI and lead to decreased analytical performance [173]. Several strategies can be perused to avoid or at least minimize the formation of clusters and aggregates. Reducing the sample thickness is one option, and the results will be discussed later.

The bradykinin mass spectrum in RG obtained from the same region is presented in **Figure 4.3**, panel B. An elevated baseline with a peak of around 300 m/z is also discernable. The signal intensity is comparable to that obtained from the center of the semi-thick film in the previous experiment (**Figure 4.2**, panel A).

Panel C) and D) divulge the mass spectrum region with small masses. Although different in shape, water monomer (19 m/z), dimer (37 m/z), and trimer (56 m/z) signals can be identified for both geometries. Presumably, the data acquisition algorithm for the mass spectra and the low mass resolution contributed to the signal form. Until now, this is the first successful record of a peptide in RG and TG under cryogenic conditions.

#### 4.2.3 Thin Ice Films

Motivated by the fact that bradykinin mass spectra can be obtained at the rim of the semi-thick sample, suggesting that a thinner ice layer might be beneficial for obtaining a good analyte signal in TG, even thinner ice films were employed. An explanation for this observation might be that irradiation from the back first heat up the lower layers of water, while superficial layers are still ice. Pressure increase breaks up the top layer, but clusters and aggregates are primarily released instead of gaseous ions. Such a scenario affects the analytical performance because the aggregates are ejected in random directions, which carry the analyte molecules otherwise accessible for the analyses if in a gaseous phase. The aforementioned phenomenon is of greater concern for thicker ice films. Therefore thinner ice film can provide a solution for the described phenomenon.

The applied volume and the wetted surface were accounted for the thickness calculation, which led to an average of 12  $\mu\text{m}$ . In the first attempt to produce, acceptable mass spectra from 100  $\mu\text{M}$  solutions failed in RG as well as in TG. Only a tenfold increase led to meaningful mass spectra. **Figure 4.4**, panel A presents a mass spectrum of bradykinin obtained in the TG with a signal-to-noise ratio of 6:1 and a mass resolution of  $R = 100$ . **Figure 4.4**, panel C shows a brightfield image of the ablation area. The mass spectrum gained multiple signals in the low mass range with higher pulse energies, expanding the window for high abundant peaks up to 300  $m/z$  (**Figure 4.4**, panel B). Most notably, the difference between those signals is 28  $m/z$ , which corresponds to the most frequent silicon isotope ( $u = 28.085$ ). Due to the low mass resolving power, the silicon clusters appeared as one broad signal, but multiple silicon isotopes are actually overlapping. Other high-intensity peaks represent water clusters.

In contrast to **Figure 4.3** panel A (semi-thick films), doubly protonated bradykinin is absent in the transmission geometry. A reason for this might be the overall low intensity of the analyte. Another difference is the formation of adducts. The masses with the highest adduct peaks are 1102  $m/z$  and 1148  $m/z$ . With a mass difference of 46  $m/z$ , the former peak represents the attachment of potassium to bradykinin. The exact mass for potassium is 39.1  $m/z$  and reasonably supports the assumption. Furthermore, potassium is a well-known adduct in UV-MALDI [167] and IR-MALDI [174]. This element's source is most likely bradykinin, which in our case was not purified before usage. The source for the mass 1148  $m/z$ , which has a mass difference of 87  $m/z$  to the quasimolecular bradykinin ion, could not be ascribed to any known adduct.

**Figure 4.4**, panel D features the bradykinin mass spectrum in RG for thin-water-film, while panel F shows the ablation area. The signal can be obtained throughout the thin film, but generally, with low intensity, reflecting the result already observed during the irradiation of the rim of the semi-thick samples (**Figure 4.2**, panel C). Remarkably, both oversampling as well as SSpS mode provided similar results. This finding indicates that oversampling mode is superior, but only when the interaction volume is sufficiently large. **Figure 4.4**, panel E zooms into the smaller masses region of panel D. Contrary to **Figure 4.4**, panel B, the mass window produced in RG lacks any abundant cluster formation. The proton is the most intense signal for RG, but it is the silicon monomer for the mass spectrum obtained in TG.

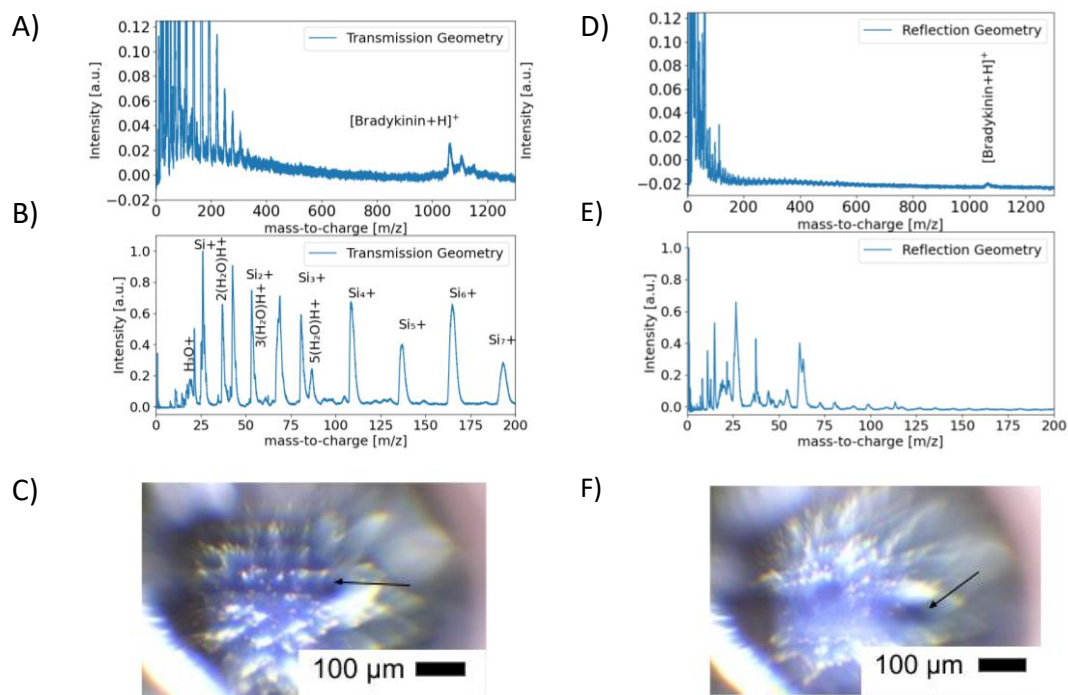


**Figure 4.4** Bradykinin mass spectrum obtained from thin-film (12  $\mu\text{m}$ ). The focused laser beam diameter was approximately 150  $\mu\text{m}$ . The recording temperature was  $-140\text{ }^\circ\text{C}$ , and bradykinin concentration was 1 mM, while 750 nl were pipetted. The pulse energies at the sample stage were 104 and 89  $\mu\text{J}$  for front and back illumination, respectively. In total, 30 single shots were averaged for the presented mass spectra. A) Bradykinin mass spectrum produced by back illumination. B) Zoom into the small mass region, showing water and silicon clusters. C) A brightfield image of the original sample inside the mass spectrometer. The arrow indicates laser impact location. D) Mass spectrum produced by irradiation from the front using oversampling mode. E) Zoom into the small mass region. F) A brightfield image of the original sample. The arrow indicates laser impact location.

The preparation of thin ice films allowed to conduct single shot MS of known volume (height = 12  $\mu\text{m}$ , diameter = 100  $\mu\text{m}$ , and  $C_{\text{Bradykinin}} = 1\text{ mM}$ ) and estimate the limit of detection. Ultimately, a sensitivity of roughly 2 nanomoles per shot was achieved. This value is acceptable for IR-MALDI but is several orders of magnitude below UV-MALDI, consuming 500 attomoles per shot [175].

Overall this finding suggests that obtaining a signal from thin films for RG and TG is possible. However, the signal quality decreases dramatically for the RG compared to the signal obtained from bulk frozen water and semi-thick films. Also noticeable is the interaction between laser light and the substrate during the irradiation in TG, resulting in high-intensity silicon clusters almost nonexistent in RG. In addition to the

described phenomena, we also wanted to investigate the impact of even thinner aqueous films in the upcoming subsection.

#### 4.2.4 Ultra-thin Ice Films

The previous chapter used 750 nl of a 1 mM sample solution to produce 12  $\mu\text{m}$  thick ice films. In this chapter, we used less volume leading to a protocol with an overall 200 nl for an ultra-thin film of about 2  $\mu\text{m}$  height. Throughout this chapter, ultra-thin film and thin film refer to sample thicknesses of 2 and 12  $\mu\text{m}$ , respectively. In addition to previous data, the impact of temperature rise was scrutinized.

The first studies were conducted with 1 mM bradykinin concentration, but analyte signal could not be obtained. A tenfold increase in concentration provided unsatisfactory results, and different sample areas led to the high standard deviation for the analyte signal in RG as well as TG. Increasing the pulse energy and changing the extraction fields did not produce the desired. We rejected the idea of increasing the analyte concentration further because such a high concentration is impractical and undesired as analytical methods are developed to trace low concentrations of a specimen. Therefore the signal onset during temperature rise was investigated. As temperature measurements were only possible without high voltage, a temperature profile was recorded before the initial experiments. Hence, the elapsed time was used to estimate the sample stage temperature. To provide an unbiased picture between the runs in RG and TG, we assured that each mass spectrum was recorded within a short time window. Further, all spectra were generated from an area size of 0.25 mm<sup>2</sup>. Small sample area reduces sample and substrate-related inhomogeneity, providing a more objective picture. Finally, the laser pulse energies were increased to obtain bradykinin signal intensities from thin ice films similar to those from bulk frozen water droplets and semi-thick films.

**Figure 4.5** panel A shows a series of bradykinin mass spectra in RG for different temperatures. The first two mass spectra were recorded at -140 °C, and -107 °C (blue and orange trace), lacking an analyte signal, but substrate ions and the non-zero baseline were present. The absence of the analyte seems to contradict the finding in subsection 4.2.3, because a signal was obtained under cryogenic conditions. However, this apparent conflict might be resolved by looking at the amount of ejected particles. First, we estimate the amount of material in the excited volume. Assuming that the crater diameter produced by the laser pulse was the same (100  $\mu\text{m}$ ) for both samples and all material was ejected, the calculated moles are  $n_{\text{bradykinin}, 12\mu\text{m}} = 6.3 \cdot 10^{-13}$  and  $n_{\text{bradykinin}, 2\mu\text{m}} = 3.7 \cdot 10^{-13}$ . Hence, on average more particles were ejected in a 12  $\mu\text{m}$  rather than in a 2  $\mu\text{m}$  thin film.

---

The warm-up phase continued, and the following mass spectrum (**Figure 4.5**, panel A, green trace) showed a bradykinin signal for the first time. The mass spectrum was recorded when the temperature at the sample stage was  $-104\text{ }^{\circ}\text{C}$  (64 minutes in the warm-up). An important piece of information here is that ice sublimation started 60 minutes after the liquid nitrogen supply was cut and continued for the next 30 minutes (**Figure 4.5**, panel B). The finding suggests that the water-analyte ratio was preferably reduced for a signal onset, at least for very thin films. Additionally, a bradykinin dimer, trimer, and even tetramer appeared with a sizable intensity.

The following mass spectrum (**Figure 4.5**, panel A, red trace) features a bradykinin signal, while multimer formation was absent. At this point, the sample stage temperature was at  $-86\text{ }^{\circ}\text{C}$  (104 minutes), and a substantial pressure drop indicated that a considerable part of the ice was already sublimated (**Figure 4.5**, panel B). This finding suggests that the residual water / ice is sufficient to promote a signal onset with IR-(MA)LDI and is in line with an earlier report [35]. However, the same group also discovered that signal could only be maintained when the sample stage was actively cooled, which is not the case in our experiment. Another study further deposited only protein powder on the silicon substrate. Subsequently, protein signals were obtained without ice/water [117]. Unfortunately, the report did not mention how long the signal persisted while the sample was in the mass spectrometer. As protein and peptides are always covered by a residual water layer, which was also intact when analyte was in the low-pressure conditions, a possible explanation might be a hydration shell, which supports analyte desorption and ionization. However, our findings suggest that hydration shell/residual water is active and supports desorption up to an hour after the sublimation onset. Once the ice sublimation is completed, the analyte signal also started to vanish. One exception is a mass spectrum showing the bradykinin signal at  $T = -4\text{ }^{\circ}\text{C}$ , which is likely an artefact because only very few areas provided such observation.

Remarkably, the low baseline between masses 100 and 500  $m/z$  was presented in all mass spectra before ice sublimation (**Figure 4.5**, panel A). As described above, we suspected that neutral species that experienced post source ionization were mainly responsible for the pronounced chemical background. After this experiment, we are confident that water/ice clusters contributed to the non-zero baseline.



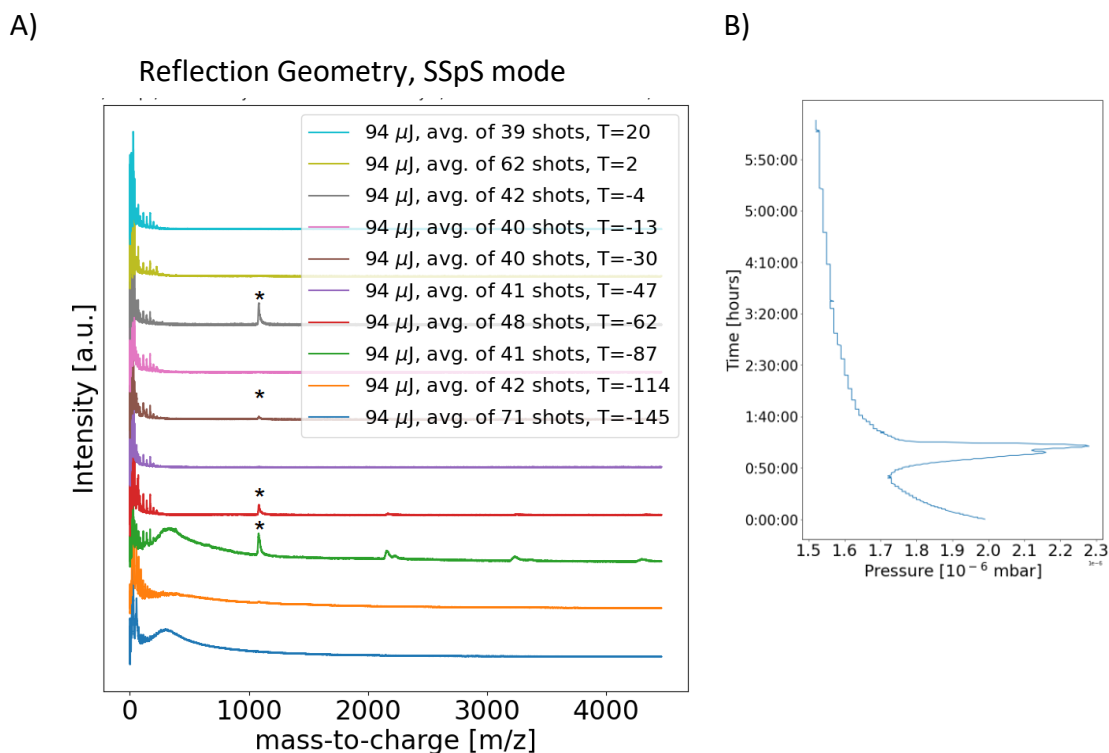


**Figure 4.5** Mass spectra of 10 mM bradykinin (in pure water) obtained in reflection geometry on ultra-thin films (2  $\mu\text{m}$ ). Data collection was performed in SSpS. A) Bradykinin mass spectra at different time points. The lowest trace (blue) is the first recorded mass spectrum after turning off liquid nitrogen supply  $t = 0$ . The temperature in the legend is provided in Celsius. The asterisks indicates the bradykinin signal. B) Recorded pressure in the mass spectrometer during the experiment.

The following mass spectrum (**Figure 4.5** panel A, purple trace) shows substrate signals, but water aggregates and the analyte signals were missing. This observation further solidifies the hypothesis that some hydration shell or residual water must exist to obtain a successful signal [34], as, at this time point, most of the bulk water was presumably sublimated.

All mass spectra recorded afterward shared the same features, and the bradykinin signal was mostly absent while substrate signals persisted. In addition to previously published reports, we were able to detect bradykinin embedded in pure water and without any additives like organic solvent or trifluoroacetic acid [1], [35]. This dispense is the next step toward investigating peptides, proteins, and other biological components under nearly native conditions.

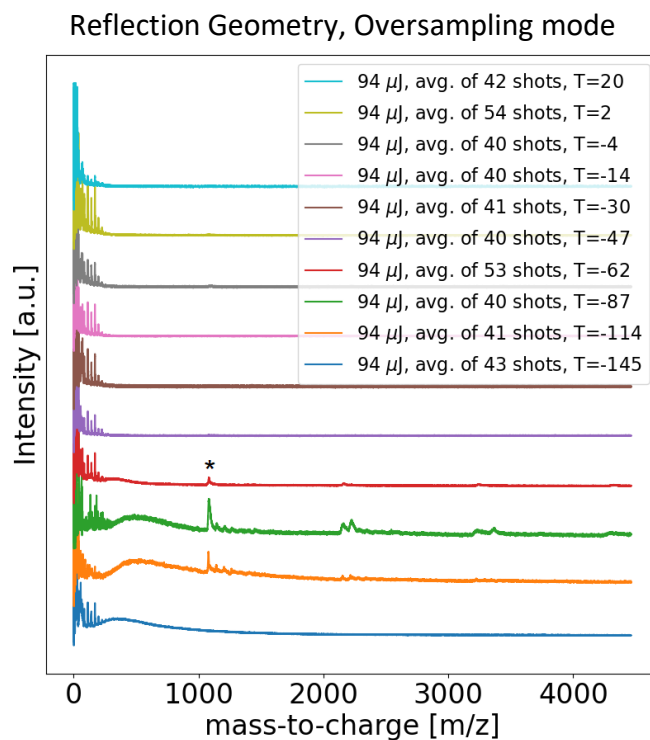


**Figure 4.6** Mass spectra of 10 mM bradykinin (pure water) obtained in reflection geometry on ultra-thin films (2  $\mu\text{m}$ ). Data collection was performed in an oversampling mode in 20  $\mu\text{m}$  steps. Beam waist diameter was approximately 150  $\mu\text{m}$ . The lowest trace (blue) is the first recorded mass spectrum after turning off liquid nitrogen supply  $t = 0$ . The temperature in the legend is provided in Celsius. The asterisks indicates the bradykinin signal.

In **Figure 4.6**, bradykinin mass spectra were obtained in RG using the oversampling mode at different temperatures. The results were similar for the oversampling and SSpS mode, with a single exception. Most notably is the appearance of the bradykinin signal in the second mass spectrum (**Figure 4.6**, orange trace), which was recorded 28 minutes (-114  $^{\circ}\text{C}$ ) after the liquid nitrogen supply was stopped, whereas at this time point analyte signal was missing for SSpS mode (**Figure 4.5**, orange trace). This observation suggests that oversampling, in contrast to SSpS mode, can desorb and ionize the analyte with a higher water-analyte ratio. We speculate that the local temperature increase produced by consecutive laser shots might be a driving factor for signal onset at lower temperature. Besides, signal quality obtained in oversampling and SSpS mode are similar during the ongoing ice sublimation (**Figure 4.6** and **Figure 4.5** green trace) and the upcoming mass spectra.

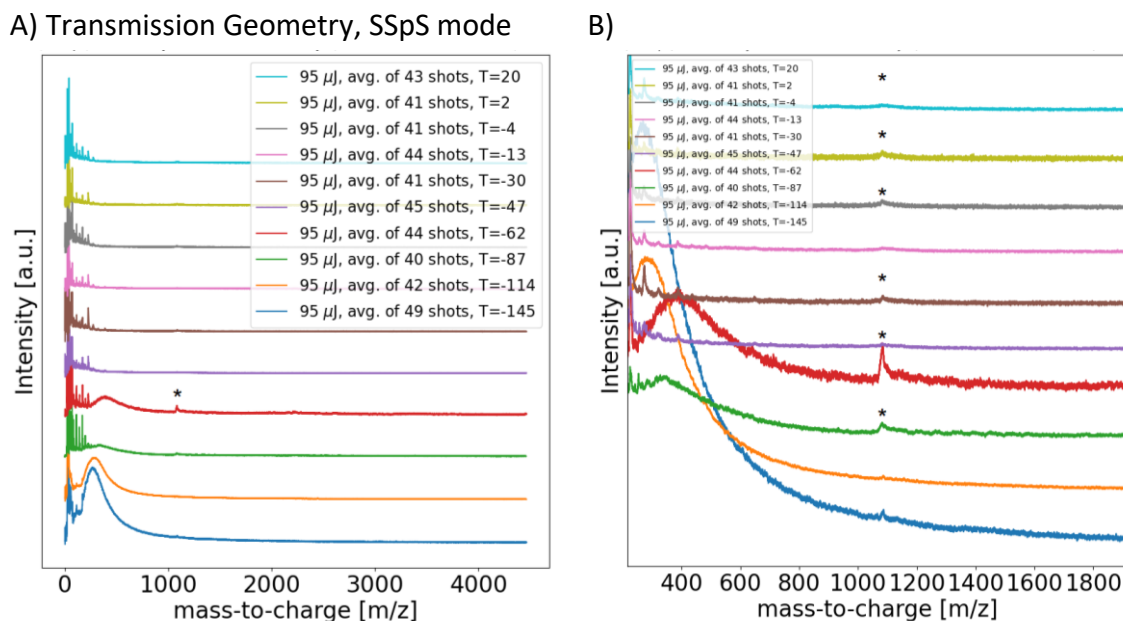


**Figure 4.7** Mass spectra of 10 mM bradykinin (in pure water) obtained in transmission geometry on ultra-thin films (2 μm). Data collection was performed in a single-shot-per-spot (SSpS) mode, while the pulse energy was constant at 95 μJ. Beam waist diameter was approximately 100 μm. A) Bradykinin mass spectra at different time points. The lowest trace (blue) is the first recorded mass spectrum after turning off liquid nitrogen supply  $t = 0$ . The temperature in the legend is provided in Celsius. B) Zoom into the mass range 500-2500 m/z. The asterisks indicates the bradykinin signal.

**Figure 4.7** panel A represents a series of bradykinin mass spectra obtained in TG at different temperatures. A clear distinction between the irradiation geometries is that the analyte signal can be generated throughout the experiment for the back (**Figure 4.7**) but not the front irradiation (**Figure 4.6** and **Figure 4.5**). Possible laser-substrate interaction might be involved because the analyte signal is visible even several hours after the ice sublimation. For such a long time in low-pressure conditions, bulk water should not be present. In addition, photon energies of near-infrared pulses are too low to cause direct ionization of the analyte, which further favors laser-substrate interaction facilitating desorption and ionization. However, irradiation in TG produced inferior signal intensities compared to those obtained in RG.

Conclusively, for some UV-MALDI experiments, thin samples produce higher mass resolution [166]. A possible explanation is that the spatial spread along the z-axis of the same species within a thin film is smaller than in a thicker film. However, the same trend was not observed in our experiments. Semi-thick samples (subsection 4.2.2) produced the highest mass resolution ( $R = 92$ ), followed by ultra-thin samples ( $R =$

---

53). Finally, the sensitivity for the ultra-thin film for TG and RG is roughly 600 femtomoles per shot. An ablation crater diameter of 100  $\mu\text{m}$ , 10 mM bradykinin concentration, and sample thickness of 2  $\mu\text{m}$  are considered for the calculation.

## 4.3 Additives for Infrared Laser Desorption and Ionization

In search of improving signal quality and the sensitivity of the IR-(MA)LDI experiments, we decided to conduct additional runs with sucrose and glycerol. To our best knowledge, the former has not yet found its application as an IR-MALDI matrix, while the latter is a prevalent agent under non-cryogenic conditions and showed the great potential of providing mass spectra of proteins and peptides [101], [176], [177], [178]. By convention, this work uses the abbreviation IR-(MA)LDI in the context of pure water samples, whereas the IR-MALDI abbreviation is used for specimens containing glycerol.

### 4.3.1 Sucrose and Glycerol

Sucrose is a disaccharide and possesses multiple OH groups, which absorb 3  $\mu\text{m}$  light efficiently, like glycerol. In addition, both reduce water's surface tension, favoring a more homogenous thin ice film. Initial runs were conducted with 10 Brix sucrose and glycerol, corresponding to 10 % (w : w) (**Figure 4.8**). A noticeable improvement in signal intensity was achieved in both cases compared to the signal of angiotensin I embedded in pure water obtained with oversampling mode (**Figure 4.2**). In **Figure 4.8**, panel A, the angiotensin signal is accompanied by a series of adducts, which are marked with an asterisk and exemplify  $[\text{AngI}+\text{glycerol}+\text{H}]^+$ ,  $[\text{AngI}+2 \text{ glycerol}+\text{H}]^+$ ,  $[\text{AngI}+3 \text{ glycerol}+\text{H}]^+$ ,  $[\text{AngI}+4 \text{ glycerol}+\text{H}]^+$ , respectively. Reducing the glycerol concentration also minimized the adduct formation and improved analytical performance to a certain degree. In addition, the water cluster accompanied the mass spectrum and reached masses up to 400 m/z (orange trace).

However, we irradiated the specimen under different temperatures and various pulse energies, but the sucrose-based specimen signal was always broader compared to the glycerol-based sample. Another identification mark for the sucrose-based specimen is the left-skewed signal, which minimized mass resolution (**Figure 4.8** panel B). The findings indicate that matrix selection significantly impacts arrival time distribution and is supported by a previously published work [179]. However, a study confronted the mass resolution problem by implementing a grid between the specimen and incident laser beam [180]. In such a configuration, the mass resolving power of IR-MALDI can be as good as that in UV-MALDI. However, this modification was not implemented due to steric constraints.

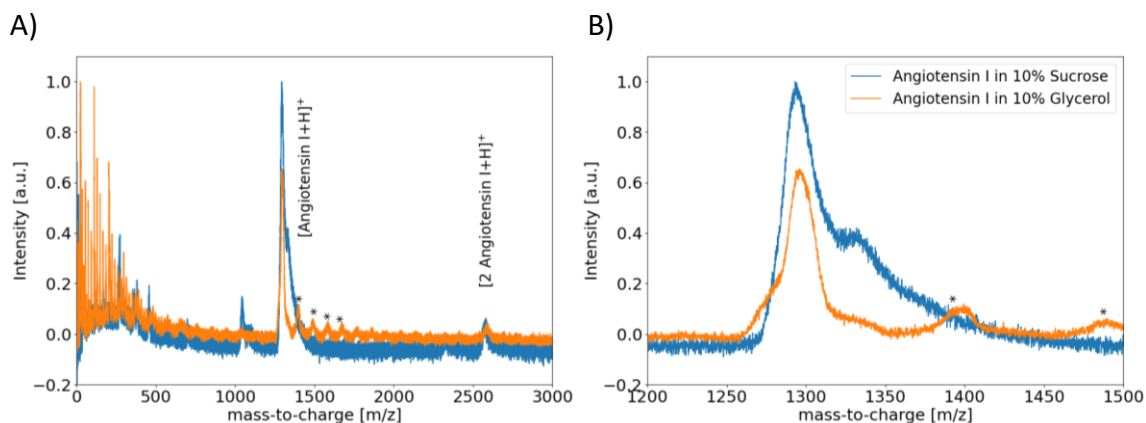


**Figure 4.8** Angiotensin mass spectra with sucrose and glycerol as an additive in IR-(MA)LDI. Data were obtained in reflection geometry with laser pulse energies of 72 and 74  $\mu\text{J}$  for sucrose and glycerol-based samples, respectively. A volume of 2  $\mu\text{l}$  was used during sample preparation, which corresponds to a sample thickness of 30  $\mu\text{m}$ . The angiotensin concentration was 3 mM. A) Angiotensin mass spectrum with the quasimolecular ion species and a dimer. B) Comparison of the signal shape obtained from sucrose (blue trace) and glycerol (orange trace).

The mean arrival time for the angiotensin I in sucrose and glycerol was 24.00  $\mu\text{s}$  and 23.95  $\mu\text{s}$ , respectively (length of the mass spectrometer was 1.14 m). The source for the 50 nanosecond difference was most likely a small modification in the extraction region between the experiments. For our experiments, sucrose and glycerol have a similar impact on flight time. Nevertheless, for UV-MALDI, it is known that matrices influence the flight time of an analyte [181].

An attempt to improve the mass resolution for angiotensin I embedded in sucrose by reducing the content led to signal depletion for the analyte. However, the spread of signal arrival time was somewhat the same. Also, the ultra-thin film for sucrose did not produce satisfying results, unlike glycerol. For these reasons, further studies were conducted on the latter.

#### 4.3.2 Semi-Thick Films with Water and Glycerol

Water-glycerol is a eutectic system meaning that a mixture of different components melts or solidifies at the same temperature. For water with  $\sim 5\%$  glycerol, the solidification temperature is at  $-6\text{ }^\circ\text{C}$  [182]. A previous publication reported difficulties in obtaining peptide signals from water-glycerol solutions. However, they employed a glycerol-to-water ratio of 60% and investigated the specimen at  $-140\text{ }^\circ\text{C}$  [178]. In subsection 4.2.2, we introduced semi-thick films with pure water and obtained a bradykinin signal with a signal-to-noise ratio of 11:1. This paragraph

investigates semi-thick films with bradykinin and a glycerol weight ratio of 2.5 and 5 %. All data presented here were recorded in RG as TG failed to produce meaningful results. Data collection in a SSpS was also possible, but the oversampling mode provided more robust and reproducible results.

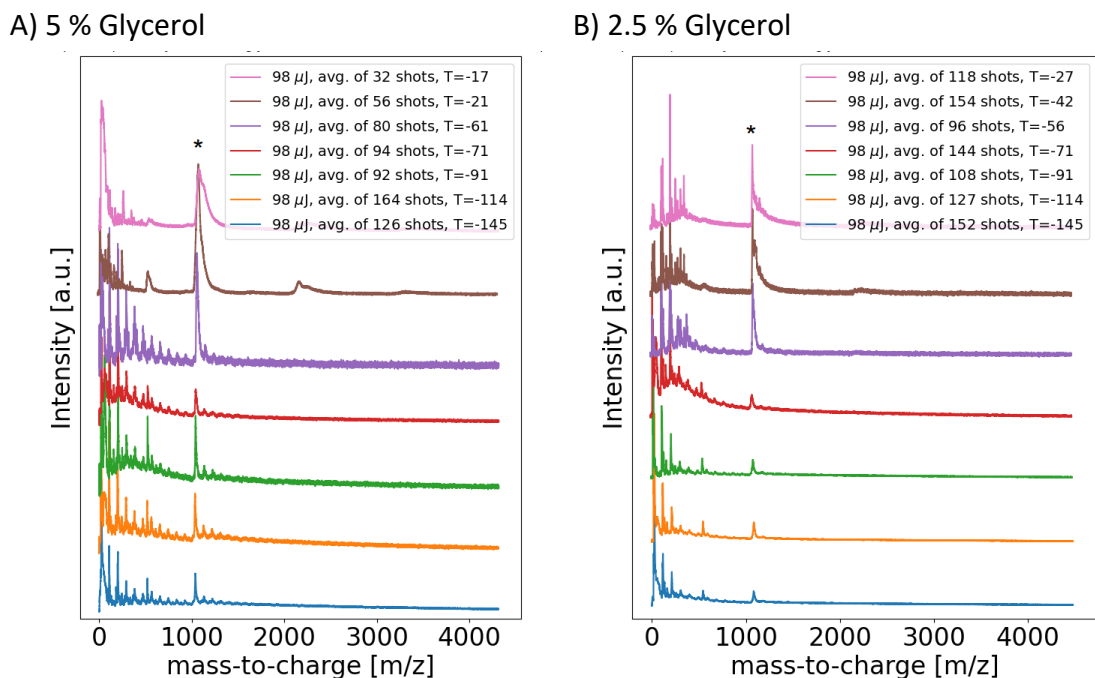


**Figure 4.9** Temperature-dependent series of mass spectra of 100  $\mu\text{M}$  bradykinin in different water-to-glycerol ratios. The temperature in the legend is provided in Celsius. After the liquid nitrogen supply was cut, the warm-up phase started. More details about the temperature profile can be found in subsection 4.2.4. For sample preparation, 2  $\mu\text{l}$  were pipetted, which corresponds to 30  $\mu\text{m}$  thin film thickness. Irradiation was performed in reflection geometry, and data were acquired in an oversampling mode, while the pulse energies were held constant at 98  $\mu\text{J}$ . A) Bradykinin embedded in 5 % glycerol. B) Bradykinin embedded in 2.5 % glycerol. The asterisks indicates the bradykinin signal.

**Figure 4.9**, panel A shows a series of bradykinin mass spectra recorded between -140  $^{\circ}\text{C}$  and -50  $^{\circ}\text{C}$  in 5 % glycerol. Under cryogenic conditions (blue trace), the singly and doubly charged bradykinin signal is immediately visible when the oversampling mode is used for data acquisition. Besides the intact peptide species, the mass spectrum features low-intensity peaks at higher mass than bradykinin. These signals are glycerol adduct and follow the order  $[\text{Bradykinin} + \text{Glycerol} + \text{H}]^+$ ,  $[\text{Bradykinin} + 2\text{Glycerol} + \text{H}]^+$ , and  $[\text{Bradykinin} + 3\text{Glycerol} + \text{H}]^+$ . However, glycerol cluster formation up to 1000  $m/z$  is also present in the mass spectrum. The mass spectra (orange and green trace, **Figure 4.9**, panel A) were similar to the mass spectrum

obtained under cryogenic conditions (blue trace). The red trace was recorded during ice sublimation, which was also captured with a pressure rise inside the mass spectrometer. Shortly after the pressure stabilization, the glycerol clusters were still visible, indicating that bulk ice was completely sublimated. The glycerol clusters disappear only after 190 minutes in the warm-up phase (brown and pink trace). In addition, the last two traces show a severe broadening of the singly and doubly charged quasimolecular bradykinin ion species. Furthermore, bradykinin dimer and trimer formations were visible. A study dealing with IR-MALDI found that proteins embedded in glycerol tend to form multimers [183]. The result shown here suggests that the water-to-glycerol impacts the signal intensity and the mass resolution. If a sufficient amount of ice has sublimated, then the analyte tends to form multimers with the glycerol.

**Figure 4.9**, panel B shows a series of mass spectra of bradykinin embedded in 2.5 % glycerol. Under cryogenic conditions (blue trace), the singly and doubly charged species were generated. However, the signal intensity was lower for bradykinin in 2.5 % versus 5 % glycerol (**Figure 4.9**, panel A and B, blue trace). Glycerol adduct formation as well as glycerol multimers were visible for 5 % and less pronounced for 2.5 % glycerol specimen. The upcoming measurements (**Figure 4.9**, panel B, orange and green trace) show a similar bradykinin mass spectrum obtained under cryogenic conditions. Once again, ice sublimation was monitored between 60 and 90 minutes in the warm-up phase – 91 °C and – 71 °C, respectively. Besides a high baseline, the mass spectrum obtained shortly after ice sublimation shares similar features with those obtained before ice sublimation (**Figure 4.9**, panel B, red trace). Onwards in the temperature-dependent series, a signal with the highest mass resolution and intensity can be generated, which is in line with the result for the analyte embedded in 5 %. Measurements at higher temperatures revealed that the bradykinin signal was accompanied by multimers formation in 2.5 % and 5 % glycerol. An important finding here is that with higher glycerol concentrations, the signal got broader. Additional experiments with 7.5 % glycerol confirmed this trend (Appendix, **Figure A 1**). Accounting for this drawback leads to the decision not to investigate higher glycerol concentration.

Finally, the bradykinin mass spectra were similar in semi-thick films containing pure water (subsection 4.2.2), 2.5 %, and 5 % glycerol. Also, the intensity ratio between the singly and doubly charged bradykinin species was for all samples comparable, although the signal intensity for bradykinin in 5 % glycerol was the highest. The main difference between samples containing glycerol and just pure water is that the former facilitates clusters up to 1000 m/z, which interferes with the analyte signal. In a more complex mixture with multiple peptides, the benefit of gained signal intensity would be outweighed because glycerol clusters interfere with relevant molecules of interest.

---

---

Lastly, further dilution to 10  $\mu\text{M}$  resulted in insufficient shot-to-shot repeatability. This was also the limit of detection for bradykinin in pure water semi-thick samples.

### 4.3.3 Ultra-thin Films with Water and Glycerol

In subsection 4.2.4, a temperature-dependent measurement was introduced with 2  $\mu\text{m}$  thick films, but this time the experiment was repeated with glycerol as an additive and 10 mM bradykinin. The preliminary result was encouraging, so further measurements were conducted with 100  $\mu\text{M}$  analyte solutions. In addition, the experiment included specimens with 2.5 %, 5 %, and 7.5 % glycerol weight ratios, while the sample irradiation was performed in RG and TG.

In **Figure 4.10**, a series of temperature-dependent bradykinin mass spectra is presented. The figure is split into three panels, showing bradykinin mass spectra with 7.5, 5, and 2.5 % glycerol concentrations. As the obtained mass spectra from different glycerol samples were similar, the upcoming section will focus on the differences only.

The first mass spectra (blue trace) of the panels (A-C) were recorded at -140  $^{\circ}\text{C}$ . The consecutive two mass spectra (orange and green trace) for all glycerol concentrations lacked any occurrence of the bradykinin signal and were accompanied by a non-zero baseline. The background for the latter phenomenon is discussed in subsection 4.2.2.

The fourth mass spectrum (**Figure 4.10**, red trace) was recorded within the first 80 minutes (between -71  $^{\circ}\text{C}$  and -81  $^{\circ}\text{C}$ ) and shows no bradykinin signal for 7.5 % glycerol but for 5 % and 2.5 %.

The fifth spectrum (**Figure 4.10**, purple trace) was recorded (between -56  $^{\circ}\text{C}$  and -59  $^{\circ}\text{C}$ ) 100 minutes after the liquid nitrogen supply was cut and represented for all glycerol concentrations a well-pronounced bradykinin signal. However, the signal quality was mixed, and the bradykinin signal in 5 % glycerol showed significant broadening.

The sixth mass spectrum (**Figure 4.10**, brown trace) gives rise to a high-quality bradykinin signal embedded in 7.5 % and 2.5 % glycerol. The signal-to-noise ratio (S : N) and the mass resolution (R) for the analyte signal is 80 and 150 in 7.5 % and 5 % glycerol, respectively. However, the bradykinin signal in 5 % glycerol was discernable, but the intensity was low.

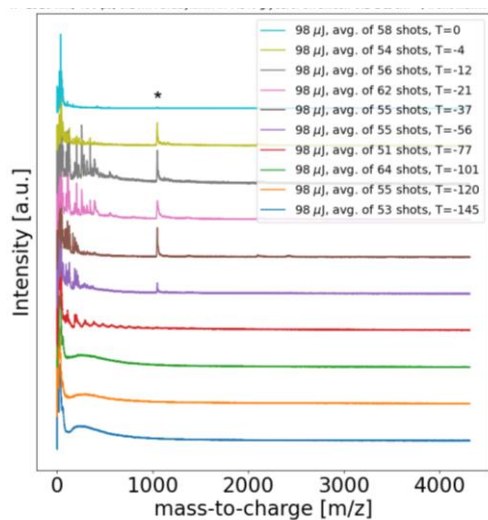
In the following mass spectrum (**Figure 4.10**, pink trace) the bradykinin signal in 2.5 % glycerol disappeared for the rest of the experiment, while it was still visible in 7.5 % and 5 % glycerol. In the progress of the experiment, the bradykinin signal vanished in 5 % glycerol and later also for the highest glycerol concentration. The bradykinin signal was still produced 247 minutes (-4  $^{\circ}\text{C}$ ) after the start of the



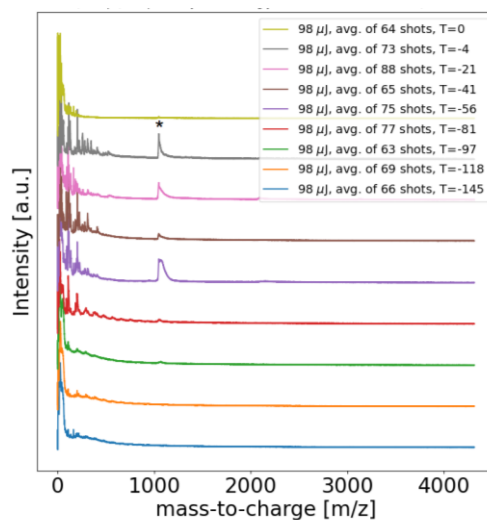
experiment. This observation led to the conclusion that glycerol also diminished over time.

#### 4.3.3.1 Reflection geometry

##### A) 7.5 % Glycerol



##### B) 5 % Glycerol



##### C) 2.5 % Glycerol

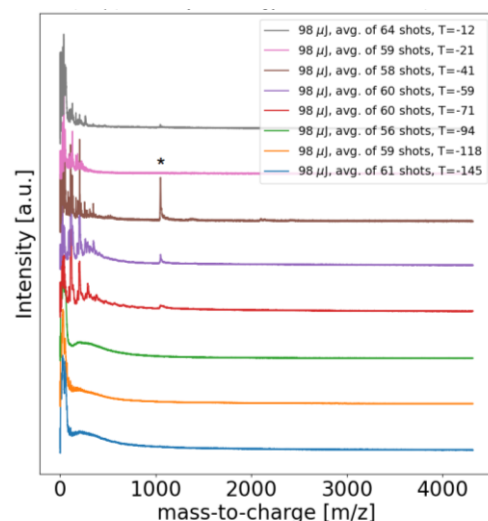


**Figure 4.10** A series of temperature-dependent mass spectra of 100  $\mu\text{M}$  bradykinin in different water-to-glycerol ratios. The temperature in the legend is provided in Celsius. After the liquid nitrogen supply was cut, the temperature gradually increased similarly to in subsection 4.2.4. For sample preparation, 200 nl were pipetted, which corresponds to 2.5  $\mu\text{m}$  average film thickness. Irradiation was performed in RG, and the pulse energy was held constant at 94  $\mu\text{J}$ . Bradykinin embedded in 7.5 % A), 5 % B), and 2.5 % glycerol. The asterisks indicates the bradykinin signal.

Small amounts of glycerol in ultra-thin films dramatically increase the sensitivity of IR-MALDI in contrast to pure water samples. Counter to the results in subsection 4.2.4, analyte concentrations can be reduced one hundredfold. The low sensitivity of IR-MALDI with glycerol as an additive is also described in other studies. Hillenkamp and co-workers studied water and glycerol-based samples with a 2.94  $\mu\text{m}$  laser and concluded that water as an IR matrix is less promising [35]. Their work continued with glycerol as a matrix giving an overall good analytical performance akin to UV-MALDI [160], [184].

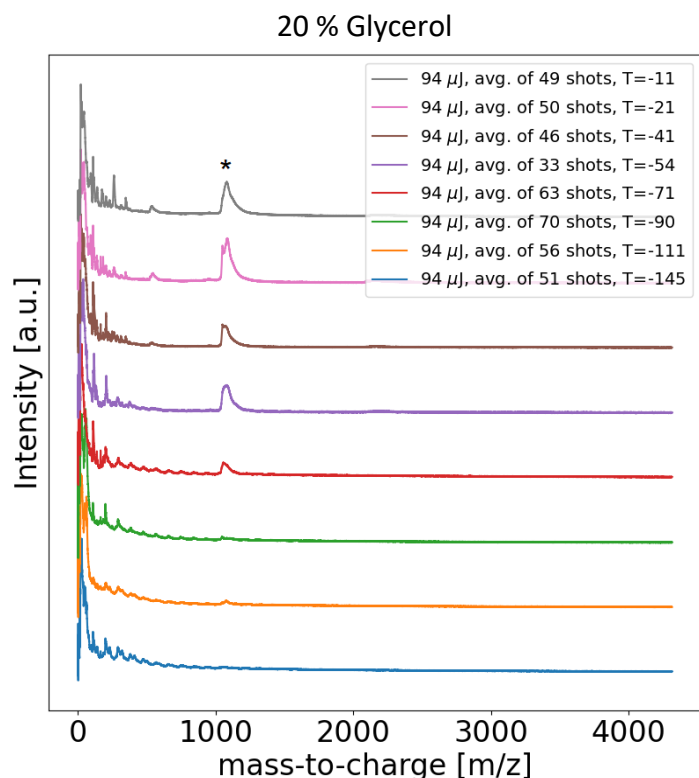


**Figure 4.11** A series of temperature-dependent mass spectra of 100  $\mu\text{M}$  bradykinin in 20 % glycerol. The temperature in the legend is provided in Celsius. After the first measurement, the liquid nitrogen supply was cut, and the temperature gradually increased. More details can be found in subsection 4.2.4. For sample preparation, 200 nl were pipetted, which corresponds to 2.5  $\mu\text{m}$  film thickness. Irradiation was performed in RG, and the pulse energy was held constant at 95  $\mu\text{J}$ . The asterisks indicates the bradykinin signal.

The sensitivity for bradykinin reached 10 femtomoles and was several orders of magnitude higher than in pure water. The calculation included a laser impact crater diameter of 150  $\mu\text{m}$ , a 2.5  $\mu\text{m}$  sample thickness, and 100  $\mu\text{M}$  analyte concentration. The number is in line with the previous glycerol studies for a single shot in RG [176].

The best signal-to-noise ratio and mass resolution values for bradykinin signal in ultra-thin pure water samples were  $S : N = 15$  and  $R = 55$ , respectively (**Figure 4.6**), while these numbers were at least for at least threefold higher glycerol-based samples. The upcoming experiment will clarify whether the increased glycerol content will further increase the sensitivity and improve mass resolution.

The assumption that higher glycerol concentration might further increase the signal-to-noise ratio and mass resolution was refuted in the following **Figure 4.11**. The bradykinin signal is absent under cryogenic conditions (**Figure 4.11**, blue trace), but a low-intensity signal was discernable before ice sublimation (**Figure 4.11**, orange and green trace), which was not the case for lower glycerol concentrations. The bradykinin signal intensified after the ice sublimation (**Figure 4.11**, red trace) but included a severe broadening and reducing mass resolution. A previous study concerned with protein samples containing 50 % glycerol has also reported a loss of mass resolution for analytes [160].

#### 4.3.3.2 Transmission Geometry

The data acquisition for TG was performed in parallel to the datasets in the RG. Special care was put to conduct the front and back illumination spatially close. Therefore a direct comparison between the two geometries with the same water-to-glycerol ratio is possible to a certain degree. In addition, the pulse energies used in the following measurements are similar to those used in **Figure 4.10** and **Figure 4.11**. However, before comparing RG and TG, the results for the latter are presented first. **Figure 4.12** contains three panels representing a series of temperature-dependent mass spectra with different glycerol-to-water ratios. The data acquisition was performed in SSpS mode.

For all glycerol concentrations in **Figure 4.12**, the bradykinin signal (blue, orange, and green trace) is absent along with the non-zero baseline, a reoccurring RG component. The first mass spectrum is represented with the red trace after ice sublimation (**Figure 4.12**, panel A - C). This trace shows a small signal for 5 % glycerol-to-water ratio in the temperature-dependent series for the first time, while the analyte signal was missing for lower glycerol ratios at this time point. This observation suggests that lower water content is beneficial for analyte signal onset. An alternative explanation is that signal intensity increases with temperature rise, which is beneficial for desorption and ionization. However, the latter is less likely since gradual bradykinin signal improvement is missing, and instead, a leap in signal intensity was observed supporting the former scenario. In addition, this phenomenon was also recognized in RG, provoking the conclusion that for both irradiation directions, a lower water-to-glycerol ratio is advantageous.

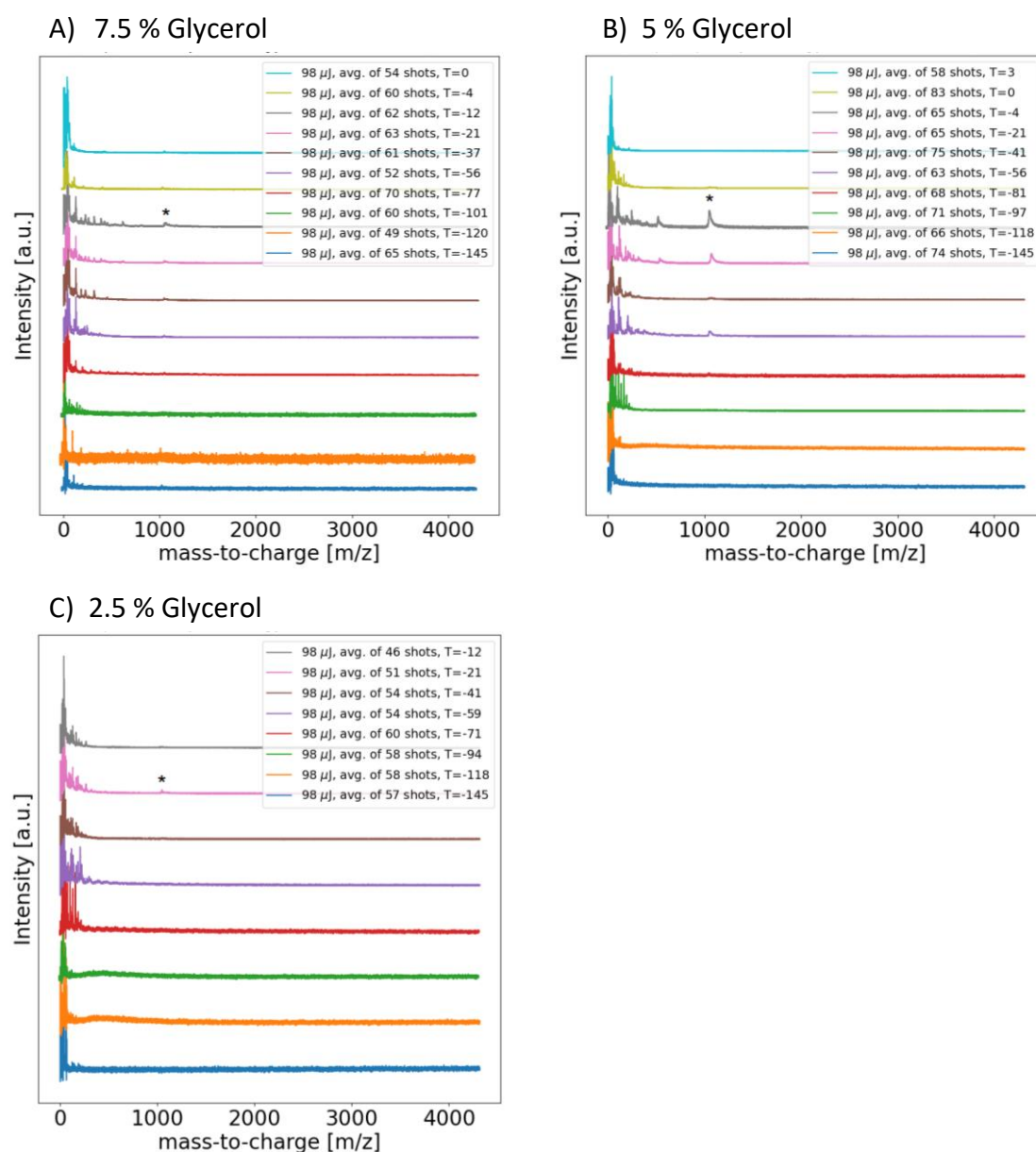


**Figure 4.12** A series of temperature-dependent mass spectra of 100 μM bradykinin in different water-to-glycerol ratios. The temperature in the legend is provided in Celsius. After the liquid nitrogen supply was cut, the temperature gradually increased. More details can be found in subsection 4.2.4. For sample preparation, 200 nl were pipetted, which corresponds to 2.5 μm average film thickness. Irradiation was performed in TG, and the pulse energies were held constant at 98 μJ. Bradykinin embedded in 7.5 % A), 5 % B), and 2.5 % glycerol. The asterisks indicates the bradykinin signal.

In addition, a successful signal generation was possible for 5 % and 7.5 % glycerol concentrations up to an hour after the liquid nitrogen supply was cut (**Figure 4.12** panels A and B, purple and brown trace). However, mass spectra recorded at a later

stage lacked any signal for all glycerol concentrations (**Figure 4.12**, panels A - C). The sample with 2.5 % glycerol did not yield any signal throughout the experiment. Nevertheless, glycerol as an additive supports bradykinin signal onset because mass spectra can be obtained with a hundredfold less analyte concentration compared to the pure water study in a TG (**Figure 4.7**).

Although bradykinin mass spectra can be generated in TG, the intensity was inferior to the bradykinin signal intensity obtained in RG for the same glycerol concentration. The following comparison underlines the RG advantage over TG. The highest analyte intensities in TG were obtained in 5 % glycerol, but those were fourfold less intense than those obtained in RG. The comparison of mass resolution is difficult since the signal intensities for back illumination are several orders of magnitude lower than those generated in front illumination. However, the sensitivity was good and reached  $\approx 10$  fmol per shot for both geometries. For the calculation, a spot diameter of 100  $\mu\text{m}$ , sample thickness of 2.5  $\mu\text{m}$ , and bradykinin concentration of 100  $\mu\text{M}$  were used.

To investigate the impact of a higher glycerol-to-water ratio on the bradykinin signal in TG, an experiment with 20 % glycerol was conducted. The same experiment was performed on the identical sample in RG and is presented and discussed in the previous subsection. **Figure 4.13** shows a series of temperature-dependent mass spectra in 20 % glycerol. The lowest trace (blue) was recorded at an estimated temperature of about  $-140$  °C. The first four traces (blue, orange, green, and red) were recorded before ice sublimation and lacked a bradykinin signal, which is in line with previous data (**Figure 4.12**). A bradykinin signal was observed in the fifth trace (**Figure 4.13**, purple) after ice sublimation. However, a severe broadening has also accompanied the analyte signal, as already seen in RG (**Figure 4.11**). Despite low mass resolution, consequent measurements give a stable bradykinin signal, and successful data collection was possible for several hours after ice sublimation.

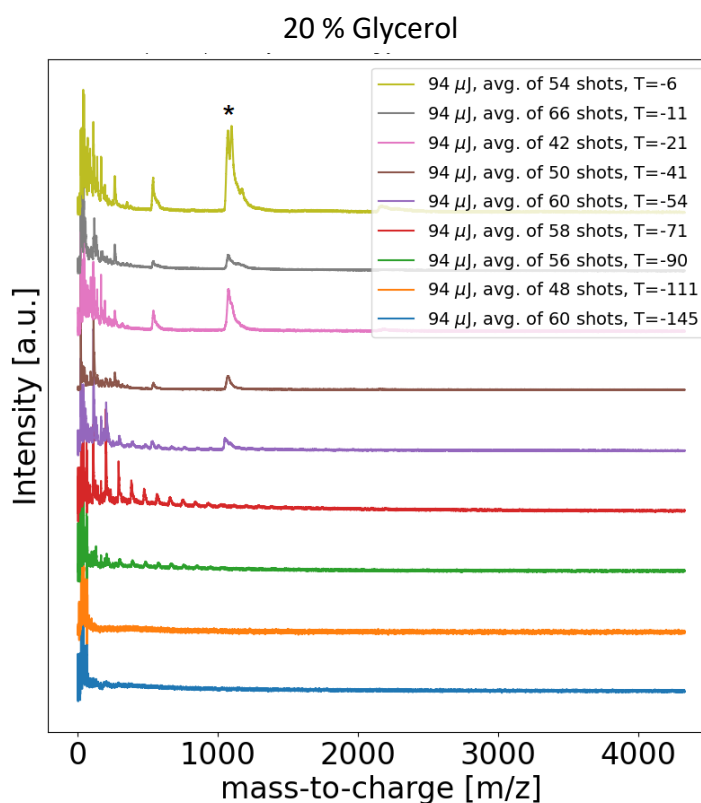


**Figure 4.13** A series of temperature-dependent mass spectra of 100  $\mu\text{M}$  bradykinin in 20 % glycerol. The temperature in the legend is provided in Celsius. After the first measurement, the liquid nitrogen supply was cut, and the temperature gradually increased. More details can be found in subsection 4.2.4. For sample preparation, 200 nl were pipetted, which corresponds to an average thickness of 2  $\mu\text{m}$ . Irradiation was performed in TG, and the pulse energies were held constant at 95  $\mu\text{J}$ . The asterisks indicates the bradykinin signal.

Bradykinin signal intensity obtained in TG can be improved when higher glycerol concentrations are used. However, this improvement bolstered signal broadening and effectively reduced the mass resolution. For instance, mass resolution for the singly charged bradykinin in 5 % glycerol was around  $R = 50$ , consequently twofold higher than in 20 % glycerol.

Finally, the signal from bradykinin in 20 % glycerol in RG and TG showed subtle but distinct differences (**Figure 4.11** and **Figure 4.13**). The first is that, the bradykinin signal in RG was measured shortly before ice sublimation, while the signal onset was only observed afterward in the transmission setup. In general, the shape of the bradykinin signal is different, and the mass resolution in RG and TG is higher for the former. Despite the signal broadening, which decreased analytical performance, the signal intensity for bradykinin in 20 % glycerol in both geometries was good and

consequently higher than in samples with lower glycerol proportion. However, while adding more glycerol only slightly improves the signal intensity in reflection geometry, it dramatically affects the intensity in TG.

## 4.4 Analytical Performance of DIVE Mass Spectrometry

### 4.4.1 Limit of Detection – Water

Semi-thick films with a peptide concentration of around 100  $\mu\text{M}$  can be routinely measured and give rise to a signal-to-noise ratio of 11:1. Consequently, the investigation of a tenfold-diluted specimen was performed. However, the shot-to-shot repeatability was low, along with unsatisfactory signal intensities. The aforementioned measurements were performed under cryogenic conditions, however, neither the increasing sample stage temperature nor higher laser pulse energies could improve the outcome.

Since ultra-thin films required high analyte concentration for signal onset, while semi-thick- and thin-film delivered signal intensities with two and one orders of magnitude less analyte, respectively, we wanted to improve the status quo. Next, a 1 mM bradykinin solution was investigated in the same manner as in subsection 4.2.4. The sample preparation procedure, as well as laser pulse energy, were initially the same. However, a tenfold dilution reduced the signal intensity to such an extent that repeated runs led to high standard deviation, which prevented qualitative and quantitative statements in RG, while the analyte signal in TG was absent (**Figure 4.14**).

Our attention was drawn to the sample preparation protocol to improve the results presented in **Figure 4.14**. Despite the careful handling, we noticed that a signal was not obtainable in the worst-case scenario, and for better cases, thin-films possessed "sweet spots" an area where high-quality signals could be generated, while the rest of the sample remained analyte-free. Lacking a high-resolution camera or microscope, further investigation and make conclusions of the thin film morphology and the impact on the signal onset was not possible. Therefore, different parameters during sample preparation were changed to increase the reproducibility. First, we noted that during sample loading, the contact with the sample and ambient air must be avoided otherwise a condensate was formed on top of the coverslip, and the subsequent analysis usually failed. The sample deposition procedure was conducted 0.5 cm above the liquid nitrogen surface to minimize contact between the sample and ambient air. The benefit of this convergence is the constant evaporation of liquid nitrogen, which displaces ambient air and prevents deposition. An approximation to a liquid nitrogen surface with the sample stage is impractical in the current setup since removing the upper coverslip becomes difficult. However, although the aforementioned measures

increased reproducibility, the overall signal intensity for 10  $\mu\text{M}$  solution was not satisfying.

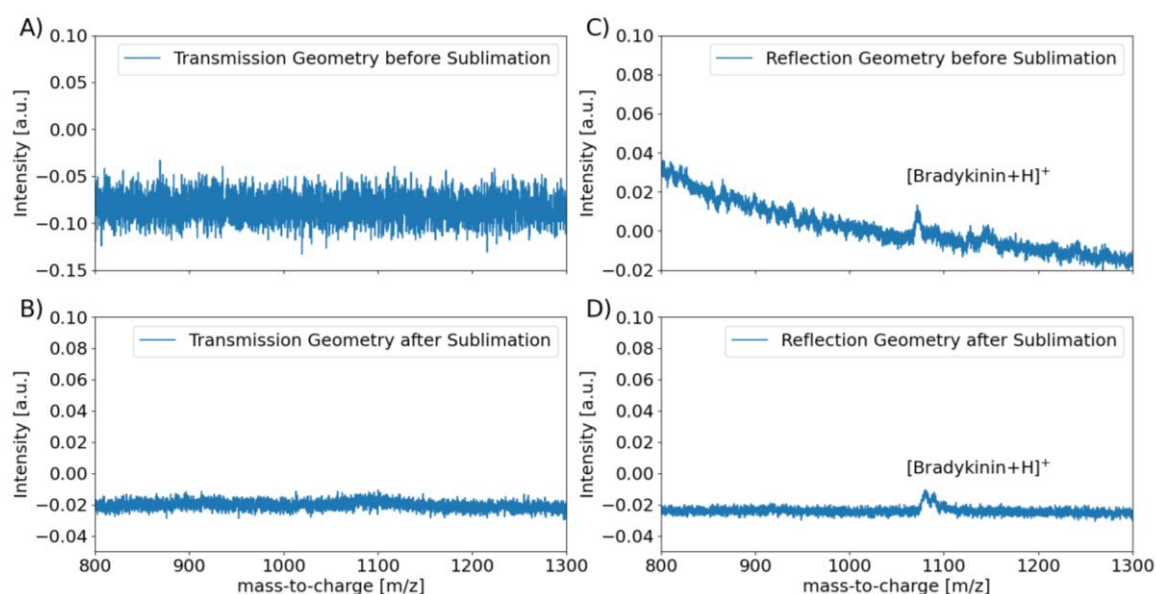


**Figure 4.14** Limit of detection: 1 mM bradykinin mass spectra in TG and RG. The average sample thickness is estimated to be about 2  $\mu\text{m}$ , while pulse energies were between 87 and 92  $\mu\text{J}$ . A) No signal for bradykinin before the ice sublimation in TG. B) Signal is also not visible after the ice sublimation in TG. C) A weak signal for bradykinin in RG before ice sublimation. D) Improved signal after ice sublimation in RG.

#### 4.4.2 Limit of Detection – Glycerol

The limit of detection measurements was performed for ultra-thin films in the same manner as in subsection 4.3.3 but with tenfold less analyte. For comparison reasons, the pulse energies are similar to those used in subsection 4.3.3 and pivoted around 95  $\mu\text{J}$ . However, all glycerol concentrations performed poorly with the 10  $\mu\text{M}$  bradykinin. **Table 4-1** summarizes the results for bradykinin signal onset in different glycerol concentrations.

No signal could be obtained from the specimen in 5 % and 10 % glycerol in TG as well as in RG. A feeble bradykinin signal could be generated from the highest glycerol concentration. Assuming an ablation crater of 100  $\mu\text{m}$  and 150  $\mu\text{m}$  for the back and front illumination, respectively, the sensitivity of IR-(MA)LDI with glycerol is around  $\approx 1$  femtomole. This value is the lowest sensitivity so far achieved in this work for IR-MALDI and only two-fold behind UV-MALDI [175]. However, a study with a 2.94  $\mu\text{m}$  wavelength and 6 ns pulse duration laser source reported similar sensitivity but increased pulse durations [179]. The group worked on a traditional MALDI instrument



and therefore used stainless steel as a substrate in contrast to a silicon converslip used in this work.

**Table 4-1** Summary of the limit of detection experiment. X indicates a failed attempt to produce a signal, while o indicates a successful run. All evaluations were drawn from mass spectra recorded after ice sublimation. The average sample thickness is estimated to be about 2  $\mu\text{m}$ , while pulse energies were between 92-98  $\mu\text{J}$ .

Glycerol-water ratio [%]	Reflection Geometry	Transmission Geometry
	x = no bradykinin signal o = bradykinin signal	x = no bradykinin signal o = bradykinin signal
5	x	x
10	x	x
20	o	o

In an additional experiment to improve the sensitivity, we established a setup that provides two consecutive pulses on the same spot in RG. The idea behind such a setup is that the first incoming pulse would increase the local temperature, and the consecutive laser pulse would drive the ablation and ionization. Depending on which type of lasers are used, such setup has different names in literature, such as post-ionization [185], when UV lasers are involved, or post-desolvation [173] when infrared lasers are implemented for the second pulse. It is suggested that the separation of desorption and ionization process increases the overall ionization probability leading to higher signal intensities [152] and, therefore, better sensitivity. Those methods were only applied in MALDI, and studies for frozen aqueous solutions have not been reported yet.

In our setup, the output laser beam was split with a separator plate and the specimen was irradiated from the back. The pre-heating pulse, as well as the ablation pulse, came from the same laser source. The long path of the second pulse produced delays of 2, 6, and 10 ns (Appendix, **Figure A 2**). The first laser beam contained roughly 25 % energy, while the remaining energy was carried with the second pulse. The energy provided by the first laser beam should ideally cause a phase transition from ice to water, without an ablation onset. This would result in a blue shift of specimen towards higher absorption of the 2.92  $\mu\text{m}$  irradiation. The first beam was attenuated with borosilicate plates, and mass spectra were recorded in-between to assure the previous statement. In addition, the laser power for the first pulse was calibrated by preliminary studies on thin ice film containing bradykinin. The second pulse was delayed by 2, 6, and 10 ns. A translational stage was used for ideal

---

overlapping of the consecutive laser beams, but this was tedious work requiring frequent realignment of the two laser beams and frequent control measures.

Despite careful handling and alignment of the two consecutive pulses, the signal intensity produced by the single laser shot and the double laser shot setup fluctuated to such an extent that the results were inconclusive. Multiple considerations on the experimental process as well as on the theory can be made. A report using picosecond infrared laser under ambient conditions stated that after applying 100 ps pulses, the thermodynamic evolution of water is primarily supercritical water for 2 ns, but during plume expansion, the phase diagram is dominated by liquid/vapour phase [57]. However, this study was done under ambient conditions, which might influence the time-dependent event in one way or another. Also, the report stated that within the exciting volume, a pressure of  $\sim 1$  GPa is build-up. The water's phase diagram shows that the pressure and temperature increase to  $\sim 50$  °C are required to perform the phase transition of ice to liquid water. Whether and how long this liquid state is 'intact' as non-expanding volume is not apparent. The temperature increase in a given local position after laser-matter interaction is certain, but whether the pressure of 1 GPa is reached is not clear. Less pressure would cause direct sublimation, and as a result, the liquid state would be skipped. Such conditions are less beneficial since the interaction between the second pulse, and the liquid phase is highly favorable to increasing signal intensity.

To do a successful double-pulse experiment, first it is essential to understand the lifetime of the liquid phase state, which dictates the arrival time of the second pulse and is therefore crucial.

#### 4.4.3 Mass Limit – Water

According to the literature, IR-(MA)LDI producing masses exceeding 10 kDa has been reported twice [35], [165]. IR-(MA)LDI is capable of producing masses above 150 kDa but only under moderate pressure conditions [102]. However, we wanted to investigate the upper mass limit of the IR-(MA)LDI in RG and TG for DIVE MS. Also, the previously introduced sample preparation techniques are compared (semi-thick, thin-, and ultra-thin films). Initially, the experiments started with 10 mM lysozyme, and the laser pulse energies were between 90 and 100  $\mu$ J.

While the techniques producing thin- and ultra-thin films did not yield a signal for 10 mM solutions, the semi-thick film reveals double and single-charge lysozyme species (**Figure 4.15**, panel B). These charge states are also observed in UV-MALDI [11]. However, this result was only possible in front illumination and the oversampling mode, whereas the back illumination failed to produce any lysozyme signal. As in previous results for bradykinin, the mass spectrum was dominated by

additional masses in the small region (**Figure 4.15**, panel A). The latter saturated the detector to such an extent that the baseline for the lysozyme mass spectrum tilted.

Interestingly, the highest peak is placed around 28 m/z, representing the silicon monomer. Higher pulse energies could not be used since the latter caused severe detector oversaturation and depleted sensitivity. While ion deflection in MALDI is a common technique, high voltage deflection plates in the used mass spectrometer were missing.

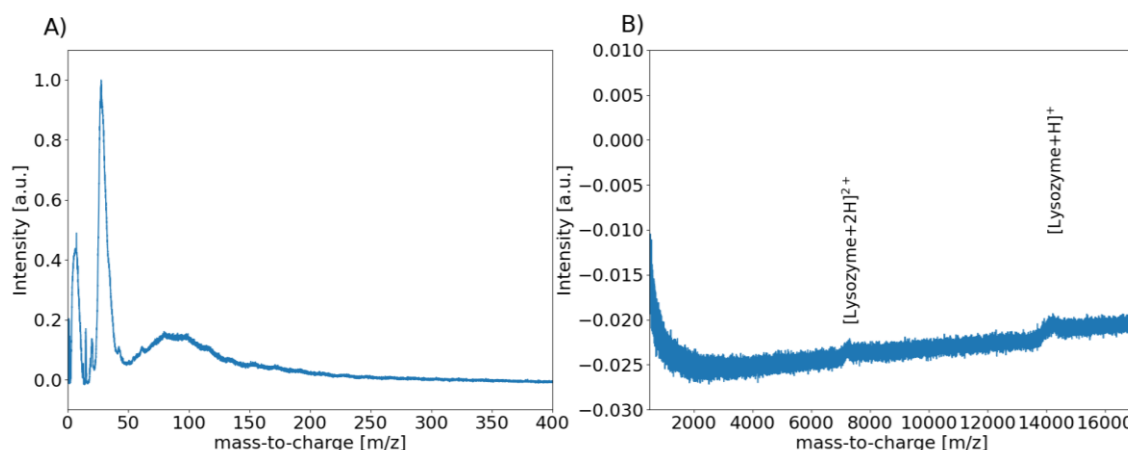


**Figure 4.15** Mass spectrum of lysozyme produced in RG from semi-thick films. Pulse energies were 95  $\mu\text{J}$ , and the oversampling steps were set to 20  $\mu\text{m}/\text{Hz}$ . The analyte concentration was 10 mM, and the mass spectrum was recorded at -140  $^{\circ}\text{C}$ .

Although the signal quality is low, the aforementioned results facilitate the capability to bring high masses in the gas phase by irradiating pure water samples with an infrared laser. In addition, no proton donor agent was used in contrast to other studies [35], [186]. The laser wavelength can be fine-tuned to the OH-stretch in ice to achieve higher desorption and possibly ionization rates. The absorption maximum for ice water is red-shifted and around 3100 nm, while the PIRL output is at 2920 nm. According to a previously published work [99], the absorption coefficient in ice for the latter wavelength is 20 % less.

#### 4.4.4 Mass Limit – Glycerol

In subsection 4.4.3, lysozyme is the highest mass that can be determined (14.3 kDa). Semi-thick films combined with oversampling mode for data collection yielded the best results. However, 10 mM lysozyme concentration also represented the limit of detection. With the addition of glycerol, we wanted to surpass the current limit of detection. However, despite using different glycerol and analyte concentrations as

well as laser energies, analyte signal could only be irregularly obtained from semi-thick films for lysozyme under cryogenic conditions. Unfortunately, temperature-dependent studies were not conducted, which facilitates signal onset in ultra-thin films, as presented in the next paragraph.

Next, we wanted to investigate whether lysozyme signal can be obtained from ultra-thin films. A series of temperature-dependent measurements was administered, but only those mass spectra are shown, which were recorded after ice sublimation, as only then the lysozyme signal appeared. **Figure 4.16** features the lysozyme mass spectra in TG and RG. The y-axis is clipped at 0.2 to stretch the mass spectrometric traces and improve readability. For the generation of this data set, only 1 mM sample solution was used. This value corresponds to the single-shot sensitivity of  $\approx 500$  nanomoles if the ablation crater is 100  $\mu\text{m}$  in diameter and the sample thickness is 2.5  $\mu\text{m}$ .

Remarkably, such high masses are observed in TG for IR-MALDI for the first time. However, while the highest signal intensity for RG is observed for the 10 % glycerol concentration in TG, the most potent signal comes from 20 % glycerol. The same trend was already observed for bradykinin in RG (**Figure 4.11**) and TG (**Figure 4.13**). For higher glycerol concentration, the signal in TG was more intense than in RG. Unfortunately, additional dilution to 100  $\mu\text{M}$  lysozyme did not yield a signal. Nevertheless, we showed that high masses can be extracted in nanomole quantities from frozen specimens with this experiment.

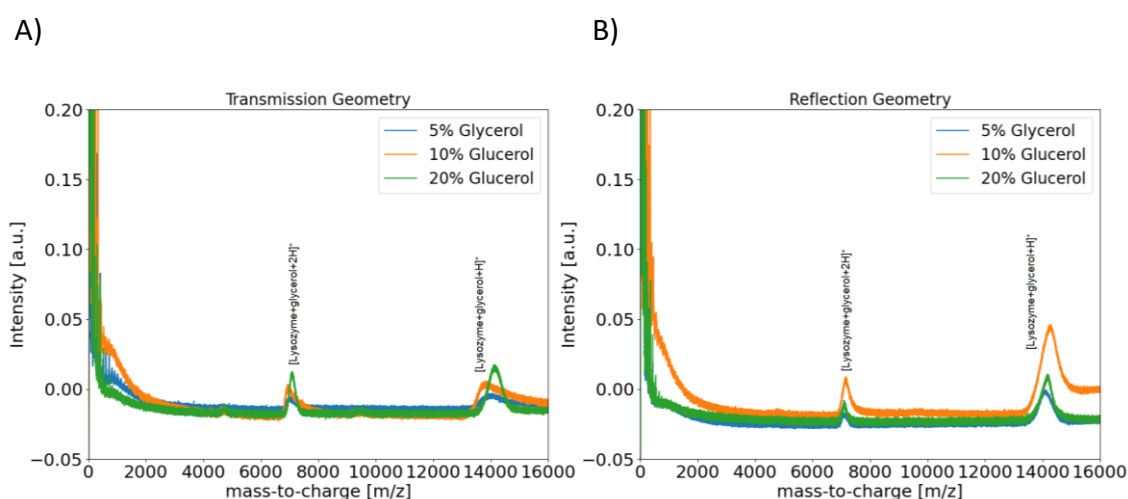


**Figure 4.16** Mass spectra of 1 mM lysozyme embedded in three different glycerol concentrations and recorded in A) TG and B) RG. For the experiments, the protocol for ultra-thin films with 300 nl sample solution was used. The temperature at the sample stage was -90 °C, while the oversampling mode was used for data acquisition in reflection and the SSpS mode for transmission geometry.

#### 4.4.5 Multimer Formation for Mass Calibration

In UV-MALDI, commercially available peptide mix or gold clusters [187] are used to calibrate the mass spectrometer before analysis. In principle, IR-MALDI can use the former mixture, but the chemicals are cost-intensive. Therefore, we wanted to investigate whether a more accessible mass calibrant can be employed in IR-MALDI. An easy and economical way to prepare a mass calibrant is the usage of multiple peptides along with a high glycerol concentration. The result was the formation of dimers and trimers up to 3.5 kDa with well-defined peaks (**Figure 4.17**). In principle, various peptides and proteins can be used to cover different mass ranges.

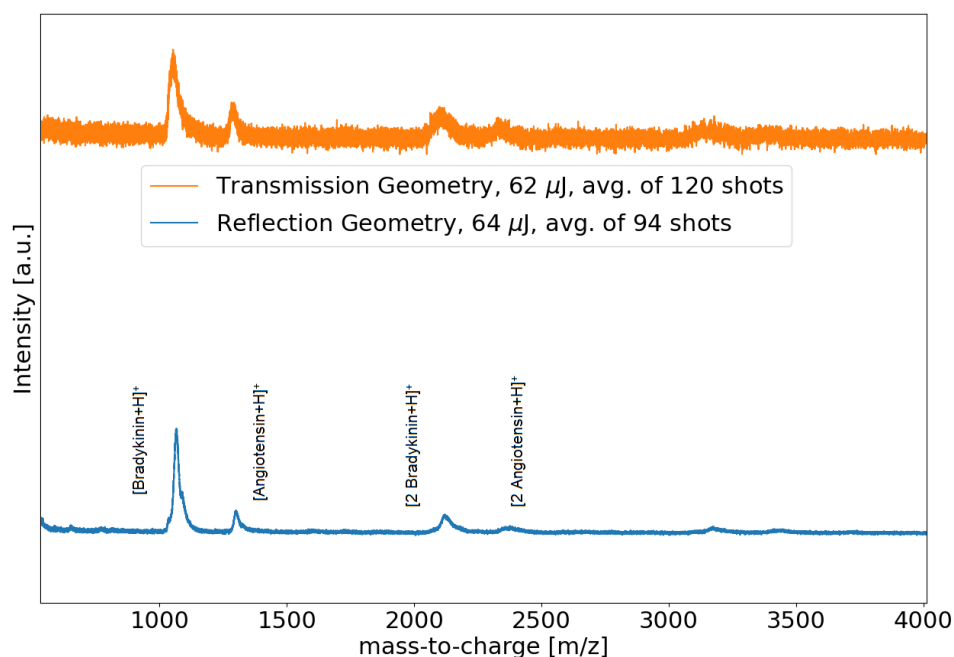


**Figure 4.17** High concentration of bradykinin (20 mM) and angiotensin I (10 mM) in 20 % glycerol generate dimers and trimers, providing an affordable mass calibrant over a wide range for IR-(MA)LDI. A volume of 1  $\mu\text{l}$  was used during sample preparation, which corresponds to a sample thickness of 13  $\mu\text{m}$ . SSps mode was used for data acquisition while pulse energies were between 62 and 64  $\mu\text{J}$ . The small letter t indicates the time interval between the two measurements.

#### 4.5 Ion Collection Yield

The PYTHON script for ion collection yield and the consequent assumptions were introduced and discussed in subsection 3.2.5. We applied the program on a dataset obtained from a sample with a thickness of 2.5  $\mu\text{m}$  and a bradykinin concentration of

---

5 mM to determine the ion collection yield. The specimen was embedded and analyzed in pure water. In addition, the laser diameter was 150  $\mu\text{m}$ , and the data was acquired in SSpS mode. The amount of ejected analyte can be estimated to be around 15 picomoles or  $\approx 10^{12}$  particles with the aforementioned numbers. The number of ions arriving at the detector must be known to calculate the ion collection yield.

**Figure 4.18** shows a scatter plot of different bins, which consist of 8 ns of data points obtained from single-shot mass spectra. We used a linear fit function provided by the PYTHON library `lmfit`. The resulted slope shows how much ions produce a specific voltage. Equipped with this parameter, it is possible to translate the number of ions in each bin. The calculated sum of all bins gives 645 ions. Dividing the latter number by the amount of ejected particles gives an ion collection yield of  $8 \cdot 10^{-11}$ . This number is very low in comparison to the UV-MALDI results, which are around  $10^{-5}$  [76]. Infrared laser desorption is known for low ionization efficacy [152], which is also reflected in the calculation.

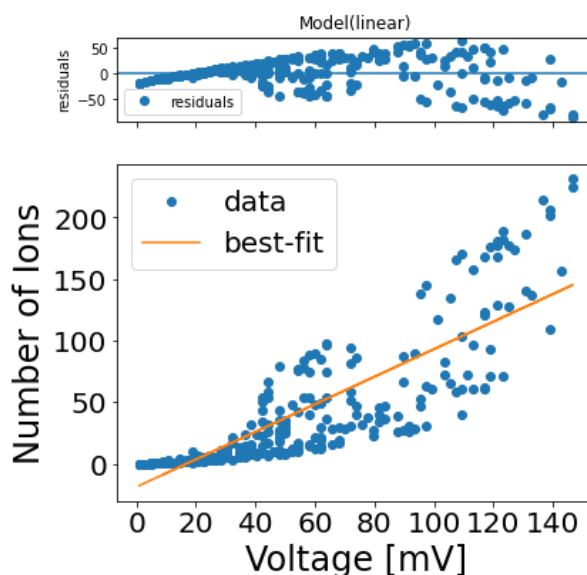


**Figure 4.18** Signal (voltage) intensity depending on the number of ions. A) A graph shows residuals from the linear fit function. B) A scatter plot of bins that were extracted from single-shot mass spectra. According to the linear fit function slope, a single ion produces 1.08 mV. The function parameters are  $y = 1.12 \cdot x - 18.7$ . Overall, 20 single-shot mass spectra were used for the calculation.

## 4.6 Substrate Contribution to Desorption and Ionization

From UV-MALDI experiments, it is known that substrates have a significant impact on desorption and ionization [188]. This study wanted to investigate whether and

---

how much the substrate impacts desorption and ionization. For this purpose, a solvent was used, which dissolves biological molecules, but is not resonantly excited by the PIRL laser system. Therefore a 1 mM bradykinin solution in deuterated water was prepared. The solution was kept for a single day at -4 °C before usage. Hydrogen water has a large absorption coefficient at 2.94  $\mu\text{m}$  caused by the stretching mode of OH. Exchanging the hydrogen atom by heavier deuterium reduces the frequency of the stretching mode as in a harmonic oscillator [189]. Consequently, the absorption coefficient of heavy water is red-shifted, resulting in peak absorption at 4  $\mu\text{m}$ .

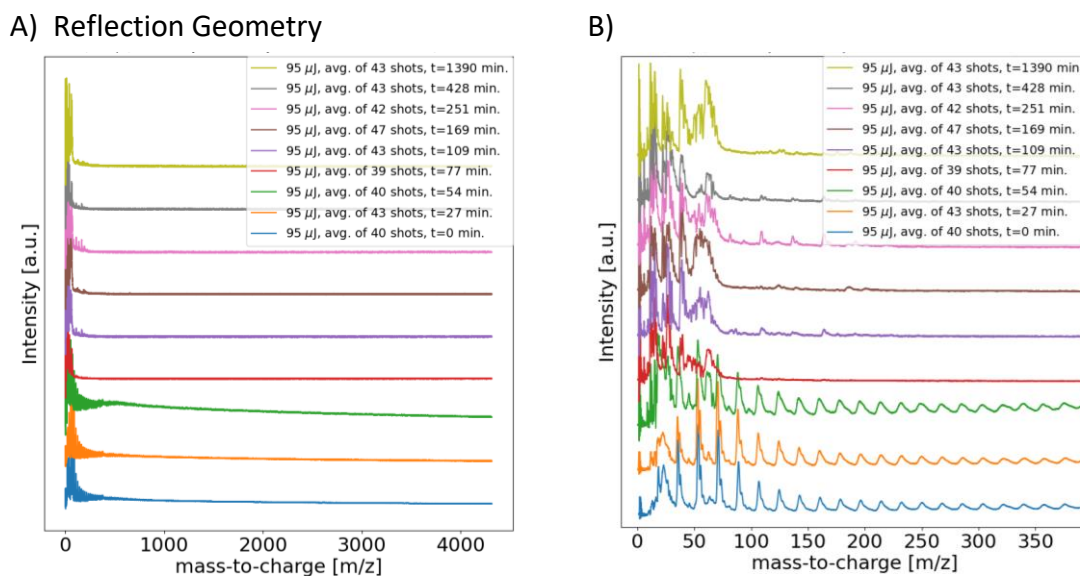


**Figure 4.19** A series of temperature-dependent bradykinin mass spectra in RG. The lowest mass spectrum was recorded at -140 °C. After the first measurement, the liquid nitrogen supply was cut, and the temperature gradually rose. More details can be found in subsection 4.2.4. Bradykinin was prepared in deuterated water resulting in a 1 mM solution. For sample preparation, 200 nl were pipetted, which corresponds to an average thickness of 2  $\mu\text{m}$ . The pulse energies were held constant at 95  $\mu\text{J}$ . A) The whole mass range of bradykinin mass spectra. B) Zoom-in of the bradykinin mass spectra to show the overlapping signal of light and heavy water clusters.

The assumption here is that irradiation with 3  $\mu\text{m}$  would not produce a DIVE-driven ablation hence the bradykinin signal observed with pure hydrogen water should be absent in this experiment. Conversely, a bradykinin signal should be visible if laser-induced substrate heating drives desorption and ionization. However, using a thin film is essential as substrate laser interaction rather impacts the desorption and ionization more when the investigated analyte is spatially close to the substrate.

Next, bradykinin in heavy water was prepared as a thin aqueous film (2  $\mu\text{m}$ ). In **Figure 4.19**, panel A shows that the bradykinin signal in front illumination could not

---

be obtained in RG at different temperatures. Before ice sublimation, the low mass region was accompanied by water clusters. **Figure 4.19** panel B represents water clusters consisting of hydrogen and deuterated water signals, whereas the former has a higher intensity, and the latter appears as the right shoulder of the signal. Although MS is not considered quantitative, the signal for deuterated water should be more intense than the light water as 99.9 % D<sub>2</sub>O was used. However, the reason for this observation remains inconclusive. The bradykinin signal was still absent after the heavy water sublimated. Also, after several hours, DIVE cannot produce a signal from a non-resonant matrix. Another aspect that contrasts with the results in subsection 4.2.4 are that a non-zero baseline in a “belly” shape form is not present here. Instead, the mass spectrum was dominated by distinct water clusters in the low mass region. The results suggest that laser-induced substrate heating plays an inferior role in the DIVE-driven desorption/ablation process in RG.

In TG, as for RG, the bradykinin signal is absent before ice sublimation (**Figure 4.20**). Also, water clusters consisting of hydrogenated and deuterated water molecules are observed in the low mass region. However, after ice sublimation, the bradykinin signal was observed (red trace). While the subsequent measurement (purple trace) lacked a signal, the upcoming mass spectrum showed a bradykinin signal (brown trace). Although mass spectra were recorded in closely neighboured areas, a high shot-to-shot fluctuation could not be avoided. As this phenomenon continued throughout different analytical runs, and several attempts to improve the situation failed, the noisy data was still used for the presentation.

The interpretation of the results presented for RG and TG is not trivial. The total absence of a bradykinin signal for different temperatures in reflection geometry suggests that substrate involvement in the DIVE process is inferior, while a small bradykinin signal in TG indicates a supportive role of the substrate in the desorption and ionization process. Additional experiments in the future using different substrates should elucidate the substrate role in IR-(MA)LDI.



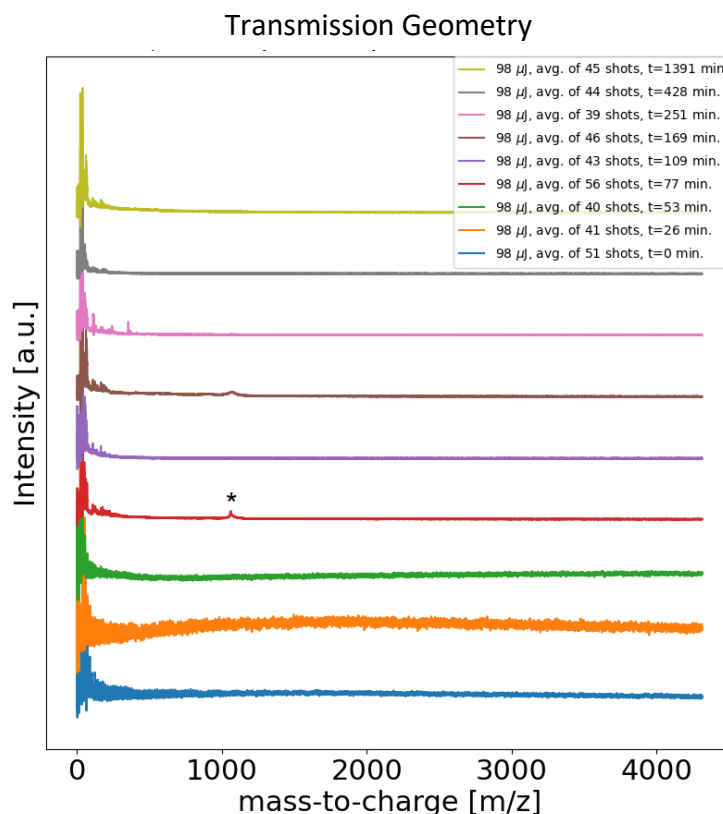


**Figure 4.20** A series of temperature-dependent mass spectra of bradykinin in TG. Bradykinin was prepared in deuterated water. The lowest mass spectrum was recorded at  $-140^{\circ}\text{C}$ . After the first measurement, the liquid nitrogen supply was cut, and the temperature gradually rose. More details can be found in subsection 4.2.4. For sample preparation, 200 nl were pipetted, which corresponds to an average thickness of  $2\ \mu\text{m}$ . The pulse energies were held constant at  $98\ \mu\text{J}$ .

## 4.7 Summary

It was shown that DIVE MS can successfully produce mass spectra of peptides and proteins embedded in frozen aqueous solutions as well as in solutions with glycerol as an additive. In analogy to the conventional MALDI dried droplet protocol, we prepared pure water samples similarly. However, signal generation was only possible from the very rim of the frozen droplet. To overcome this limitation, we developed a novel and fast sample preparation protocol for semi-thick frozen films. An average sample thickness of  $30\ \mu\text{m}$  facilitated to collect data throughout the whole sample area. It was shown that oversampling leads to superior results, and is especially effective when the step size is limited to several micrometers. In the present experiment, this value was between  $10$  and  $20\ \mu\text{m}$ . It is important to mention here

---

that previous reports concerned with IR-(MA)LDI did not use such sampling techniques. Most probably due to hardware limitations. In fact, some reports labeled water as an inadequate matrix for MS purposes, whereas our result shows that sampling is an important parameter in data acquisition, and protein and peptides can be extracted from pure water and without proton donor agents.

Further, 100  $\mu\text{M}$  analyte in pure water was the lowest concentration, which provided a good signal-to-noise ratio (11 : 1). The achieved sensitivity was 200 femtomoles per laser shot, but probably even less since the oversampling technique only consumed a fraction of the total laser focus area. This sensitivity limit is in line with previous reports concerned with IR-(MA)LDI, but this number is at least a hundredfold higher than classical UV-MALDI. In the mass spectrometer, the possibility existed to irradiate the specimen from the back. However, encouraging results for back irradiation in semi-thick samples were only at the rim of the film. Since this area is considered thinner than the center of the film, and the measurements with thinner samples were conducted.

We further explored the signal onset in an aqueous thin film with an average thickness between 2  $\mu\text{m}$  and 12  $\mu\text{m}$ . First, experiments started with the latter thickness. For both irradiation geometries, no signal could be obtained for solutions with 100  $\mu\text{M}$  bradykinin; successful detection was only possible with a concentration equal to or higher than 1 mM. Nevertheless, even with 1 mM analyte concentration, the signal-to-noise ratio was low (5 >), and the sensitivity was 50 picomoles. Overall, ice films with an average thickness of 12  $\mu\text{m}$  performed poorly.

Thin ice film with an average thickness of 2  $\mu\text{m}$  lacked any signal for 1 mM analyte solutions. Another tenfold analyte increase was necessary to generate the bradykinin signal for such thickness. However, the data acquisition was dominated by sweet spots, and only those provided high-quality analyte signals.

Bradykinin signal onset in 2  $\mu\text{m}$  thin film with a concentration of 10 mM was investigated in a series of temperature-dependent measurements. Our results show that temperature increase only indirectly impacted the signal onset. Once the ice sublimation temperature was reached, the signal can be frequently obtained in RG and TG. We hypothesize that hydration shell water is sufficient to cause ablation and desorption of the analyte. This statement is supported by the fact that the analyte signal can still be generated hours after ice sublimation.

Whether substrate effect support desorption and ionization was investigated in the upcoming experiment, here, the temperature-dependent runs with deuterated water were prepared. As deuterated water absorbs at different wavelengths and DIVE conditions are not fulfilled, only laser-induced substrate heating would promote a signal onset. No signal could be obtained under cryogenic conditions for RG as well as TG. In addition, the hydration shell hypothesis can be further solidified, as the bradykinin signal was not present during and shortly after ice sublimation. This

---

observation suggests that specimen-like tissue sections can be investigated in a vacuum containing only a fraction of their original water content. However, a weak bradykinin signal was obtained in TG but not in RG after ice sublimation. Such observation suggests that substrate effects have some impact on signal onset in TG.

In search to improve DIVE sensitivity, additives as a small fraction of the total specimen solution volume was employed. Semi-thick, thin, and ultra-thin water-glycerol films were investigated. Overall, an improvement in analytical performance can be achieved, but this observation was limited after ice sublimation. After ice sublimation, irradiation of ultra-thin films with glycerol and 100  $\mu$ M bradykinin provided a good signal for both geometries. This is a hundredfold sensitivity improvement in contrast to pure water samples containing bradykinin and ultimately leads to a sensitivity of about 1 femtomole per shot. This is a superior sensitivity for IR-MALDI, but still some orders of magnitude lower than values for UV-MALDI.

The highest measurable mass in this paragraph was lysozyme. In pure water, lysozyme could only be detected in RG, and the lowest concentration was 10 mM. Adding glycerol facilitated signal generation in RG and improved the signal-to-noise ratio. However, this observation is limited to the time after ice sublimation. Additionally, lysozyme can also be detected after ice sublimation in TG when mixed with glycerol. Optimal analytical values were achieved using 5 % or 7.5 % glycerol. An increased glycerol content (20 %) led to a lower signal-to-noise ratio and loss of mass resolution. Applying high glycerol and a high analyte concentration has another advantage, and this is the possibility of having a low cost and easily implementable mass calibrant. Two different peptides (bradykinin and angiotensin) were tested, but proteins can also be, in principle, used for the calibration.

Finally, we investigated the collection ion yield for the DIVE MS. The calculated value was  $10^{-11}$ , which is several orders of magnitude lower than the common ionization yields for UV-MALDI, but still in line with known or suggested ionization yield for IR-MALDI.

Fragmentation was not visible throughout all experiments for bradykinin, angiotensin, and lysozyme. This observation aligns with previous reports investigating IR-(MA)LDI under cryogenic conditions. However, previous reports used proton donor agents to promote signal onset. Such additives were unnecessary for the present experiments and, therefore it can be concluded that DIVE MS can extract biological components out of their native environment.



# 5 Non-resonant Femtosecond Pulses for Matrix-free Detection of Peptides and other Organic Molecules

*The scientific supporting unit provided the LabView framework for device communication and conceived the sample loading mechanism. Djordje Gitaric and Josef Gonshior conducted the design and assembly of the time-of-flight mass spectrometer. Frederik Busse wrote MATLAB software for creating two-dimensional images. Glaynel M.L. Alejo wrote the PYTHON script for the shot-to-shot repeatability experiment.*

## ● Preamble

This chapter investigates desorption and ionization under fs irradiation. Fs pulses possess high peak powers, which lead to higher excited states of molecules often accompanied by fragmentation. The theory for different fragmentation pathways is covered in chapter 2. In the beginning, the direct analysis of biological samples from frozen aqueous solutions on various target plates is investigated under cryogenic conditions. In a systematic study, the impact of temperature rise of the sample stage on the bradykinin signal onset under fs irradiation was examined. In addition, two different wavelengths were employed to explore possible changes in fragmentation pattern and signal intensity. The overall analytical performance of fs MS is determined by the limit of detection, mass limit, and shot-to-shot repeatability, which ultimately can be linked to the sample preparation protocol. Finally, the ion collection yield is determined.

---

## 5.1 Introduction

Despite MALDI's popularity, molecular weight compounds below 700 Da are challenging to access because of the matrix interference in the low mass region. As already mentioned in chapter 2, SALDI, as well as DIOS, are two novel techniques allowing to investigate molecules without the need for any organic matrix to catalyze the desorption and ionization process as is the case in MALDI. While most publications dealing with SALDI or DIOS detection implement the use of a nitrogen laser (337 nm) [190], other laser ionization sources are rare [53], [120].

DIOS surfaces are fabricated by galvanostatic etching procedures leading to nanopores on the surface where the analyte accumulates. Creating an uneven substrate surface is essential for a successful experiment, as a flat and smooth surface was reported to be disadvantageous for signal production [114]. However, porous silicon substrates are sensitive to contamination, and the storage time is limited to one year after production [191]. A method development that minimizes the aforementioned bottlenecks is therefore desirable.

Although the desorption and ionization mechanism for SALDI and DIOS is still debated, the biomedical area has already taken advantage of SALDI mass spectrometric imaging. As in MALDI IMS [192], SALDI and DIOS MS imaging used matrix-like elements, including titanium oxide [193] as well as silver nanoparticles [51] and graphene oxide [194]. This contradicts the initial idea of a matrix-free technique, however, multiple lipid species could be obtained from a single measurement which is challenging in MALDI IMS [39]. A true matrix-free approach for SALDI was recently established. Here the specimen was placed on top of a silicon target. In a desiccator, the tissue–substrate interaction was promoted in such a way that after tissue removal, biomolecules were attached at the silicon surface. The subsequent measurement allowed detection and imaging of the residual molecules [51]. The published work show that molecules in close proximity to the target plate can be detected without a matrix. Another study successfully avoided using a matrix by cutting the tissue sections to 3 – 5  $\mu\text{m}$  thick layers. Again successful signal in the SALDI or DIOS technique is achieved when the molecules of interest are in close proximity to the target.

The described reports point towards matrix-free tissue imaging. However, this method would also greatly benefit if substrate modification can be avoided. The desired substrate functionalization can be time-consuming, costly, and often commercially not available [195]. Moreover, finding the optimal modification requires testing for each molecule of interest. Hence, this work introduces a novel technique to desorb and ionize biomolecules without any surface modification or

---

artificial matrix. We also used specimens embedded in water to show the feasibility of the method for interacting with water-rich targets.

## 5.2 Substrate Effect and Signal Onset in Femtosecond Laser Mass Spectrometry

Before the routine use of cryogenic MS-based techniques, a fast and straightforward sample preparation method must be established. Several studies worked under cryogenic conditions, but a protocol for sample preparation was not in scope [53], [102]. In chapter 3 the sampling protocol for thin-film was already introduced and adopted for this experiment. The sample volumes were between 150 to 250 nl, and the spreading area is estimated to be about 0.64 cm<sup>2</sup>. According to the latter numbers, the mean thickness is approximately 2 to 4 μm.

First, the thin film sample protocol was investigated under cryogenic conditions on silicon, chalcogenide glass, and indium tin oxide. In principle, thin-film preparation works with all substrates, but the most reproducible results were achieved with silicon, followed by indium tin oxide and chalcogenide glass. The latter turned out to be fragile and tended quickly to break during sample preparation, while for indium tin oxide, half of the thin film was glued to the upper coverslip resulting in an inhomogeneous thin film layer on the target substrate. However, the molecular ion bradykinin signal was acquired on all substrates (**Figure 5.1**) without any proton donor agents like trifluoroacetic acid, used in the previous report [53]. Different behavior of data acquisition in comparison to hitherto reported results was observed [53]. Obtaining a signal of satisfactory quality under cryogenic conditions was challenging. However, the signal could not be acquired throughout the whole sample, and only some "sweet spots" provided a successful analyte signal. Increasing the pulse energies did not provide a sufficient gain for the analyte signal, and instead, the substrate and small mass molecules oversaturated the detector resulting in an overall reduced analytical performance. As our mass spectrometer was not equipped with deflection plates or gating rods, reducing the intensity of low mass ions was impossible. If a "sweet spot"-position was found, collecting mass spectra with the analyte was performed in SSpS mode. Additional shots on the same spot did not cause any analyte signal, suggesting complete sample desorption after the first shot. A reason for this observation might be due to the very thin nature of the thin film used here. Finally, laser pulse energies used in the present work are fivefold lower than the aforementioned report [53].

Next, the bradykinin signal quality was compared on the three different substrates used. A good signal could be obtained on silicon and indium tin oxide (ITO), while

signals on chalcogenide glass suffer an amplified broadening making neighboring peaks challenging to distinguish. The electrical properties of the substrate might influence the potential field in the extraction region. An additional drawback of chalcogenide glass, which is also shared with silicon, is the mass spectra's elevated noise. Since other experimental parameters were constant, the source is supposable to the substrate, but further investigations were not made. The three substrates also differ in threshold energies for bradykinin's signal onset. Differences in the pulse energy might be connected to sample carrier reflectivity for 1026 nm. The lowest values were measured for ITO (0.06), followed by chalcogenide glass (0.41) and silicon (0.5) (Appendix, **Figure A 3**). The increase in reflectivity might favor ablation conditions hence reducing laser pulse energy.

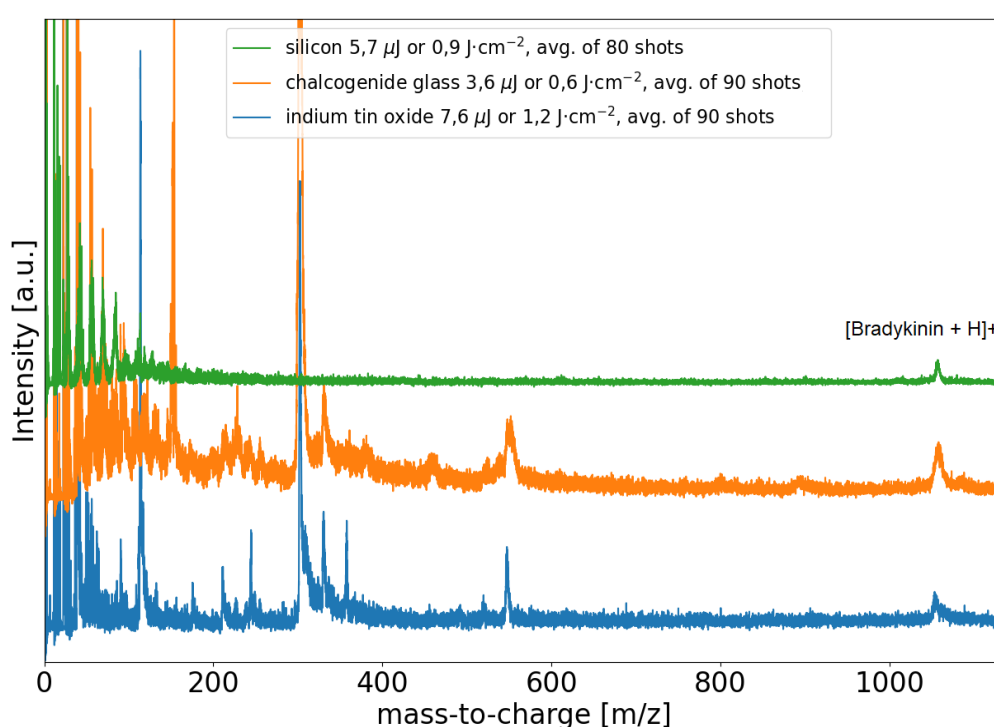


**Figure 5.1** Cryogenic fs mass spectra of 100 μM bradykinin on three substrates. Chalcogenide glass (green), silicon (orange), and indium tin oxide (blue). Between 80 and 90, single-shot spectra were averaged to produce the traces.

Borosilicate as a substrate was also investigated. Unlike the aforementioned substrates, no bradykinin signal could be obtained. High fluences (>6 J·cm<sup>-2</sup>) only generated high intense substrate signals, while fluences around 1 J·cm<sup>-2</sup> generated low-intensity substrate signals (Appendix, **Figure A 3** and **Figure A 4**). The reflectivity for borosilicate was measured for 1026 nm and had a value of 0.06. The latter is comparable with ITO, but on ITO bradykinin signal could be obtained. Besides



unsatisfactory results during mass spectrometric analysis, sample preparation with borosilicate turned out to be the most difficult. Following the protocol for ultra-thin films, the film mostly remained on the upper coverslip. Only sporadically, the thin film stayed on the target plate and could be used for further analysis. However, due to the latter property of the borosilicate, further analysis and investigation were not performed.

### 5.2.1 Ablation Crater Produced with Femtosecond Pulses

The ablation crater produced by fs pulses could not be investigated in the mass spectrometer. The crater sizes were too small to be resolved with the brightfield imaging setup. Instead, a microscope was used to investigate the crater sizes produced with fs pulses *in situ*. **Figure 5.2** shows five pairs of craters produced with different pulse energies between 5 and 25  $\mu\text{J}$ . The pair consists of a crater produced with a single and a double shot on the same spot. For better visibility of the laser impact zone, the image was recorded in a brightfield mode. With increased pulse energy, the crater size gains size for single as well as for double shots on the same spot. However, the size did not increase linearly with the pulse energy.

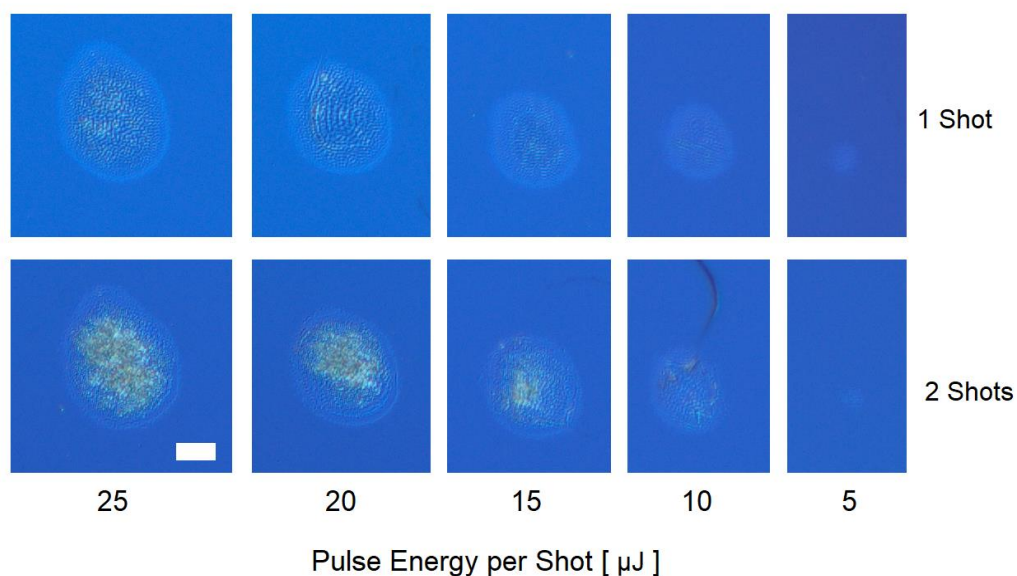


**Figure 5.2** Brightfield images of craters on a silicon wafer produced with fs pulses. The irradiation wavelength was 1026 nm. The crater on the top row of the image were produced by a single shot on the same spot, while in the bottom row the craters were produced by a double shot. The craters were produced when the sample stage was at 0  $^{\circ}\text{C}$ . The white bar indicates 100  $\mu\text{m}$ .

Fs cryogenic MS experiments were frequently conducted with pulse energies between 3 and 8  $\mu\text{J}$ . A single shot with 5  $\mu\text{J}$  is barely visible and produced a crater size about 6.5  $\mu\text{m}$  in diameter. A jump in crater size diameter was achieved with 10  $\mu\text{J}$  resulting in 24  $\mu\text{m}$ . However, laser pulses of about 10  $\mu\text{J}$  were rarely used for data acquisition. The linear trend for the decreased crater diameter with less pulse energy is interrupted once pulse energies from 10  $\mu\text{J}$  to 5  $\mu\text{J}$  are used, which might be explained by the ablation threshold of silicon. As the laser beam profile was Gaussian-shaped, only the beam center deposited enough energy to drive surface changes on silicon [196]. Hence, 20  $\mu\text{m}$  has a more extensive sampling area, effectively changing the laser impact diameter.

Next, we wanted to investigate how the silicon's surface changes towards the impact of the laser beam. **Figure 5.3** shows AFM images of the laser impact zones with laser pulse energies between 10 and 25  $\mu\text{J}$ . The brightfield camera in the AFM did not provide enough contrast to detect the impact zones of the 5  $\mu\text{J}$  single and double shots.

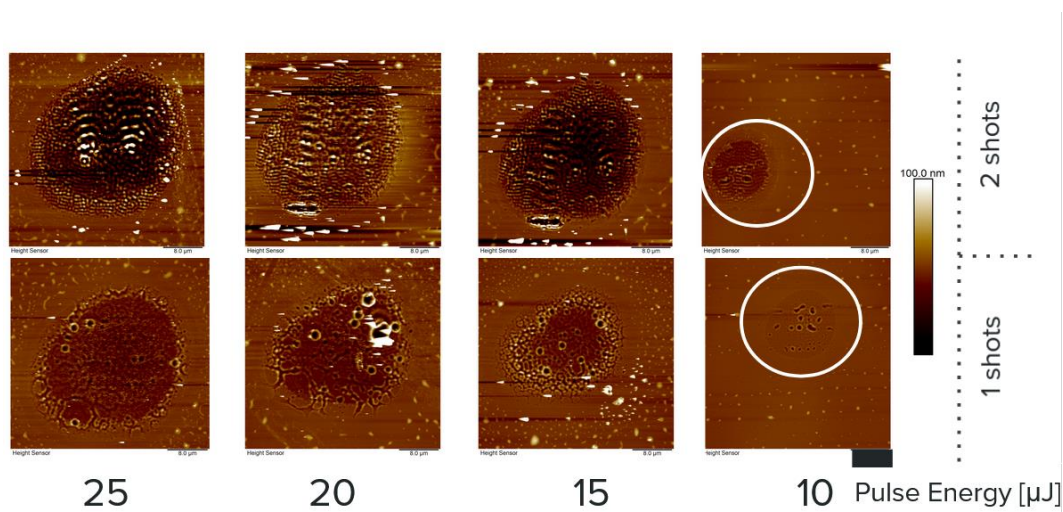


**Figure 5.3** Atomic force microscopy images of craters on silicon wafer produced with fs pulses and an irradiation wavelength of 1026 nm. The gradient bar displays sample heights between 0 and 100 nm. The white stains in the image around the impact zone are artifacts, most probably residual bradykinin salt. The black bar indicates 8  $\mu\text{m}$  distance.

AFM confirms that with increased laser pulse energies, the crater diameter also surges. The lowest pulse energy and single shot on the silicon reveal some dark spots in the crater's center. Those spots are the darkest hence the deepest areal in the image compared to the average height of the silicon surface, which is around 50 nm. Besides the dark spots, the circular impact zone shows little change in morphology. Around a clearly visible impact zone, a corona is formed. Here bright dots are missing. The

assumption was made that the white dots were the dried bradykinin salt, as the wafers were not washed or cleaned after the experiment and directly investigated with the AFM. A study investigating single fs pulses on a silicon wafer under ambient conditions but with a similar wavelength presents slightly different results. The authors did not observe any dark spots within the center of the ablation crater [197]. However, the impact zone's central region is considered the melt region, and the corona is the re-solidification zone [198], [199].

Two consecutive shots on the same spot with the 10  $\mu$ J pulses produce dark spots in the center and melting of the silicon—the melting structure is built of multiple streaks. The corona structure is more defined in this image, and the white dots representing bradykinin salt are also missing. Overall the ablation depth after two consecutive laser pulses is some tens of nanometers, and the peaks of some streaks were elevated to a height close to 80 nm. The morphology changes were more severe with higher pulse energies, but the trend continues in the same manner. Nevertheless, 10  $\mu$ J and higher pulse energies were not applied in the mass spectrometric analysis.

Finally, the AFM images show that fs pulses under experimental conditions (10  $\mu$ J pulse energy or less) change the silicon surface. Whether this change is beneficial or not is not fully cleared in the study. Further experiments have to be done to fully understand the structural changes and their impact on bradykinin signal onset.

### 5.2.2 Femtosecond Pulse Interaction with Substrates at Different Temperature and the Impact on Film Thickness

Data obtained femtosecond laser MS on pure silicon under cryogenic and non-cryogenic conditions produces high-intensity signals in the region between 0 - 120 m/z accompanied by lower intensity signals in the area 100 - 1000 m/z. Since fs pulses are known for high peak powers resulting in photodissociation and fragmentation of biological components, it was interesting whether those signals can be associated with bradykinin as a source. For simplicity, further experiments were conducted with silicon as a substrate only, and the mass range between 0 - 120 m/z was investigated. In addition, measurements with the substrate were run under cryogenic, non-cryogenic, and under the normal condition where bradykinin thin film is applied on the silicon coverslip (**Figure 5.4**).

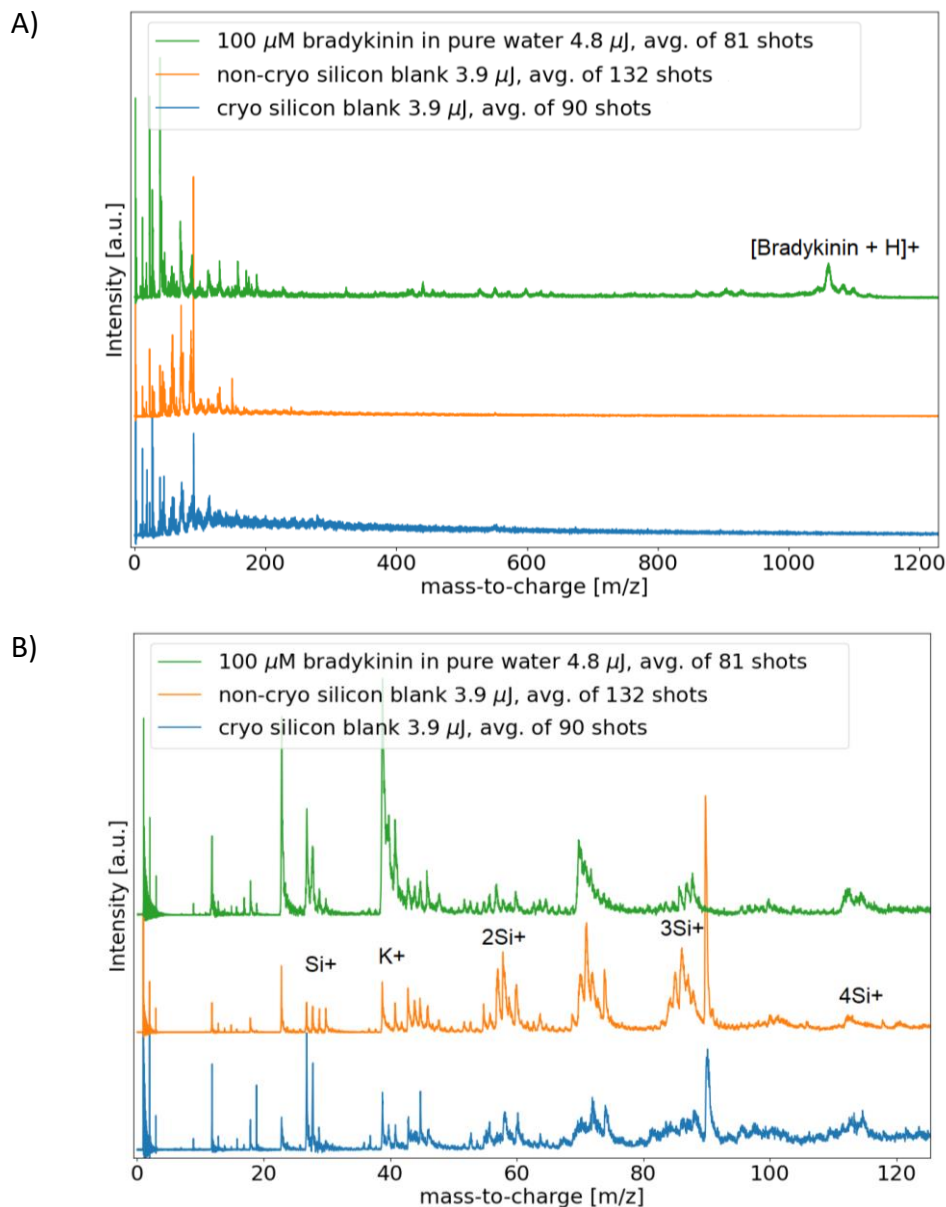


**Figure 5.4** Substrate signal under different conditions produced by fs pulses. A) Mass Spectra of cryogenic (blue) and non-cryogenic (green) silicon substrate and, for comparison, a mass spectrum of 100  $\mu$ M bradykinin on silicon (orange). Cryogenic conditions were established as follows: First, the sample carrier inside the mass spectrometer was cooled for 30 minutes, and after the sample stage with the silicon substrate was mounted. B) A zoom-in into the small mass region to provide a better overview. Clusters at similar positions are dominating the mass window for all conditions.

All three traces show prominent peaks between 0 and 100 m/z, supporting the likelihood of substrate as an ion source for masses in a low mass window. **Table S1** in the appendix annotating the signals. First, silicon under cryogenic and non-cryogenic conditions reveals two cluster groups (**Figure 5.4**, panel A, blue and orange

trace). The first starts with 28 m/z, produced by a silicon atom, and continues with multimer formation with masses up to 160 m/z. The second group starts at 40 m/z, which should be produced by potassium. From this signal, a multimer formation separated by the mass of 28 m/z continues up to 180 m/z. However, the mass spectrum generated under non-cryogenic conditions possesses the highest mass resolution (**Figure 5.4**, panel B, orange trace). Peak cluster position at the aforementioned masses for the bradykinin mass spectrum were discernable but less pronounced (**Figure 5.4**, panel B, green trace). This observation further solidifies that fs pulses do not solely interact with the analyte's solution, even when the ice-thin film is present. Also, the fact that silicon clusters are ejected into the mass spectrometer suggests that at least the upmost layer is removed upon laser irradiation. *Ex situ* measurements reveal that a crater is not formed under experimental conditions but surface melting characterized by forming circular nanometer-sized cavities with a depth of less than 10 nm. Fluences above 1 J·cm<sup>-2</sup> are known to change solid surfaces through plasma formation and multiphoton ionization [200], [201], and in the present experiment applied fluences were at the edge of the threshold value. The analyte signal onset threshold was determined to be 3.2 μJ or 0.9 J·cm<sup>-2</sup> on silicon (see discussion), suggesting the significant contributor for sample removal is rapid heating followed by bubble nucleation. Only at higher fluences, where the solid surface changes into a gaseous plasma via multiphoton ionization, the silicon unveils crater formation consists of a melted core with visible ripples [202] surrounded by a modification zone caused by oxidation/amorphization [197].

The aforementioned observation suggests that ablation or desorption of the analyte is caused by laser-induced heat and following melting rather than substrate-supported spallation. This heat is sufficient to desorb the analyte, but only when the water layer is sufficiently thin. For ice layers between several hundred nanometers up to a micrometer, thermal processes induced by irradiation are not promoting desorption. However, since substrate ions are visible in the mass spectrum, desorption or ablation is still taking place, and it is possibly supporting desorption to a certain degree.

### 5.3 Femtosecond Laser Mass Spectrometry at Different Temperatures

Next, the impact of temperature on the mass spectral quality was investigated. The liquid nitrogen supply was cut, and the temperature started to rise (chapter 3). For all measurements, laser pulse energy and mass spectrometer voltages were constant. Due to high intensity substrate peaks, working at lower laser fluence range was required. Attempts to reduce the low mass signal intensities with less laser pulse

---

---

energy failed because the analyte signal intensity was also diminished. Finally, each mass spectrum was recorded in a single shot per spot mode in a 21 x 21 array, resulting in overall 441 shots being averaged for the final mass spectrum.

**Figure 5.5** documents the impact of temperature on the bradykinin signal over time. We decided to scan over the same area for all the traces for a better comparison and exclude sample-related biases. The pattern for this is illustrated in **Figure A 6** (Appendix). The blue trace (**Figure 5.5A**, panel 1,  $t = 0$  min.) lacked a bradykinin signal. This is because no attempt was made to find a “sweet spot” to obtain a signal at the beginning of the measurement. Different runs showed similar results for the analyte signal conducted between  $-140$  °C and  $-100$  °C or up to 50 minutes after liquid nitrogen supply was interrupted. The corresponding 2D image is in **Figure 5.5B** panel 1. The second recording ( $t = 56$  min.) already presented the desired analyte signal, and **Figure 5.5B** panel 2 provides the corresponding 2D image. Similar results can be achieved in repeated runs in a temperature window between  $-100$  °C and  $-70$  °C or between 50 and 80 minutes. **Figure 5.5A** panel 2 ( $t = 56$  min.) revealed an intense signal locality at the right edge of the image, while the former lacked a signal throughout the scanned area. The accumulation of signal in the right edge of the image was expected since the frame was chosen to be one part on a silicon substrate without a sample, while the other part of the frame was on the thin film. A closer look at the area with the analyte signal offered higher and lower intensity areas. This image accurately represents the phenomenon observed during sample irradiation, where “sweet spots” were the primary source for data acquisition and significantly impacted spectral quality. One reason for such behavior can be related to sample thickness. For instance, darker regions produce a more pronounced signal (Appendix, **Figure A 7**) and are considered thinner than bright regions. The third trace or image (**Figure 5.5A** and **5B**, panel 3) was recorded when the pressure peaked, indicating ice sublimation was almost completed. The mass spectrum was similar during the second and third run, although signal intensity for bradykinin decreased for the latter.

After sublimation, the signal intensity is moderately higher, and the bradykinin signal is only appearing on the right edge of the image. The mass spectra of **Figure 5.5B**, panel 3, 4, and 5 were recorded in a temperature window between  $-70$  °C and  $10$  °C or between 80 and 340 minutes after liquid nitrogen supply was interrupted. Within this temperature window, no significant changes in mass spectral quality were observed. When the signal ultimately faded was not investigated, but the measurement a day later resulted in a lack of signal. However, if the same experiment was repeated with tenfold or hundredfold higher bradykinin concentrations, a signal could be obtained a day after

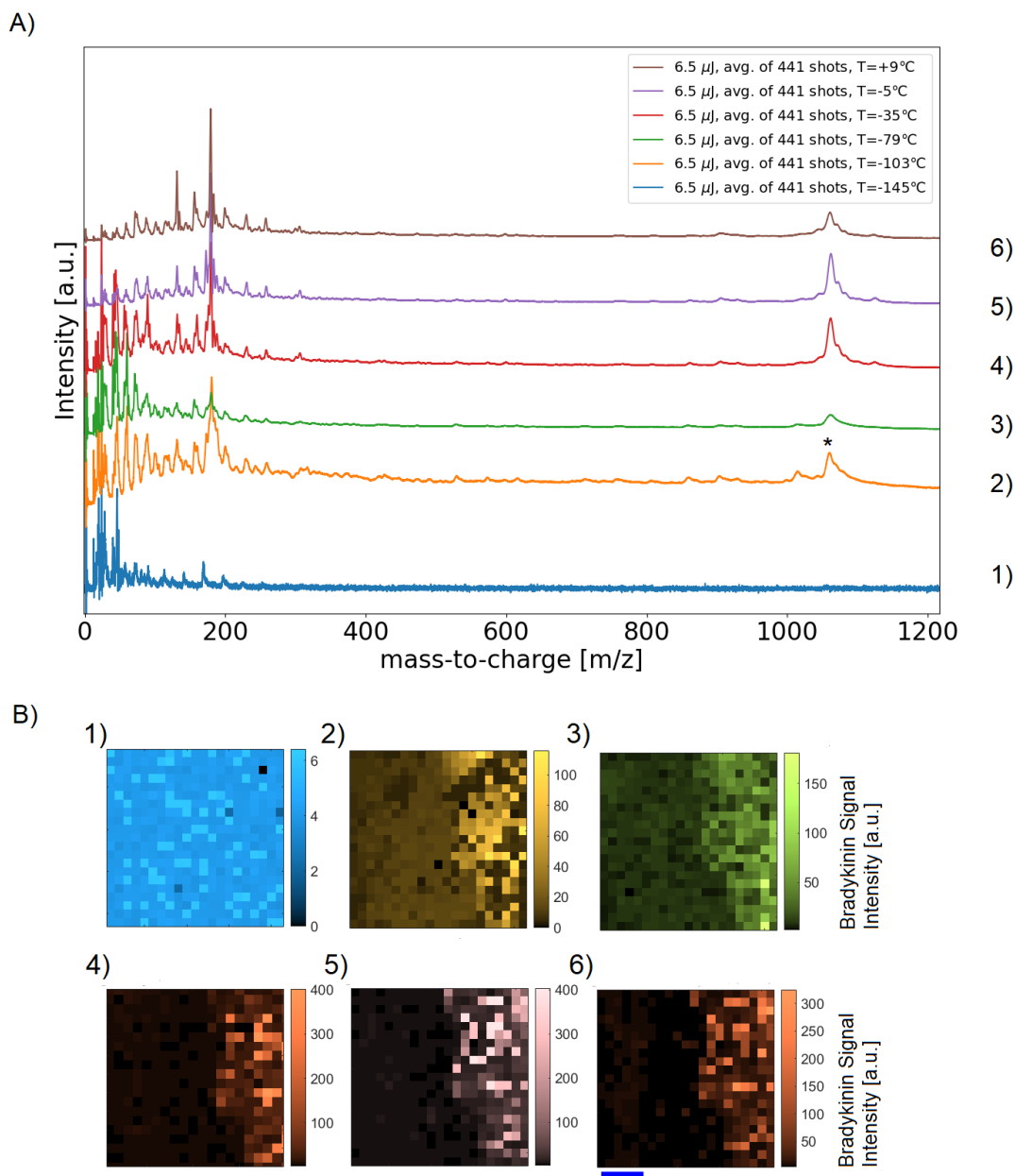


**Figure 5.5** Mass spectra of bradykinin under cryogenic conditions at different temperatures. Overall, 175 nl of a 100  $\mu$ M analyte solution were pipetted. A) Mass spectra produced by 1026 nm irradiation with an average pulse energy of 6.5  $\mu$ J. In total, 441 shots were averaged for a single mass spectrum. The asterisk in the figure marks the bradykinin position for all traces. B) Corresponding 2D images of bradykinin signal created on an area of 5 x 3 mm (x and y). The color intensity of each pixel correlates with bradykinin signal intensity, which is described by the color bar to the right of an image. The blue box indicates 1mm.

According to the presented data, three main measurement windows can be distinguished. The criteria for the differentiation were the signal-to-noise ratio of the

---

bradykinin signal. In contrast to the hitherto report [53] mass spectra were challenging to obtain directly from ice under cryogenic conditions.

The discrepancy of the observation might be due to the difference in laser pulse energies and sample thickness. The possibility of obtaining a bradykinin signal directly from ice cannot be excluded if laser pulse energies could be increased sufficiently, but the current setup in the mass spectrometer prevented such a regime.

However, when the temperature rose, mass spectra were sporadically generated from various spots on the ice film. The significant impact on signal intensity was the sublimation of the ice. High-quality spectra can be recorded several hours after ice sublimation, but a measurement a day later failed to produce any signal. The explanation for the latter observation is the lack of a hydration shell, which should cover the peptide for some hours in a vacuum. Therefore, a signal was visible shortly after ice sublimation, but it faded the longer the specimen was in a vacuum. A hypothesis was made that the solvation shell must play an essential role in signal generation and water or ice is not crucial in generating a solid signal with fs pulses.

The presented outcome was surprising, but before making any conclusions about the reasons for signal onset, the measurement above with a different wavelength was repeated. The second harmonic of the laser system irradiated the specimen while keeping all other parameters constant. As already used for recording the mass spectra with the fundamental, a 21 x 21 array served here to acquire the data set, but for the second harmonic, the array was moved 40  $\mu\text{m}$  in the x-direction. Such adjustment minimized biases induced by sample inhomogeneity. Since parallel measurements of the two wavelengths were not feasible, each data set was recorded with several minutes delay.

A similar mass spectral quality was achieved with the fundamental and the second harmonic of the laser when the laser pulse energy was twice as high for the latter (**Figure 5.6**). The reason for the pulse energy difference was presumably the focused area. This discrepancy was introduced through the optical elements in the mass spectrum used for both rays. The same behavior for signal detection (before and after ice sublimation) was observed for the second harmonic as for the fundamental. Lower bradykinin concentration did not give rise to a signal when the specimen was kept in a vacuum overnight. Only after the increase of the analyte concentration up to 10 mM could a signal be observed.



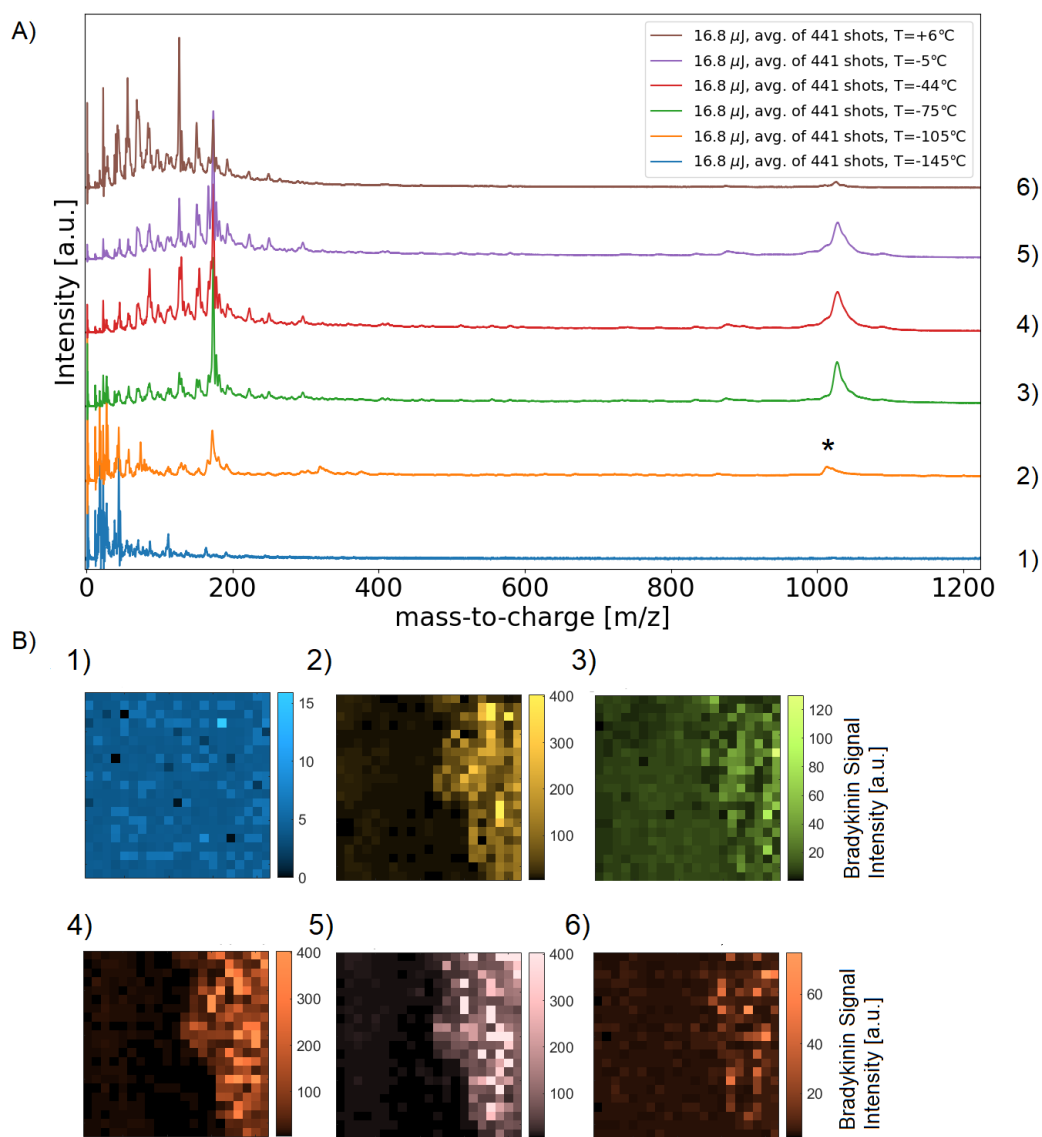


**Figure 5.6** Mass spectra of bradykinin under cryogenic conditions at different temperatures. Overall, 175 nl of a 100  $\mu\text{M}$  analyte solution were pipetted. A) Mass spectra produced by 513 nm irradiation with an average pulse energy of 16.8  $\mu\text{J}$ . In total, 441 shots were averaged to a single mass spectrum. The asterisk in the figure marks the bradykinin position for all traces. B) Corresponding 2D images of bradykinin signal created on an area of 5 x 3 mm (x and y). The color intensity of each pixel correlates with bradykinin signal intensity, which is described by the color bar to the right of an image. The blue box indicates 1 mm.

Interestingly, mass spectral quality does not change with different photon energies as long as photon densities are the same. Due to lack of mass resolution, further

---

conclusions cannot be made whether a radical cation species or a quasi-molecular bradykinin ion arrive at the detector or even both. A radical species would suggest that laser – analyte interaction is the dominant mechanism for analyte ionization and follows the ladder climbing or switching ionization pathway [125]. Plasma formation and multiphoton ionization are common sources for such pathways and can produce excited state species that tend to fragment. These observations will be discussed later.

However, a protonated molecular ion would suggest that upon ionization of the analyte, the prime interaction with the laser light is the (hydration shell) water before a proton is dissociated and passed to the analyte. The hypothesis of a protonated analyte is supported by the fact that the bradykinin species also arrived at the detector with sodium attachment. The latter is indicated by the right shoulder of the signal with a delta mass of 23 m/z. The source for alkali cations is most likely bradykinin, which was not purified before experiments.

Another possibility to ionize the analyte is plasma creation on the surface of the target. Surface melting has been suggested as a potential pathway for ionization of analyte molecules in SALDI's environment [39], [203]. For this, laser-substrate interaction was investigated by looking at the low range of the mass spectrum of the pure substrate under cryogenic conditions and room temperature as well as when silicon is covered with a micrometer thin ice film containing bradykinin.

## 5.4 Fragmentation

High laser peak intensities eventually lead to plasma formation known to produce fragmentation patterns in biological specimens [133]. Recent studies employ fs pulses as an activation method which is called infrared multiphoton dissociation (IRMPD), to elucidate the sequence of unknown peptides and proteins [204], [205], [206], [207]. Detection of a molecular ion and the associated fragments from a "neutral" specimen has not been reported yet. Fragment ions identification was accomplished by comparison of theoretical and measured mass. Masses difference less than 2 Da were considered as a match. Besides substrate signals, 30 (on silicon) and 26 (on indium tin oxide) structurally significant ions were identified as originating from the protonated molecular ion. Only 7 ions produced on chalcogenide glass could be annotated as fragments of bradykinin. Two factors may lead to that lower number. First, a severe signal broadening leads to the overlapping of neighboring peaks. Second, mass spectra produced on chalcogenide glass tend to generate higher substrate noise which, might cover low-intensity fragmentation ions. The detailed list of all fragmentation ions can be found in **Table S2** (Appendix), while **Figure 5.7**, panel A shows a mass spectrum with annotated peaks.

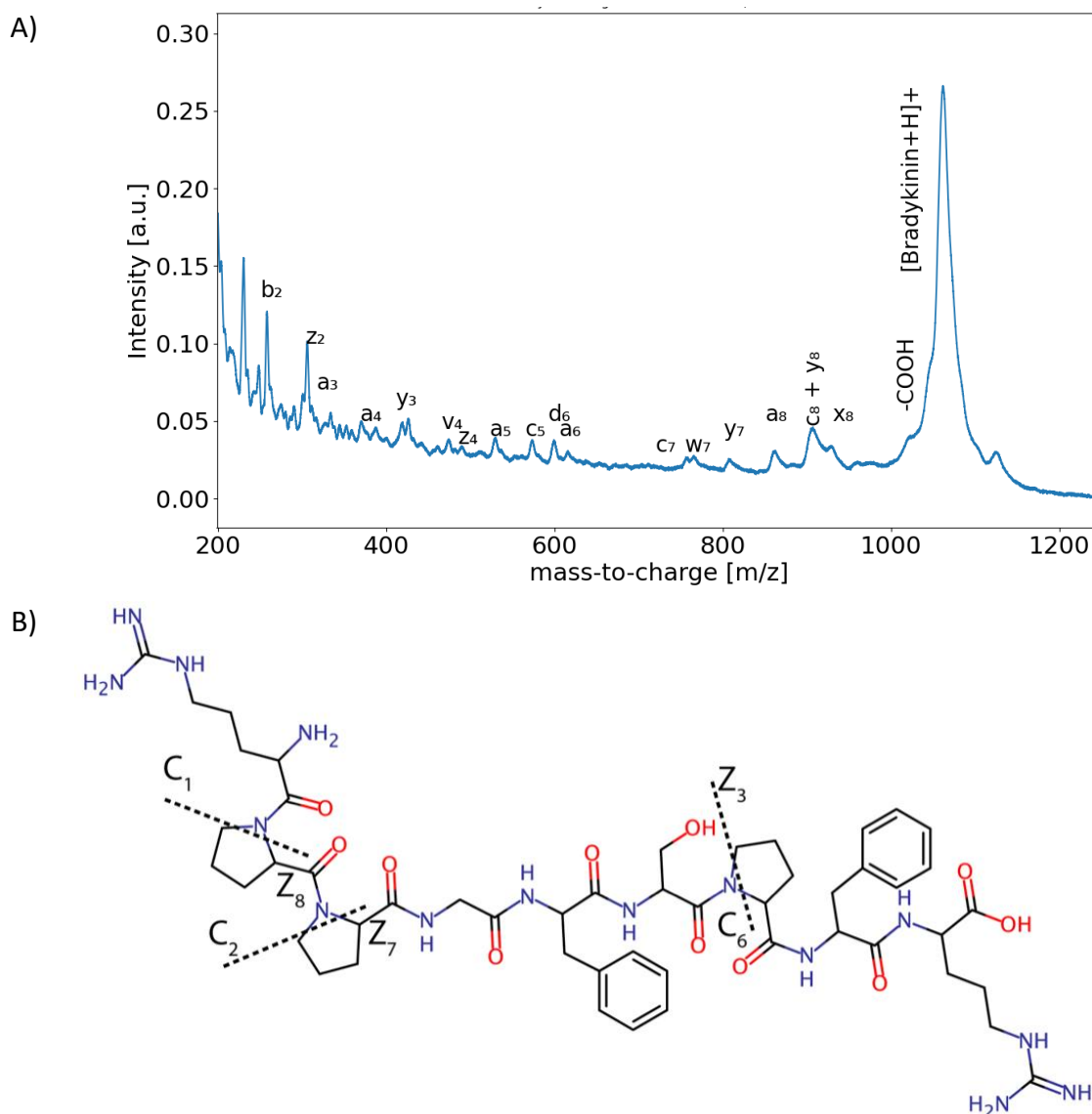


**Figure 5.7** Fs MS produced a vibrant pattern of bradykinin fragment. A) Mass spectrum of 100  $\mu$ M bradykinin on silicon. B) Dotted lines indicate Proline cleavage for the creation of  $c_n$  and  $z_n$  ions.

Overall, we observed a vibrant fragmentation pattern throughout the main chain where C- and N-terminal ions are equally distributed. In addition, our data suggest that cleavage of the existing side-chain groups occurred [133], [208]. An interesting observation was made with the amino acid Proline. The position in bradykinin is the second, third, and seventh place. Fragment ions of the series  $c_n$  and  $z_n$  were missing at these positions. Since these fragments evolve through the cleavage between secondary nitrogen and *alpha*-carbon, the amino acid's structure must be considered (**Figure 5.7**, panel B). Proline possesses a five-member ring, which is included in the peptide backbone. The absence of fragment peaks suggests the unlikelihood of the

---

double-cleavage event. For the same reasoning,  $z_3$ ,  $z_7$ , and  $z_8$  C-terminal fragments were not detected.

In addition to single cleavage fragmentation, the data shows satellite ions [209], [210]. The experiment produced the following ions  $v_2$ ,  $w_3$ ,  $d_6$ , and  $w_7$ . These fragments result from a peptide backbone cleavage followed by the loss of the lateral side chain. Those fragments were usually observed in high-energy (10 keV) collision-induced dissociation (CID) spectra [209]. For our data, 1 - 2 eV/photon energies were sufficient to deliver a similar picture.

## 5.5 Analytical Performance of Femtosecond Laser Mass Spectrometry

### 5.5.1 Shot-to-shot Repeatability

To make a statement about the repeatability [142] of the method introduced in this study, 51 datasets on different substrates and days were collected and analyzed. Each dataset contains between 200 and 400 single-shot spectra acquired at a sample stage between -95 °C and -70°C. A successful mass spectrum was considered when the bradykinin signal had a signal-to-noise ratio above 3 : 1. First, shot-to-shot repeatability was calculated by taking the number of spectra with bradykinin signal and divided by the total number of shots used in the same dataset. Next, these results were summarized in a histogram (**Figure 5.8**).

The distribution of datasets with various shot-to-shot repeatabilities is skewed to the left. Half of the data is between 70 and 90 % shot-to-shot repeatabilities, with a median of 70 %. Notably, silicon has the highest shot-to-shot repeatability, while ITO and chalcogenide glass experience a broader distribution of shot-to-shot repeatabilities. Mass spectra generated on the silicon coverslip showed the best shot-to-shot repeatability during femtosecond IR-LDI.

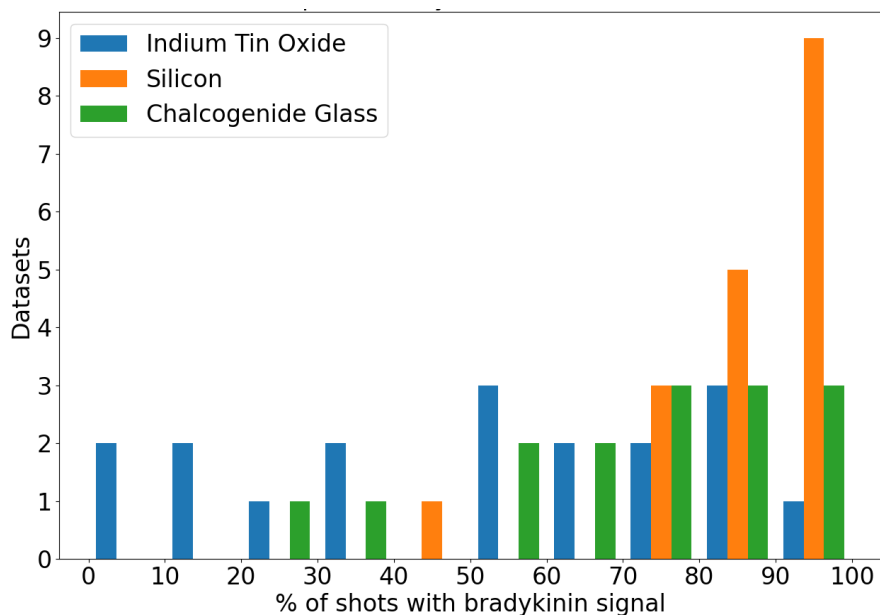


**Figure 5.8** A histogram of shot-to-shot repeatabilities for bradykinin signal on three substrates. 51 datasets were acquired by irradiating a 100  $\mu\text{M}$  bradykinin thin film with 1026 nm femtosecond laser pulses. For each dataset, shot-to-shot repeatability was calculated and plotted into the histogram. These colors represent the following substrates: Silicon (orange), ITO (blue), and chalcogenide glass (green).

### 5.5.2 Limit of Detection

A dilution series with 100  $\mu\text{M}$ , 10  $\mu\text{M}$ , and 1  $\mu\text{M}$  bradykinin solutions was performed. For sample concentration below 10  $\mu\text{M}$ , peptide signal was obtained with a signal-to-noise ratio of 20 : 1, but the lowest concentration provided unsatisfactory results. Assuming a concentration of 10  $\mu\text{M}$  and an ablation crater diameter of 20  $\mu\text{m}$  the total amount for signal generation adds up to a sensitivity of 25 attomoles. However, MALDI imaging using a SpSS mode reports a sensitivity of about 500 attomoles [175]. Higher sensitivity in MSI is usually achieved when tailored sample pretreatment removes salt and other components [15]. In contrast to MALDI imaging, in a typical UV-MALDI experiment, peptides are usually detected several magnitudes lower, and the signal is visible for 25 pM solution [211].

### 5.5.3 Mass Limit

Previous studies reported the mass limit for DIOS application to be around 3 kDa [212] and for cryogenic femtosecond laser MS up to 6 kDa [53]. We investigated the mass limit at different temperatures and two different wavelengths. All experiments

---

were initially performed on silicon as a target plate. Bradykinin with the mass 1061 Da and Angiotensin I (1291 Da) can be routinely detected with the femtosecond laser's second harmonic and fundamental. The next investigated mass was endothelin I (2492 Da). The latter showed similar detection behavior as presented in subsection 5.3. Briefly, while the signal can only be obtained under cryogenic conditions once "sweet spots" are found at elevated temperatures, the signal is more pronounced. After ice sublimation the signal can be detected throughout the thin film area with a high shot-to-shot repeatability. However, signal-to-noise ratio for endothelin I was not satisfying in comparison to bradykinin or angiotensin I. One reason might be the lower ionization efficacy of the endothelin I compared to bradykinin or angiotensin I. To figure this out a set of comparable mass molecules should be investigated. A second reason is the possible mass resolution loss towards higher masses. Both reasons were not in the scope of this study and were not further investigated.

The endothelin I signal onset was investigated on different target plates. Indium tin oxide, as well as chalcogenide glass, gave rise to a small endothelin I signal. Also, here, we show that successful detection of biomolecules with femtosecond pulses is not limited to silicon and can imply another sample carrier.

Finally, whether endothelin I was still detectable when additional analyte like bradykinin was mixed into the same solution was investigated in the upcoming experiment. **Figure 5.9** shows the mass spectra with bradykinin plus endothelin I obtained with 513 nm and 1026 nm irradiation. The spectra are similar, and for both wavelengths, the endothelin signal is visible. This experiment shows the possible mass range that can be obtained with fs pulses and that different species can be desorbed and ionized simultaneously.

Obtaining masses above 2.5 kDa was impossible to even when using trifluoroacetic acid, glycerol, or higher analyte concentrations.

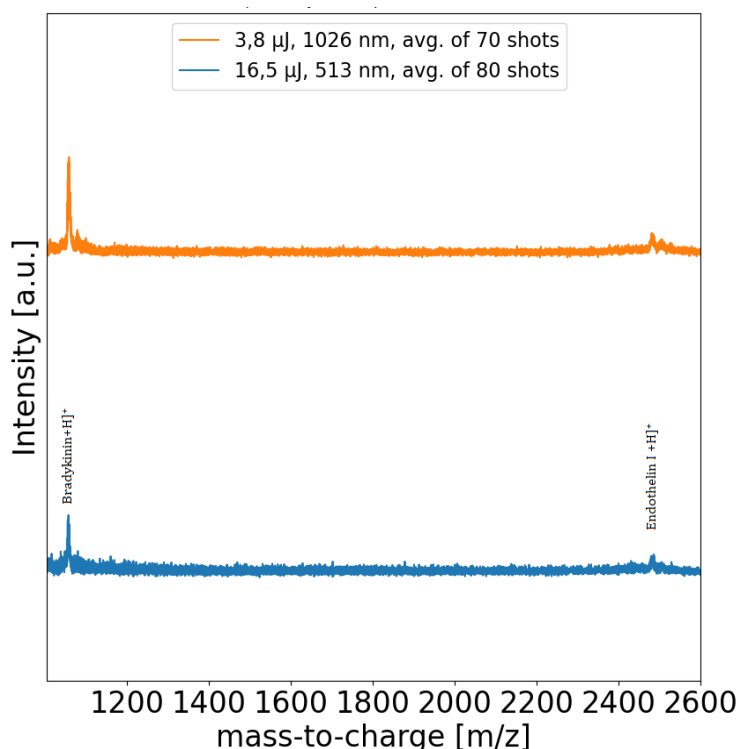


**Figure 5.9** Mass spectra of bradykinin (1061 Da) and endothelin (2491 Da). The concentration of peptides was 100  $\mu\text{M}$ . The orange trace shows the mass spectrum generated with 1026 nm irradiation, while the blue trace was obtained with 513 nm irradiation. The temperature at the sample stage was - 100  $^{\circ}\text{C}$ .

#### 5.5.4 Mass Calibration

A typical MALDI workflow consistently implements the use of a mass calibration agent. The latter consists of multiple species, of which masses are known. Since fs IR-LDI is a novel technique, mass calibration agents are not commercially available or widely known. A group using a nitrogen laser and irradiating caesium iodide generated clusters up to 20000 m/z [213]. In the initial runs, it was dissolved in water and investigated. However, the results were not satisfying. Changing the solvent to methanol, ethanol, and acidifying the solution was equally unsuccessful. Finally, mass calibration was performed using some known substrate ions and the bradykinin signal (see subsection 3.2.5).

---

## 5.6 C60 Fullerene – A Hydrophobic Molecule in a Non-polar Solvent

Fullerene has been used as an MALDI matrix because of its extended  $\pi$ -system, which absorbs the light of a typical MALDI laser (337 nm, photon energy 3.67 eV) [188]. Under high laser fluence, C60 tends to sequentially lose C2 fragments and form clusters, making it an ideal quantification candidate. Since C60 lacks any protons, the number of pathways for ionization is favorably reduced. The ionization energy was experimentally found to be 7.6 eV [214], and the electronegativity is about 2.6 – 2.8 eV [215], [216]. Due to the high degrees of freedom, C60 can store large amounts of energy through the rapid conversion of electronic excitation to vibrational excitation, by that a delayed ionization process occurs [217].

To make use of the sample preparation technique introduced in subsection 3.2.3 C60 fullerene was diluted in toluene to the desired concentrations. Since the toluene has a high vapor pressure, pipetting volumes less than 500 nl was challenging. Therefore prior to sample preparation, the specimen and the pipette tip were cooled in liquid nitrogen for 10 - 20 seconds. Initial studies with 100  $\mu$ M C60 gave unsatisfactory results, and the fundamental and the second harmonic did not produce any analyte signal. With higher concentrations (1 mM), high signal-to-noise mass spectra for C60 were achieved. Data acquisition was performed in parallel for the two wavelengths on the same specimen and the same areal. Laser shots for the wavelength were 50  $\mu$ m apart to minimize sample-related biases. In the following section, the mass spectra obtained with 1026 nm are discussed, and in the follow-up section, the results obtained with 513 nm are the topic.

**Figure 5.10** shows a series of temperature-dependent mass spectrums of C60 fullerene generated with 1026 nm. Besides substrate signal, initial irradiation of the thin film gave no signal associated with C60. The same observation was made in the previous subsection 4.2.4 for aqueous thin-films and bradykinin. Shortly before toluene started to sublime, a mass spectrum revealed the intact C60 species (720 m/z). The latter was also accompanied by broad and higher mass signals, which sustained up to 3000 m/z. Remarkably, those signals share a common mass interval of roughly 360 m/z, which corresponds to the doubly charged species of C60. A fragment of the C60 with a mass 360 m/z is less likely since it would involve multiple bond cleavage. A different study with a nitrogen laser with a pulse width of 3 ns did not observe such cluster formation [188].



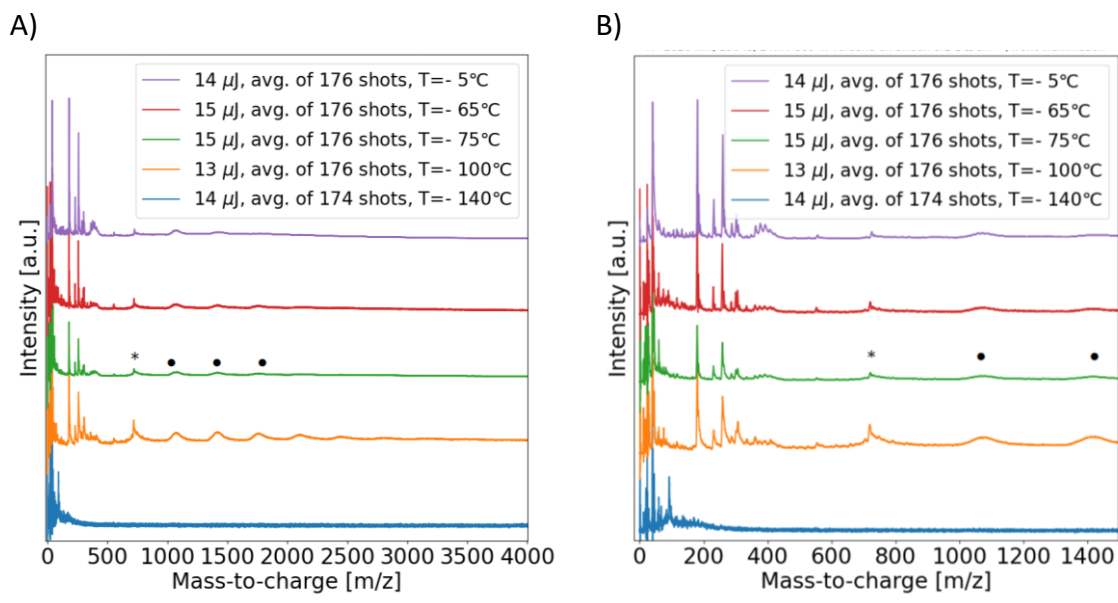


**Figure 5.10** Temperature-dependent mass spectra of fullerene C<sub>60</sub> obtained with 1026 nm irradiation. The analyte concentration was 1 mM, and the pulse energies were between 13 – 15  $\mu\text{J}$ . A) A full range mass spectrum. B) A zoom-in of the original mass spectrum in the range between 700 – 2700 m/z. The asterisks indicates the singly charged C<sub>60</sub> species, while the dots are associated with C<sub>60</sub> multimers.

The next mass spectrum was recorded after toluene sublimation and showed a similar signal pattern qualitatively as before. The upcoming measurements give a comparable picture, although the clusters are only present up to 2000 m/z. Signals from the specimen can be obtained almost five hours after the toluene sublimation. Once again, this experiment showed that high analyte-solvent ratio is not beneficial for non-resonant fs studies. A thin film below 2  $\mu\text{m}$  may deliver instant results after the sample mount, but such a flat film was not in the scope of our method.

If C<sub>60</sub> is exposed to high irradiation energies, which are common for fs pulses, a series of C<sub>2</sub> losses are observed in the mass spectrum in various studies [119], [120] and that observation is verified in the presented experiment. Although lacking a sufficient mass resolution, a C<sub>2</sub> loss in the mass spectrum is implied in the left shoulder of the intact C<sub>60</sub> fullerene.

**Figure 5.11** shows a series of temperature-dependent mass spectra of C<sub>60</sub> fullerene obtained with 513 nm irradiation. The first mass spectrum generated with 513 nm did not give any signal and is in line with the results created by 1026 nm irradiation. The upcoming mass spectrum, before toluene sublimation, gives rise to an excellent signal with a superior signal-to-noise ratio (3000 : 1). In contrast to the 1026 nm the higher mass is not accompanied by sequential cluster formation. Instead, the mass spectrum features a weak and broad signal for the dimer (1440 m/z). A very similar

mass spectrum was achieved when a laser with 337 nm and 3 ns pulse width was applied [188]. After toluene sublimation, C60 signal persisted with a comparable signal intensity to the previous mass spectrum, though the signal intensity decreased for the last measurement (purple trace).

In contrast to mass spectra generated with 1026 nm C2 loss can be easily observed in mass spectra obtained with 513 nm. A C60 missing six carbon atoms is the lowest fragment observed under fs irradiation. In a study, the authors used a 400 nm and 200 fs laser with intensities ten times lower than in the present work and observed a doubly charged C60. However, neither the fundamental nor the second harmonic produced a double-charged C60 species. The effect of the substrate can be excluded since the work here, and the publication used silicon as a target [120].

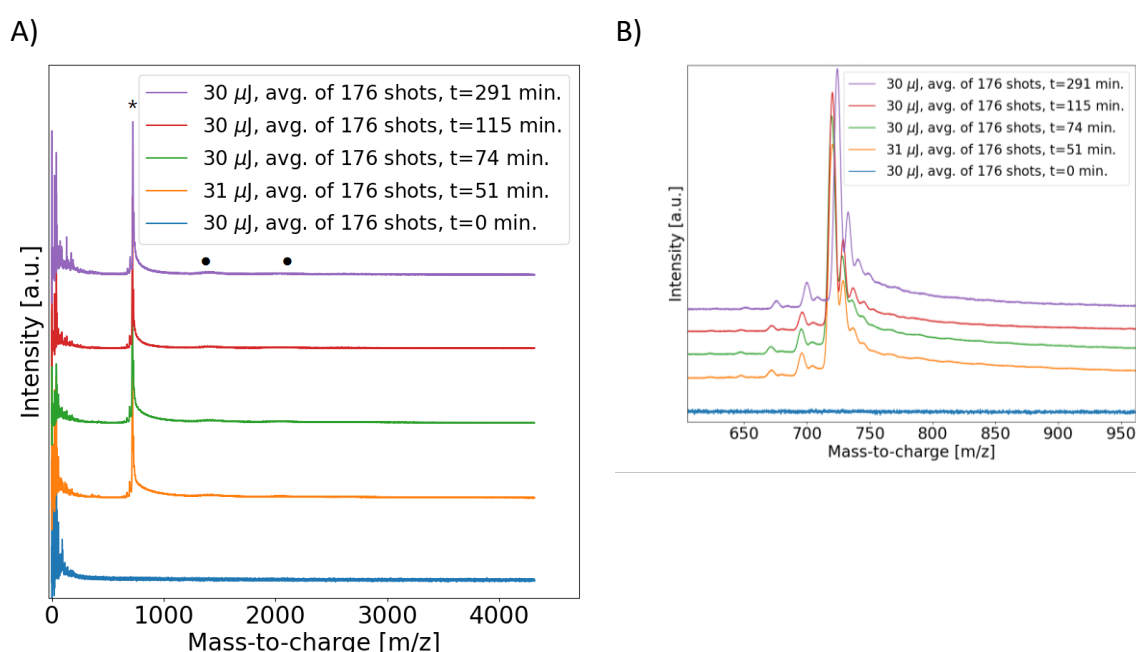


**Figure 5.11** Temperature-dependent mass spectra of fullerene C60 obtained with 513 nm irradiation. The analyte concentration was 1 mM, and the pulse energies were between 13 – 15  $\mu\text{J}$ . The first mass spectrum was recorded at  $-140\text{ }^\circ\text{C}$ . A) An overview of mass spectrum. B) A zoom-in into the mass region 600-950 m/z. The window reveals the C2 loss from the intact species. A fragment of C60 with a total 6 carbon atom loss is the lowest mass observed in this cleavage series. The asterisks indicate a C60 fullerene dimer.

Irradiation with 1026 nm and 513 nm produced a signal with a right-skewed shape. As mentioned in the introduction, the tails raised from delayed ionization of the exciting C60 molecule after multiphoton absorption have been attributed to thermionic emission [218]. Since toluene has no acid protons and C60 fullerene only consists of carbon atoms, the pathways for ionization are limited. In the shape of fs

irradiation, a multiphoton ionization (MI) seems to be the most reasonable ionization pathway leading to a positively charged C60 radical. In addition to MI, photothermal ionization and energy pooling models are dominant mechanisms for ionization [188].

This study showed that 513 nm produced a superior mass spectrum of C60 over the 1026 nm under similar conditions. A possible explanation is the C60 fullerene absorption coefficient, which is several times higher for 513 nm than for 1026 nm [219]. A study dealing with nanosecond pulses and C60 fullerene showed a mass spectra similar to those acquired with 513 nm and fs pulses. This observation can conclude that a successful C60 detection is less dependent on the pulse duration during an fs IR-LDI experiment. However, further studies should be conducted to get a clearer picture.

## 5.7 Ion Collection Yield

The program for ion collection yield and the consequent assumptions were introduced and discussed in subsection 3.2.5. To determine ion collection yield, dataset obtained from a bradykinin solution in pure water was used. The key parameters to calculate the ejected amount of particles are listed in **Table 5-1**. For simplification purposes, the laser-sample interaction volume was approximated to be cylindrical.

**Table 5-1** Key parameter for the calculation of the ion collection yield.

Bradykinin Concentration	10 $\mu$ M
Laser Beam Diameter	10 $\mu$ m
Thin Film Thickness	2 $\mu$ m
Laser-Sample Interaction Volume	0.6 picoliter
Ejected Particles with a Single Laser Shot	$4 \cdot 10^7$

**Figure 5.12** shows a scatter plot of different bins obtained from single-shot mass spectra. A single bin accumulated 8 ns of data. A linear fit function provided by the PYTHON module lmfit (Version 1.0.2) was used. The resulted slope shows how much ions produce a specific voltage. Equipped with the parameter of the function, it is possible to translate the number of ions in each bin. The sum of all bins gave 1960 ions. Dividing the latter number by the amount of ejected particles gives the ion collection yield of  $5 \cdot 10^{-5}$ . For these results, signal intensity higher than 40 mV was involved in the calculation. From the same dataset, bradykinin signals with an

---

intensity lower than 40 mV were also investigated, and the sum of all bins was 970 (Appendix, **Figure A 8**). Although different numbers were calculated, both approaches resulted in similar ions per area unit. In addition, the aforementioned ion collection yield is in line with previous reports for UV-MALDI [76].

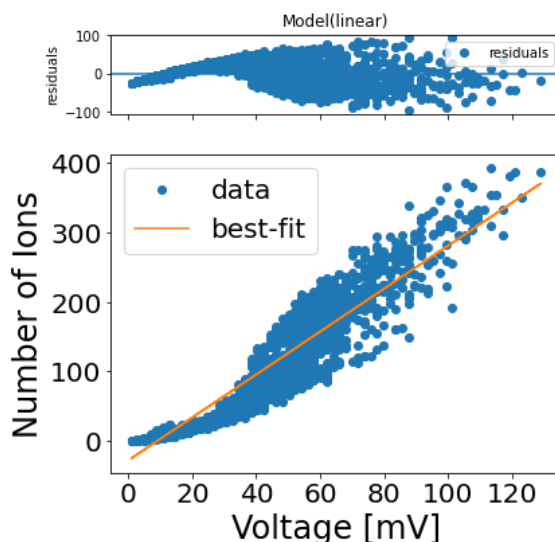


**Figure 5.12** Signal voltage intensity independence of the number of ions. A) A graph shows residuals from the linear fit function. B) A scatter plot of bins obtained from single-shot mass spectra. According to the slope of the linear fit function, a single ion is producing 1.08 mV. The function parameters are  $y = 3.09 \cdot x - 6.39$ . Overall, 109 single-shot mass spectra were used for the calculation.

## 5.8 Summary

This paragraph explored the behavior of biological components embedded in thin ice films after fs laser irradiation in a mass spectrometric environment. This is the first systematic study where temperature dependency, substrate effects, various wavelengths, and different solvents were investigated. Throughout the whole study, thin films with an average of 2  $\mu\text{m}$  thickness were prepared. Among indium tin oxide, chalcogenide glass, silicon, and borosilicate glass, the latter did not give any signal independent of pulse energies. Even substrate ions, which were visible for other target plates, were absent. Borosilicate possesses the highest transmittance for 1026 nm and has the lowest conductivity and heat capacity. Most probably, these factors prevent analyte signal onset. The remaining three target plates showed a bradykinin signal after laser irradiation with 513 nm and 1026 nm in comparable quality. Nevertheless, only some areas provided a good signal, and data acquisition was limited to these localities. Bradykinin signal broadening was observed when the

---

specimen was placed on a chalcogenide glass. Indium tin oxide and silicon are the best candidates for fs MS experiments, but the decision was made to pursue further experiments with silicon only. The reason was the sample preparation step as the thin film between two indium tin oxide coverslips tended to stick to both resulting in an inhomogeneous film on the target plate. This behaviour was rarely observed for silicon.

Temperature-dependent experiments were performed only with silicon as the target plate. Three different temperature zones could be distinguished. Under cryogenic conditions or  $-140\text{ }^{\circ}\text{C}$  a few sweet spots provided a signal of inadequate quality. These areas expanded between  $-140\text{ }^{\circ}\text{C}$  and  $-70\text{ }^{\circ}\text{C}$  making data acquisition easier. After ice sublimation bradykinin signal could be obtained throughout the film, these observations are made for 513 nm as well as for 1026 nm. As signal quality improved for the latter case, a conclusion was made that the substrate surface has to play a major role in the desorption and ionization of the analyte. For several hours after ice sublimation, the bradykinin signal was stable. Only a day later, the signal was absent. A reasonable explanation can be that a hydration shell that evaporates after several hours in low-pressure conditions also plays a role in signal onset. Unspecific fragments accompanied the intact species of bradykinin, and up till now, the first-ever observed result under such conditions. Fragmentation in biomolecules is caused by high electron densities (plasma formation) or multiphoton ionization. Because the employed fluences were close to  $1\text{ J}\cdot\text{cm}^{-2}$  plasma formation is less likely, and multiphoton ionization may shape the bradykinin fragmentation pattern. However, the low intensity of the fragments suggests that either multiphoton ionization primarily excites the intact species without further bond cleavage or photodissociation only appears at the center of the laser impact, where laser peak powers are the highest. AFM target plate images revealed the impact zone is accompanied by surface melting for high pulse energies, but the surface is almost unchanged for pulse energies used in the experiment. Nevertheless, substrate ions can always be found in the mass spectra. Such observation may support the argument that substrate ions support the desorption mechanism in fs-laser MS.

In a series of experiments, fs MS produces meaningful data, but the pathways for desorption and ionization are somewhat complex. As peptides usually have a low absorption coefficient between 513 nm and 1026 nm the impact of the laser wavelength is difficult to measure. Therefore, an additional experiment with fullerene C60 mixed with toluene was conducted. As toluene possesses no acidic protons as well as C60, protonation as a primary ion source can be excluded or at least occurs less frequently. Further C60 light absorption is higher for 513 nm than for 1026 nm. In a comparison experiment, 513 nm produced a higher intensity signal in contrast to 1026 nm. This experiment shows that the laser also interacts with the analyte.

---

---

However, a low-intensity signal for C60 appears after 1026 nm irradiation, suggesting that laser-analyte interaction occurred.

Cryogenic fs laser MS can detect mass up to 2.5 kDa, which is an excellent alternative to measure small mass molecules. For MALDI, this mass range usually is problematic since matrix ion peak is interfering with the analyte. The sensitivity is at 25 attomoles which is superb compared to MALDI, SALDI or DIOS. Such a method can be well implemented in a mass spectrometric imaging setup. Here, high sensitivity is important since MS is a disruptive method, and target volume can only be investigated once. In addition to the sensitivity, the shot-to-shot repeatability of the thin film was explored. Silicon provided the highest values, with several datasets reaching over 90 %. Such numbers are also important for mass spectrometric imaging as robust signal generation from different areas allows better judgment about the sample overall.

## 6 Discussion

### • Sample Preparation

As mentioned in the introduction, ultra-fast laser pulses were previously employed to extract biological components embedded in thin ice films. The constraints regarding laser parameter variation, especially the use of sub-nanosecond pulse durations, were not addressed. Moreover, a detailed sample preparation protocol was hitherto not rigorously investigated. The presented work was motivated by the fact that current state-of-the-art MS methodologies, such as MALDI, are limited in the direct analysis of biomolecules due to the mandatory preprocessing steps of the specimen. Water can serve as a matrix as it is a natural solvent of biomolecules and constitutes the major part of a cell and other organelles. A mass spectrometric approach targeting water would facilitate a direct analysis of biomolecules close to *in vivo* conditions.

In order to perform cryogenic MS experiments with a daily routine, a robust sample preparation protocol is foundational. Hence, in the present work, several sample preparation protocols were developed for cryogenic MS experiments and can be separated into two approaches. The first approach deliver an average sample thickness between 20  $\mu\text{m}$  and 30  $\mu\text{m}$ , depending on the volume applied. The design concept of the thin films was inspired by thin tissue sections obtained with microtoming. For this, a commercial *Prolene* foil was used as a top cover, while the aqueous sample was either on silicon, ITO, or a CG coverslip. Once the scaffold was ready and dropped in liquid nitrogen, the *Prolene* foil was removed with a tweezer. A great advantage of this technique is that it is highly reproducible while the demand for technical skills is very low and is easy to master. However, because the *Prolene* foil is very thin and therefore highly flexible, the thin ice film has an uneven surface. To counteract this, an additional coverslip pressed on top of the *Prolene* foil can be used. An assumption can be made that more even ice film would be formed with additional pressure, but unfortunately, this was not the case, and locally close areas still fluctuated in analytical performance. This problem can be further approached by exchanging the *Prolene* foil with a stiffer foil, but this experiment was not conducted.

---

A second approach produces a thin ice film with less thickness fluctuation, which was achieved with two coverslips of the same kind. A verification experiment conducted with the sample preparation protocol shows minor signal fluctuation while a large area with 4 x 4 cm is rastered (Appendix, **Figure A 9**). The general observation was that the ice film tends to stick to a hydrophilic coverslip, and in principle, Teflon, known for its high hydrophobicity, could be employed, but this was not investigated. However, this method is limited to an average thickness of 2  $\mu\text{m}$  – 12  $\mu\text{m}$ . In this work, sample preparation using a vitrobot could have been performed [220] to create an ice film down to several hundred nanometers with thickness fluctuation less than tens of nanometer. Vitrobot is a sample preparation device for cryo-electron microscopy and prepares thin ice films on TEM grids with meshes. However, as vitrobot parameters are optimized for TEM grids, the other targets as used in the present experiment (silicon, ITO, CG) would require additional calibration. An additional bottleneck occurs as TEM grids are offered only 3 mm in diameter, and a new sample carrier design for the time-of-flight mass spectrometer would have been necessary. Nevertheless, whether ice films with nanometer thickness and marginal thickness fluctuations are ideal for cryogenic MS must be verified in future experiments.

#### • DIVE MS with Cryogenic Thin Ice Films

The DIVE process is a special regime of water excitation and can be considered in a broader sense as a form of resonant IR-(MA)LDI. Despite encouraging aspects in terms of minimal sample preparation, ‘soft’ desorption, and ionization process allowing labile species to be investigated, the method also suffers from low ion yield, the lack of sample preparation protocols, and of systematic studies (especially with IR lasers) aimed at a better understanding of the underlying desorption and ionization mechanism. Presently, these issues are restrictive and hamper the use of resonant IR-(MA)LDI in a broad analytical sense and therefore were investigated in the present work.

Ultra-fast laser pulses have been primarily employed to extract bradykinin and angiotensin out of ice films. The first and most relevant report concerned with resonant IR-(MA)LDI is by Berkenkamp *et al.* [35]. The authors used a laser with a 150 ns pulse duration and a central wavelength of about 3000 nm. A similar wavelength was used in the present experiment, but the pulse duration was 400 picoseconds, hence 375 times shorter. Berkenkamp *et al.* detected peptides from bulk frozen droplets but not directly and only by adding proton donor agents such as TFA. In short, the published work reported superior results when the droplet containing the analyte was pipetted on the target and dried under ambient conditions. Consequently, freezing and mounting the target in the mass spectrometer provided a signal for peptides and proteins. In addition, to produce mass spectra of higher masses with a quality comparable with UV-MALDI, the specimen was premixed with

---



Tris·HCl. Finally, the author stated that low sensitivity seems to limit the general applicability of water as a matrix in IR-MALDI and direct extraction from bulk frozen droplets gave unsatisfactory results. Conversely, the observations mentioned above were not reproducible in the setup used in this work, although a similar sample preparation protocol was followed. For instance, the direct extraction of biomolecules from frozen droplets is routinely possible without any proton donor agent, though only from the droplet's rim. A shorter pulse duration might produce a discrepancy between the results here and the published work [35]. This statement is speculative since a laser system with a longer pulse duration was unavailable for verification, but a study using a laser with 5 ns pulse duration and 3000 nm wavelength obtained protein mass spectra from samples embedded in methanol or isopropanol under cryogenic conditions [154]. The pulse duration of 5 ns is 30 x shorter than the laser pulses used by Berkenkamp *et al.*. In light of the presented results, a conclusion from this work might suggest that shorter pulse durations are beneficial for extracting biomolecules from IR-sensitive matrices.

However, besides pulse duration, sampling conditions during the ablation also impact the outcome. Only the droplet rim gave a high-intensity signal, whereas no analyte could be successfully detected in the droplet's center. A possible explanation for the latter observation might be that the propagation angle of ejected material created during the ablation was unfavorable and failed to reach the orifice and further the detector.

For thin ice films oversampling and SpSS mode yielded different results. For instance, the analyte signals generated with SpSS mode were exposed to high fluctuation in intensity accompanied by low shot-to-shot repeatability. A dramatic change in the observed laser-sample interaction was obtained using the oversampling mode, which produced a stable signal with great shot-to-shot repeatability (**Figure 6.1**). Oversampling was achieved by adjusting the laser repetition rate to 1 Hz and moving the irradiation area with the same frequency by a fraction of the laser beam's waist. This sampling method has not previously been investigated or commented on in available literature under low-pressure conditions but under ambient conditions. Most probably due to hardware limitations since most IR-MALDI studies were conducted at the beginning of the 2000s, and sample stages were initially less sensitive.

Intriguing results were obtained from the rim of the frozen droplet, and a sample preparation protocol was pursued where an ice film was created with a comparable height to the droplet rim. Consequently, the semi-thick sample preparation protocol has been developed, producing ice films with a thickness of about 20  $\mu\text{m}$  - 30  $\mu\text{m}$ . As for droplet rim and oversampling showed the most robust results, but the whole sample area also provided an analyte signal out of a 200  $\mu\text{M}$  bradykinin solution. The sensitivity is calculated to be about 200 fmol when a cylindrical crater is assumed as

ablation volume, but this value is probably even less as oversampling mode only desorbs a fraction of the laser beam waist. Sample preparation impacts signal generation and thinner ice films were investigated further.

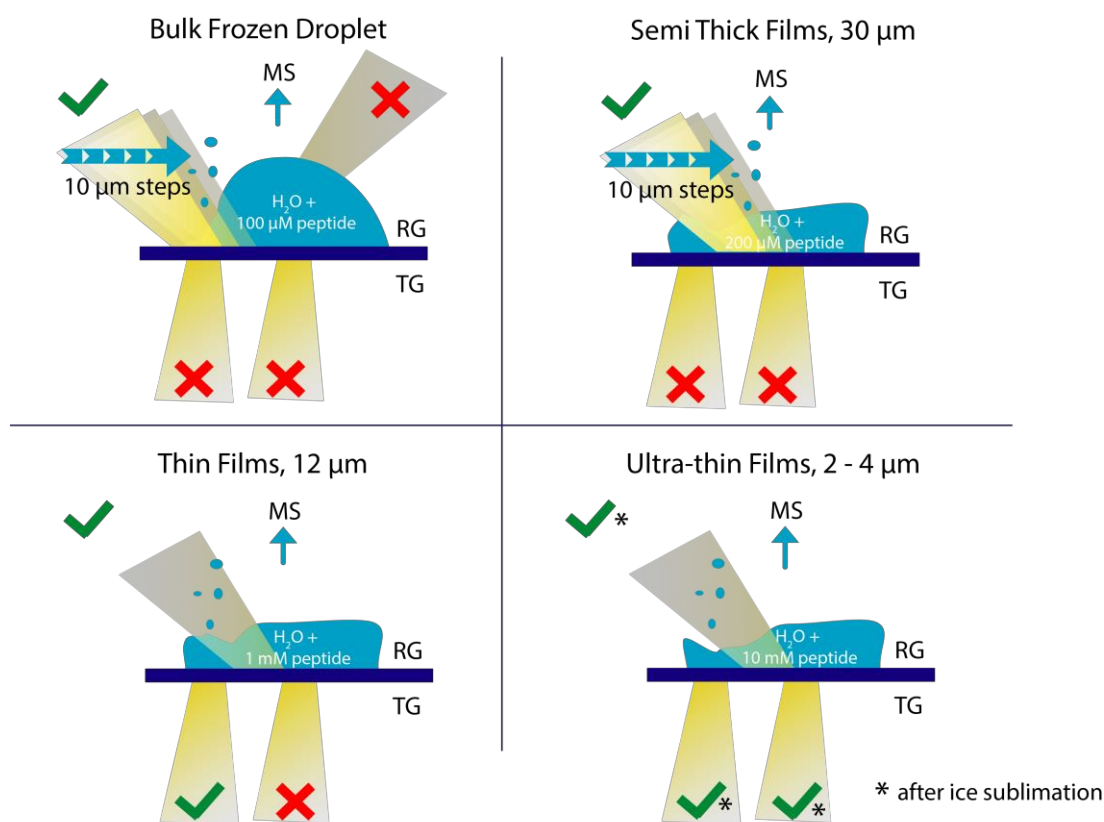


**Figure 6.1** Various thin ice films were prepared and investigated under reflection geometry (RG) or transmission geometry (TG). The yellow cone indicates a laser beam while the green checkmark represents a successful and the red cross a failed extraction of bradykinin or angiotensin. All images represent a cross-section of a silicon coverslip and an aqueous sample in the mass spectrometer (MS).

Several considerations motivated the application of thinner ice films. First, irradiating a small volume, which is ultimately represented as a thin film, produces a plume with a lower density of ions than a larger volume. Particle interactions in the expanding plume are a known phenomenon that can reduce the overall analytical performance by recombining ion-ion [89], [221]. Hence, thinner ice films would be an intriguing solution to this phenomenon. Of course, a tighter laser focus can be employed, but high photon densities accompany such adjustment, enhancing the probability of non-linear processes leading to vibrant fragmentation patterns [205], [207], [222].

A more practical aspect of using thin ice films is the irradiation geometry. The results discussed in the paragraph before were produced in RG, but bulk frozen droplets and semi-thick films did not provide a signal in TG (**Figure 6.1**). The assumption was that penetration depth must play an important role, which is of the order of micrometers at 3000 nm in water [223], given a  $1/e$  absorption length of 3  $\mu\text{m}$ . While the superficial layer of the specimen is directly exposed to the laser beam in the RG and excited molecules can freely expand into the vacuum, this is not the case for irradiation in TG, where top layers impede the molecular expansion. Thus, a sufficiently thin ice film should reduce the previously described effect. Furthermore, the advantage of TG is that optical elements with higher numerical apertures can be employed, resulting in a tighter focus, which is useful when higher spatial resolution is desired, especially in the case of IMS [224]. Last, thin films might be useful as a low-cost calibrant outside the scope of the present work. Before IMS experiments, thin ice films, which mimic a tissue section, can be used to test various parameters prior to the investigation of a unique specimen.

Therefore, a study was conducted for the first time where thin ice films (between 2 and 12  $\mu\text{m}$ ) were irradiated in TG and RG (**Figure 6.1**). First, the thickness of ice film with a 12  $\mu\text{m}$  (thin film) is discussed. A bradykinin or angiotensin signal was difficult to obtain from 100  $\mu\text{M}$  solutions, which the reduced amount of ejected particles can explain such observation. Hence, only an increase to 1 mM analyte solution granted the desired results for both geometries under cryogenic conditions. Unfortunately, the mass spectra were overshadowed by increased substrate noise in TG, which limited the use of higher laser pulse energies. Gating or deflection plates are common techniques to hinder small mass ions from reaching the detector, but hardware limitations restrict such an approach. Conclusively, thin films provided mixed results, and the overall sensitivity was reduced to 50 pmol per shot.

In this context, it is less surprising that using even thinner films in the range of 2 – 4  $\mu\text{m}$  (ultra-thin film) revealed additional challenges in TG and RG (**Figure 6.1**). To grasp a better understanding of the underlying desorption and ionization mechanism, a temperature-dependent study was performed. Despite multiple approaches to produce an analyte signal from 1 mM solution, analyte ion generation was only possible from 10 mM bradykinin solution during cryogenic conditions, but with unsatisfying shot-to-shot repeatability, which substantially improved once ice sublimation began. High water content in the residual gas of the mass spectrometer can be observed before and towards the end of the ice sublimation, which correlates with the signal intensity of bradykinin during the same period. Because of this observation, a speculative hypothesis can be made that water in form of a hydration shell is sufficient for desorption and ionization. The hypothesis was supported by bradykinin signal intensity drop after ice sublimation in RG and to some extent in TG. The ideal analyte-water ratio could not be determined, but the most intense signal for

---

both geometries was obtained during ice sublimation. Overall ultra-thin films show a low sensitivity in TG and RG, and further studies, for instance, with different targets, are needed to make a statement about the overall performance.

A low intensity bradykinin signal can be observed several hours after ice sublimation in TG, which led to the assumption that through decreasing ice film thickness, substrate-related effects might promote the signal onset. To investigate such interactions, protonated water was exchanged with deuterated water, which lacks a high absorption coefficient at the incident wavelength [189], reducing the matrix's role in the desorption and ionization process. A 10 mM bradykinin solution and a 3  $\mu\text{m}$  thin ice film were prepared and irradiated in a temperature-dependent study. In TG, the bradykinin signal embedded in  $\text{D}_2\text{O}$  can be generated after ice sublimation, but the signal is less intense than in the  $\text{H}_2\text{O}$  sample. This experiment suggests that substrate effects are to some extent involved in analyte desorption and ionization in TG. However, in RG, no bradykinin signal could be obtained before, during, and after ice sublimation, suggesting an absence of a substrate effect.

To increase analytical performance for ultra-thin films, glycerol as an additive was investigated. Although this adds a step to the sample preparation protocol, it is also considered a good IR-MALDI matrix that is compatible with most biological substances [172], [176]. The specimens was prepared in accordance with the ultra-thin film sample preparation protocol. However, only a small fraction (2.5 % - 20 %, (w : w)) of glycerol was used, which considerably improved the outcome. Specimen with an analyte concentration of 100  $\mu\text{M}$  can be routinely analyzed, increasing the sensitivity hundredfold (10 fmol per shot) in comparison to the analyte in pure water (1 pmol per shot) for both irradiation geometries. In a limit of detection study, even from 10  $\mu\text{M}$  bradykinin solution, improving the sensitivity further but still in the same range as reported by other authors (**Table 6-1**). Such relation of the sensitivity might not be sufficiently informative as other have worked with pure glycerol samples and different sample stage temperatures, but this analogy is the best comparison as studies with a similar setup are not available or limited to a single work [35]. Also, sensitivity depends on pulse duration, different sample preparation protocols, sampling conditions, and the employed mass spectrometer. Nevertheless, based on the uncertainties mentioned above sub-nanosecond pulse durations employed in this work performed reasonably well, but a final statement about the sub-nanosecond pulse duration impacting the sensitivity, ion yield, or mass resolution is inconclusive. However, this work's IR-(MA)LDI method stands in great contrast to previous results where direct extraction of biomolecules from ice was unsuccessful. Whether the outcome is linked to pulse duration should be investigated in future studies.

**Table 6-1** Selected publications concerned with IR-MALDI using glycerol as a matrix under different temperatures. Experiments were conducted in reflection geometry while some were actively cooled and others were investigated at room temperature (RT). The asterisks denotes that the sample was a water-glycerol mixture (w : w, 20 : 80).

	Temperature at the sample stage [°C]	Pulse duration [ns]	Fluence [J·cm <sup>-2</sup> ]	Analyte concentration [μM]
S. Berkenkamp <i>et al.</i> [160]	- 123	80	-	1
Y. J. Bae <i>et al.</i> [93]	- 15	7	6.8	-
C. Menzel <i>et al.</i> [184]	RT	6	3.5	30
	RT	98	4.2	30
	RT	185	4.2	30
J. C. Hyun <i>et al.</i> [180]	- 30	5	1.1	5
V. L. Talrose <i>et al.</i> [225]	RT	70	0.2	1
<b>This Work</b>	- 140	0.4	1.1	10*

**Table 6-2** gives a qualitative overview of whether a bradykinin signal can be produced in different solvents by RG or TG conditions. The present results verify that glycerol can increase the IR-MALDI sensitivity hundredfold without additional optimization than equivalent sample preparation with pure water (ultra-thin films). For semi-thick films (30 μm) the addition of glycerol can produce an analyte signal not obtained with pure water samples in TG (**Table 6-2**). Although this outcome encouraged testing the limit of detection, further dilution yielded an analyte signal with high fluctuation, making it complicated to find a concise conclusion. The temperature-dependent study revealed that an analyte signal could be generated from semi-thick films before and after ice sublimation in RG and TG, though the signal intensity was lower for both geometries before ice sublimation. This observation suggests that an already small addition of glycerol improves the laser solvent interaction, leading to a successful peptide extraction before ice sublimation. A study investigating different glycerol-water mixtures with neutron scattering suggested that glycerol changes the water structure. The hydrogen bond network is extended with glycerol, which might change the properties of the mixture [226]. The addition of glycerol is beneficial for signal onset in IR-MALDI, but glycerol weight ratios exceeding 7.5 % (w : w) resulted in signal broadening, reducing the mass resolution. A previous study concerned with protein samples containing 50 % glycerol has also reported a loss of mass resolution [180]. The authors encountered this issue by placing a grid perpendicular to the expanding plume, which improved the mass resolution significantly, but the implementation of such a design was not feasible due to spatial constraints in our mass spectrometer. Nevertheless, the optimal glycerol

weight ratio is about 5 % (w : w, 5 : 95), which slightly worsen the analytes mass resolution but significantly improved the sensitivity.

**Table 6-2** Results of the performed resonant IR-MALDI experiments in reflection (RG) and transmission geometry (TG). The table summarizes the experiments with pure water and glycerol-water mixture sample, which are separated by a slash sign (pure water/glycerol-water mixture). Green and red dots imply a successful or unsuccessful experiment, respectively. Additionally, the 'x' denotes a not conducted experiment, while the checkmark indicates whether a temperature-dependent series for a given sample was conducted.

Irradiation Geometry	TG		RG	
	30	2 - 4	30	2 - 4
Ice Film Thickness [ $\mu\text{m}$ ]	30	2 - 4	30	2 - 4
Signal at $-140\text{ }^\circ\text{C}$	●/●	●/●	●/●	●/●
Temperature-dependent series	x/✓	✓/✓	x/✓	✓/✓
Before ice sub.	x/●	●/●	x/●	●/●
During ice sub.	x/●	●/●	x/●	●/●
After ice sub.	x/●	●/●	x/●	●/●

**Table 6-3** summarizes the ablation threshold for the bradykinin in pure water and a water-glycerol mixture in RG. The ablation threshold energy did not depend on the sample thickness or the matrix but on the sampling conditions, such as oversampling, which showed the lowest fluences for signal onset. This might be because successive laser pulses locally increased the temperature and reduced the ablation threshold energy. This statement include sufficiently thick samples such as bulk frozen droplets and semi-thick films, as for thinner ice films, the effect was not noticeable. Also, when SSpS mode was applied to semi-thick films, a slight increase in pulse energy was necessary to achieve a similar analyte signal intensity compared to oversampling mode.

In an additional study, the mass limit of the resonant IR-(MA)LDI in pure water and water-glycerol mixture was determined. Lysozyme is the highest molecular mass that can be extracted from both solvents in RG using the oversampling mode, while a successful signal in TG was only possible in a water-glycerol mixture during and after ice sublimation. Remarkably, in both geometries, fragmentation was absent for proteins and peptides during the course of this work under resonant IR irradiation.

Higher mass protein such as BSA was investigated but provided no outcome. Whether non-optimal adjustment in the mass spectrometer led to disappointing results or other parameters cannot be distinguished. Additional measurements are required in another mass spectrometer to make a comprehensive conclusion.

**Table 6-3** Signal threshold fluences for samples with various ice thicknesses, sampling conditions, and solvents. Superscript I stands for oversampling mode, while II denotes single shot per spot mode. The asterisks marks a successful signal detection after ice sublimation.

Solvent	Sample	Routinely used pulse energies [ $\mu$ J]	Threshold pulse energy for signal onset [ $\mu$ J]	Fluence [ $\text{J}\cdot\text{cm}^2$ ]
H <sub>2</sub> O	Bulk Frozen Droplet	56	50 ± 15	1.1 <sup>I</sup>
	Semi Thick Films	60	55 ± 12	1.2 <sup>I</sup>
	Semi Thick Films	70	65 ± 17	1.3 <sup>II</sup>
	Thin Films	104	70 ± 19	2.2 <sup>II</sup>
	Ultra-thin Films	94	92 ± 13*	2.0 <sup>II</sup>
H <sub>2</sub> O/ Glycerol	Semi Thick Films	98	81 ± 14	2.1 <sup>II</sup>
	Ultra-thin Films	98	100 ± 21*	2.1 <sup>II</sup>

Resonant IR-(MA)LDI wider use was mainly hampered by expensive laser sources, low ion yield, lack of reproducible as well as reliable sample preparation protocol, and also systematics studies to better understand the desorption and ionization process. First, the IR laser sources are still more expensive than UV lasers, but the price difference is shrinking, making such systems more affordable. In the present work, novel and reproducible sample preparation protocols were developed to facilitate the application of resonant IR-(MA)LDI and make it more accessible to a broader community. In a systematic approach, it was shown that not only sample preparation but also sampling condition as well as the temperature at the sample stage impact the mass spectrum. The information gained from this work can be further adapted by other scientists who desire to work in a mass spectrometric environment close to *in vivo* conditions. The determined ion yield in this work is still lower in IR-(MA)LDI than in UV-MALDI, but with different sample preparation protocols, we increased the current detection limit and showed that direct extraction of biomolecules from ice without proton donor agents was possible, even for high mass species such as lysozyme. Further parameters can be investigated and optimized, and more information is given in the outlook chapter.

---

### • Femtosecond Laser Mass Spectrometry

Unlike in resonant IR-(MA)LDI, in non-resonant fs IR LDI, laser-matrix interaction is less important, and laser-substrate interaction is primarily responsible for analyte desorption and ionization. General application of fs lasers has been extensively employed under ambient conditions in combination with Q-TOF mass spectrometer with particular emphasis on the investigation of bio- [56], [129], [227] and carbon-based molecules [228] and as a post-ionization source in ion traps [206] or TOF instruments [229]. Nonetheless, the implementation of non-resonant fs IR-LDI in a low-pressure environment is, to the best of our knowledge, limited to the publications listed in **Table 6-4**. A remarkable report from this list is the study by Walker *et al.*, where lipid extraction from pancreas tissue was conducted, but unfortunately, severe fragmentation led to ambiguous results. Another seminal publication in the context of fs IR-LDI investigated thin ice films under cryogenic conditions and inspired the present work here. Berry *et al.* [53] used a laser with a central wavelength of 400 nm and 200 fs pulses to extract biomolecules up to 6 kDa with minor fragmentation from acidic ice films under cryogenic conditions. The authors also investigated various substrates and suggested that desorption and ionization are solely driven by laser-substrate interaction, mostly due to local heat increase. However, this promising methodology's broader utilization or follow-up publications did not yet appear. Therefore, it was even more intriguing to investigate the aforementioned results in our laboratory and use non-resonant fs pulses with the wavelength of 1026 nm (fundamental) and 513 nm (second harmonic) to extract bradykinin and angiotensin out of thin ice films. In addition, a temperature-dependent study was conducted to investigate the ice layer's impact.

Initially, the specimen was a simple mixture of water and a peptide prepared in a semi-thick ice film, but all attempts to reproduce the observation reported by Berry *et al.* failed. Variation in the TFA content and the increase in laser energy did not yield the desired outcome. The prime worry was that a sparse laser-substrate interaction resulted in the absence of ablation. As a consequence, the sample preparation protocol for ultra-thin films was adopted, leading to a successful signal detection but only from certain areas. Increasing the laser intensity or adding TFA improved the outcome marginally on silicon, ITO, and CG. The intensity was limited to fluences below  $6 \text{ J cm}^{-2}$  as higher energies produced an abundance of small molecular ions, which oversaturated the detector, reducing the analytical performance. Ion deflection for small molecular species was not possible because of hardware limitations. It cannot be excluded that an analyte signal could have been obtained with higher fluences because the fluences employed in the work of Berry *et al.* were between 4 and  $9 \text{ J cm}^{-2}$  and up to 5 times higher.



**Table 6-4** Selected publications concerned with fs laser MS of organic molecules and samples under low-pressure conditions.

	The temperature at the sample stage [°C]	Wavelength [nm]	Pulse duration [fs]	Fluence [J·cm <sup>-2</sup> ]	Highest mass [Da]	Sample
Berry <i>et al.</i> [53]	- 173	400	200	6.1	5800	Thin ice film
Samek <i>et al.</i> [230]	RT	775	170	4.89	60	Plant leaf
Kobayashi <i>et al.</i> [119], [231]	RT	400/ 800	120	1.7	720	C <sub>60</sub> powder
Walker <i>et al.</i> [52]	RT	800	100	-	900	Pancreatic tissue
<b>This Work</b>	- 140 - RT	513/ 1026	190	0.9	2400	Thin ice film

A radical change was observed once a temperature-dependent series was conducted. During the experiments, a residual gas analyzer measured the environment in the mass spectrometer, and the gauge pressure output was also monitored. **Figure 6.2** illustrates three distinct states of the thin ice films before, during, and after ice sublimation. In **Figure 6.2** panel A, under this conditions obtaining an analyte signal was only possible from some regions, and a speculative assumption is made that those areas are thinner than the average thickness, while in **Figure 6.2**, panel B, those regions expand. The water content in this observation must play an important role as signal onset did not incrementally increase with rising temperature but abruptly gained in intensity once ice sublimation started. A high analyte-water ratio seems favorable, but matrix-free analyte desorption and ionization was also possible. (**Figure 6.2**, panel C). The figure shows that the spatial peptide orientation was expected to be maintained after ice sublimation, similar to freeze-drying experiments with protein and peptides. However, the suggestions above are speculative, and panel C shows a more complex picture. Analyte signal from a 100  $\mu$ M solution can only be obtained multiple hours after ice sublimation. Our explanation for the latter observation is the hydration shell consisting of several water atoms. This solvation shell should stay intact under low-pressure conditions for some hours. This statement is supported by the fact that when the water signal vanished in the RGA mass spectrum, the signal for the analyte vanished in the TOF-MS some hours later. A possible explanation for the observed phenomena could be a conformational change experienced by the analyte when the water ratio dropped

---

below a critical threshold. However, higher analyte concentration showed that an analyte signal could be generated even a day after. With a higher peptide concentration, a more dense peptide network can be expected once ice was sublimated. Whether this network was beneficial for signal onset could not be clarified in this work.

Conclusively, cryogenic fs MS is possible, but the most favorable condition is when the specimen is sufficiently thin and/or the analyte-water ratio is low. Once the ice is completely sublimated, the specimen is left without matrix, and the method is more accurately coined fs SALDI. A comparison with nanosecond and fs SALDI reveals slightly different desorption and ionization processes, discussed in the upcoming section.

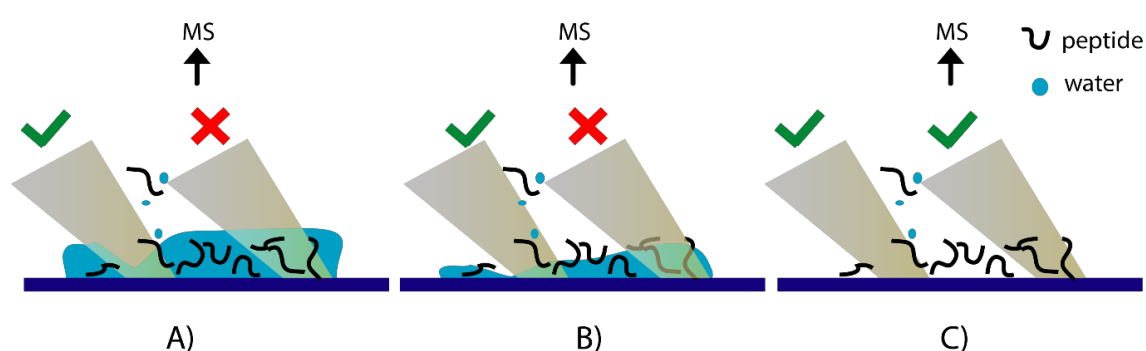


**Figure 6.2** Ice thin-film status before A), during B), and after C) sublimation. Some areas provide an analyte signal before ice sublimation and under cryogenic conditions, while most ice films only show substrate peaks. Laser energy increase does not change the outcome. During ice sublimation, the analyte signal intensity increases along with the area where a successful analyte signal can be obtained. After ice sublimation signal can be generated from the most location of the thin film.

Fs pulses hitting ice layers with biomolecules produce a dizzying array of phenomena. Generally, the possible mixing of different effects is difficult to entangle, and further investigations are needed.

The laser light first interacts with the superficial layer of the ice film and induces rapid heating or ionization of the material. Once the laser light transverse the ice layer, it subsequently interacts with the substrate. Here similar phenomena can occur as with the ice layer. Next, the laser light can penetrate the substrate or is reflected to the extent that depends on wavelength and intensity (e.g. focusing conditions). A substantial amount of laser energy can be sent back through the sample film a second time and interacts with the ice layer again. The remaining intensity is either absorbed in the substrate layer or partly transmitted. The ice film and substrate interface region is prone to plasma effects above certain intensities. The electric field distribution is

---

fully inaccessible, and so is the energy of potentially liberated electrons, ions, and clusters, which would be available to initiate desorption and ionization processes.

As mentioned above, bradykinin signal onset is highly dependent on the sublimation progress. The substrate was more exposed to the impinging laser light when the absorptive ice and water was getting thinner. A correlation must be assumed as more laser light interacted with the substrate and improved the analyte signal intensity. Further, the substrate irradiation under cryogenic and non-cryogenic conditions with fs pulses forming high-intensity silicon clusters solidifies laser-substrate interaction [232]. The observations above outline the predominant role of laser-substrate interactions in promoting analyte desorption. Another possibility might be that clusters ejected from the substrate material facilitate bradykinin desorption. Although substrate signals for most mass spectra accompany the bradykinin signal, several exceptions can be found without substrate signals (Appendix, **Figure A 10**). The latter observation suggests that desorption is not solely relying on the liberation of substrate ions.

Another factor driving analyte desorption is the laser-induced heat. Surface melting has been suggested as a potential pathway for ionizing analyte molecules in the SALDI environment [39], [203]. However, in SALDI or DIOS, nanosecond ultraviolet lasers are employed. The interaction between the substrate surface and fs pulses differs from nanosecond pulses [233], [234]. The energy of a shorter laser pulse mainly couples to the electrons of the excited material [121]. The heat affecting zone produced after laser pulse impact is proportional to the square root of the pulse duration [235]. This phenomenon is of minor impact [236], [237] when fs pulses are employed. The experiment in this work supports that laser-induced heat zones were barely visible under experimental conditions, while only higher pulse energies caused typical heat-induced patterns on the silicon coverslip. However, this work did not clarify whether fs laser pulses solely desorb the analyte by heat and subsequent temperature rise or in combination with other phenomena.

In addition, for the 1026 nm wavelength, we have found that the analyte signal originates from a fairly narrow 20  $\mu\text{m}$  wide region with local energy densities above 0.6  $\text{J}\cdot\text{cm}^{-2}$  in the center of the beam (**Figure 6.3B**). The bradykinin signal is observed after the first laser pulse, but subsequent laser pulses on the same region failed to produce an additional signal. This is remarkable since the FWHM diameter of the laser beam is 30  $\mu\text{m}$ , and the analyte could interact with the outer region of the laser beam profile. A certain laser threshold energy seems to be necessary for signal onset, which was also confirmed by another study [196].

The near-IR irradiation and its second harmonic (green) produce a similar mass-spectrometric result. However, the boundary conditions are very different concerning beam size, absorption in the substrate, number of photons in the region of 20  $\mu\text{m}$  (where the bradykinin signal of the near-IR originates), and energy density. Given that

second harmonic wavelength has higher pulse energy, their energy density in the center of the beam is less compared to the fundamental, and so is the number of photons compared to the spatially narrower yet weaker near-IR pulse (**Figure 6.3A**).

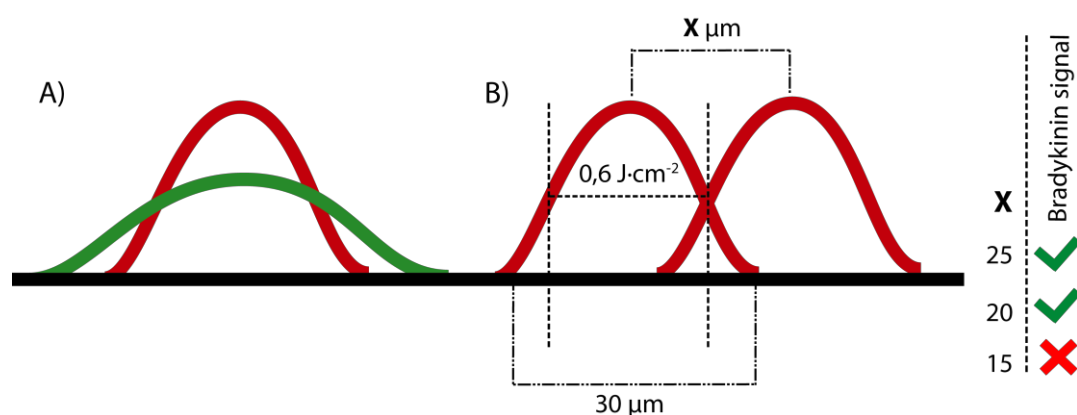


**Figure 6.3** Laser profile of the second harmonic (513 nm) and fundamental (1026 nm) during ablation. A) A comparison between 513 nm (green) and 1026 nm (red). B) Bradykinin signal onset dependence on the distance of adjacent pulses.

The desorption of an analyte is the first step toward detection, but in MS, typically, only ionic species are observable. As mentioned in the introduction, several pathways can ionize the molecule of interest, which leads to a different outcome. The molecule of interest can arrive at the detector as quasimolecular protonated species like in MALDI, with electron deficit, or even both. Due to limits in the mass resolution of the used mass spectrometer, resolving molecular species by proton mass was impossible. To investigate the possibility of the arrival of an electron deficit species, an additional experiment with C60 fullerene and toluene was conducted. C60 fullerene and the solvent are neither accepting nor providing protons. However, C60 was detected, hinting that an electron deficit species cannot be ruled out (**Figure 5.10** and **Figure 5.11**) for bradykinin as a prime molecule of interest. Two possible ionization pathways may be associated with creating an electron deficit species. Either the analyte is ionized through multiphoton ionization [37] or electrons liberated by the laser light, thermal effects or photoeffect and subsequently ionized [238] by electron impact. Both regimes are plausible and can cause the vibrant fragmentation observed in the present experiment.

Multiphoton ionization could create the observed fragmentation picture through ladder climbing or switching [37], but the direct laser-analyte interaction must be assumed here. Ionization can also occur through other channels, and the ionization potential of the experimental constituents could give a probability of such events. The ionization potential for silicon, ITO, and water is 8, 4.5, and 13 eV, respectively [239], [240], [241], but it is difficult to distinguish for bradykinin. However, the ionization

threshold energy for peptides with a mass of 1 kDa is around 8 eV [242]. The sudden onset of the bradykinin signal as a function of pulse energy does not support the idea that single-photon ionization is prominent. Unfortunately, the energy window with a bradykinin signal is too narrow to quantitatively infer the number of photons involved by sweeping over large intensity changes (Appendix, **Figure A 11** and **Figure A 12**). Nevertheless, the sudden onset of 1 kDa peptide signal after reaching an ionization threshold would, on its own, call for multiphoton ionization to be a candidate to overcome the energy barrier and therefore play an essential role in signal onset either through direct or indirect interaction with the analyte, water, or the substrate.

Another path to desorption and ionization is through laser-induced plasma formation. Fluences above  $1 \text{ J}\cdot\text{cm}^{-2}$  are known to cause plasma formation [200], [201], but in the present experiment, the employed pulse fluences had a similar value, which makes a clear distinction laborious. The analyte signal onset threshold was at  $5.7 \mu\text{J}$  pulse energy corresponding to  $0.9 \text{ J}\cdot\text{cm}^{-2}$  on silicon during ice sublimation (Appendix, **Figure A 11** and **Figure A 12**). The presented experimental data cannot answer whether plasma formation is the driving ablation and ionization pathway, but the vibrant fragmentation pattern observed in our experiment would call for such a condition.

The possible ionization pathways discussed above are possibly the main contributor to signal onset, or multiple phenomena simultaneously contribute to the observed mass spectra. The details of contributions from multiphoton, photoelectrons, or plasma formation to the ionization of bradykinin species and its fragments must be investigated in future studies and probably in tailored experiments.

Finally, non-resonant fs IR and UV pulses extracted endothelin I (2490 Da), which is sufficient for lipid extraction from tissue sections, but lags behind the report by Berry *et al.* showing mass limit up to 5800 Da. A possible explanation might be that specimen ablation was performed under cryogenic conditions and with much higher pulse energies. Higher pulse energies produce a larger number of ejected particles escorted by larger recoil formations [243]. Recoil formation is the product of indirect laser-matter interaction and carries larger amounts of material than the gaseous plume, which is considered more relevant for MS detection. The pulse energy might change the outcome, but due to the lack of high voltage deflection plates, small mass ions generated during the irradiation oversaturated the detector, reducing the analytical performance.

Fs pulses tuned to 1026 nm and 513 nm generated mass spectra of bradykinin species on different substrates under cryogenic conditions, while wavelength independence has been identified. Yet only film thickness below  $3 \mu\text{m}$  with a limitation to some regions, promote bradykinin onset. In a temperature-dependent

---

study, those regions enlarged prior to ice sublimation. After ice sublimation, a robust and stable analyte signal can be obtained throughout the thin film. As a vibrant fragmentation pattern occurs in the mass spectra compared to ns SALDI the assumption was made that additional ionization pathways can occur.

A conducted shot-to-shot repeatability of the bradykinin signal statistic showed a 90 % success rate for several samples. In addition, this method reveals superb sensitivity of about 25 amol and a mass limit of 2.5 kDa, making the ionization source a potential candidate for ultra-sensitive IMS.

The ion collection yield of a singly charged bradykinin species produced with fs pulses was determined using the beam waist diameter and the height of the thin film. The ionization probability is around  $10^{-5}$  and is comparable with UV-MALDI [76]. Successful extraction of organic molecules from pure water and toluene effectively renders the cryogenic non-resonant fs IR-LDI as a general analytical method. Due to the high ionization efficacy of non-resonant fs IR-LDI and the minimal sample preparation requirement, the method allows full automation and offers its use clinical environment, as sample pretreatment is minimum, allowing rapid analysis.

# 7 Outlook

- **Preamble**

The presented work investigated new frontiers in water-based MS to detect biological materials without any artificial matrix or additives. The goal was to create a simple yet effective method for ion generation with different IR lasers in aqueous solutions. This thesis developed two methods in which only water carried the molecules of interest. However, not all experiments were feasible in the laboratory due to various reasons. This chapter gives an overview of possible and interesting follow-up experiments.

- **DIVE MS with Cryogenic Thin Ice Films**

For the first time, an affordable and detailed sample preparation protocol is introduced for cryogenic MS, which allows sample preparation within minutes needed for a routine investigation of various specimens in water. This method is especially useful for biomolecules prone to acidic conditions tending to precipitate, such as recombinant proteins [244], can now be investigated under moderate conditions. Recombinant proteins are commonly used to produce pharmaceutical products, and therefore an analytical method capable of analyzing these species can facilitate medical research.

A recent publication concerned with IR-MALDESI used oversampling under ambient conditions, and was able to extract biomolecules from thin tissue sections [33]. We showed in this work that oversampling is superior to a single shot per spot mode for samples with 30  $\mu\text{m}$  thickness. Hence, an investigation of a tissue section with a similar thickness under low-pressure conditions would be interesting. It is also important to mention that during ice sublimation, the produced signal from a pure ice/water sample has the highest intensity, and accurate regulation of the sample stage temperature would facilitate the investigation of the specimen under optimal conditions.

Successful signal detection depends not only on laser parameter or sample preparation but also on the substrate used in the experiment. In this work, a silicon coverslip doped with phosphor was used. However, due to time constraints, additional IR transparent coverslips were not investigated, and in the future, silicon

---

---

coverslips with different dopants should be investigated to increase the IR-MALDI performance possibly.

• **Femtosecond Laser Mass Spectrometry**

The present work showed that fs pulses produce an array of fragments in a biomolecule, but whether different substrates can produce different dissociation was not investigated. In a future study, this question can be answered by the investigation of multiple substrates. A published work suggests that a low thermal conductivity might favor desorption processes in UV-MALDI [188], which sparks the idea of whether this might be a similar case for non-resonant fs IR-LDI.

To our best knowledge, fs laser tuned to water absorption maximum was not applied yet. If the laser is tuned to 3  $\mu\text{m}$ , the desorption process would be promoted, as a higher absorption coefficient would lead to more ejected material and, in combination with the high ionization efficacy, probably also to higher sensitivity. If such a laser system had been employed, a possible reduction down to several hundred femtoseconds (>500) in pulse duration might be necessary as high peak powers in combination with high absorption coefficient might produce a rich fragmentation pattern.

A publication dealing with SALDI MSI showed that surface molecules of a tissue section that was pressed and then removed from a substrate can be detected in high quality [51]. In this work, we showed that shortly before ice sublimation, a high-quality signal could be obtained, and as a consequence, a sufficiently thin ice layer seems to be suitable for the extraction of biomolecules. A tissue section not thicker than 1  $\mu\text{m}$  would be an interesting target for fs laser-based MS.



## 8 Bibliography

- [1] C. He, "Special Issue on Regulating the Central Dogma," *Biochemistry*, vol. 58, no. 5, pp. 295–296, 2019.
- [2] N. Slavov, "Single-cell protein analysis by mass spectrometry," *Curr. Opin. Chem. Biol.*, vol. 60, pp. 1–9, 2021.
- [3] J. M. Heather and B. Chain, "The sequence of sequencers: The history of sequencing DNA," *Genomics*, vol. 107, no. 1, pp. 1–8, 2016.
- [4] L. Zhang and A. Vertes, "Single-Cell Mass Spectrometry Approaches to Explore Cellular Heterogeneity," *Angew. Chemie - Int. Ed.*, vol. 57, no. 17, pp. 4466–4477, 2018.
- [5] S. J. Thomson, "LXXXIII. Rays of positive electricity," *London, Edinburgh, Dublin Philos. Mag. J. Sci.*, vol. 20, no. 118, pp. 752–767, 1910.
- [6] W. C. Wiley and I. H. McLaren, "Time-of-flight mass spectrometer with improved resolution," *Rev. Sci. Instrum.*, vol. 26, no. 12, pp. 1150–1157, 1955.
- [7] C. H. Townes, "Theodore H. Maiman (1927–2007)," *Nature*, vol. 447, no. 7145, pp. 654–654, 2007.
- [8] F. J. Vastola, R. O. Mumma, and A. J. Pirone, "Analysis of organic salts by laser ionization," *J. Mass Spectrom.*, vol. 3, no. 1, pp. 101–104, 1970.
- [9] T. Wang *et al.*, "Perspective on Advances in Laser-Based High-Resolution Mass Spectrometry Imaging," *Anal. Chem.*, vol. 92, no. 1, pp. 543–553, Jan. 2020.
- [10] J. Griffiths, "A Brief History of Mass Spectrometry," *Anal. Chem.*, vol. 80, no. 15, pp. 5678–5683, 2008.
- [11] M. Karas and F. Hillenkamp, "Laser Desorption Ionization of Proteins with Molecular Masses Exceeding 10 000 Daltons," *Anal. Chem.*, vol. 60, no. 20, pp. 2299–2301, 1988.
- [12] A. Overberg, M. Karas, F. Hillenkamp, and R. J. Cotter, "Matrix-assisted laser desorption of large biomolecules with a TEA-CO<sub>2</sub>-laser," *Rapid Commun. Mass Spectrom.*, vol. 5, no. 3, pp. 128–131, 1991.
- [13] C. V. Robinson, "John Fenn (1917-2010).," *Nature*, vol. 469, no. 7330, p. 300, 2011.
- [14] M. Niehaus and J. Soltwisch, "New insights into mechanisms of material ejection in MALDI mass spectrometry for a wide range of spot sizes," *Sci. Rep.*, vol. 8, no. 1, pp. 1–10, 2018.
- [15] J. L. Norris and R. M. Caprioli, "Analysis of Tissue Specimens by Matrix-Assisted Laser Desorption/Ionization Imaging Mass Spectrometry in Biological and Clinical Research," *Chem. Rev.*, vol. 113, no. 4, pp. 2309–2342, 2013.
- [16] F. E. Regnier and J. Kim, "Proteins and Proteoforms: New Separation Challenges," *Anal. Chem.*, vol. 90, no. 1, pp. 361–373, 2018.
- [17] E. H. Seeley and R. M. Caprioli, "MALDI imaging mass spectrometry of human tissue: Method challenges and clinical perspectives," *Trends Biotechnol.*, vol. 29, no. 3, pp. 136–143, 2011.
- [18] M. Niehaus, J. Soltwisch, M. E. Belov, and K. Dreisewerd, "Transmission-mode MALDI-2 mass spectrometry imaging of cells and tissues at subcellular resolution," *Nat. Methods*, vol. 16, no. 9, pp. 925–931, 2019.
- [19] A. J. Taylor, A. Dexter, and J. Bunch, "Exploring Ion Suppression in Mass Spectrometry Imaging of a Heterogeneous Tissue," *Anal. Chem.*, vol. 90, no. 9, pp. 5637–5645, 2018.
- [20] D. Veličković *et al.*, "Response Surface Methodology As a New Approach for Finding Optimal MALDI Matrix Spraying Parameters for Mass Spectrometry Imaging," *J. Am. Soc. Mass Spectrom.*, vol. 31, no. 3, pp. 508–516, 2020.
- [21] M. Kandiah and P. L. Urban, "Advances in ultrasensitive mass spectrometry of organic molecules," *Chem. Soc. Rev.*, vol. 42, no. 12, p. 5299, 2013.

- 
- [22] A. Smolira and J. Wessely-Szponder, "Importance of the Matrix and the Matrix/Sample Ratio in MALDI-TOF-MS Analysis of Cathelicidins Obtained from Porcine Neutrophils," *Appl. Biochem. Biotechnol.*, vol. 175, no. 4, pp. 2050–2065, 2015.
- [23] S. Laugesen and P. Roepstorff, "Combination of two matrices results in improved performance of MALDI MS for peptide mass mapping and protein analysis," *J. Am. Soc. Mass Spectrom.*, vol. 14, no. 9, pp. 992–1002, 2003.
- [24] M. Zellner *et al.*, "Quantitative validation of different protein precipitation methods in proteome analysis of blood platelets," *Electrophoresis*, vol. 26, no. 12, pp. 2481–2489, 2005.
- [25] A. Vogel and V. Venugopalan, "Mechanisms of Pulsed Laser Ablation of Biological Tissues," *Chem. Rev.*, 2003.
- [26] Y. Li, B. Shrestha, and A. Vertes, "Atmospheric pressure infrared MALDI imaging mass spectrometry for plant metabolomics," *Anal. Chem.*, vol. 80, no. 2, pp. 407–420, 2008.
- [27] A. Vertes, P. Nemes, B. Shrestha, A. A. Barton, Z. Chen, and Y. Li, "Molecular imaging by Mid-IR laser ablation mass spectrometry," *Appl. Phys. A*, vol. 93, no. 4, pp. 885–891, 2008.
- [28] B. Shrestha, P. Nemes, J. Nazarian, Y. Hathout, E. P. Hoffman, and A. Vertes, "Direct analysis of lipids and small metabolites in mouse brain tissue by AP IR-MALDI and reactive LAESI mass spectrometry," *Analyst*, vol. 135, no. 4, pp. 751–758, 2010.
- [29] V. V. Laiko *et al.*, "Desorption/ionization of biomolecules from aqueous solutions at atmospheric pressure using an infrared laser at 3  $\mu\text{m}$ ," *J. Am. Soc. Mass Spectrom.*, vol. 13, no. 4, pp. 354–361, 2002.
- [30] B. Fatou *et al.*, "Remote atmospheric pressure infrared matrix-assisted laser desorption-ionization mass spectrometry (remote IR-MALDI MS) of proteins," *Mol. Cell. Proteomics*, vol. 17, no. 8, pp. 1637–1649, 2018.
- [31] G. Robichaud, J. A. Barry, and D. C. Muddiman, "IR-MALDESI Mass Spectrometry Imaging of Biological Tissue Sections Using Ice as a Matrix," *J. Am. Soc. Mass Spectrom.*, vol. 25, no. 3, pp. 319–328, 2014.
- [32] M. Nazari and D. C. Muddiman, "MALDESI: Fundamentals, Direct Analysis, and MS Imaging," in *Advances in MALDI and Laser-Induced Soft Ionization Mass Spectrometry*, R. Cramer, Ed. Cham: Springer International Publishing, 2016, pp. 169–182.
- [33] M. Nazari and D. C. Muddiman, "Cellular-level mass spectrometry imaging using infrared matrix-assisted laser desorption electrospray ionization (IR-MALDESI) by oversampling," *Anal. Bioanal. Chem.*, vol. 407, no. 8, pp. 2265–2271, 2015.
- [34] M. T. Bokhart and D. C. Muddiman, "Infrared matrix-assisted laser desorption electrospray ionization mass spectrometry imaging analysis of biospecimens," *Analyst*, vol. 141, no. 18, pp. 5236–5245, 2016.
- [35] S. Berkenkamp, M. Karas, and F. Hillenkamp, "Ice as a matrix for IR-matrix-assisted laser desorption/ionization: mass spectra from a protein single crystal," *Proc. Natl. Acad. Sci. U. S. A.*, vol. 93, no. 14, pp. 7003–7, 1996.
- [36] A. Pirkel, J. Soltwisch, F. Draude, and K. Dreisewerd, "Infrared matrix-assisted laser desorption/ionization orthogonal-time-of-flight mass spectrometry employing a cooling stage and water ice as a matrix," *Anal. Chem.*, vol. 84, no. 13, pp. 5669–5676, 2012.
- [37] K. Franjic, "Studies of Laser Ablation of Liquid Water Under Conditions of Impulsive Heat Deposition Through Vibrational Excitations (IHDVE)," University of Toronto, 2010.
- [38] J. Zou, C. Wu, W. D. Robertson, L. V. Zhigilei, and R. J. D. D. Miller, "Molecular dynamics investigation of desorption and ion separation following picosecond infrared laser (PIRL) ablation of an ionic aqueous protein solution," *J. Chem. Phys.*, vol. 145, no. 20, p. 204202, 2016.
- [39] W. H. Müller, A. Verdin, E. De Pauw, C. Malherbe, and G. Eppe, "Surface-assisted laser desorption/ionization mass spectrometry imaging: A review," *Mass Spectrom. Rev.*, pp. 1–48, 2020.
- [40] S. A. Iakab *et al.*, "SALDI-MS and SERS Multimodal Imaging: One Nanostructured Substrate to Rule Them Both," *Anal. Chem.*, vol. 94, no. 6, pp. 2785–2793, 2022.
- [41] Y. F. Huang and H. T. Chang, "Nile red-adsorbed gold nanoparticle matrixes for determining aminothiols through surface-assisted laser desorption/ionization mass spectrometry," *Anal. Chem.*, vol. 78, no. 5, pp. 1485–1493, 2006.
- [42] S. F. Ren, L. Zhang, Z. H. Cheng, and Y. L. Guo, "Immobilized carbon nanotubes as matrix for MALDI-TOF-MS analysis: Applications to neutral small carbohydrates," *J. Am. Soc. Mass Spectrom.*, vol. 16, no. 3, pp. 333–339, 2005.
- [43] C. Y. Lo, J. Y. Lin, W. Y. Chen, C. T. Chen, and Y. C. Chen, "Surface-Assisted Laser Desorption/Ionization Mass Spectrometry on Titania Nanotube Arrays," *J. Am. Soc. Mass Spectrom.*, vol. 19, no. 7, pp. 1014–1020, 2008.
-

- [44] E. P. Go *et al.*, "Desorption/ionization on silicon nanowires," *Anal. Chem.*, vol. 77, no. 6, pp. 1641–1646, 2005.
- [45] W. Y. Chen and Y. C. Chen, "Reducing the alkali cation adductions of oligonucleotides using sol-gel-assisted laser desorption/ionization mass spectrometry," *Anal. Chem.*, vol. 75, no. 16, pp. 4223–4228, 2003.
- [46] S. Xu, Y. Li, H. Zou, J. Qiu, Z. Guo, and B. Guo, "Carbon Nanotubes as Assisted Matrix for Laser Desorption/Ionization Time-of-Flight Mass Spectrometry," *Anal. Chem.*, vol. 75, no. 22, pp. 6191–6195, 2003.
- [47] W. Y. Chen, L. S. Wang, H. T. Chiu, Y. C. Chen, and C. Y. Lee, "Carbon nanotubes as affinity probes for peptides and proteins in MALDI MS analysis," *J. Am. Soc. Mass Spectrom.*, vol. 15, no. 11, pp. 1629–1635, 2004.
- [48] R. Nayak and D. R. Knapp, "Matrix-free LDI mass spectrometry platform using patterned nanostructured gold thin film," *Anal. Chem.*, vol. 82, no. 18, pp. 7772–7778, 2010.
- [49] C.-K. Chiang, W.-T. Chen, and H.-T. Chang, "Nanoparticle-based mass spectrometry for the analysis of biomolecules," *Chem. Soc. Rev.*, vol. 40, no. 3, pp. 1269–1281, 2011.
- [50] Y. Gao *et al.*, "Single-cell elemental analysis via high irradiance femtosecond laser ionization time-of-flight mass spectrometry," *Anal. Chem.*, vol. 85, no. 9, pp. 4268–4272, 2013.
- [51] M. Ronci, D. Rudd, T. Guinan, K. Benkendorff, and N. H. Voelcker, "Mass spectrometry imaging on porous silicon: Investigating the distribution of bioactives in marine mollusc tissues," *Anal. Chem.*, vol. 84, no. 21, pp. 8996–9001, 2012.
- [52] A. V. Walker *et al.*, "Femtosecond laser desorption ionization mass spectrometry imaging and multivariate analysis of lipids in pancreatic tissue," *Biointerphases*, vol. 13, no. 3, p. 03B416, 2018.
- [53] J. I. Berry, S. Sun, Y. Dou, A. Wucher, and N. Winograd, "Laser desorption and imaging of proteins from ice via UV femtosecond laser pulses," *Anal. Chem.*, vol. 75, no. 19, pp. 5146–5151, 2003.
- [54] J. Zou *et al.*, "Ambient Mass Spectrometry Imaging with Picosecond Infrared Laser Ablation Electrospray Ionization (PIR-LAESI)," *Anal. Chem.*, vol. 87, no. 24, pp. 12071–12079, 2015.
- [55] C. E. Von Seggern, S. C. Moyer, and R. J. Cotter, "Liquid Infrared Atmospheric Pressure Matrix-Assisted Laser Desorption/Ionization Ion Trap Mass Spectrometry of Sialylated Carbohydrates," *Analytical Chemistry*, 2003.
- [56] J. J. Brady, E. J. Judge, and R. J. Levis, "Nonresonant femtosecond laser vaporization of aqueous protein preserves folded structure," *Proc. Natl. Acad. Sci. U. S. A.*, vol. 108, no. 30, pp. 12217–12222, 2011.
- [57] K. Franjic, R. J. D. Miller, and D. Miller, "Vibrationally excited ultrafast thermodynamic phase transitions at the water/air interface," *Phys. Chem. Chem. Phys.*, vol. 12, no. 20, pp. 5225–5239, 2010.
- [58] J. H. Gross, *Massenspektrometrie*, 1st ed. Berlin, Heidelberg: Springer Berlin Heidelberg, 2011.
- [59] L. Konermann, E. Ahadi, A. D. Rodriguez, and S. Vahidi, "Unraveling the Mechanism of Electrospray Ionization," *Anal. Biochem.*, no. 85, pp. 2–9, 2013.
- [60] Y. Zhang, B. R. Fonslow, B. Shan, M. C. Baek, and J. R. Yates, "Protein analysis by shotgun/bottom-up proteomics," *Chem. Rev.*, vol. 113, no. 4, pp. 2343–2394, 2013.
- [61] M. Beccaria and D. Cabooter, "Current developments in LC-MS for pharmaceutical analysis," *Analyst*, vol. 145, no. 4, pp. 1129–1157, 2020.
- [62] C. N. McEwen and B. S. Larsen, "Fifty years of desorption ionization of nonvolatile compounds," *Int. J. Mass Spectrom.*, vol. 377, no. 1, pp. 515–531, 2015.
- [63] A. J. Dempster, "A new Method of Positive Ray Analysis," *Phys. Rev.*, vol. 11, no. 4, pp. 316–325, 1918.
- [64] R. J. Cotter, "Laser Mass Spectrometry: An Overview of Techniques, Instruments and Applications," *Anal. Chim. Acta*, vol. 195, pp. 45–59, 1987.
- [65] F. Hillenkamp, R. C. Beavis, and T. Brian, "Matrix Assisted Laser Desorption/Ionization Mass Spectrometry of Biopolymers," *Anal. Chem.*, vol. 63, no. 24, 1991.
- [66] J. Griffiths, "A brief history of mass spectrometry," *Anal. Chem.*, vol. 80, no. 15, pp. 5678–5683, 2008.
- [67] M. R. Wilkins *et al.*, "Progress with proteome projects: Why all proteins expressed by a genome should be identified and how to do it," *Biotechnol. Genet. Eng. Rev.*, vol. 13, no. 1, pp. 19–50, 1996.
- [68] M. Niehaus and J. Soltwisch, "New insights into mechanisms of material ejection in MALDI mass spectrometry for a wide range of spot sizes," *Sci. Rep.*, vol. 8, p. 7755, 2018.
- [69] T. W. Jaskolla and M. Karas, "Compelling Evidence for Lucky Survivor and Gas Phase Protonation: The Unified MALDI Analyte Protonation Mechanism," *J. Am. Soc. Mass Spectrom.*, vol. 22, no. 6, pp. 976–988, 2011.

- 
- [70] J. Soltwisch, T. W. Jaskolla, and K. Dreisewerd, "Color matters - Material ejection and ion yields in UV-MALDI mass spectrometry as a function of laser wavelength and laser fluence," *J. Am. Soc. Mass Spectrom.*, vol. 24, no. 10, pp. 1477–1488, 2013.
- [71] S. Trimpin *et al.*, "A mechanism for ionization of nonvolatile compounds in mass spectrometry: Considerations from MALDI and inlet ionization," *J. Am. Soc. Mass Spectrom.*, vol. 23, no. 10, pp. 1644–1660, 2012.
- [72] C. N. McEwen and B. S. Larsen, "Fifty years of desorption ionization of nonvolatile compounds," *Int. J. Mass Spectrom.*, vol. 377, pp. 515–531, 2015.
- [73] W. C. Chang *et al.*, "Matrix-assisted laser desorption/ionization (MALDI) mechanism revisited," *Anal. Chim. Acta*, vol. 582, no. 1, pp. 1–9, 2007.
- [74] M. Karas and R. Krüger, "Ion Formation in MALDI: The Cluster Ionization Mechanism," *Chem. Rev.*, vol. 103, no. 2, pp. 427–440, 2003.
- [75] S. P. Liang, I. C. Lu, S. T. Tsai, J. L. Chen, Y. T. Lee, and C. K. Ni, "Laser Pulse Width Dependence and Ionization Mechanism of Matrix-Assisted Laser Desorption/Ionization," *J. Am. Soc. Mass Spectrom.*, vol. 28, no. 10, pp. 2235–2245, 2017.
- [76] K. N. Robinson, R. T. Steven, A. M. Race, and J. Bunch, "The Influence of MS Imaging Parameters on UV-MALDI Desorption and Ion Yield," *J. Am. Soc. Mass Spectrom.*, vol. 30, no. 7, pp. 1284–1293, 2019.
- [77] M. Wiegmann, K. Dreisewerd, and J. Soltwisch, "Influence of the Laser Spot Size, Focal Beam Profile, and Tissue Type on the Lipid Signals Obtained by MALDI-MS Imaging in Oversampling Mode," *J. Am. Soc. Mass Spectrom.*, vol. 27, no. 12, pp. 1952–1964, 2016.
- [78] L. V. Zhigilei and B. J. Garrison, "Microscopic mechanisms of laser ablation of organic solids in the thermal and stress confinement irradiation regimes," *J. Appl. Phys.*, vol. 88, no. 3, pp. 1281–1298, 2000.
- [79] J. H. Moon, Y. S. Shin, Y. J. Bae, and M. S. Kim, "Ion Yields for Some Salts in MALDI: Mechanism for the Gas-Phase Ion Formation from Preformed Ions," *J. Am. Soc. Mass Spectrom.*, vol. 23, no. 1, pp. 162–170, 2012.
- [80] H. Hu and R. G. Larson, "Marangoni effect reverses coffee-ring depositions," *J. Phys. Chem. B*, vol. 110, no. 14, pp. 7090–7094, 2006.
- [81] A. Bencsura, V. Navale, M. Sadeghi, and A. Vertes, "Matrix-guest energy transfer in matrix-assisted laser desorption," *Rapid Commun. Mass Spectrom.*, vol. 11, no. 6, pp. 679–682, 1997.
- [82] R. E. Johnson, "Models for matrix-assisted desorption by a laser-pulse," *Int. J. Mass Spectrom. Ion Process.*, vol. 139, no. C, pp. 25–38, 1994.
- [83] J. H. Brannon, J. R. Lankard, A. I. Baise, F. Burns, and J. Kaufman, "Excimer laser etching of polyimide," *J. Appl. Phys.*, vol. 58, no. 5, pp. 2036–2043, 1985.
- [84] L. V. Zhigilei and B. J. Garrison, "Microscopic mechanisms of laser ablation of organic solids in the thermal and stress confinement irradiation regimes," *J. Appl. Phys.*, vol. 88, no. 3, pp. 1281–1298, 2000.
- [85] A. Wortmann, T. Pimenova, S. Alves, and R. Zenobi, "Investigation of the first shot phenomenon in MALDI mass spectrometry of protein complexes," *Analyst*, vol. 132, no. 3, pp. 199–207, 2007.
- [86] R. Zenobi and R. Knochenmuss, "Ion formation in maldi mass spectrometry," *Mass Spectrom. Rev.*, vol. 17, no. 5, pp. 337–366, 1998.
- [87] R. Knochenmuss and R. Zenobi, "MALDI Ionization: The Role of In-Plume Processes," *Chem. Rev.*, vol. 103, no. 2, pp. 441–452, 2003.
- [88] R. Knochenmuss, "Ion formation mechanisms in UV-MALDI," *Analyst*, vol. 131, no. 9, pp. 966–986, 2006.
- [89] R. Knochenmuss, "Ion Yields in the Coupled Chemical and Physical Dynamics Model of Matrix-Assisted Laser Desorption/Ionization," *J. Am. Soc. Mass Spectrom.*, vol. 26, no. 10, pp. 1645–1648, 2015.
- [90] R. Knochenmuss, "MALDI ionization mechanisms: the coupled photophysical and chemical dynamics model correctly predicts 'temperature'-selected spectra," *J. Mass Spectrom.*, vol. 48, no. 9, pp. 998–1004, 2013.
- [91] M. Karas, M. Glückmann, and J. Schäfer, "Ionization in matrix-assisted laser desorption/ionization: singly charged molecular ions are the lucky survivors," *J. Mass Spectrom.*, vol. 35, no. 1, pp. 1–12, 2000.
- [92] Y. J. Bae, K. M. Park, and M. S. Kim, "Reproducibility of temperature-selected mass spectra in matrix-assisted laser desorption ionization of peptides," *Anal. Chem.*, vol. 84, no. 16, pp. 7107–7111, 2012.
-

- [93] Y. J. Bae, J. H. Moon, and M. S. Kim, "Expansion Cooling in the Matrix Plume is Under-Recognized in MALDI Mass Spectrometry," *J. Am. Soc. Mass Spectrom.*, vol. 22, no. 6, pp. 1070–1078, 2011.
- [94] R. Knochenmuss, "Energetics and Kinetics of Thermal Ionization Models of MALDI," *J. Am. Soc. Mass Spectrom.*, vol. 25, no. 9, pp. 1521–1527, 2014.
- [95] K. Dreisewerd, "The Desorption Process in MALDI," *Chem. Rev.*, vol. 103, no. 2, pp. 395–426, 2003.
- [96] A. A. Poretzky, D. B. Geohegan, G. B. Hurst, M. V. Buchanan, and B. S. Luk'yanchuk, "Imaging of Vapor Plumes Produced by Matrix Assisted Laser Desorption: A Plume Sharpening Effect," *Phys. Rev. Lett.*, vol. 83, no. 2, pp. 444–447, 1999.
- [97] F. Hillenkamp, *Laser Induced Ion Formation from Organic Solids (Review)*. Springer Berlin Heidelberg, 1983.
- [98] D. Fenyó, Q. Wang, J. A. DeGrasse, J. C. Padovan, M. Cadene, and B. T. Chait, "MALDI sample preparation: The ultra thin layer method," *J. Vis. Exp.*, no. 3, pp. 2–3, 2007.
- [99] C. Focsa *et al.*, "Wavelength-selective vibrationally excited photodesorption with tunable IR sources," *J. Phys. Condens. Matter*, vol. 18, no. 30, 2006.
- [100] P. Kraft, S. Alimpiev, E. Dratz, and J. Sunner, "Infrared, surface-assisted laser desorption ionization mass spectrometry on frozen aqueous solutions of proteins and peptides using suspensions of organic solids," *J. Am. Soc. Mass Spectrom.*, vol. 9, no. 9, pp. 912–924, 1998.
- [101] A. Koch, A. Schnapp, J. Soltwisch, and K. Dreisewerd, "Generation of multiply charged peptides and proteins from glycerol-based matrices using lasers with ultraviolet, visible and near-infrared wavelengths and an atmospheric pressure ion source," *Int. J. Mass Spectrom.*, vol. 416, pp. 61–70, 2017.
- [102] L. Witt *et al.*, "Water Ice is a Soft Matrix for the Structural Characterization of Glycosaminoglycans by Infrared Matrix-Assisted Laser Desorption/Ionization," *Anal. Chem.*, vol. 86, no. 13, pp. 6439–6446, 2014.
- [103] J. Zou, C. Wu, W. D. Robertson, L. V. Zhigilei, and R. J. D. Miller, "Molecular dynamics investigation of desorption and ion separation following picosecond infrared laser (PIRL) ablation of an ionic aqueous protein solution," *J. Chem. Phys.*, vol. 145, no. 20, 2016.
- [104] S. J. Linke *et al.*, "A new technology for applanation free corneal trephination: The picosecond infrared laser (PIRL)," *PLoS One*, vol. 10, no. 3, pp. 1–12, 2015.
- [105] M. Kwiatkowski *et al.*, "Homogenization of tissues via picosecond-infrared laser (PIRL) ablation: Giving a closer view on the in-vivo composition of protein species as compared to mechanical homogenization," *J. Proteomics*, vol. 134, pp. 193–202, 2016.
- [106] M. Kwiatkowski *et al.*, "Ultrafast extraction of proteins from tissues using desorption by impulsive vibrational excitation," *Angew. Chemie - Int. Ed.*, vol. 54, no. 1, pp. 285–288, 2015.
- [107] A. Krutilin *et al.*, "Sampling of Tissues with Laser Ablation for Proteomics: Comparison of Picosecond Infrared Laser (PIRL) and Microsecond Infrared Laser (MIRL)," *J. Proteome Res.*, vol. 18, pp. 1451–1457, 2019.
- [108] S. Amini-Nik *et al.*, "Ultrafast mid-IR laser scalpel: Protein signals of the fundamental limits to minimally invasive surgery," *PLoS One*, vol. 5, no. 9, pp. 1–6, 2010.
- [109] F. A. M. G. van Geenen, F. W. Claassen, M. C. R. Franssen, H. Zuilhof, and M. W. F. Nielen, "Laser Ablation Electrospray Ionization Hydrogen/Deuterium Exchange Ambient Mass Spectrometry Imaging," *J. Am. Soc. Mass Spectrom.*, vol. 31, no. 2, pp. 249–256, 2020.
- [110] J. Zou *et al.*, "Molecular dynamics investigation of desorption and ion separation following picosecond infrared laser (PIRL) ablation of an ionic aqueous protein solution Molecular dynamics investigation of desorption and ion separation following picosecond infrared la," vol. 204202, no. 2016, 2017.
- [111] R. A. Picca, C. D. Calvano, N. Cioffi, and F. Palmisano, "Mechanisms of nanophase-induced desorption in LDI-MS. A short review," *Nanomaterials*, vol. 7, p. 75, 2017.
- [112] Y. Coffinier and R. Boukherroub, "Porous silicon based mass spectrometry," *Handb. Porous Silicon Second Ed.*, vol. 2–2, pp. 1337–1353, 2018.
- [113] J. Wei, J. M. Buriak, and G. Siuzdak, "Desorption-ionization mass spectrometry on porous silicon," *Nature*, vol. 399, no. 6733, pp. 243–246, 1999.
- [114] Z. Shen *et al.*, "Porous silicon as a versatile platform for laser desorption/ionization mass spectrometry," *Anal. Chem.*, vol. 73, no. 3, pp. 612–619, 2001.

- 
- [115] J. J. Thomas, Z. Shen, J. E. Crowell, M. G. Finn, and G. Siuzdak, "Desorption/ionization on silicon (DIOS): A diverse mass spectrometry platform for protein characterization," *Proc. Natl. Acad. Sci. U. S. A.*, vol. 98, no. 9, pp. 4932–4937, 2001.
- [116] Q. Liu, Z. Guo, and L. He, "Mass spectrometry imaging of small molecules using desorption/ionization on silicon," *Anal. Chem.*, vol. 79, no. 10, pp. 3535–3541, 2007.
- [117] S. H. Bhattacharya, T. J. Raiford, and K. K. Murray, "Infrared Laser Desorption/Ionization on Silicon," *Anal. Chem.*, vol. 74, no. 9, pp. 2228–2231, 2002.
- [118] J. Wei, J. M. Buriak, and G. Siuzdak, "Desorption – ionization mass spectrometry on porous silicon," *Nature*, vol. 399, no. May, pp. 243–246, 1999.
- [119] T. Kobayashi, T. Kato, Y. Matsuo, M. Kurata-Nishimura, Y. Hayashizaki, and J. Kawai, "Wavelength-dependent fragmentation and clustering observed after femtosecond laser ablation of solid C60," *J. Chem. Phys.*, vol. 127, no. 11, 2007.
- [120] T. Kobayashi, T. Kato, Y. Matsuo, M. Kurata-Nishimura, J. Kawai, and Y. Hayashizaki, "Ionization and fragmentation of solid C60 by femtosecond laser ablation," *J. Chem. Phys.*, vol. 126, no. 6, pp. 10–13, 2007.
- [121] M. V. Shugaev *et al.*, "Fundamentals of ultrafast laser-material interaction," *MRS Bull.*, vol. 41, no. 12, pp. 960–968, 2016.
- [122] V. S. Antonov, I. N. Knyazev, V. S. Letokhov, V. M. Matiuk, V. G. Movshev, and V. K. Potapov, "Stepwise laser photoionization of molecules in a mass spectrometer: a new method for probing and detection of polyatomic molecules," *Opt. Lett.*, vol. 3, no. 2, p. 37, 1978.
- [123] D. M. Lubman and M. N. Kronlck, "Mass Spectrometry of Aromatic Molecules with Resonance-Enhanced Multiphoton Ionization," *Anal. Chem.*, vol. 54, no. 4, pp. 660–665, 1982.
- [124] D. E. Spence, P. N. Kean, and W. Sibbett, "60-fsec pulse generation from a self-mode-locked Ti : sapphire laser," vol. 16, no. 1, pp. 42–44, 1991.
- [125] K. W. D. Ledingham and R. P. Singhal, "High intensity laser mass spectrometry — a review," *Int. J. Mass Spectrom. Ion Process.*, vol. 163, no. 3, pp. 149–168, May 1997.
- [126] T. Streibel and R. Zimmermann, "Resonance-enhanced multiphoton ionization mass spectrometry (REMPI-ms): Applications for process analysis," *Annu. Rev. Anal. Chem.*, vol. 7, pp. 361–381, 2014.
- [127] F. Shi, P. M. Flanigan, J. J. Archer, and R. J. Levis, "Direct Analysis of Intact Biological Macromolecules by Low-Energy, Fiber-Based Femtosecond Laser Vaporization at 1042 nm Wavelength with Nanospray Postionization Mass Spectrometry," *Anal. Chem.*, vol. 87, no. 6, pp. 3187–3194, 2015.
- [128] Y. Coello *et al.*, "Atmospheric Pressure Femtosecond Laser Imaging Mass Spectrometry," *Anal. Chem.*, vol. 82, no. 7, pp. 2753–2758, 2010.
- [129] E. J. Judge, J. J. Brady, and R. J. Levis, "Mass Analysis of Biological Macromolecules at Atmospheric Pressure Using Nonresonant Femtosecond Laser Vaporization and Electrospray Ionization," *Anal. Chem.*, vol. 82, no. 24, pp. 10203–10207, 2010.
- [130] P. M. Flanigan, L. L. Radell, J. J. Brady, and R. J. Levis, "Differentiation of eight phenotypes and discovery of potential biomarkers for a single plant organ class using laser electrospray mass spectrometry and multivariate statistical analysis," *Anal. Chem.*, vol. 84, no. 14, pp. 6225–6232, 2012.
- [131] E. J. Judge, J. J. Brady, P. E. Barbano, and R. J. Levis, "Nonresonant femtosecond laser vaporization with electrospray postionization for ex vivo plant tissue typing using compressive linear classification," *Anal. Chem.*, vol. 83, no. 6, pp. 2145–2151, 2011.
- [132] H. Kragh, "To be or not to be: The early history of H3 and H3+," *Philos. Trans. R. Soc. A Math. Phys. Eng. Sci.*, vol. 370, no. 1978, pp. 5225–5235, 2012.
- [133] R. D. Macfarlane, "Californium-252 Plasma Desorption Mass Spectrometry," *Anal. Chem.*, vol. 191, no. 12, pp. 1247A–1250A, 1983.
- [134] A. Benninghoven and D. Jaspers, "Secondary-ion Emission of Amino Acids," *Appl. Phys. A*, vol. 39, pp. 35–39, 1976.
- [135] F. Lanucara, S. W. Holman, C. J. Gray, and C. E. Eyers, "The power of ion mobility-mass spectrometry for structural characterization and the study of conformational dynamics," *Nat. Chem.*, vol. 6, no. 4, pp. 281–294, 2014.
-

- [136] N. Iwamoto and T. Shimada, "Recent advances in mass spectrometry-based approaches for proteomics and biologics: Great contribution for developing therapeutic antibodies," *Pharmacol. Ther.*, vol. 185, no. December 2017, pp. 147–154, 2018.
- [137] K. Wiangnon and R. Cramer, "Sample Preparation: A Crucial Factor for the Analytical Performance of Rationally Designed MALDI Matrices," *Anal. Chem.*, vol. 87, no. 3, pp. 1485–1488, 2015.
- [138] F. T. Zohora, M. Z. Rahman, N. H. Tran, L. Xin, B. Shan, and M. Li, "DeepIso: A Deep Learning Model for Peptide Feature Detection from LC-MS map," *Sci. Rep.*, vol. 9, no. 1, pp. 1–13, 2019.
- [139] R. Aebersold and M. Mann, "Mass spectrometry-based proteomics: Abstract: Nature," *Nature*, vol. 422, no. 6928, pp. 198–207, 2003.
- [140] A. Glaynel, "MassSpec Repository," *GitHub*, 2020. <https://github.com/galejo09/massspec>
- [141] W. C. Wiley and I. H. McLaren, "Time-of-Flight Mass Spectrometer with Improved Resolution," *Rev. Sci. Instrum.*, vol. 26, no. 12, pp. 1150–1157, 1955.
- [142] A. G. Brenton and A. R. Godfrey, "Accurate mass measurement: Terminology and treatment of data," *J. Am. Soc. Mass Spectrom.*, vol. 21, no. 11, pp. 1821–1835, 2010.
- [143] M. L. Gross, "Accurate masses for structure confirmation," *J. Am. Soc. Mass Spectrom.*, vol. 5, no. 2, p. 57, 1994.
- [144] C. A. Hack and W. H. Benner, "A simple algorithm improves mass accuracy to 50-100 ppm for delayed extraction linear matrix-assisted laser desorption/ionization time-of-flight mass spectrometry," *Rapid Commun. Mass Spectrom.*, vol. 16, no. 13, pp. 1304–1312, 2002.
- [145] Robert J. Cotter, *Time-of-flight mass spectrometry: Instrumentation and applications in biological research*, vol. 1. Washington, DC: The American Society, 1997.
- [146] M. Schürenberg, T. Schulz, K. Dreisewerd, and F. Hillenkamp, "Matrix-assisted Laser Desorption/Ionization in Transmission Geometry: Instrumental Implementation and Mechanistic Implications," *Rapid Commun. Mass Spectrom.*, vol. 10, no. 15, pp. 1873–1880, 1996.
- [147] R. Liu, Q. Li, and L. M. Smith, "Detection of large ions in time-of-flight mass spectrometry: Effects of ion mass and acceleration voltage on microchannel plate detector response," *J. Am. Soc. Mass Spectrom.*, vol. 25, no. 8, pp. 1374–1383, 2014.
- [148] S. Deepaisarn, P. D. Tar, N. A. Thacker, A. Seepujak, and A. W. McMahon, "Quantifying biological samples using Linear Poisson Independent Component Analysis for MALDI-ToF mass spectra," *Bioinformatics*, vol. 34, no. 6, pp. 1001–1008, 2018.
- [149] N. A. Thacker, P. D. Tar, A. P. Seepujak, and J. D. Gilmour, "The statistical properties of raw and preprocessed ToF mass spectra," *Int. J. Mass Spectrom.*, vol. 428, pp. 62–70, 2018.
- [150] A. Krutilin and G. Alejo, "Ion Count Analysis," *Ion Count Analysis*, 2021.
- [151] R. T. Steven and J. Bunch, "Repeat MALDI MS imaging of a single tissue section using multiple matrices and tissue washes," *Anal. Bioanal. Chem.*, vol. 405, no. 14, pp. 4719–4728, 2013.
- [152] E. U. Brockmann, A. Pottho, S. Tortorella, J. Soltwisch, and K. Dreisewerd, "Infrared MALDI Mass Spectrometry with Laser-Induced Postionization for Imaging of Bacterial Colonies," *J. Am. Soc. Mass Spectrom.*, , no. 32, pp. 1053–1064, 2021.
- [153] P. Nemes, and A. Vertes, "Laser ablation electrospray ionization for atmospheric pressure, in vivo, and imaging mass spectrometry," *Anal. Chem.*, vol. 79, no. 21, pp. 8098–8106, 2007.
- [154] K. K. Murray, "Infrared matrix-assisted laser desorption/ionization using a frozen alcohol matrix," *J. Mass Spectrom.*, no. 35, pp. 95–97, 2000.
- [155] P. Williams, "Time of flight mass spectrometry of DNA laser-ablated from frozen aqueous solutions: applications to the Human Genome Project," *Int. J. Mass Spectrom. Ion Process.*, vol. 131, pp. 335–344, 1994.
- [156] D. M. Schieltz, C.-W. Chou, C.-W. Luo, R. M. Thomas, P. Williams, and C. H. Becker, "Mass spectrometry of DNA mixtures by laser ablation from frozen aqueous solution," *Rapid Commun. Mass Spectrom.*, vol. 6, no. 10, pp. 631–636, 1992.
- [157] R. W. Nelson, R. M. Thomas, and P. Williams, "Time-of-flight mass spectrometry of nucleic acids by laser ablation and ionization from a frozen aqueous matrix," *Rapid Commun. Mass Spectrom.*, vol. 4, no. 9, pp. 348–351, 1990.

- 
- [158] M. Baltz-Knorr *et al.*, "Infrared laser desorption and ionization of polypeptides from a polyacrylamide gel," *J. Mass Spectrom.*, vol. 37, no. 3, pp. 254–258, 2002.
- [159] S. Berkenkamp, C. Menzel, F. Hillenkamp, and K. Dreisewerd, "Measurements of Mean Initial Velocities of Analyte and Matrix Ions in Infrared Matrix-Assisted Laser Desorption Ionization Mass Spectrometry" *J. Am. Soc. Mass Spectrom.*, no. 13, pp. 209–220, 2002.
- [160] S. Berkenkamp, C. Menzel, M. Karas, and F. Hillenkamp, "Performance of Infrared Matrix-assisted Laser Desorption/Ionization Mass Spectrometry with Lasers Emitting in the 3  $\mu$ m Wavelength Range," *Rapid Commun. Mass Spectrom.*, vol. 11, no. 13, pp. 1399–1406, 1997.
- [161] D. Hildebrand, P. Merkel, L. F. Eggers, and H. Schlueter, "Proteolytic Processing of Angiotensin-I in Human Blood Plasma," *PLoS One*, vol. 8, no. 5, p. e64027, 2013.
- [162] L. Qiao *et al.*, "Electrostatic-spray ionization mass spectrometry," *Anal. Chem.*, vol. 84, no. 17, pp. 7422–7430, 2012.
- [163] J. A. Loo, P. Hu, and R. D. Smith, "Interaction of angiotensin peptides and zinc metal ions probed by electrospray ionization mass spectrometry," *J. Am. Soc. Mass Spectrom.*, vol. 5, no. 11, pp. 959–965, 1994.
- [164] K. Dreisewerd, "Recent methodological advances in MALDI mass spectrometry," *Anal. Bioanal. Chem.*, vol. 406, no. 9–10, pp. 2261–2278, 2014.
- [165] F. Busse, "Mechanisms of Picosecond Infrared Laser Desorption Ionization," 2019. [Online]. Available: <https://ediss.sub.uni-hamburg.de/handle/ediss/8292>
- [166] Y.-H. Cai and Y.-S. Wang, "Impact of uneven sample morphology on mass resolving power in linear MALDI-TOF mass spectrometry – a comprehensive theoretical investigation," *J. Mass Spectrom.*, no. October 2017, pp. 361–368, 2018.
- [167] A. Vertes, L. Balazs, and R. Gijbels, "Matrix-assisted laser desorption of peptides in transmission geometry," *Rapid Commun. Mass Spectrom.*, vol. 4, no. 7, pp. 263–266, 1990.
- [168] M. Schürenberg, T. Schulz, K. Dreisewerd, and F. Hillenkamp, "Matrix-assisted laser desorption/ionization in transmission geometry: Instrumental implementation and mechanistic implications," *Rapid Commun. Mass Spectrom.*, vol. 10, no. 15, pp. 1873–1880, 1996.
- [169] A. Zavalin, E. M. Todd, P. D. Rawhouser, J. Yang, J. L. Norris, and R. M. Caprioli, "Direct imaging of single cells and tissue at sub-cellular spatial resolution using transmission geometry MALDI MS," *J. Mass Spectrom.*, vol. 47, no. 11, pp. 1473–1481, Nov. 2012.
- [170] A. R. Buchberger, K. DeLaney, J. Johnson, and L. Li, "Mass Spectrometry Imaging: A Review of Emerging Advancements and Future Insights," *Anal. Chem.*, vol. 90, no. 1, pp. 240–265, 2018.
- [171] L. V. Zhigilei, "Dynamics of the plume formation and parameters of the ejected clusters in short-pulse laser ablation," *Appl. Phys. A Mater. Sci. Process.*, vol. 76, no. 3, pp. 339–350, 2003.
- [172] A. Leisner, A. Rohlfing, U. Röhling, K. Dreisewerd, and F. Hillenkamp, "Time-resolved imaging of the plume dynamics in infrared matrix-assisted laser desorption/ionization with a glycerol matrix," *J. Phys. Chem. B*, vol. 109, no. 23, pp. 11661–11666, 2005.
- [173] L. Diologent, G. Bolbach, C. Focsa, M. Ziskind, and I. Fournier, "Laser induced post-desolvation of MALDI clusters," *Int. J. Mass Spectrom.*, vol. 416, pp. 29–36, 2017.
- [174] M. L. Baltz-Knorr, K. E. Schriver, and R. F. Haglund, "Infrared laser ablation and ionization of water clusters and biomolecules from ice," *Appl. Surf. Sci.*, vol. 197–198, pp. 11–16, 2002.
- [175] K. Chughtai and R. M. A. Heeren, "Mass spectrometric imaging for biomedical tissue analysis," *Chem. Rev.*, vol. 110, no. 5, pp. 3237–3277, 2010.
- [176] K. Dreisewerd, S. Berkenkamp, A. Leisner, A. Rohlfing, and C. Menzel, "Fundamentals of matrix-assisted laser desorption / ionization mass spectrometry with pulsed infrared lasers," vol. 226, pp. 189–209, 2003.
- [177] K. L. Caldwell and K. K. Murray, "Mid-infrared matrix assisted laser desorption ionization with a water/glycerol matrix," *Appl. Surf. Sci.*, vol. 127–129, pp. 242–247, May 1998.
- [178] P. Kraft, S. Alimpiev, E. Dratz, and J. Sunner, "Infrared, surface-assisted laser desorption ionization mass spectrometry on frozen aqueous solutions of proteins and peptides using suspensions of organic solids," *J. Am. Soc. Mass Spectrom.*, vol. 9, no. 9, pp. 912–924, 1998.
-



- [179] C. Menzel, K. Dreisewerd, S. Berkenkamp, and F. Hillenkamp, "The role of the laser pulse duration in infrared matrix-assisted laser desorption/ionization mass spectrometry," *J Am Soc Mass Spectrom*, vol. 13, no. 8, pp. 975–984, 2002.
- [180] J. C. Hyun, H. M. Jeong, M. S. Kim, H. J. Cha, J. H. Moon, and M. S. Kim, "Resolution of infrared matrix-assisted laser desorption/ionization time-of-flight mass spectrometry using glycerol; enhancement with a disperse laser beam," *Rapid Commun. Mass Spectrom.*, vol. 21, no. 8, pp. 1468–1474, 2007.
- [181] P. Juhasz, M. L. Vestal, and S. A. Martin, "On the Initial Velocity of Ions Generated by Matrix-Assisted Laser Desorption Ionization and its Effect on the Calibration of Delayed Extraction Time-of-Flight Mass Spectra," *J. Am. Soc. Mass Spectrom.*, vol. 8, no. 96, pp. 209–217, 1997.
- [182] L. B. Lane, "Freezing Points of Glycerol and its Aqueous Solutions," *Ind. Eng. Chem.*, vol. 17, no. 9, p. 924, 1925.
- [183] C. Menzel, K. Dreisewerd, S. Berkenkamp, and F. Hillenkamp, "Mechanisms of energy deposition in infrared matrix-assisted laser desorption/ionization mass spectrometry," *Int. J. Mass Spectrom.*, vol. 207, no. 1, pp. 73–96, 2001.
- [184] C. Menzel, K. Dreisewerd, S. Berkenkamp, and F. Hillenkamp, "The role of the laser pulse duration in infrared matrix-assisted laser desorption/ionization mass spectrometry," *J Am Soc Mass Spectrom*, vol. 13, no. 8, pp. 975–984, 2002.
- [185] S. R. Ellis, J. Soltwisch, M. R. L. Paine, K. Dreisewerd, and R. M. A. Heeren, "Laser post-ionisation combined with a high resolving power orbitrap mass spectrometer for enhanced MALDI-MS imaging of lipids," *Chem. Commun.*, vol. 53, no. 53, pp. 7246–7249, 2017.
- [186] S. König, O. Kollas, and K. Dreisewerd, "Generation of highly charged peptide and protein ions by atmospheric pressure matrix-assisted infrared laser desorption/ionization ion trap mass spectrometry," *Anal. Chem.*, vol. 79, no. 14, pp. 5484–5488, 2007.
- [187] L. Kolářová *et al.*, "Clusters of Monoisotopic Elements for Calibration in (TOF) Mass Spectrometry," *J. Am. Soc. Mass Spectrom.*, vol. 28, no. 3, pp. 419–427, 2017.
- [188] G. P. Zeegers, B. F. Günthardt, and R. Zenobi, "Target Plate Material Influence on Fullerene-C60 Laser Desorption/Ionization Efficiency," *J. Am. Soc. Mass Spectrom.*, vol. 27, no. 4, pp. 699–708, 2016.
- [189] V. G. Artemov, E. Uykur, S. Roh, A. V. Pronin, H. Ouerdane, and M. Dressel, "Revealing excess protons in the infrared spectrum of liquid water," *Sci. Rep.*, vol. 10, no. 1, pp. 1–9, 2020.
- [190] W. G. Lewis, Z. Shen, M. G. Finn, and G. Siuzdak, "Desorption/ionization on silicon (DIOS) mass spectrometry: background and applications," *Int. J. Mass Spectrom.*, vol. 226, no. 1, pp. 107–116, 2003.
- [191] M. Rainer, M. N. Qureshi, and G. K. Bonn, "Matrix-free and material-enhanced laser desorption/ionization mass spectrometry for the analysis of low molecular weight compounds," *Anal. Bioanal. Chem.*, vol. 400, no. 8, pp. 2281–2288, 2011.
- [192] M. Aichler and A. Walch, "MALDI Imaging mass spectrometry: current frontiers and perspectives in pathology research and practice | Laboratory Investigation," *Lab. Investig.*, vol. 95, no. 4, pp. 422–431, 2015.
- [193] L. Morosi *et al.*, "Determination of Paclitaxel Distribution in Solid Tumors by Nano-Particle Assisted Laser Desorption Ionization Mass Spectrometry Imaging," *PLoS One*, vol. 8, no. 8, pp. 1–9, 2013.
- [194] S. W. Kim, S. Kwon, and Y. K. Kim, "Graphene oxide derivatives and their nanohybrid structures for laser desorption/ionization time-of-flight mass spectrometry analysis of small molecules," *Nanomaterials*, vol. 11, no. 2, pp. 1–19, 2021.
- [195] Y. K. Kim *et al.*, "Synergistic effect of graphene oxide/MWCNT films in laser desorption/ionization mass spectrometry of small molecules and tissue imaging," *ACS Nano*, vol. 5, no. 6, pp. 4550–4561, 2011.
- [196] Y. Cui, I. V. Veryovkin, M. W. Majeski, D. R. Cavazos, and L. Hanley, "High lateral resolution vs molecular preservation in near-IR fs-laser desorption postionization mass spectrometry," *Anal. Chem.*, vol. 87, no. 1, pp. 367–371, 2015.
- [197] R. Moser, M. Domke, J. Winter, H. P. Huber, and G. Marowsky, "Single pulse femtosecond laser ablation of silicon—a comparison between experimental and simulated two-dimensional ablation profiles," *Adv. Opt. Technol.*, vol. 7, no. 4, pp. 255–264, 2018.
- [198] P. P. Pronko, P. A. Van Rompay, C. Horvath, X. Liu, T. Juhasz, and G. Mourou, "Avalanche ionization and dielectric breakdown in silicon with ultrafast laser pulses," *Conf. Lasers Electro-Optics Eur. - Tech. Dig.*, vol. 58, no. 5, p. 511, 1998.
- [199] P. Allenspacher, B. Huettner, and W. Riede, "Ultrashort pulse damage of Si and Ge semiconductors," *Laser-Induced Damage Opt. Mater. 2002 7th Int. Work. Laser Beam Opt. Charact.*, vol. 4932, no. May 2003, p. 358, 2003.

- 
- [200] M. Hada *et al.*, "Cold ablation driven by localized forces in alkali halides," *Nat. Commun.*, vol. 5, pp. 1–8, 2014.
- [201] A. Cavalleri, K. Sokolowski-Tinten, J. Bialkowski, M. Schreiner, and D. von der Linde, "Femtosecond melting and ablation of semiconductors studied with time of flight mass spectroscopy," *J. Appl. Phys.*, vol. 85, no. 6, pp. 3301–3309, Mar. 1999.
- [202] J. Bonse, S. Baudach, J. Krüger, W. Kautek, and M. Lenzner, "Femtosecond laser ablation of silicon-modification thresholds and morphology," *Appl. Phys. A Mater. Sci. Process.*, vol. 74, no. 1, pp. 19–25, 2002.
- [203] K. Werner *et al.*, "Single-Shot Multi-Stage Damage and Ablation of Silicon by Femtosecond Mid-infrared Laser Pulses," *Sci. Rep.*, vol. 9, no. 1, pp. 1–13, 2019.
- [204] C. L. Kalcic, T. C. Gunaratne, A. D. Jones, M. Dantus, and G. E. Reid, "Femtosecond laser-induced Ionization/dissociation of protonated peptides," *J. Am. Chem. Soc.*, vol. 131, no. 3, pp. 940–942, 2009.
- [205] S. A. Raspopov, A. El-Faramawy, B. A. Thomson, and K. W. M. Siu, "Infrared multiphoton dissociation in quadrupole time-of-flight mass spectrometry: Top-down characterization of proteins," *Anal. Chem.*, vol. 78, no. 13, pp. 4572–4577, 2006.
- [206] J. S. B. and J. J. Wilson, "Infrared Multiphoton Dissociation in Quadrupole Ion Traps," *Mass Spectrom. Rev.*, vol. 28, pp. 390–424, 2009.
- [207] M. C. Crowe, J. S. Brodbelt, B. J. Goolsby, and P. Hergenrother, "Characterization of erythromycin analogs by collisional activated dissociation and infrared multiphoton dissociation in a quadrupole ion trap," *J. Am. Soc. Mass Spectrom.*, vol. 13, no. 6, pp. 630–649, 2002.
- [208] C. Brunet, R. Antoine, P. Dugourd, F. Canon, A. Giuliani, and L. Nahon, "Formation and fragmentation of radical peptide anions: Insights from vacuum ultra violet spectroscopy," *J. Am. Soc. Mass Spectrom.*, vol. 23, no. 2, pp. 274–281, 2012.
- [209] R. S. Johnson, S. A. Martin, K. Biemann, J. T. Stults, and J. T. Watson, "Novel Fragmentation Process of Peptides by Collision-Induced Decomposition in a Tandem Mass Spectrometer: Differentiation of Leucine and Isoleucine," *Anal. Chem.*, vol. 59, no. 21, pp. 2621–2625, 1987.
- [210] R. S. Johnson, S. A. Martin, and K. Biemann, "Collision-induced fragmentation of (M + H)<sup>+</sup> ions of peptides. Side chain specific sequence ions," *Int. J. Mass Spectrom. Ion Process.*, vol. 86, no. C, pp. 137–154, 1988.
- [211] S. G. Musharraf *et al.*, "Benzimidazole, coumrandione and flavone derivatives as alternate UV laser desorption ionization (LDI) matrices for peptides analysis," *Chem. Cent. J.*, vol. 7, no. 1, pp. 1–13, 2013.
- [212] G. J. Patti *et al.*, "Nanostructure-initiator mass spectrometry (NIMS) imaging of brain cholesterol metabolites in Smith-Lemli-Opitz syndrome," *Neuroscience*, vol. 170, no. 3, pp. 858–864, 2010.
- [213] X. Lou, J. L. J. van Dongen, and E. W. Meijer, "Generation of csi cluster ions for mass calibration in matrix-assisted laser desorption/ionization mass spectrometry," *J. Am. Soc. Mass Spectrom.*, vol. 21, no. 7, pp. 1223–1226, 2010.
- [214] J. de Vries *et al.*, "Single-photon ionization of C60- and C70-fullerene with synchrotron radiation: determination of the ionization potential of C60," *Chem. Phys. Lett.*, vol. 188, no. 3–4, pp. 159–162, 1992.
- [215] L. S. Wang, J. Conceicao, C. Jin, and R. E. Smalley, "Threshold photodetachment of cold C-60," *Chem. Phys. Lett.*, vol. 182, no. 1, pp. 5–11, 1991.
- [216] C. and R. E. S. S.H. Yang, C.L. Pettiette, J. Conceicao, "UPS Of Buckminsterfullerenes and Other Large Cluster of Carbon," *Chem. Phys. Lett.*, vol. 139, no. 3, pp. 233–238, 1987.
- [217] K. R. Lykke and P. Wurz, "Direct detection of neutral products from photodissociated C60," *J. Phys. Chem.*, vol. 96, no. 8, pp. 3191–3193, 1992.
- [218] E. E. B. Campbell, G. Ulmer, and I. V. Hertel, "Delayed ionization of C60 and C70," *Phys. Rev. Lett.*, vol. 67, no. 15, pp. 1986–1988, 1991.
- [219] T. E. Saraswati, U. H. Setiawan, M. R. Ihsan, I. Isnaeni, and Y. Herbani, "The Study of the Optical Properties of C60 Fullerene in Different Organic Solvents," *Open Chem.*, vol. 17, no. 1, pp. 1198–1212, 2020.
- [220] C. V. Iancu *et al.*, "Electron cryotomography sample preparation using the Vitrobot," *Nat. Protoc.*, vol. 1, no. 6, pp. 2813–2819, 2007.
- [221] R. Knochenmuss, "MALDI mechanisms: wavelength and matrix dependence of the coupled photophysical and chemical dynamics model," *Analyst*, vol. 139, no. 1, pp. 147–156, 2014.
-

- [222] M. C. Crowe and J. S. Brodbelt, "Infrared multiphoton dissociation (IRMPD) and collisionally activated dissociation of peptides in a quadrupole ion trap with selective IRMPD of phosphopeptides," *J. Am. Soc. Mass Spectrom.*, vol. 15, no. 11, pp. 1581–1592, 2004.
- [223] M. Ichikawa, "Infrared Spectra Of Penetration Depth Into Water And Of Water Refraction-Index," *Infrared Technol. XV*, vol. 1157, no. January 1990, p. 318, 1990.
- [224] A. Zavalin, J. Yang, K. Hayden, M. Vestal, and R. M. Caprioli, "Tissue protein imaging at 1  $\mu\text{m}$  laser spot diameter for high spatial resolution and high imaging speed using transmission geometry MALDI TOF MS," *Anal. Bioanal. Chem.*, vol. 407, no. 8, pp. 2337–2342, 2015.
- [225] V. L. Talrose, M. D. Person, R. M. Whittal, F. C. Walls, A. L. Burlingame, and M. A. Baldwin, "Insight into absorption of radiation/energy transfer in infrared matrix-assisted laser desorption/ionization: the roles of matrices, water and metal substrates†," *Rapid Commun. Mass Spectrom.*, vol. 13, no. 21, pp. 2191–2198, 1999.
- [226] J. J. Towey and L. Dougan, "Structural examination of the impact of glycerol on water structure," *J. Phys. Chem. B*, vol. 116, no. 5, pp. 1633–1641, 2012.
- [227] Y. Coello, A. D. Jones, T. C. Gunaratne, and M. Dantus, "Atmospheric Pressure Femtosecond Laser Imaging Mass Spectrometry," *Anal. Chem.*, vol. 82, no. 7, pp. 2753–2758, 2010.
- [228] Adan Li, "Suppression of fragmentation in multiphoton ionization mass spectrometry using a near-infrared femtosecond laser as ionization source," *Analyst*, vol. 142, p. 3942, 2017.
- [229] R. C. Wickramasinghe *et al.*, "Femtosecond Laser Desorption Postionization MS vs ToF-SIMS Imaging for Uncovering Biomarkers Buried in Geological Samples," *Anal. Chem.*, vol. 93, no. 48, pp. 15949–15957, 2021.
- [230] O. Samek, V. Margetic, N. Von Wirén, A. Michels, K. Niemax, and R. Hergenröder, "Femtosecond laser analytical mass spectrometry applied to plant samples," *Appl. Phys. A Mater. Sci. Process.*, vol. 79, no. 4–6, pp. 957–960, 2004.
- [231] T. Kato *et al.*, "Comparison between femtosecond and nanosecond laser ablation of solution samples applied on a substrate," *J. Phys. Conf. Ser.*, vol. 59, no. 1, pp. 372–375, 2007.
- [232] A. V. Bulgakov, I. Ozerov, and W. Marine, "Cluster emission under femtosecond laser ablation of silicon," *Thin Solid Films*, vol. 453–454, pp. 557–561, 2004.
- [233] B. N. Chichkov, C. Momma, S. Nolte, F. von Alvensleben, and A. Tünnermann, "Femtosecond, picosecond and nanosecond laser ablation of solids," *Appl. Phys. A Mater. Sci. Process.*, vol. 63, no. 2, pp. 109–115, 1996.
- [234] B. Zhang, M. He, W. Hang, and B. Huang, "Minimizing matrix effect by femtosecond laser ablation and ionization in elemental determination," *Anal. Chem.*, vol. 85, no. 9, pp. 4507–4511, 2013.
- [235] X. Zeng, X. L. Mao, R. Greif, and R. E. Russo, "Experimental investigation of ablation efficiency and plasma expansion during femtosecond and nanosecond laser ablation of silicon," *Appl. Phys. A*, vol. 80, no. 2, pp. 237–241, 2005.
- [236] K. H. Leitz, B. Redlingshöer, Y. Reg, A. Otto, and M. Schmidt, "Metal ablation with short and ultrashort laser pulses," *Phys. Procedia*, vol. 12, pp. 230–238, 2011.
- [237] M. Tulej *et al.*, "Current progress in femtosecond laser ablation/ionisation time-of-flight mass spectrometry," *Appl. Sci.*, vol. 11, no. 6, 2021.
- [238] G. M. Petrov, A. Davidson, D. Gordon, B. Hafizi, and J. Peñano, "Thermionic emission of electrons from metal surfaces in the warm dense matter regime," *Phys. Plasmas*, vol. 28, no. 8, 2021.
- [239] O. Kostko, S. R. Leone, M. A. Duncan, and M. Ahmed, "Determination of ionization energies of small silicon clusters with vacuum ultraviolet radiation," *J. Phys. Chem. A*, vol. 114, no. 9, pp. 3176–3181, 2010.
- [240] K. B. Snow and T. F. Thomas, "Mass spectrum, ionization potential, and appearance potentials for fragment ions of sulfuric acid vapor," *Int. J. Mass Spectrom. Ion Process.*, vol. 96, no. 1, pp. 49–68, 1990.
- [241] T. Fukano, T. Motohiro, T. Ida, and H. Hashizume, "Ionization potentials of transparent conductive indium tin oxide films covered with a single layer of fluorine-doped tin oxide nanoparticles grown by spray pyrolysis deposition," *J. Appl. Phys.*, vol. 97, no. 8, p. 084314, 2005.
- [242] W. Cui, M. S. Thompson, and J. P. Reilly, "Pathways of peptide ion fragmentation induced by vacuum ultraviolet light," *J. Am. Soc. Mass Spectrom.*, vol. 16, no. 8, pp. 1384–1398, 2005.
- [243] A. Vogel and V. Venugopalan, "Mechanisms of Pulsed Laser Ablation of Biological Tissues," *Chem. Rev.*, vol. 103, no. 2, pp. 577–644, 2003.

---

[244] H. Oshikane, M. Watabe, and T. Nakaki, "A simple and effective method for detecting precipitated proteins in MALDI-TOF MS," *Anal. Biochem.*, vol. 546, no. November 2017, pp. 1–4, 2018.

## 9 Appendix

### 9.1 Figures

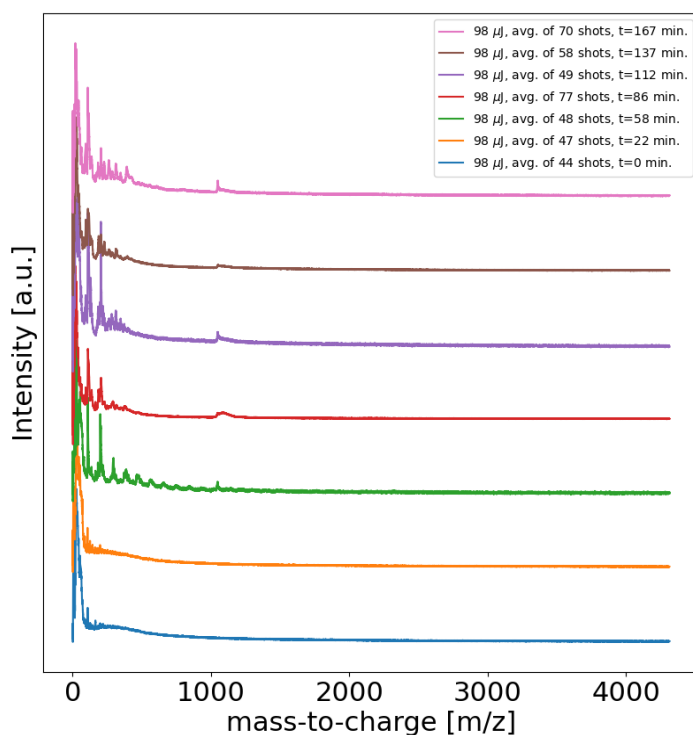


**Figure A 1** Temperature-dependent series of mass spectra of 100  $\mu\text{M}$  bradykinin in different water-glycerol ratios. The lowest mass spectrum was recorded at  $-140\text{ }^\circ\text{C}$ . After the liquid nitrogen supply was cut, the warm-up phase started. More details about the temperature profile can be found in subsection 4.2.4. For sample preparation, 750 nl were pipetted, which corresponds to 30  $\mu\text{m}$  thickness. Irradiation was performed in reflection geometry, and data were acquired in an oversampling mode, while the pulse energies were held constant at 98  $\mu\text{J}$ . Bradykinin embedded in 7.5 % glycerol.

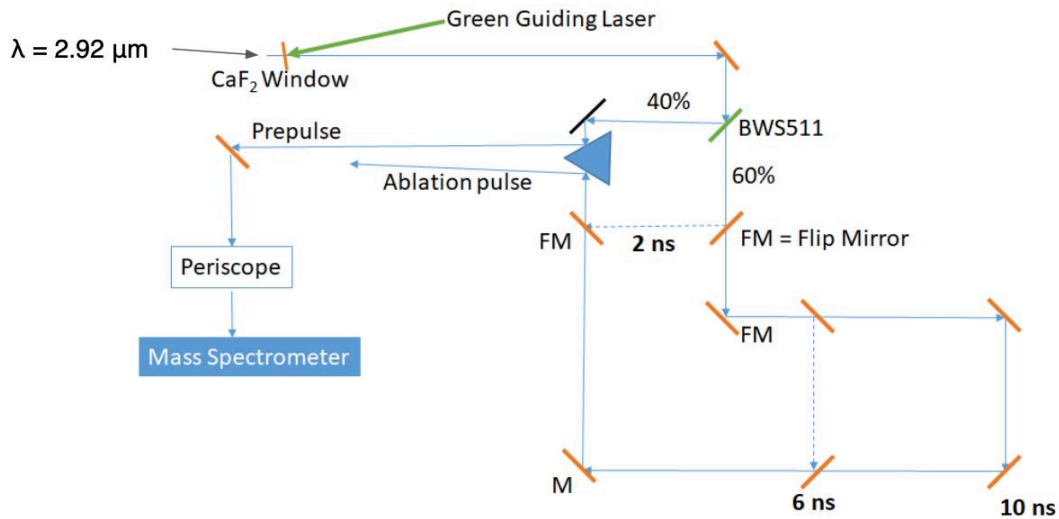
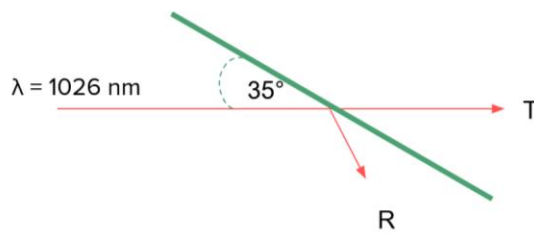


**Figure A 2** Mirror arrangement and laser beam paths in a pre-pulse experiment.



	Reflected Energy [%]	Transparent Energy [%]
No Substrate	-	100
Indium Tin Oxide	6	93
Silicon	50	48
Borosilica	6	92
Chalcogenide glass	41	58

**Figure A 3** Substrates were irradiated with 1026 nm under an angle of 35°. The transmitted (T) and reflected (R) laser beam was measured with Coherent LabMax power meter and a C120VC head.

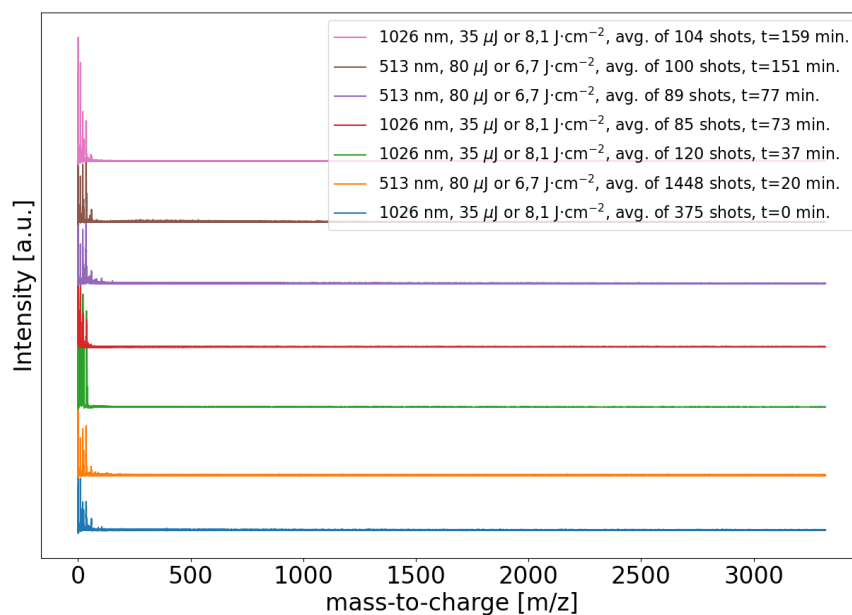


**Figure A 4** Temperature-dependent series of mass spectra of 100  $\mu\text{M}$  bradykinin on borosilicate. The lowest mass spectrum was recorded at  $-140\text{ }^\circ\text{C}$ . After the liquid nitrogen supply was cut, the warm-up phase started. More details about the temperature profile can be found in subsection 4.2.4. For sample preparation, 200 nl were pipetted, which corresponds to  $2\text{ }\mu\text{m}$  thickness. On average higher laser pulse energies were used compared to other substrates (Silicon, ITO and chalcogenide glass). Only substrate signals could be detected and no bradykinin signal is visible.

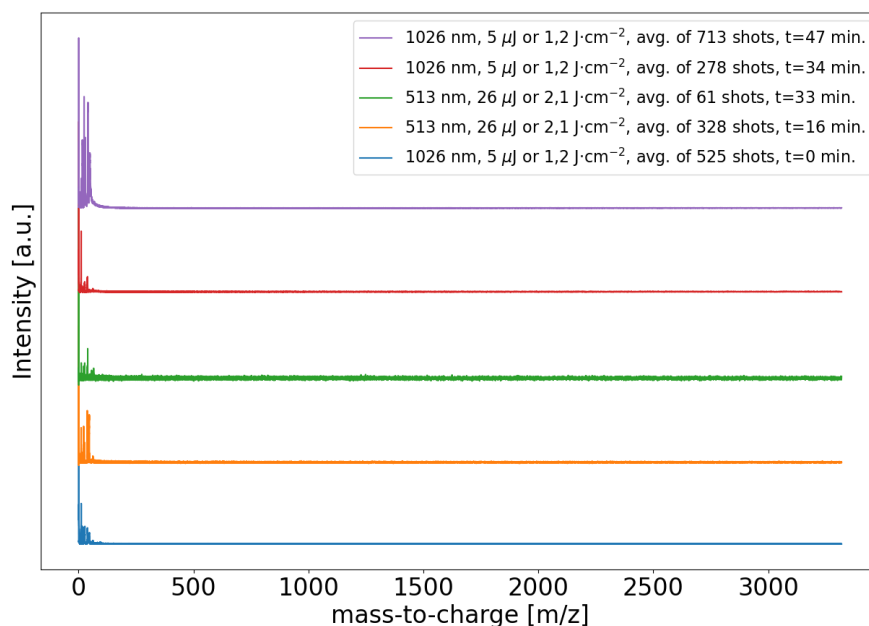


**Figure A 5** Temperature-dependent series of mass spectra of 100 μM bradykinin on borosilicate. The lowest mass spectrum was recorded at -140 °C. After the liquid nitrogen supply was cut, the warm-up phase started. More details about the temperature profile can be found in subsection 4.2.4. For sample preparation, 200 nl were pipetted, which corresponds to 2 μm thickness. Only substrate signals could be detected and no bradykinin signal is visible. Experimental condition were the same compared to Figure A3 except the lower pulse energies here. Substrate peaks have a lower intensity and the bradykinin signal is absent.



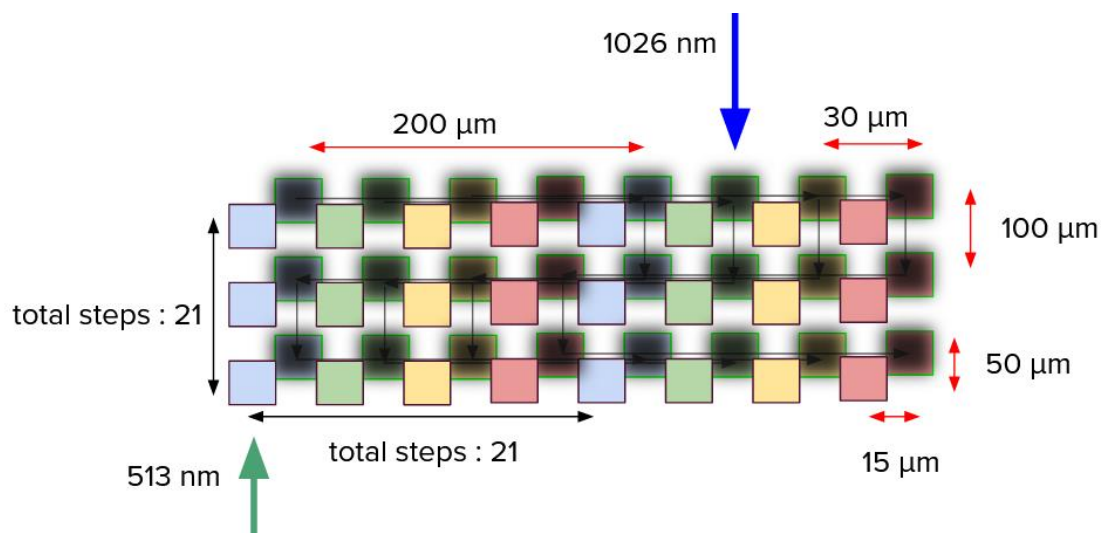


**Figure A 6** Data acquisition strategy to minimize biases introduced with sample inhomogeneity. The squares represent a single laser shot on a substrate. The different colors combine a group of laser shots to acquire a single mass spectrum. Each row of the same color is distanced  $200\ \mu\text{m}$  in y-direction. Different mass spectra were acquired by placing the laser shots  $30\ \mu\text{m}$  apart in y-direction. Such distance prevents undesired overlapping of laser shots. The dark blurred squares represent the pattern for data acquisition with another wavelength. The data acquisition is the same as described above. In total for a single mass spectrum a  $21 \times 21$  array was scanned resulting in 441 shots.

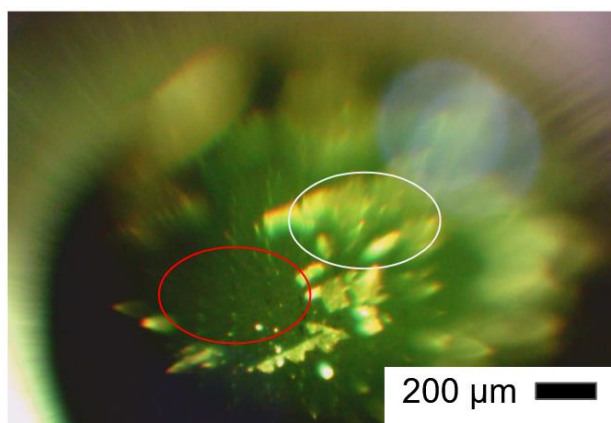


**Figure A 7** A brightfield image in the mass spectrometer. The white circle indicates a sample region with low intensity bradykinin signal and the red circle indicates an area with high intensity signal.

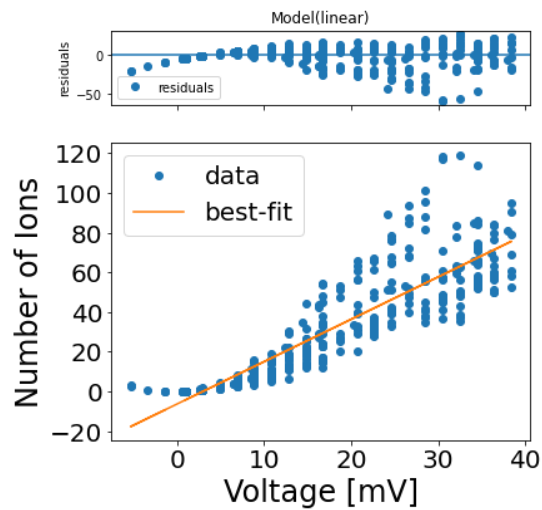


**Figure A 8** Signal voltage intensity in dependence of the number of ions. A) A graph shows residuals from the linear fit function. B) A scatter plot of bins which were obtained from single shot mass spectra. According to the slope of the linear fit function a single ion is producing 1.08 mV. The function parameters are  $y = 2.13 \cdot x - 6.39$ . Overall 19 single shot mass spectra were used for the calculation. datum 2020-09-21

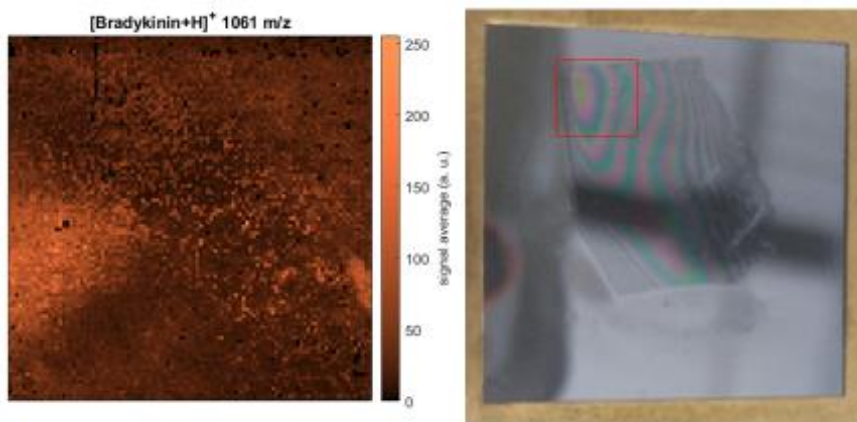


**Figure A 9** Non-resonant IR-LDI imaging of a thin ice film containing 100  $\mu\text{M}$  Bradykinin. A) The intensity of the bradykinin signal is plotted. B) A brightfield image of the specimen.

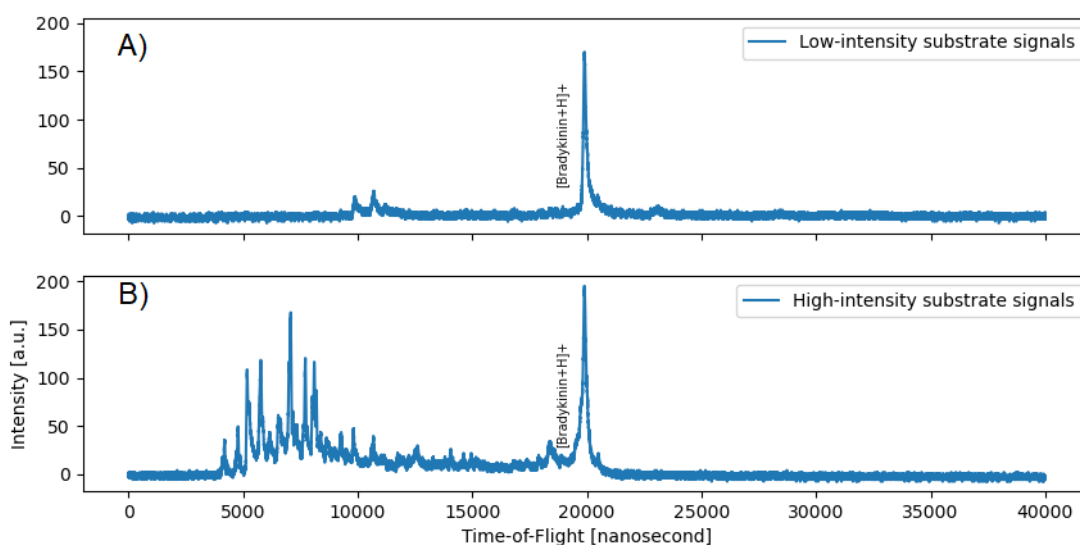


**Figure A 10** Single shot mass spectra of 100  $\mu\text{M}$  bradykinin from the same data set. A) Bradykinin arriving at the detector almost as a single species. B) Bradykinin signal is accompanied by substrate ions.

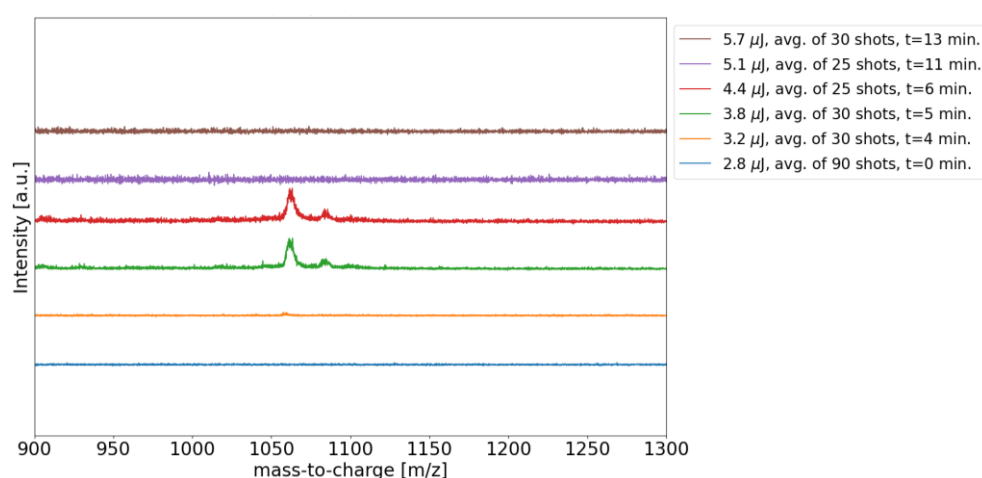


**Figure A 11** Threshold fluence for bradykinin signal onset on a silicon substrate for during **1026 nm irradiation**. During the investigation, the temperature at the sample stage was estimated to  $-70\text{ }^{\circ}\text{C}$ . While pulse energies between 2.8 and 3.2  $\mu\text{J}$  missed to produce an analyte signal, higher pulse energies between 3.8 and 4.4  $\mu\text{J}$  gave a signal with a high signal-to-noise ratio. Pulse energies above 5  $\mu\text{J}$  did not produce a signal. A possible explanation is the intense substrate signals (not in the image), which oversaturates the detector and reduces analytical performance. For the experiment 100  $\mu\text{M}$  bradykinin solution and 170 nanoliters were used.

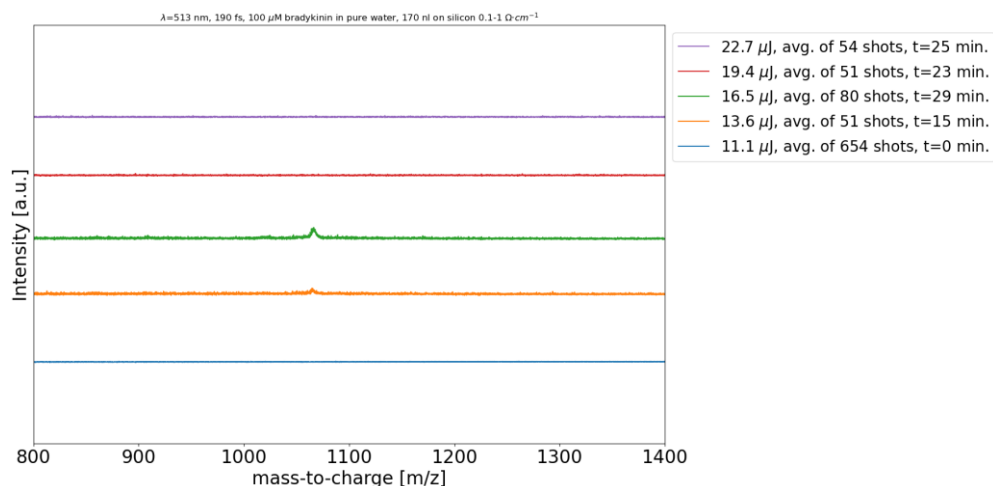


**Figure A 12** Threshold fluence for bradykinin signal onset on a silicon substrate **during 513 nm** irradiation. During the investigation, the temperature at the sample stage was estimated to  $-70$   $^{\circ}\text{C}$ . While pulse energies below 11  $\mu$ J missed to produce an analyte signal, higher pulse energies between 13.6 and 16.5  $\mu$ J gave a signal with a high signal-to-noise ratio. Pulse energies above 19.4  $\mu$ J did not produce a signal. A possible explanation is the intense substrate signals (not in the image), which oversaturates the detector and reduces analytical performance. For the experiment 100  $\mu$ M bradykinin solution and 170 nanoliters were used.

## 9.2 Tables

**Table A1** Ions produced after femtosecond irradiation (1026 nm) under cryogenic and non-cryogenic condition of a silicon cover slip.

Calculated Mass [m/z]	Flight Time [ $\mu$ s]	Element/Molecules	Theoretical Mass [m/z]
0.993	0.996	Proton	1.008
2.043	0.586	H <sub>2</sub> <sup>·</sup>	2.016
2.988	0.161	Tritium	3.024
8.931	0.037	-	
11.787	0.346	<sup>12</sup> C	12.011
12.753	0.048	<sup>13</sup> C	13.019
14.853	0.027	-	
15.777	0.040	O <sup>+</sup> <sup>·</sup>	15.999
16.890	0.070	OH <sup>+</sup> <sup>·</sup>	17.007
17.835	0.140	H <sub>2</sub> O <sup>+</sup> <sup>·</sup>	18.015
18.990	0.273	H <sub>3</sub> O <sup>+</sup>	19.023
22.812	0.837	Na <sup>+</sup>	22.989
26.739	0.486	<sup>28</sup> Si <sup>+</sup>	28.085
27.810	0.359	<sup>29</sup> Si <sup>+</sup>	29.093
28.776	0.104	<sup>30</sup> Si <sup>+</sup>	30.101
38.646	0.992	K <sup>+</sup>	39.098
39.717	0.416	Ca <sup>+</sup>	40.078
43.791	0.128	SiO <sup>+</sup>	44.084
44.841	0.243	SiOH <sup>+</sup>	45.092
55.593	0.111	2 <sup>28</sup> Si <sup>+</sup>	56.17
56.874	0.258	<sup>28</sup> Si <sup>+</sup> and <sup>29</sup> Si <sup>+</sup>	57.085
57.924	0.280	2 <sup>29</sup> Si <sup>+</sup>	58.186
59.919	0.184	<sup>29</sup> Si <sup>+</sup> and <sup>30</sup> Si <sup>+</sup>	59.194

**Table A2** All possible fragmentation ions from bradykinin. In addition frequently occurring satellite ions are also captured within the table. Fragmentation ions marked with an asterisks require a double cleavage. The masses presented in this table include a proton attachment.

Bradykinin Fragment + Proton [m/z]	Name	Bradykinin Fragment+ Proton [m/z]	Name
130.19	a1	533.59	x4
158.2	b1	556.67	b5
159.19	z1	571.68	c5
173.22	c1*	615.74	a6
174.2	y1	637.73	z5
202.21	x1	643.75	b6
227.31	a2	652.75	y5
255.32	b2	658.76	c6*
270.34	c2*	680.76	x5
306.37	z2	694.79	z6
321.38	y2	709.81	y6
324.42	a3	712.85	a7
349.39	x2	737.82	x6
352.44	b3	740.86	b7
367.45	c3	755.88	c7
381.48	a4	793.92	z7*
405.5	z3*	806.92	y7
409.49	b4	834.93	x7
418.45	y3	860.03	a8
424.51	c4	888.04	b8
446.51	x3	891.04	z8*
490.56	z4	903.06	c8
505.57	y4	904.04	y8
528.66	a5	932.5	x8

---

## 10 Acknowledgment

Although written by a single person, this work could not have been published without the help of many talented people, and I was fortunate to encounter and work with them. I want to thank Prof. R. J. Dwayne Miller for giving me the chance to work on an exciting project and be a part of this grand vision for the mass spectrometric community. Thank you for all the discussion and patience during the project. I also want to thank Prof. Dr. Hartmut Schlueter for being my first supervisor and for the many discussion and hands-on advice for the experiments. My special thanks goes to Prof. Dr. Arwen Pearson for being not only my second supervisor but also for the motivating and encouraging talks during the project.

Many thanks to Dr. Sascha W. Epp for the immense support throughout the whole project. You supported me with your critical question at the right time and your vast knowledge in the laboratory environment. It was a rewarding time working with you and your guidance. The very first introduction in the laboratory and the working principles of the submarine were given by Frederik Busse. Many thanks for the time and patience you invested in me, and I know it took me a bit longer to understand some techniques. Also, many thanks for the friendship also after our career path split. My special thank goes to Glaynel Alejo and her impact on the data analysis of the present work. I am still impressed by your decision to stay and finish the project we started, although the pandemic's impact was not foreseeable. I am well aware, and I know the research question would otherwise have taken much longer. Many thanks for this commitment.

I need to thank for the immense support from our workshop. Djordje Gitaric and Josef Gonshior for helping to build the time-of-flight mass spectrometer and the constant support. Thank you also for the rapid realization of small changes in the instrument during crucial experimental times. My thanks also extend to Friedjof Tellkamp, Jan P. Leimkohl, Hendrik Schikora, and Martin Kollwe for helping with all the lab issues and the support concerning the sample loading and sample stage. Also, I would like to thank Elena Koenig for helping in measuring and analyzing AFM images.

---

I would like to express my gratitude to my subgroup colleagues Heinrich Schwoerer, Gabrielle Tauscher, Meghanad Kayanattil, and Zhipeng Huang. Most notably, the long discussions and constant input concerning all aspects of the project, especially the data analysis and interpretation. My other working colleagues, Maria Katsiaflanka, Guenther Kassier, Vandana Tiwari, Hyein Huang, and Johannes Kaub. I would like to thank you for answering my questions, help, and opinion whenever I needed it most. Also, I am looking back at some fun evenings which we spent together. Special thanks to Wesley D. Robertson, who was only at the beginning of my project in the group but still provided help across the Atlantic ocean.

In addition, I would like to express my gratitude to my office mates Ajay Jha and Zheng Li. It was an honor to spend time with two highly skilled scientists listening to your opinions and views and talking about culture, food, and an atmosphere that welcomed life beyond science.

I would like to thank my collaboration partner Jan Hahn at the UKE. For fruitful discussion and the opportunity to learn from you. This collaboration involved Clarissa Klenke, who did a great job in protein extraction out of artificial matrices. This was a big leap as others failed to do so. Thank you for the endurance until the very last days of the experiment.

I like to thank all members of the IMPRS school and all the Ph.D. fellows who supported me during the time being. Here is a special thanks to Karina Kazarian, who is still practicing with me my Russian skills. I am very grateful to Julia Quante, who believed in me as a person from the beginning. In the IMPRS environment, I am very glad to have met Neda Lotfiomran. I am still thrilled by your passion for helping the students whenever you can. I know certain things would have run differently if I did not have your advice.

Modern science usually requests not only good ideas but also a good infrastructure in case things need to be done quickly. The purchasing team Ulrike Kruger and Sergiy Devgopol did an exceptional job and whenever things needed to be ordered fast. That saved a lot of time in messy times. Also, special thanks to the human resource team Kathja Schroeder and Tania Hartin, for running things smoothly in the background. Also, I would like to thank Kirsten Teschke for all the small favors throughout the time in the Max Planck Institute.

Although not present in the project, I would like to thank Anna Kreuziger and Jan Willem de Vries for their support during my bachelor's and master and for paving for me the way to become the scientist I am now.

Finally, I would like to thank my mother and grandmother for their constant support. I truly appreciate your trust in my decisions and the fact that you always helped me out wherever you could. Lastly, a special thank to my friends for cheering me up when times were difficult.

---



---

## 11 CMR-Chemicals

No carcinogenic, mutagenic and toxic chemicals with the GHS categories 1A and 1B were used in this work.

---

## 12 Affidavit (eidesstattliche Erklärung)

Hiermit versichere ich an Eides statt, dass die vorliegende Arbeit von mir selbständig verfasst wurde und ich keine anderen als die angegebenen Hilfsmittel – insbesondere keine im Quellenverzeichnis nicht benannten Internet-Quellen – benutzt habe und die Arbeit von mir vorher nicht einem anderen Prüfungsverfahren eingereicht wurde. Die eingereichte schriftliche Fassung entspricht der auf dem elektronischen Speichermedium. Ich bin damit nicht einverstanden, dass die Masterarbeit veröffentlicht wird.

A handwritten signature in black ink, consisting of stylized, cursive letters.

Hamburg, 05.12.2022